Institut National Polytechnique de Grenoble

Thèse

pour obtenir le grade de

docteur de l'INPG

Spécialité « Océans, Atmosphères, Hydrologie »

préparée au sein du

Laboratoire des Écoulements Géophysiques et Industriels

dans le cadre de

l'École Doctorale Terre, Univers et Environnement

présentée et soutenue publiquement par

Rodrigo A. CIENFUEGOS C.

le 24 Novembre 2005

Modélisation Numérique des Houles Bidimensionnelles et du Déferlement Bathymétrique

Numerical Modelling of Two Dimensional Water Wave Propagation Processes and Topographically Induced Breaking

---

Directeur de Thèse

Eric BARTHÉLEMY

Co-encadrant

Philippe BONNETON

JURY

Dr.	P. Foray, Professeur, INPG	Président du jury
Dr.	P. Sergent, Directeur Scientifique DRIM-CETMEF	Rapporteur
Dr.	M. Brocchini, Professeur Associé, Universita' di Genova	Rapporteur
Dr.	M. Stive, Professeur, TU Delft	Examinateur
Dr.	F. Ardhuin, Chercheur au SHOM	Examinateur
Dr.	E. Barthélemy, Professeur, INPG	Directeur de Thèse
Dr.	P. Bonneton, Chargé de Recherche CNRS, UMR EPOC	Co-encadrant

Pour Maïté et Diego

"Se debe escribir en una lengua que no sea materna."
"Los cuatro puntos cardinales son tres : el sur y el norte."

Vicente Huidobro
extrait du Préface de "Altazor"

Remerciements

Le travail qui s'achève avec l'impression de ce manuscrit n'a pas toujours été facile, mais a toujours bénéficié du soutien et encouragement de nombreuses personnes que je tiens à remercier ici.

Tout d'abord je voudrais addresser ma gratitude et reconnaissance envers mon directeur de thèse, Eric Barthélemy, qui a fait preuve de la plus grande ouverture scientifique et humaine, en me transmettant un sens critique ainsi que des bases théoriques indispensables, tout en me donnant la possibilité de travailler avec grande autonomie et dans un cadre idéal. J'en serais toujours reconnaissant.

Mon co-directeur de thèse, Philippe Bonneton, a lui aussi contribué de manière importante à ce que ce travail s'achève correctement. Les discussions scientifiques qu'on a pu avoir, mais aussi les nombreux échanges amicaux qu'on a entretenus, ont sans aucun doute favorisé le bon déroulement de cette thèse.

À cette ocasion, je voudrais remercier les membres du Jury d'avoir accepté d'évaluer mes travaux de recherche. Le grand soin qu'ils ont accordé à cette tache et les suggestions et commentaires qu'ils ont pu fournir ont permis d'améliorer de façon importante le contenu scientifique de ce travail. Je remercie Pierre Foray, qui m'a accueilli avec enthousiasme dès mon arrivée en France, d'avoir accepté de présider le Jury. Ma reconnaissance s'addresse aussi aux Professeurs Stive et Brocchini, qui par leur grande expérience et connaissances scientifiques ont contribué à situer cette thèse dans le contexte international. Enfin, ma gratitude s'addresse de la même manière à Philippe Sergent et Fabrice Ardhuin, pour avoir accepté de faire partie du Jury et de représenter ainsi la communauté française travaillant dans le domaine de l'ingénierie côtière.

Ce travail de recherche n'aurait jamais été possible sans le soutien humain et financier de Conicyt, le Ministère des Affaires Étrangères français, et l'École d'Ingénierie de l'Université Catholique de Santiago du Chili. J'espère sincèrement avoir pu être à la hauteur des attentes scientifiques que ces différents partenaires s'étaient fixées.

Je tiens à remercier à tous les membres de l'équipe Houle, dont Hervé Michallet, Philippe Larroudé, David Hurther, Jean-Marc Barnoud, Maryam Kamalinezhad, Mickael Bricault, Benoît Camenen, André Temperville et Emmanuel Mignot, avec lesquels j'ai pu partager des moments importants, et qui ont aussi, d'une manière ou d'une autre, contribué à faire ce parcours plus agréable et passionnant.

J'en saurai jamais remercier assez les nombreux amis, "nouveaux" et "anciens", qui par leur soutien et chaleureuse amitié ont permis d'enrichir mon séjour en France en le rendant particulièrement plaisant. Je ne les oublierai jamais.

Je n'oublie pas non plus les membres de ma famille, qui par leur encouragement permanent et leur mots de soutien, ont toujours été très près de moi, même en étant à plusieurs milliers de kilomètres d'ici.

Le soutien inconditionnel, la tendresse et l'amour que Maïté m'a toujours apportés ont été une source permanente d'énergie et d'inspiration pour pouvoir mener cette thèse à bon port. Elle y est pour beacoup !

Enfin, je voudrais remercier le petit Diego qui est venu au monde à la fin de ma première année de thèse, et a donc pu y participer de manière très active. Les beaux souvenirs que je garderai de cette période sont bien évidemment étroitement liés à cet évênement magique. Merci Diego pour ton sourire et ton regard d'enfant !

Contents

List of Figures

List of Tables

Chapter 1

Introduction Générale

1.1 Intérêts et enjeux scientifiques

Le travail de recherche qui sera présenté dans cette thèse s'insère de manière générale dans le domaine de l'ingénierie côtière. Nous aborderons en particulier des aspects théoriques et pratiques en rapport avec la description et la prédiction de l'hydrodynamique littorale depuis des profondeurs intermédiaires et jusqu'au trait de côte. Les outils mathématiques à développer devront alors être capables de fournir une description fiable et précise des différents processus, essentiellement non linéaires, qui s'avèrent être les principaux responsables de la déformation spatio-temporelle que les vagues subissent lors de leur propagation sur des bathymétries complexes.

L'intérêt croissant que la communauté scientifique internationale a porté ces dernières années aux aspects hydrodynamiques liés à la propagation de la houle et du déferlement bathymétrique a été en grande partie motivé par l'aggravation progressive et généralisée des problèmes d'érosion côtière. Ce phénomène a pour conséquence visible une diminution importante des surfaces des terres émergées. C'est ainsi qu'une étude menée à l'échelle mondiale a montré que près de 70 % des côtes (en longueur) auraient été en phase d'érosion vers la moitié des années 1980's (cf. Bird [16]). Par ailleurs, une récente étude commanditée par l'Union Européenne conclue qu'un cinquième du littoral de ses pays membres serait fortement touché à l'heure actuelle [59]. Il s'avère de manière assez claire que cette situation préoccupante est la conséquence, plus ou moins directe, des effets que les activités humaines peuvent avoir sur l'environnement.

D'autre part, il est de plus en plus évident que les enjeux économiques et sociaux liés aux zones littorales sont considérables. En effet, une partie importante de la population mondiale habite à moins de dix kilomètres des côtes [16] et les activités tel que le transport maritime et portuaire, l'industrie et le tourisme sont particulièrement

concernées. D'un autre côté, les sites naturels situés à la frontière entre la terre et la mer produisent souvent un cadre propice pour le développement d'une biodiversité richissime et constituent donc un patrimoine écologique inestimable. Malheureusement, ces écosystèmes privilégiés sont la plus part du temps le résultat d'intéractions biophysiques subtiles et leur existence même peut être compromise lorsque les équilibres naturels sont légèrement perturbés.

Tout le long du XXème siècle, la lutte contre l'érosion des côtes a été principalement abordée à l'aide de solutions radicales qui ont nécessité la mise en place de structures lourdes tel que des digues ou des brises-lames, produisant les effets attendus seulement de manière très locale. En effet, on commence à comprendre aujourd'hui que ces ouvrages d'ingénierie modifient de façon importante le transit sédimentaire naturel provoquant dans le moyen ou le long terme une aggravation globale du problème initialement visé. Par conséquence, une gestion du littoral respectueuse des équilibres naturels qui trouverait un compromis efficace et durable entre la protection des intérêts anthropiques et de l'environnement doit être encouragée par les autorités concernées. Bien évidemment, la tâche est d'envergure, non seulement en raison des divers conflits politiques, économiques ou environnementaux qui en découlent, mais aussi et surtout parce que l'état actuel des connaissances scientifiques qui permettrait de fournir des réponses plus ou moins objectives, reste encore largement insuffisant.

Les predictions de court ou moyen terme des évolutions hydrosédimentaires des plages sableuses ont été jusqu'à présent abordées surtout à partir de modèles méso-échelles. Ces outils résultent d'un moyennage des équations du mouvement, à la fois spatial sur la profondeur d'eau et temporel sur une période caractéristique de la houle incidente. Dans la pratique, cette approche méso-échelle permet de fournir des informations importantes sur l'organisation globale des courants moyens dans la zone côtière. Cependant, elle s'avère inefficace dans la prediction de certains processus sédimentaires qui nécessitent la prise en compte de phénomènes plus fins. C'est le cas en particulier de la dynamique complexe des barres sableuses dans la zone de déferlement. Or, ces barres littorales constituent une protection naturelle contre l'érosion en favorisant la dissipation de l'énergie incidente des houles et en fournissant du sable pour remblayer les plages.

Dans les dernières années quelques constributions marquantes suggèrent que des efforts de recherche visant à améliorer la prédiction numérique, à la fois dans l'espace et dans le temps, de l'évolution des profils des vagues doivent être poursuivis. C'est ainsi qu'à l'aide d'une modélisation discrète d'un lit de grains de sable soumis à un forçage hydrodynamique périodique de forme paramétrique, Drake et Calantoni [52] furent en mesure de confirmer qu'un flux net de sédiments dans la direction de propa-

gation de la houle pouvait être engendrée sous l'influence des effets d'accéleration que l'écoulement introduisait dans la couche limite de fond. En particulier, le coefficient d'asymétrie horizontal associé à la série temporelle de la vitesse du fluide fut identifié comme étant le paramètre responsable de ce type de réponse hydro-sédimentaire. Il est important d'attirer l'attention du lecteur sur le fait que ce résultat théorique a des conséquences pratiques importantes en ce qui concerne la conception de solutions alternatives pour lutter contre les problèmes d'érosion évoqués précédemment. En effet, Drake et Calantoni [52] ont pu mettre en évidence le mécanisme physique responsable du remblayement naturel des plages qui est normalement observé en périodes d'accalmie.

L'idée sous jascente dans les méthodes de protection du littoral dites « douces » consiste justement à renforcer ou favoriser le mécanisme naturel de rechargement des plages par le biais d'apports supplémentaires de sédiments stratégiquement placés visant par exemple à la création ou le rétablissement d'un système dunaire au large des sites concernés. Cependant, cette stratégie qui s'avère être respectueuse de l'environnement ne pourra être envisagée efficacement qu'à condition de disposer d'outils de prédiction fiables qui tiendraient compte au minimum des effets non linéaires responsables de la déformation spatio-temporelle des houles par le fond.

Les conclusions apportées par l'étude de Drake et Calantoni [52] ont été récemment confirmées dans le milieu naturel par Hoefel et Elgar [78] qui ont réussi a reproduire numériquement la migration vers la côte d'une barre de sable longitudinale en utilisant une formule de transport sédimentaire incluant les effets d'accélération dissymétrique du fluide près du fond. Ce mécanisme d'accrétion sédimentaire serait en effet efficace lorsque le courant de retour est faible, ce qui expliquerait pourquoi le remblayement naturel des zones littorales a lieu pincipalement en périodes de beau temps.

Dans l'état actuel des connaissances, une description mathématique complète des processus physiques concernés n'est pas encore possible. En particulier en raison de la compléxité inhérente aux interactions houle-courant-turbulence qui mobilisent une quantité non négligeable de sédiments dans le zone affectée par le déferlement. Cependant les travaux cités plus haut fournissent des pistes précieuses en ce qui concerne les mécanismes que nous devons au minimum être en mesure de décrire.

Dans ce contexte, les travaux présentés dans cette thèse cherchent en particulier à fournir un outil de prédiction fiable et efficace de la déformation spatio-temporelle que subit la houle sous l'influence du fond lors de sa propagation vers la côte. L'effort est porté, en raison des arguments exposés précédemment, sur une modélisation hydrodynamique capable de fournir une description détaillée de la propagation des ondes de gravité à proximité du littoral. Nous cherchons à développer une approche numérique

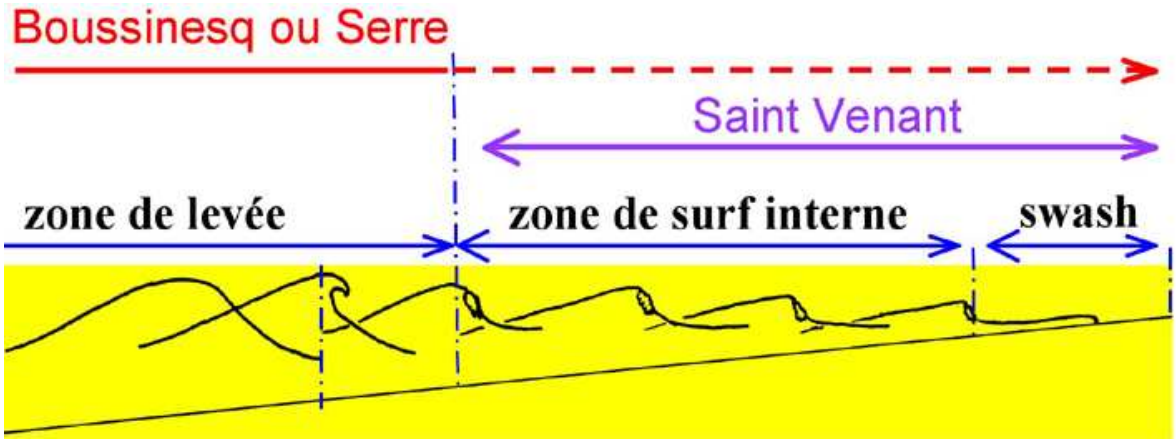

Figure 1.1: Définition schématique des domaines d'application des équations de Boussinesq et Serre ainsi que les équations de l'eau peu profonde de Saint-Venant.

qui, d'une part permettrait de décrire les principaux mécanismes non linéaires responsables de l'évolution des vagues dans la zone de levée, et d'autre part, qui inclurait le phénomène du déferlement en introduisant une dissipation d'énergie à l'échelle macroscopique en accord avec la réalité physique tout en reproduisant la forme caractéristique des vagues en dent de scie dans la zone de déferlement.

Les équations dites de la famille de Boussinesq répondent parfaitement au cahier des charges établi pusiqu'elles se situent à mi chemin entre une modélisation 3D complète, qui s'avère très coûteuse en terme de ressources informatiques, et une approche méso-échelle moyennée dans la phase qui nécessite une paramétrisation supplémentaire de façon à reconstruire les profils temporels des vagues. En effet, et contrairement aux équations de Saint-Venant qui sont tout au mieux valables dans la zone de surf interne (cf. [17, 174]), les versions les plus récentes des modèles de Boussinesq permettent une description convenable de la propagation de la houle depuis des profondeurs intermédiaires et jusqu'au trait de côte (voir par exemple la référence [87] ainsi que le schéma présenté dans la Figure 1.1). Cependant, des efforts sont encore requis en ce qui concerne la paramétrisation du déferlement dans le cadre d'application de cette famille d'équations, en particulier de manière à décrire correctement à la fois la décroissance en amplitude des ondes qui a lieu dans la zone affectée par le déferlement et l'asymétrie horizontale qui caratérise l'évolution spatio-temporel des profils de surface libre.

Il est important de noter que même si le travail développé tout le long de cette thèse s'insère dans une optique hydrodynamique visant à terme des aspects sédimentaires, le domaine d'application des équations de Boussinesq dépasse ce cadre. Elles constituent un outil prédictif performant utilisable, par exemple, dans des études d'agitation portuaire (e.g. [182]), ou encore sur des problèmes d'interaction houle-structure (e.g. [64]).

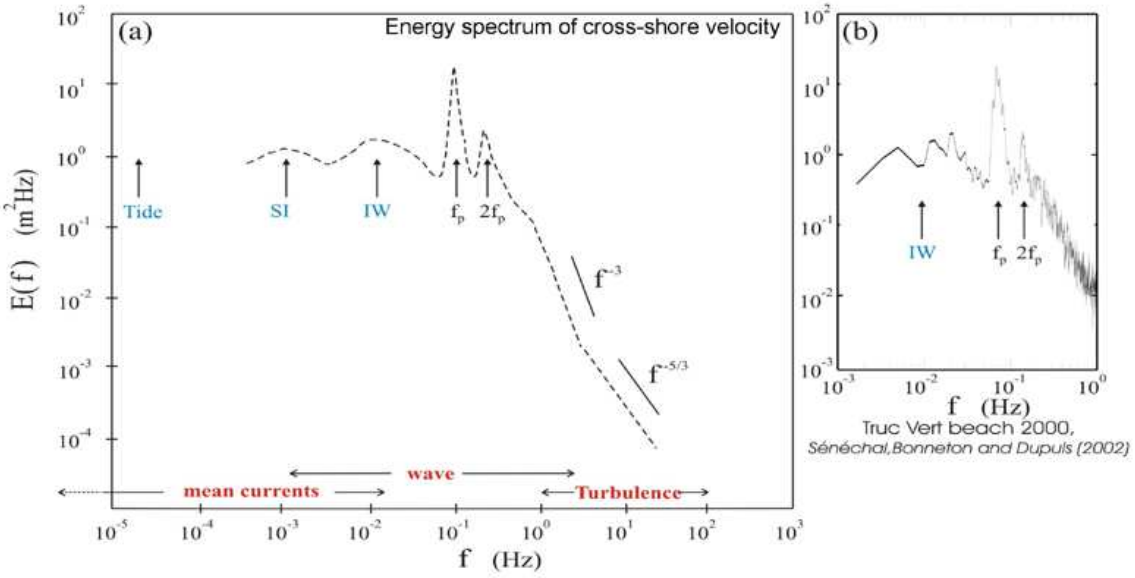

Figure 1.2: Spectre idéalisé de l'énergie incidente sur une plage apportée par les marées et les houles (d'après Bonneton [20]).

1.2 Contexte scientifique : le projet PATOM

Le travail scientifique developpé dans cette thèse fait partie d'un projet plus ambitieux mené depuis l'année 2001 au sein de la communauté Française. Il s'agit du projet « Hydrodynamique dans la zone affectée par le déferlement » conduit au sein du « Programme National Atmosphère et Océan à Multiéchelles » du CNRS-INSU[1]. Ce projet, animé par H. Michallet, regroupe 11 équipes de recherche et aborde des aspects en rapport avec la propagation de la houle dans la zone littorale et plus particulièrement le phénomène du déferlement bathymétrique. Il s'agit de proposer des améliorations pratiques sur la représentation mathématique des divers processus hydrodynamiques concernés. Ces améliorations devraient permettre à terme d'aborder des aspects sédimentaires en rapport avec les problèmes d'érosion evoqués dans la section précédente.

Dans le cadre du PATOM, des actions sont menées visant à la fois à un approfondissement des connaissances physiques fondamentales à l'aide d'expériences de laboratoire et in-situ ainsi qu'à l'amélioration de la modélisation de l'hydrodynamique littorale. Les axes de recherche concernent diverses échelles physiques comme le montre le contenu fréquentiel d'énergie qui atteint la côte dans la Figure 1.2. Ces différentes échelles spatio-temporelles sont étudiées avec des outils adaptés de manière à mieux

[1]Programme PATOM, Centre National de la Recherche Scientifique (CNRS), Institut National des Sciences de l'Univers (INSU).

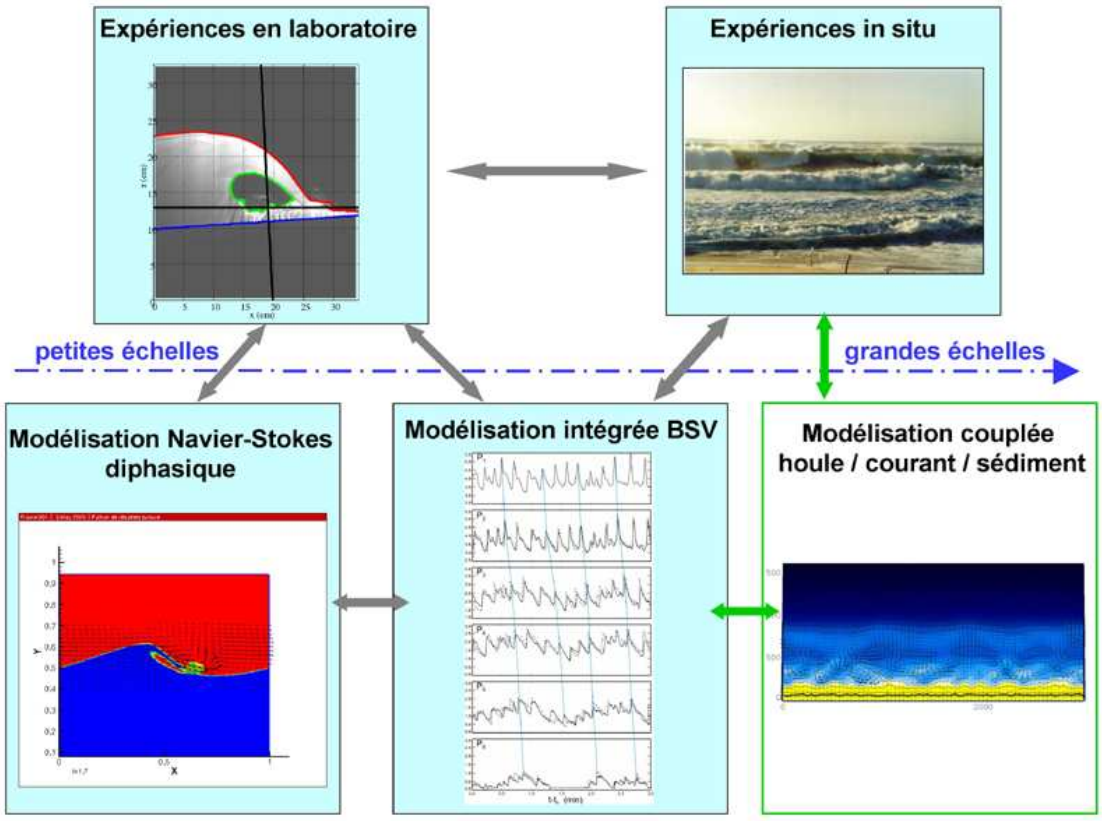

Figure 1.3: Principales actions de recherche menées par la communauté Française dans le cadre du projet « Hydrodynamique dans la zone affectée par le déferlement » du PATOM (d'après la présentation à la « Réunion Prospectives Septembre 2005 »).

apréhender les mécanismes responsables du rapide transfert de quantité de mouvement et de masse qui ont lieu au cours du déferlement. Il s'agit en même temps d'explorer des techniques opérationnelles ayant pour but de simuler numériquement leur évolution (voir schéma de la Figure 1.3).

C'est ainsi que des études en laboratoire sont en cours dans le canal à houle du LEGI (36 m) où des conditions d'équilibre morphodynamique résultant d'un forçage de houle aléatoire sur un fond mobile ont été obtenus [82, 83] (voir cliché de la Figure 1.4). Cette expérience originale fourni un cadre favorable à l'obtention de nouvelles informations indispensables à la compréhension des processus hydro-sédimentaires complexes responsables, entre autres, de la formation de profils à barre dans la nature. Il faut ajouter à cela que des mesures fines de turbulence ainsi que de la mobilisation des sédiments sous les vagues déferlées ont été déjà réalisées et devront fournir dans le futur proche une base de données adaptée à la validation du couplage entre les modèles numériques de propagation de houle et des formules de transport sédimentaire.

Figure 1.4: Déferlement d'une vague sur un fond granulaire dans le canal à houle du LEGI (photo prise par E. Perrin, CNRS).

Parallèlement, des expériences menèes par les équipes EGIM-IRPHE basées à Marseille sur une plage uniforme de pente 1:15 ont permis d'obtenir une représentation fine du champs des vitesses sous des vagues déferlantes à l'aide de la technique d'imagerie de particules (PIV) [86]. Ces mesures constituent une contribution novatrice au sein de la communauté internationale et devraient permettre de mieux appréhender les mécanismes de génération de vorticité et du transport d'énergie turbulente au cours du déferlement dans des conditions très proches de la réalité. Il est important de remarquer que l'obtention de tels mesures a nécessité la mise au point d'un savoir faire expérimental assez unique. La Figure 1.5 présente un exemple du champ de vorticité déterminé par la technique d'imagerie de particules.

Des mesures in-situ ont été réalisées par le laboratoire EPOC de l'Université Bordeaux dans l'océan Atlantique (campagne du Truc Vert, 2001 [138]) et par l'Université de Perpignan sur la plage de Sète en Méditerranée [33]. Ces expériences de terrain visaient à étudier d'une part les mécanismes de transfert non linéaire de l'énergie de la houle incidente vers des basses fréquences et le transport d'énergie turbulente à l'échelle nature, et d'autre part l'intéraction entre le forçage hydrodynamique et la morphologie des plages. De la même manière, les données disponibles pourront servir à poursuivre la validation des modèles de propagation de houle actuellement en développement.

Les aspects de modélisation numérique ont été abordés au sein du projet en utili-

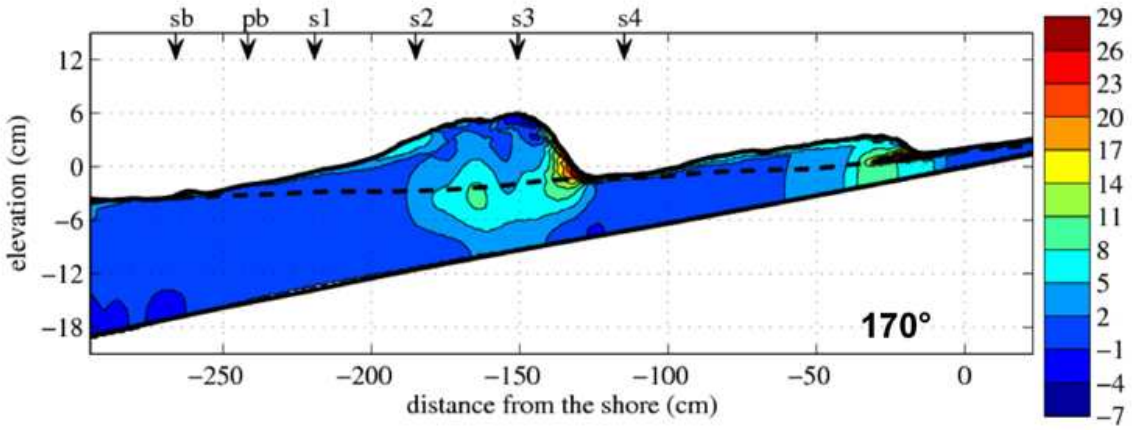

Figure 1.5: Exemple des mesures de vorticité sous des vagues déferlantes obtenues par l'équipe EGIM-IRPHE dans le canal à houle de Marseille (d'après Kimmoun et Branger [86]).

sant des approches Navier-Stokes 3D complètes (NS3D) très sophistiquées (e.g. [56, 103]), des stratégies « Boundary Element Methods » sur les équations d'Euler (e.g. [61]), des équations intégrées sur la profondeur type Saint-Venant et Boussinesq (e.g. [21, 39]), ainsi que des modèles méso-échelles moyennés dans la phase (e.g. [32]). Il est important de noter que chacune de ces stratégies de modélisation constitue en fait un sous-ensemble de plus en plus fin, et que cette approche multi-échelle devrait permettre d'améliorer la paramétrisation des processus non-résolus par les modèles opérationnels utilisables à l'échelle kilomètrique.

Les différentes équipes ayant travaillée sur des aspects NS3D diphasique se sont consacrées de manière particulière à la description de la zone de transition qui a lieu immédiatement après qu'une onde de surface ait atteint la condition de déferlement. En effet, cette région est caractérisée par une dissipation d'énergie rapide, ainsi que par une intensité turbulente importante. Il faut noter que les paramétrisations du déferlement utilisées dans les modèles type Boussinesq ou méso-échelles ne peuvent décrire cette transition que de manière très grossière. Les efforts de modélisation NS3D constituent donc une manière intéressante de mieux représenter et analyser la dynamique de la zone de transition afin d'améliorer les approches opérationnelles.

Finalement, il est impotant de noter que la nouvelle paramétrisation du déferlement qui sera présentée dans cette thèse, est en bonne partie le résultat des intéractions scientifiques qui ont pu avoir lieu au sein du PATOM. En particulier, les travaux réalisés depuis quelques années sur les approches numériques de capture de choc visant à représenter la dynamique des vagues en zone de surf interne ont fourni une base théorique inestimable pour l'approche alternative du déferlement qui sera développée

ici dans le cadre d'application des équations de la famille de Boussinesq.

1.3 Principaux objectifs et démarche scientifique

Cette thèse vise spécifiquement au développement d'un modèle hydrodynamique capable de décrire les évolutions spatio-temporelles de la houle au cours de sa propagation le long d'un profil de plage depuis la zone de levée et jusqu'au trait de côte. De manière à remplir les exigences de départ nous utilisons le système d'équations fortement non linéaire adapté à la description des écoulements non stationnaires à forte courbure obtenu pour la première fois par Serre [140]. Les travaux de Serre, malgré leur originalité, n'ont pas eu une grande répercussion au niveau de la communauté scientifique internationale au moment de leur publication. Cependant, ils ont continué a être approfondis en France, et en particulier au sein de l'ancien Institut de Mécanique de Grenoble. C'est ainsi qu'un certain nombre de thèses de doctorat ont été, de façon plus ou moins directe, consacrées à l'étude théorique des domaines de validité des équations de Serre dans un contexte d'eau peu profonde. Nous pouvons citer à titre d'exemple les travaux de Staub [147], Temperville [159], Seabra-Santos [135] ou encore Guibourg [74] qui abordèrent des aspects mathématiques et pratiques concernant surtout des problèmes en rapport avec la propagation d'ondes solitaires non déferlantes. En effet, ce n'est que très récemment qu'une reconnaissance internationale a été accordée au système d'équations de Serre dans un contexte d'ingénierie côtière (cf. [110]).

Les équations de Serre, généralisées dans la référence [136] à des applications sur fond variable, constituent une forme particulière de ce que l'on appelle aujourd'hui dans la littéraure anglosaxone les modèles de Boussinesq « fully nonlinear » ou complètement non linéaires. Elles s'obtiennent par intégration sur la verticale des équations d'Euler prenant soin de retenir tous les termes d'accélération convective associés aux fortes courbures des lignes de courant, et cela jusqu'à l'order $O[(\frac{h}{L})^2]$ où h et L sont respectivement des grandeurs représentatives de la profondeur d'eau et de la longeur d'onde. C'est ce compromis entre des termes d'ordre supérieur, à la fois non linéaires et dispersifs, qui rendent possible l'application de ce type d'équations à des conditions de propagation d'ondes de gravité jusqu'au point de déferlement comme a été démontré en particulier par les travaux réalisés dans l'Université de Delaware aux États Unis (e.g. [69, 178]).

Ce travail de thèse reprend donc le modèle de propagation de houle au stade où il avait été produit par Guibourg [74]. Cependant un certain nombre d'améliorations indispensables à son application dans un environnement côtier seront présentées car

l'objectif principal est de rendre disponible un outil hydrodynamique opérationnel à l'échelle de l'ingénieur. De manière à étendre dans la pratique le domaine de validité des équations de Serre vers des profondeurs plus importantes, ou alternativement, vers la représentation d'ondes de longueurs plus faibles, nous adoptons les méthodes d'amélioration des propriétés dispersives proposées par Madsen et al. [109] et Madsen et Schäffer [110]. Cette approche consiste à introduire des termes d'ordre supérieur dans l'équation de conservation de la quantité de mouvement afin d'obtenir une meilleure approximation de la relation linéaire de dispersion de Stokes. Par ailleurs, une approche alternative pour l'incorporation des effets liés au déferlement sera étudiée en nous inspirant, à la fois de la théorie des chocs dans le cadre des équations de l'eau peu profonde, et de quelques résultats expérimentaux récemment publiés. De plus, un effort important sera consacré au développement d'un schéma numérique original, particulièrement adapté à la résolution du modèle hydrodynamique ainsi obtenu.

1.4 Organisation de la thèse

En accord avec les objectifs que nous nous avons fixés, le travail de thèse a été articulé en deux grandes parties. La première d'entre elles est consacrée à l'obtention d'un système d'équations étant en mesure de décrire les phénomènes non linéaires associés à la propagation de la houle sur des bathymétries complexes dans la zone de levée et jusqu'au point de déferlement. Ensuite nous décrivons une stratégie numérique originale spécialement conçue pour intégrer le système à dérivées patielles à la fois dans l'espace et le temps (Chapitres 2 et 3). Dans la deuxième partie, nous aborderons des aspects théoriques et expérimentaux en rapport avec le déferlement bathymétrique de façon à construire un modèle mathématique qui puisse introduire la dissipation d'énergie associée tout en respectant la forme caractéristique en dent de scie des vagues déferlantes (Chapitres 4 et 5).

Les aspects théoriques et pratiques concernant l'obtention du système d'équations de Serre étendu et sa résolution numérique seront développés dans les Chapitres 2 et 3. Le Chapitre 2 est consacré à la présentation de la démarche théorique permettant l'obtention des équations, les principales hypothèses requises ainsi que leurs limites d'applications. De la même manière, une description complète et analyse du nouveau schéma aux volumes finis spécialement conçu pour résoudre le système d'équations est présenté dans ce chapitre. En particulier, l'étude des propriétés spectrales, stabilité linéaire ainsi que la performance du schéma en présence de fortes non linéarités sera abordé en profondeur. Cette démarche permettra d'illustrer de manière objective les

principaux avantages pratiques que la nouvelle méthode présente par rapport aux précédentes stratégies utilisées pour intégrer des équations équivalentes. Dans un deuxième temps, le Chapitre 3 sera consacré à la validation de la pertinence physique des équations de Serre dans le cadre de l'hydrodynamique littorale. Pour cela, des conditions aux limites adaptées à la problématique visée seront développées et la performance du modèle testée à l'aide de nombreuses applications expérimentales originales ou déjà disponibles dans la littérature. Une fois cette tâche accomplie, nous pourrons ensuite avancer vers l'incorporation du déferlement dans le modèle.

Dans le Chapitre 4, une analyse critique de l'état de l'art des connaissances en rapport avec le phénomène du déferlement sera présentée. Nous nous consacrerons à étudier le concept de rouleau de déferlement tel qu'il a été introduit par Svendsen [154] en 1984. En utilisant des mesures expérimentales rigoureuses et récentes obtenues sur toute la colonne d'eau pour des ressauts quasi-stationnaires en similarité de Froude avec des vagues en zone de surf, nous évaluerons la validité du concept de rouleau de déferlement ainsi que ses limites pratiques. De la même manière, nous obtiendrons une nouvelle équation d'évolution pour l'aire du rouleau de déferlement utilisable dans les modèles hydrodynamiques à phase moyennée en prenant soin de pointer les principales différences existantes entre deux approches équivalentes présentées par Stive et De Vriend [150] et Dally et Brown [47]. Nous montrerons par ailleurs que la théorie des vagues déferlantes en équilibre développée dans un contexte d'eau profonde par Cointe et Tulin [40], peut être valable et très utile pour améliorer la modélisation du déferlement en zone de surf.

Enfin, dans le Chapitre 5, les bases théoriques pour le développement d'une nouvelle paramétrisation du déferlement pour la famille d'équations de Boussinesq seront exposées. Cette approche originale peut être considérée comme une extension du modèle de déferlement introduit par analogie avec une couche de mélange par Kennedy et al. [85], puisque la forme mathématique adoptée pour les termes supplémentaires sera elle aussi de type diffusive. Néanmoins, nous introduirons à la fois un terme de rédistribution locale de la masse dans l'équation de continuité, et un terme de déficit local de quantité de mouvement, tout les deux appliqués sur la face avant des ondes déferlantes. La paramétrisation ainsi que les valeurs numériques affectées aux différentes quantités concernées seront obtenues à l'aide d'arguments physiques étroitement liés à la téorie de choc des équations de l'eau peu profonde, et aux résultats empiriques étudiés dans le Chapitre 4. À l'aide de cas test expérimentaux, nous montrerons que le nouveau modèle permet, contrairement à celui proposé par Kennedy et al. [85], de bien représenter à la fois la décroissance en amplitude et la forme caractéristique en dent de scie des vagues en zone de surf.

Chapter 2

A High Order Finite Volume Scheme for Boussinesq-type Equations

2.1 Introduction

In recent years, important research efforts have provided a solid theoretical background for a new generation of the so-called Boussinesq-type wave equations. This new class of equations, which takes advantage of pioneering contributions made by Boussinesq [22], Korteweg and de Vries [92], Serre [140] and Peregrine [125], have proven to adequately describe most of the water wave phenomena taking place in the nearshore zone. Recent developments concern the extension of these shallow water sets of equations to deeper water propagation problems [105, 108, 109, 114, 122, 180], and to describe surf zone dynamics by adding extra wave-breaking terms [85, 133, 172, 184] and removing the originally embedded weakly nonlinear hypothesis [136, 137, 178]. Even though those important improvements have provided a powerful set of mathematical tools to describe the hydrodynamics of coastal zones, the question of constructing efficient, stable and accurate numerical schemes to solve them have received considerably less attention.

Numerical solutions of Boussinesq-type equations have been mostly tackled with finite difference methods [1, 4, 62, 70, 141, 153, 177], and to some extent, using finite element techniques [5, 141, 175, 181, 182]. On the contrary, the application of the finite volume method to discretize them has been only reported very recently [15, 24, 58, 145]. Even though finite volume techniques have been successfully applied to the strictly hyperbolic dispersionless set of nonlinear shallow water equations (NSWE) using shock capturing solvers (see [165] for a comprehensive review), parabolic terms responsible for the dispersive nature of Boussinesq-type equations make the extrapolation of such approaches to coastal applications rather difficult. However, shock capturing methods

may provide an efficient and elegant way to numerically integrate Boussinesq equations but novel strategies are to be developed in order to adequately handle the mixed hyperbolic-parabolic mathematical nature of the system. Several authors are working in that direction, developing in particular *hybrid* or *operator splitting* techniques where convective hyperbolic-type terms are treated using shock-capturing approaches while high order dispersive terms are handled with help of standard finite difference approximations (e.g. [15, 58]). Such strategies have only been reported in applications concerning weakly nonlinear forms of Boussinesq-type equations. On the other hand, achieving high order accuracy in the latter is quite demanding from a computational point of view and there is still no clear knowledge of what type of flux reconstruction strategy would be the most appropriate in the framework of dispersive wave propagation problems (see for instance reference [58]).

In the present work, a finite volume technique is applied to the fully nonlinear and weakly dispersive set of Serre equations first derived by Seabra-Santos et al. [136]. The inclusion of a dispersion correction term following the lines given in Madsen and Schäffer [110] allows for an extension of the range of application of this set into moderately deep waters. The choice of integrating equations with a finite volume technique appeared naturally because it is possible to recast continuity and momentum equations in an attractive weak conservative form using an auxiliary variable as given in reference [135]. Here *weak conservative* is used in order to make a distinction between a formulation written in terms of primitive variables, i.e. the water depth and the depth-averaged velocity, and a *strongly conservative* formulation which would require to express the momentum conservation equation in terms of the momentum flux. We recall that recent applications of finite volume methods to Boussinesq-type equations mostly concern weakly dispersive and weakly nonlinear versions of these sets (e.g., a KdV-like system in references [15, 24] and a low order Boussinesq model in references [58, 145]). Similarly, most of discretization strategies implemented in previous finite volume approaches appears to be 2nd order accurate in space. On the contrary, our aim here is to develop an efficient high order finite volume scheme applicable even for strongly nonlinear situations. However, no attempt is made to take advantage of shock-capturing methods mainly because : i) this convenient conservative set of equations is not really in a strong conservative mathematical form, ii) high order accuracy in space and time was intended at low computational cost, and iii) shocks do not naturally emerge in Boussinesq-type equations because there is a balance between nonlinear and dispersive terms [179]. Nevertheless, our numerical approach borrows some recently developed ideas from modern computational fluid dynamics (CFD) which make high order accuracy and high spectral resolution possible at an affordable computational

cost. Such techniques are based on a compact reconstruction of cell-face values at a high order by solving implicit algebraical equations [90, 93]. Indeed, fourth order accuracy is achieved by solving an implicit tridiagonal system. Similarly, spatial derivatives are estimated with a fourth order truncation error using compact differencing [95]. Finally, numerical solution is advanced in time with help of the four-stage Runge-Kutta method.

This chapter is organized as follows : in Section 2.2 governing equations are derived by vertically integrating Euler equations, while Section 2.3 deals with the numerical implementation of the newly developed compact finite volume scheme. A comprehensive linear numerical analysis of the method is given in Section 2.4 and additional information on the performance of the finite volume scheme is obtained with help of numerical experiments in Section 2.5. In particular the influence that strong nonlinearities may have in stability and accuracy is investigated.

2.2 Governing equations

Serre equations describe the 2D, irrotational and shallow water flow of an incompressible and inviscid fluid over uneven bottom bathymetries. This set of equations rules the total water depth and the depth-averaged horizontal velocity. In the following we expand on the derivation of Serre equations for horizontal bathymetries as given in reference [9].

Generally speaking, Boussinesq-like equations are valid only for long waves. Long wave dynamics are characterized by a small parameter $\sigma = h_0/L \ll 1$ where h_0 and L are respectively a vertical length scale (say a typical water depth) and a horizontal length scale of the flow. The continuity equation implies the following order of magnitude relationship,

$$\frac{w}{u} \sim \sigma, \tag{2.1}$$

where u and w are respectively the horizontal and vertical fluid velocities ($\sim$ stands for order of magnitude). The bottom boundary condition suggests that bottom slopes ξ_x should be of order σ, since $w/u = \xi_x$ at the bottom. Obviously bottom horizontal scales are not disconnected from the scales of the waves. In other words the flow length scales adapt to the bottom ones. Hence bottom slopes for long wave propagation should be mild which is what is assumed here. Even though this assumption is implictly adopted in most of the available long wave propagation models, thus introducing practical limitations in the latter, Serre equations have been successfully used to describe solitary wave propagation over a submerged step in reference [136]. This settled, the scaling

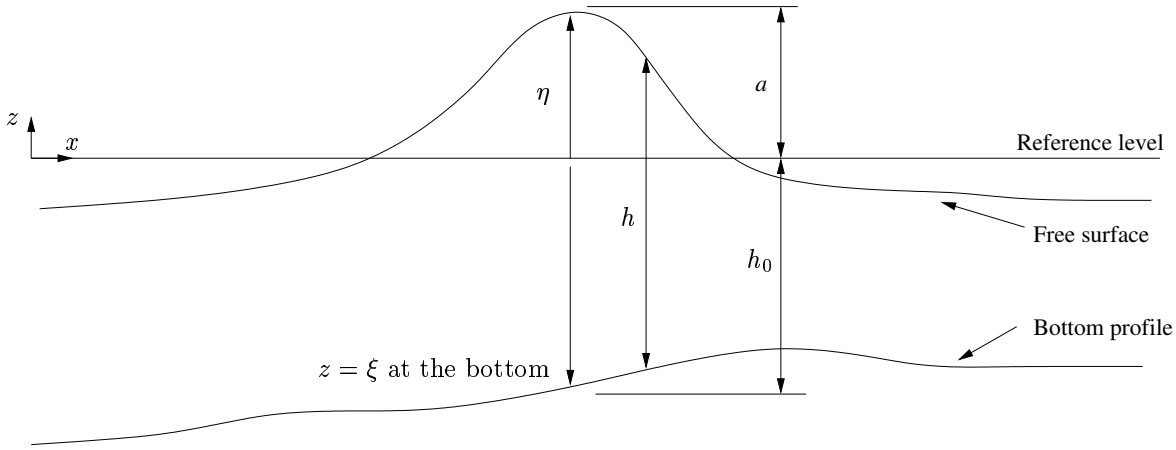

Figure 2.1: Definition sketch for wave propagation over uneven bathymetries. $z = \eta$ is the free surface elevation, $z = \xi$ is the bottom location, and $h = \eta - \xi$ is the instantaneous water depth (here ξ has a negative value).

detailed in [9] leads to the following dimensionless forms of continuity, irrotationality, momentum equations and boundary conditions,

$$\frac{\partial u^*}{\partial x^*} + \frac{\partial w^*}{\partial z^*} = 0 \tag{2.2}$$

$$\frac{\partial u^*}{\partial z^*} - \sigma^2 \frac{\partial w^*}{\partial x^*} = 0 \tag{2.3}$$

$$\epsilon \frac{\partial u^*}{\partial t^*} + \epsilon^2 \frac{\partial}{\partial x^*}(u^{*2}) + \epsilon^2 \frac{\partial}{\partial z^*}\left(u^*\ w^*\right) = -\frac{\partial p^*}{\partial x^*} \tag{2.4}$$

$$\epsilon\sigma^2\ \frac{\partial w^*}{\partial t^*} + \epsilon^2\sigma^2\ u^* \frac{\partial w^*}{\partial x^*} + \epsilon^2\sigma^2\ w^* \frac{\partial w^*}{\partial z^*} = -\frac{\partial p^*}{\partial z^*} - 1 \tag{2.5}$$

$$w^* = \ u^*\ \frac{\partial \xi^*}{\partial x^*} \quad \text{at the bottom} \quad z^* = \xi^* \tag{2.6}$$

$$w^* = \frac{\partial \eta^*}{\partial t^*} + \epsilon\ u^*\ \frac{\partial \eta^*}{\partial x^*} \quad \text{at the free surface} \quad z^* = \epsilon\ \eta^* \tag{2.7}$$

$$p^* = 0 \quad \text{at the free surface} \quad z^* = \epsilon\ \eta^* \tag{2.8}$$

Where $*$ indicates dimensionless variables. Here, p^* represents the pressure, η^* is the free surface elevation and $\epsilon = a/h_0$ is the nonlinear parameter with a being the local wave amplitude relative to the chosen reference level (see Figure 2.1). For simplicity, we introduce in the following the function,

$$\Gamma^*(x^*, z^*, t^*) = \frac{\partial w^*}{\partial t^*} + \epsilon \left(u^* \frac{\partial w^*}{\partial x^*} + w^* \frac{\partial w^*}{\partial z^*} \right), \tag{2.9}$$

which is related to the vertical acceleration of fluid particles.

Recall we seek a set of equations for the depth-averaged horizontal velocity $\overline{u^*}$ and the water depth $h^* = \epsilon\ \eta^* - \xi^*$. Depth averaging a function f^* results from applying

the following operator,

$$\overline{f^*} = \frac{1}{h^*} \int_{\xi^*}^{\epsilon\eta^*} f^* \, dz^*. \tag{2.10}$$

Depth averaging continuity equation yields,

$$\frac{\partial \eta^*}{\partial t^*} + \frac{\partial}{\partial x^*} \left[h^* \, \overline{u^*} \right] = 0. \tag{2.11}$$

Depth averaging the x-momentum equation (2.4) and following the derivation along similar lines as in reference [9] gives,

$$h^* \, \frac{\partial \overline{u^*}}{\partial t^*} + \epsilon h^* \, \overline{u^*} \, \frac{\partial \overline{u^*}}{\partial x^*} + h^* \frac{\partial \eta^*}{\partial x^*} + \sigma^2 \frac{\partial}{\partial x^*} \int_{\xi^*}^{\epsilon\eta^*} z^* \, \Gamma^* \, dz^* + \sigma^2 \frac{\partial \xi^*}{\partial x^*} \int_{\xi^*}^{\epsilon\eta^*} \Gamma^* \, dz^* = - \epsilon \, \frac{\partial}{\partial x^*} \int_{\xi^*}^{\epsilon\eta^*} \left(u^{*2} - (\overline{u^*})^2 \right) \, dz^*. \tag{2.12}$$

So far no approximation has been invoked, but the integrals in (2.12) cannot be reduced to partial differential expressions without approximating the integrands. We aim at obtaining a set of equations comprising terms at most of $O(\sigma^2)$. To be consistent, the two integrals on the left-hand side should be expanded to order 0. Further inspection is required for the one on the right-hand side which also reads,

$$\int_{\xi^*}^{\epsilon\eta^*} \left(u^{*2} - (\overline{u^*})^2 \right) \, dz^* = h^* \, \left(\overline{u^{*2}} - (\overline{u^*})^2 \right). \tag{2.13}$$

This term has given rise in the past to discussions as to whether it is of $O(\sigma^4)$ or not for uneven bathymetries. Dingemans [51] (volume II page 613) argues it is not. It has been then taken advantage of this argument to mistrust Serre equations for long wave propagation over uneven topographies. Nevertheless, it can be readily shown that (2.13) is of order σ^4. Rearranging results reported by Dingemans [51] (volume II page 656) the series expansions of u^* and w^* read (see also the alternative derivation of Serre equations given in Appendix A),

$$u^*(x^*, z^*, t^*) = u_0^*(x^*, t^*) + \sigma^2 (z^* - \xi^*) \, u_2^*(x^*, t^*) + O(\sigma^4) \tag{2.14}$$

$$w^*(x^*, z^*, t^*) = \left[\frac{\partial \xi^*}{\partial x^*} \, u_0^*(x^*, t^*) - (z^* - \xi^*) \, \frac{\partial u_0^*}{\partial x^*} \right] + \sigma^2 (z^* - \xi^*) \, w_2^*(x^*, t^*) + O(\sigma^4) \tag{2.15}$$

showing in addition that u^* and w^* also have even series expansions in σ for uneven bathymetries. Using (2.14), clearly $\overline{u^{*2}} - (\overline{u^*})^2 = O(\sigma^4)$ without having to express u_0^* and u_2^* in terms of $\overline{u^*}$ as done in [51].

Left-hand side integrals in (2.12) are evaluated with the above series expansions expressed in terms of $\overline{u^*}$,

$$u^*(x^*, z^*, t^*) = \overline{u^*}(x^*, t^*) + O(\sigma^2) \tag{2.16}$$

$$w^*(x^*, z^*, t^*) = \frac{\partial \xi^*}{\partial x^*}\ \overline{u^*} - (z^* - \xi^*)\frac{\partial \overline{u^*}}{\partial x^*} + O(\sigma^2) \tag{2.17}$$

Retaining all terms up to $O(\sigma^2)$ leads to the following set of equations expressed in terms of dimensional variables and unknowns :

$$\eta_t + (h\ \overline{u})_x = 0 \tag{2.18}$$

$$h\ \overline{u}_t + h\ \overline{u}\ \overline{u}_x + g\ h\ \eta_x + \left[h^2\left(\frac{1}{3}\mathcal{P} + \frac{1}{2}\mathcal{Q}\right)\right]_x + \xi_x h\left(\frac{1}{2}\mathcal{P} + \mathcal{Q}\right) = 0 \tag{2.19}$$

$$\mathcal{P} = -h\left[\overline{u}_{xt} + \overline{u}\ \overline{u}_{xx} - (\overline{u}_x)^2\right] \tag{2.20}$$

$$\mathcal{Q} = \xi_x\ (\overline{u}_t + \overline{u}\ \overline{u}_x) + \xi_{xx}\ \overline{u}^2, \tag{2.21}$$

where $\mathcal{P} + \mathcal{Q}$ and $\mathcal{Q}$ represent respectively the vertical fluid acceleration at the free surface and at the bottom (see Appendix A). This fully nonlinear set of equations contains all ϵ order of magnitude terms because no hypothesis have been introduced concerning nonlinearities (i.e., $\epsilon \sim O(1)$). Some of these ϵ terms are related to the convective vertical acceleration neglected in low-order Boussinesq equations [125]. One of the interesting properties of the Serre equations for horizontal bottom lies in the fact they have a closed form solitary wave solution which happens to be the Rayleigh solitary wave [75], which expression is,

$$h(x,t) = h_0 + a\ \mathrm{sech}^2\left[K\ (x - Ct)\right] \tag{2.22}$$

$$\overline{u} = C\left(1 - \frac{h_0}{h}\right) \tag{2.23}$$

$$K = \sqrt{\frac{3\,a}{4\,h_0^2\,(h_0 + a)}}\ \ ,\ \ C = C_0\sqrt{1 + \frac{a}{h_0}}\ \ \text{and}\ \ C_0 = \sqrt{g h_0} \tag{2.24}$$

where h_0 is the water depth at rest, a the amplitude, C the phase speed and K the outskirt decay parameter. This solution will be used later to numerically test the proposed finite volume scheme.

Additionally, the range of validity of this set of equations can be easily extended to wave propagation problems in deeper waters using the dispersion correction technique discussed in references [109, 110]. A Padé (2,2) expansion for Stokes linear dispersion is achieved by adding the following term in the left hand side of equation (2.19),

$$B(x,t) = -\alpha h\,\xi^2[\overline{u}_{xxt} + (\overline{u}\,\overline{u}_x)_{xx} + g(h + \xi)_{xxx}], \tag{2.25}$$

where α is an adjustable parameter ($\sim 1/15$) that must be tuned in order to match (at best) the linear Stokes dispersion relation.

Finally, it is possible to show that continuity and momentum equations, including the dispersion correction term and assumig that bottom variations are only function of the spatial coordinate x can be written in a weak quasi-conservative form by introducing a dependent variable q which aggregates all time derivatives of equation (2.19) and (2.25). This convenient mathematical form reads (see also reference [135]),

$$h_t + F_x = 0, \tag{2.26}$$

$$q_t + G_x = S, \tag{2.27}$$

$$q = (1+r)\overline{u} - \frac{1}{3h}(h^3\overline{u}_x)_x - \alpha\xi^2\overline{u}_{xx}, \tag{2.28}$$

with flux functions,

$$F = h\overline{u}, \tag{2.29}$$

$$G = q\overline{u} + g(h+\xi) - \frac{1}{2}\overline{u}^2(1+\xi_x^2) + (\xi_x\overline{u} - \frac{1}{2}h\overline{u}_x)h\overline{u}_x - \alpha\xi^2[\overline{u}_x^2 + \overline{u}\,\overline{u}_{xx} + g(h+\xi)_{xx}], \tag{2.30}$$

and the non-conservative right hand side term S (analogous to a source term) in (2.27) has the following expression,

$$S = -2\alpha\xi\xi_x\left[\overline{u}\,\overline{u}_x + g(h+\xi)_x\right]_x. \tag{2.31}$$

The latter contains a small correction for the dispersive properties of the system. Moreover, $r = (h_x+\xi_x)\xi_x + \frac{1}{2}h\xi_{xx}$ and thus traduces some bathymetric effects. In what follows, overbars will be dropped for convenience.

2.3 Numerical method

Because dispersive terms embedded in Boussinesq-type equations may have a similar mathematical form than lower order terms associated to truncation errors of discretized equations, high order schemes, both in time and space, are needed. Furtheremore, non-linear processes and frequency dispersion are responsible for the broadening/narrowing of initial wavelength scales in time and numerical methods used to solve Boussinesq equations must be able to adequately reproduce interactions between different wave modes without damping physical ones nor introducing spurious short-wave noise. In this context we will develop a 4th order compact finite volume scheme for spatial integration of equations derived in previous section over a uniform 1D staggered grid while time integration will be performed using a standard 4th order Runge-Kutta method.

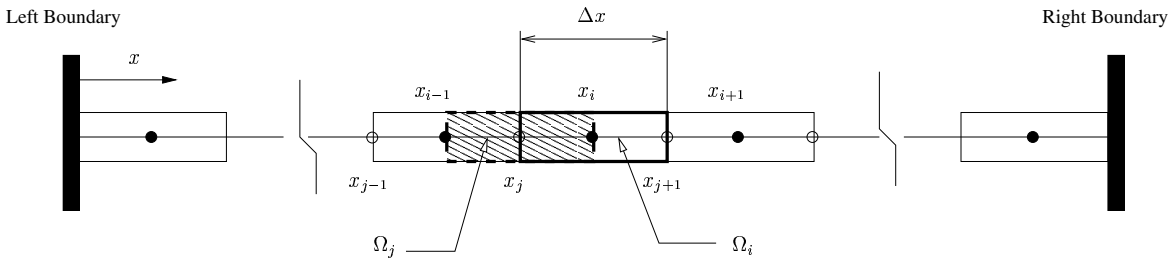

Figure 2.2: 1D computational domain meshed with staggered control volumes Ω_i and Ω_j.

2.3.1 Finite volume method for spatial discretization

The computational domain is schematically described in Figure 2.2 where Ω_i and Ω_j are control volumes centered around i-nodes ($i = 0, 1, .., I-1$) and around j-nodes ($j = 0, 1, ..., I$) respectively, i.e.,

$$\Omega_i = \{x \in [x_j, x_{j+1}]\}, \tag{2.32}$$

$$\Omega_j = \{x \in [x_{i-1}, x_i]\}, \tag{2.33}$$

where I is the number of Ω_i control volumes used to discretize the physical domain. Nodal coordinates are defined as $x_i = \Delta x/2 + i\Delta x$ and $x_j = j\Delta x$, where Δx is the constant spatial grid resolution (length of control volumes). The governing equations will be integrated over this staggered domain in order to optimize the cell face interpolation process but also to improve accuracy and minimize short-wave noise generation [55, 141].

Equations (2.26) and (2.27) can be easily integrated over control volumes Ω_i as follows,

$$\frac{\partial}{\partial t}\int_{x_j}^{x_{j+1}} h\,dx + F(x_{j+1}, t) - F(x_j, t) = 0, \tag{2.34}$$

$$\frac{\partial}{\partial t}\int_{x_j}^{x_{j+1}} q\,dx + G(x_{j+1}, t) - G(x_j, t) = \int_{x_j}^{x_{j+1}} S\,dx, \tag{2.35}$$

where flux functions are evaluated at cell faces of each control volume (j-nodes).

Unlike previous equations, the auxiliary relation (2.28) which links variable q, to the physical variables h and u will be integrated over staggered control volumes Ω_j,

$$\int_{x_{i-1}}^{x_i} \left[(1+r)u - \frac{1}{3h}(h^3 u_x)_x - \alpha\xi^2 u_{xx}\right] dx = \int_{x_{i-1}}^{x_i} q\,dx. \tag{2.36}$$

Numerical approximations will be introduced in the following to evaluate flux functions at cell faces and volume integrals.

In continuity and momentum equations (2.34) and (2.35), volume integrals of h and q can be stored as cell-averaged values and no further approximations need to be done. For example, the cell-averaged value of a generic function Φ over control volume Ω_i is written as,

$$\widehat{\Phi}_i = \frac{1}{\Delta x} \int_{x_j}^{x_{j+1}} \Phi \, dx. \tag{2.37}$$

The discretized counterpart of equations (2.34) and (2.35) is then obtained by performing the finite volume integration over the whole domain,

$$\frac{d\,\widehat{h}_i^n}{dt} = -\frac{1}{\Delta x}\left(F_{j+1}^n - F_j^n\right), \quad \text{for} \;\; i = 0, 1, ..., I-1 \;\; \text{and} \;\; j = i, \tag{2.38}$$

$$\frac{d\,\widehat{q}_i^n}{dt} = \widehat{S}_i^n - \frac{1}{\Delta x}\left(G_{j+1}^n - G_j^n\right), \quad \text{for} \;\; i = 0, 1, ..., I-1 \;\; \text{and} \;\; j = i, \tag{2.39}$$

where we have introduced for simplicity the notation $\Phi_j^n = \Phi(x_j, t_n)$, with the discrete time coordinate $t_n = n\,\Delta t$ $(n = 0, 1, ..., N)$ and Δt is the time step. The non-conservative term will be approximated using a centered in space approach where,

$$\widehat{S}_i = \frac{1}{\Delta x} \int_{x_j}^{x_{j+1}} S \, dx \simeq -\frac{2\alpha}{\Delta x} \xi_i (\xi_x)_i \left(\widetilde{S}_{j+1}^n - \widetilde{S}_j^n\right), \tag{2.40}$$

and $\widetilde{S} = u u_x + g(h+\xi)_x$. This discretized expression will introduce only slight errors in the overall numerical approximation since this term represents a small correction of $O(\sigma^4)$ for dispersive properties.

On the other hand, evaluation of flux functions at cell faces requires a reconstruction of h_j and q_j values from cell-averaged variables because time integration of equations (2.38) and (2.39) will produce $\widehat{h}_i$ and $\widehat{q}_i$. Here, cell face values will be estimated at each time step using the implicit 4th order interpolation technique developed in references [90, 93]. This approach results in the following system of $I-1$ equations for internal nodal points,

$$\frac{1}{4}\Phi_{j-1} + \Phi_j + \frac{1}{4}\Phi_{j+1} = \frac{3}{4}(\widehat{\Phi}_{i-1} + \widehat{\Phi}_i), \quad \text{for} \;\; j = 1, 2, ..., I-1 \;\; \text{and} \;\; i = j. \tag{2.41}$$

At boundary nodes, $j = 0$ and $j = I$, boundary conditions must provide the correct values for h and q.

When using equation (2.41), 4th order accuracy is achieved in the evaluation of cell face values by solving a tridiagonal system. On the contrary, using a pointwise 4th order method where volume integrals are estimated using Simpson's rule and cell face values are interpolated with piecewise cubic polynomials, it is necessary to solve a pentadiagonal system (see for instance reference [39] also reprinted in Appendix

C). Thus, computational cost is significantly reduced when implementing the present compact scheme.

Evaluation of flux functions requires in addition the prescription of depth-averaged velocity values at cell faces. The latter are obtained at the end of each time step, once h_j and q_j have been computed at internal nodes, by solving the auxiliary relation (2.36). Different integrals appearing in this equation are approximated as follows,

$$\begin{aligned}
&\frac{1}{\Delta x}\int_{x_{i-1}}^{x_i}(1+r)u\,dx \simeq (1+r_j)\,\widehat{u}_j,\\
&-\frac{1}{\Delta x}\int_{x_{i-1}}^{x_i}\frac{1}{3h}(h^3u_x)_x\,dx \simeq -\frac{1}{3\Delta x\,h_j}\left[h_i^3(u_x)_i - h_{i-1}^3(u_x)_{i-1}\right],\\
&-\frac{1}{\Delta x}\int_{x_{i-1}}^{x_i}\alpha\xi^2 u_{xx} \simeq -\frac{\alpha}{\Delta x}\xi_j^2\left[(u_x)_i - (u_x)_{i-1}\right],\\
&\frac{1}{\Delta x}\int_{x_{i-1}}^{x_i} q\,dx = \widehat{q}_j.
\end{aligned}$$

At this point, some care must be taken for the reconstruction of depth-averaged velocity values at j-nodes using equation (2.36). Since we want to obtain u_j directly and still preserve a tridiagonal structure in the discrete system, it is necessary to link cell-averaged values $\widehat{u}_j$ and diffusive fluxes to pointwise values at j-nodes carefully. The latter can be achieved using the following strategy.

On the one hand, combining Simpson's rule to evaluate volume integrals over Ω_i and Ω_j,

$$\widehat{\Phi}_i = \frac{2}{3}\Phi_i + \frac{1}{6}\left(\Phi_j + \Phi_{j+1}\right) + O(\Delta x^4), \tag{2.42}$$

$$\widehat{\Phi}_j = \frac{2}{3}\Phi_j + \frac{1}{6}\left(\Phi_{i-1} + \Phi_i\right) + O(\Delta x^4), \tag{2.43}$$

and equation (2.41), provides the following relation,

$$\widehat{\Phi}_j = \frac{1}{24}\left(\Phi_{j-1} + 22\Phi_j + \Phi_{j+1}\right) + O(\Delta x^4), \tag{2.44}$$

which still has a tridiagonal matrix form. On the other hand, the velocity gradient $(u_x)_i$ must be written in terms of pointwise u-values at j nodes. Therefore, it is preferable to use an explicit formula to approximate its spatial derivative. However, an explicit 4th order formula will break down the tridiagonal nature of the system because 5-point stencils will be necessary to compute diffusive fluxes. One way to preserve a tridiagonal structure is to use a deferred-correction approach which is expressed as [60],

$$(u_x)_i = \frac{(u_{j+1}-u_j)}{\Delta x} + \left\{\frac{(u_{j-1}-27u_j+27u_{j+1}-u_{j+2})}{24\Delta x} - \frac{(u_{j+1}-u_j)}{\Delta x}\right\}^{old}, \tag{2.45}$$

where superscript *old* is used for depth-averaged velocities evaluated at the previous level of the iterative process. Thus, the discretized equation associated to (2.36) must be solved iteratively because a 2nd order approximation is used for the implicit part, and a 4th order formula appears in the explicit contribution in brackets. When some convergence criteria will be satisfied between *old* and *new* u_j-values, the overall approximation for u_x will be 4th order accurate. In practice only few iterations will be needed to obtain sufficient accuracy. The convergence criteria for fixed-point iterations is based on a L_1 norm and reads,

$$\frac{\|\mathbf{u_j} - \{\mathbf{u_j}\}^{old}\|_1}{\|\mathbf{u_j}\|_1} \leq \tau, \tag{2.46}$$

where $\mathbf{u_j} = [u_{j=2}\ u_{j=3}\ ...\ u_{j=I-2}\ u_{j=I-1}]$ is the vector containing cell face values of the most recently computed depth-averaged velocity and τ is the tolerance for the relative error between succesive iterations. Hence, internal nodal values of u_j are obtained by solving the following implicit tridiagonal system,

$$\begin{aligned}\left\{\frac{(1+r_j)}{24} - \frac{1}{\Delta x^2}\left(\frac{h_{i-1}^3}{3h_j} + \alpha\xi_j^2\right)\right\} u_{j-1} + \left\{\frac{22(1+r_j)}{24} + \frac{1}{\Delta x^2}\left[\frac{(h_{i-1}^3 + h_i^3)}{3h_j} + 2\alpha\xi_j^2\right]\right\} u_j \\ + \left\{\frac{(1+r_j)}{24} - \frac{1}{\Delta x^2}\left(\frac{h_i^3}{3h_j} + \alpha\xi_j^2\right)\right\} u_{j+1} = \frac{1}{24}(q_{j-1}+22q_j+q_{j+1}) + \frac{1}{\Delta x^2}\left\{\frac{h_i^3}{3h_j} + \alpha\xi_j^2\right\} U_i^{old} \\ - \frac{1}{\Delta x^2}\left\{\frac{h_{i-1}^3}{3h_j} + \alpha\xi_j^2\right\} U_{i-1}^{old}, \quad \text{for } \ j = 1, 2, ..., I-1 \ \text{ and } \ i = j,\end{aligned} \tag{2.47}$$

where,

$$U_i^{old} = \frac{1}{24}\left\{u_{j-1} - 3u_j + 3u_{j+1} - u_{j+2}\right\}^{old}. \tag{2.48}$$

Near boundaries, evaluation of the last relation will require to compute depth-averaged velocity values outside the physical domain. In the case of non-periodic boundaries, *ghost nodes* values will be extrapolated from interior nodes using suitable piecewise polynomial functions. Similarly, boundary conditions must be treated with caution because there is a coupling between the cell face reconstruction of q_j values (equation (2.41)) and the right hand side of equation (2.47). However, in the present chapter only periodic bundary conditions will be considered. The special treatment of boundary and *ghost nodes* in the framework of wave propagation over a beach will be addressed in Chapter 3.

Finally, derivatives of water depth, h, and depth-averaged velocity, u, must be computed at j-nodes in order to complete the evaluation of the flux function G_j, the source term $\widehat{S}_i$ and the dependent variable r_j at each time step. Similarly, water depth values

at i-nodes must be interpolated to compute matrix coefficients in equation (2.47) while bottom function ξ and its derivatives must be prescribed at i and j nodes. The latter is not difficult because bottom bathymetry constitutes a known input data which is not time dependent. On the other hand, i-values of water depth will require an interpolation which can be performed easily from computed values of $\widehat{h}_i$ and h_j using relation (2.42). It is relevant to note that the strategy of overlapping the control volumes where equation (2.36) is integrated has allowed us to minimize this interpolation process.

Estimates of derivatives are performed using a 4th order finite difference compact scheme as described in [95]. These compact formulae have better spectral properties for short-length waves than their explicit 4th order finite difference counterpart and matching conditions at boundary nodes are less tedious. It is important to note that the highest derivative that one needs to estimate here will be of 2nd order. In fact, the finite volume method applied to the quasi-conservative set of equations derived here has allowed us to lower the highest x-derivative order by one when compared to other equivalent set of equations (e.g. [178, 181]). Derivative estimates at internal j-nodes are obtained from cell face values using the following implicit formulae [95],

$$\frac{1}{4}(\Phi_x)_{j-1} + (\Phi_x)_j + \frac{1}{4}(\Phi_x)_{j+1} = \frac{3}{4\Delta x}(\Phi_{j+1} - \Phi_{j-1}), \quad \text{for} \quad j = 1, 2, ..., I-1 \quad \text{and} \quad i = j, \tag{2.49}$$

$$\frac{1}{10}(\Phi_{xx})_{j-1} + (\Phi_{xx})_j + \frac{1}{10}(\Phi_{xx})_{j+1} = \frac{6}{5\Delta x^2}(\Phi_{j+1} - 2\Phi_j + \Phi_{j-1}), \quad \text{for } j = 1, 2, ..., I-1 \text{ and } i = j. \tag{2.50}$$

Again, special care must be taken at boundary nodes as discussed in [95, 139]. It is worth to point out that these compact forms can be verified manipulating relation (2.44).

Spatial discretization of equations (2.34), (2.35) and (2.36) using the present finite volume technique allows us to write the original system of partial differential equations (PDE) as the following set of ordinary differential equations (ODE),

$$\frac{d\,\widehat{\mathbf{x}}_\mathbf{i}^\mathbf{n}}{dt} = \mathbf{f}_\mathbf{i}^\mathbf{n}, \tag{2.51}$$

$$\mathcal{A}(\mathbf{h}_\mathbf{j}^\mathbf{n}) \cdot \mathbf{u}_\mathbf{j}^\mathbf{n} = \mathcal{B} \cdot \mathbf{q}_\mathbf{j}^\mathbf{n} + \mathcal{C}(\mathbf{h}_\mathbf{j}^\mathbf{n}) \cdot \{\mathbf{u}_\mathbf{j}^\mathbf{n}\}^{old}, \tag{2.52}$$

where,

$$\widehat{\mathbf{x}}_\mathbf{i}^\mathbf{n} = \begin{bmatrix} \widehat{\mathbf{h}}_\mathbf{i}^\mathbf{n} \\ \widehat{\mathbf{q}}_\mathbf{i}^\mathbf{n} \end{bmatrix} \qquad \text{and} \qquad \mathbf{f}_\mathbf{i}^\mathbf{n} = \begin{bmatrix} \mathbf{0} \\ \widehat{\mathbf{S}}_\mathbf{i}^\mathbf{n} \end{bmatrix} - \begin{bmatrix} \mathbf{\Delta F}_\mathbf{i}^\mathbf{n} \\ \mathbf{\Delta G}_\mathbf{i}^\mathbf{n} \end{bmatrix}.$$

Here bold letters represent vectors containig cell-averaged values of associated variables over the whole domain. Hence, a generic vector $\widehat{\mathbf{\Phi}}_{\mathbf{i}}^{\mathbf{n}}$ contains cell-averaged values over control volumes Ω_i of function Φ evaluated at time $t = t_n$. Similarly, the notation $\mathbf{\Delta\Phi}_{\mathbf{i}}^{\mathbf{n}} = \frac{1}{\Delta x}(\mathbf{\Phi}_{\mathbf{j+1}}^{\mathbf{n}} - \mathbf{\Phi}_{\mathbf{j}}^{\mathbf{n}})$ indicates a cell face flux difference vector, and $\mathcal{A}$, $\mathcal{B}$ and $\mathcal{C}$ are matrices obtained from the discretized equation (2.47). In the next subsection, we will use an explicit 4th order Runge-Kutta method to numerically integrate the system of ODE just derived.

2.3.2 Numerical time stepping

The implementation of a high order numerical ODE solver for time integration is justified since spatial derivatives are discretized using a high order scheme as well. The finite volume discretization technique is theoretically 4th order accurate in space so we wish to reach a similar discretization error when integrating the system (2.51)-(2.52) in time. The 4th order Runge-Kutta method is an attractive alternative for the solution of wave-type equations and can be quite efficient when compared to other high order schemes [55]. In the present context the standard four-stage Runge-Kutta method can be stated as follows :

First estimation at $t = t_{n+1/2}$

$$\mathbf{p}^{(\mathbf{1})} = \Delta t\, \mathbf{f}_{\mathbf{i}}^{\mathbf{n}}, \quad \widehat{\mathbf{x}}_{\mathbf{i}}^{\mathbf{n}+\frac{\mathbf{1}}{\mathbf{2}}} = \widehat{\mathbf{x}}_{\mathbf{i}}^{\mathbf{n}} + \frac{1}{2}\mathbf{p}^{(\mathbf{1})}, \tag{2.53a}$$

$$\mathbf{u}_{\mathbf{j}}^{\mathbf{n}+\frac{\mathbf{1}}{\mathbf{2}}} = \mathcal{A}(\mathbf{h}_{\mathbf{j}}^{\mathbf{n}+\frac{\mathbf{1}}{\mathbf{2}}})^{-1} \cdot \left[\mathcal{B} \cdot \mathbf{q}_{\mathbf{j}}^{\mathbf{n}+\frac{\mathbf{1}}{\mathbf{2}}} + \mathcal{C}(\mathbf{h}_{\mathbf{j}}^{\mathbf{n}+\frac{\mathbf{1}}{\mathbf{2}}}) \cdot \{\mathbf{u}_{\mathbf{j}}^{\mathbf{n}+\frac{\mathbf{1}}{\mathbf{2}}}\}^{old}\right]. \tag{2.53b}$$

Second estimation at $t = t_{n+1/2}$

$$\mathbf{p}^{(\mathbf{2})} = \Delta t\, \mathbf{f}_{\mathbf{i}}^{\mathbf{n}+\frac{\mathbf{1}}{\mathbf{2}}}, \quad \widehat{\mathbf{x}}_{\mathbf{i}}^{\mathbf{n}+\frac{\mathbf{1}}{\mathbf{2}}} = \widehat{\mathbf{x}}_{\mathbf{i}}^{\mathbf{n}} + \frac{1}{2}\mathbf{p}^{(\mathbf{2})}, \tag{2.53c}$$

$$\mathbf{u}_{\mathbf{j}}^{\mathbf{n}+\frac{\mathbf{1}}{\mathbf{2}}} = \mathcal{A}(\mathbf{h}_{\mathbf{j}}^{\mathbf{n}+\frac{\mathbf{1}}{\mathbf{2}}})^{-1} \cdot \left[\mathcal{B} \cdot \mathbf{q}_{\mathbf{j}}^{\mathbf{n}+\frac{\mathbf{1}}{\mathbf{2}}} + \mathcal{C}(\mathbf{h}_{\mathbf{j}}^{\mathbf{n}+\frac{\mathbf{1}}{\mathbf{2}}}) \cdot \{\mathbf{u}_{\mathbf{j}}^{\mathbf{n}+\frac{\mathbf{1}}{\mathbf{2}}}\}^{old}\right]. \tag{2.53d}$$

First estimation at $t = t_{n+1}$

$$\mathbf{p}^{(\mathbf{3})} = \Delta t\, \mathbf{f}_{\mathbf{i}}^{\mathbf{n}+\frac{\mathbf{1}}{\mathbf{2}}}, \quad \widehat{\mathbf{x}}_{\mathbf{i}}^{\mathbf{n+1}} = \widehat{\mathbf{x}}_{\mathbf{i}}^{\mathbf{n}} + \frac{1}{2}\mathbf{p}^{(\mathbf{3})}, \tag{2.53e}$$

$$\mathbf{u}_{\mathbf{j}}^{\mathbf{n+1}} = \mathcal{A}(\mathbf{h}_{\mathbf{j}}^{\mathbf{n+1}})^{-1} \cdot \left[\mathcal{B} \cdot \mathbf{q}_{\mathbf{j}}^{\mathbf{n+1}} + \mathcal{C}(\mathbf{h}_{\mathbf{j}}^{\mathbf{n+1}}) \cdot \{\mathbf{u}_{\mathbf{j}}^{\mathbf{n+1}}\}^{old}\right]. \tag{2.53f}$$

Second and final estimation at $t = t_{n+1}$

$$\mathbf{p}^{(\mathbf{4})} = \Delta t\, \mathbf{f}_{\mathbf{i}}^{\mathbf{n+1}}, \quad \widehat{\mathbf{x}}_{\mathbf{i}}^{\mathbf{n+1}} = \widehat{\mathbf{x}}_{\mathbf{i}}^{\mathbf{n}} + \frac{1}{6}\left(\mathbf{p}^{(\mathbf{1})} + 2\mathbf{p}^{(\mathbf{2})} + 2\mathbf{p}^{(\mathbf{3})} + \mathbf{p}^{(\mathbf{4})}\right), \tag{2.53g}$$

$$\mathbf{u}_{\mathbf{j}}^{\mathbf{n+1}} = \mathcal{A}(\mathbf{h}_{\mathbf{j}}^{\mathbf{n+1}})^{-1} \cdot \left[\mathcal{B} \cdot \mathbf{q}_{\mathbf{j}}^{\mathbf{n+1}} + \mathcal{C}(\mathbf{h}_{\mathbf{j}}^{\mathbf{n+1}}) \cdot \{\mathbf{u}_{\mathbf{j}}^{\mathbf{n+1}}\}^{old}\right]. \tag{2.53h}$$

At each step, j-values of water depth, h, and auxiliary variable q must be reconstructed from cell-averaged quantities using the implicit relation (2.41) before solving the equation for depth-averaged velocity, u. As explained in the previous subsection, the latter is solved iteratively and at each stage the last computed value of $\mathbf{u_j}$ is used as first guess. A relative tolerance for iteration errors, τ, of 10^{-4} has shown to give good accuracy by requiring only 1-3 iterations. On the other hand, the numerical scheme requires at each step the inversion of tridiagonal matrices which can be performed at low computational cost using the *Thomas* algorithm (see for instance reference [128]). The number of operations needed to solve each matrix equation will then be linearly proportional to the number of unknows in the system.

2.4 Spectral analysis and linear stability

Important information about the general performance of our finite volume resolution can be obtained by analyzing its linearized version. In this section we will study in particular the stability, accuracy in spectral space and dispersion relation preserving properties (DRP) of the scheme using spectral analysis [139]. Our main goal here is to find necessary conditions that will ensure that the numerical scheme will behave properly when describing wave propagation phenomena. For simplicity we will restrict ourself to the analysis of linear wave propagation over flat bottoms.

When using relation (2.41) in equations (2.38)-(2.39) and assuming that fixed point iterations have converged (i.e., $\{u_j^n\}^{old} = u_j^n$) in (2.47), the linearized version of the discretized system of equations can be recasted as,

$$\frac{1}{4}\frac{d\,h_{j-1}^n}{dt} + \frac{d\,h_j^n}{dt} + \frac{1}{4}\frac{d\,h_{j+1}^n}{dt} = -\frac{3}{4\Delta x}\left(F_{j+1}^n - F_{j-1}^n\right), \tag{2.54}$$

$$\frac{1}{4}\frac{d\,q_{j-1}^n}{dt} + \frac{d\,q_j^n}{dt} + \frac{1}{4}\frac{d\,q_{j+1}^n}{dt} = -\frac{3}{4\Delta x}\left(G_{j+1}^n - G_{j-1}^n\right), \tag{2.55}$$

$$\begin{aligned}\frac{\beta}{\rho^2}u_{j-2}^n + \left(1 - \frac{28\beta}{\rho^2}\right)u_{j-1}^n + \left(22 + \frac{54\beta}{\rho^2}\right)u_j^n \\ + \left(1 - \frac{28\beta}{\rho^2}\right)u_{j+1}^n + \frac{\beta}{\rho^2}u_{j+2}^n = q_{j-1}^n + 22q_j^n + q_{j+1}^n,\end{aligned} \tag{2.56}$$

where,

$$F_j^n = h_0\,u_j^n, \qquad G_j^n = gh_j^n - \alpha h_0^2\,g(h_{xx})_j^n, \qquad \beta = (1/3 + \alpha), \qquad \rho = \Delta x/h_0$$

and $h_0 = |\xi|$ is the still water depth of the horizontal bottom flume. This set of equations will be used in what follows in order to analyze the numerical properties of the scheme. It is interesting to note the close resemblance between equations (2.54)-(2.55) and the implicit formula for the first spatial derivative estimate (2.49).

2.4.1 Semi-discrete system of equations and numerical dispersion

Spectral accuracy of the spatial discretization is studied first by decomposing the numerical solution into finite Fourier series. It is important to point out that spectral accuracy is related to the ability of the scheme to resolve the different length scales present in the problem [139]. Therefore, it is paramount to assess how well the numerical scheme is able to describe the physical range of wavelengths. In order to perform this analysis we replace the following individual Fourier components into the discretized system of equations,

$$\begin{bmatrix} h_j^n \\ q_j^n \\ u_j^n \end{bmatrix} = \begin{bmatrix} h_\kappa \\ q_\kappa \\ u_\kappa \end{bmatrix} e^{\hat{\imath}\,(\kappa\, j\Delta x - \omega_r\, t)}, \tag{2.57}$$

where $\hat{\imath} = \sqrt{(-1)}$ is the imaginary constant, h_κ, q_κ and u_κ are Fourier amplitudes, κ is the wave number of the individual component and ω_r is the associated numerical frequency. Numerical dispersion can be studied by substituting (2.57) in equations (2.54), (2.55) and (2.56) and solving the resulting system of equations for ω_r. Before doing so, we need to find the spectral expression for the second spatial derivative that appears in the flux function G_j^n. The numerical estimation of this derivative has the form $(h_{xx})_j = -\tilde{\kappa}^2\, h_\kappa\, e^{\hat{\imath}\,(\kappa j\Delta x - \omega_r\, t)}$, where by substitution in the implicit difference formula (2.50) the associated numerical wave number is written as,

$$(\tilde{\kappa}\Delta x)^2 = 12\frac{(1-\cos\kappa\Delta x)}{(5+\cos\kappa\Delta x)}. \tag{2.58}$$

Similarly, substituting the Fourier components (2.57) into equation (2.56) gives the following relation between q_κ and u_κ,

$$q_\kappa = \Psi\, u_\kappa, \tag{2.59}$$

where,

$$\Psi = 1 + \frac{(1/3+\alpha)}{\rho^2}\frac{(27+\cos 2\kappa\Delta x - 28\cos\kappa\Delta x)}{(11+\cos\kappa\Delta x)} \tag{2.60}$$

Finally, if we use the Fourier components (2.57) and relation (2.59) in continuity and momentum equations (2.54)-(2.55), the compact finite volume scheme takes the following form in the Fourier space,

$$(\mathcal{K} + \mathbf{I}\,\hat{\imath}\,\omega_r) \cdot \begin{bmatrix} h_\kappa \\ u_\kappa \end{bmatrix} = 0, \tag{2.61}$$

where $\mathcal{K} = \frac{3}{\rho}\begin{pmatrix} 0 & K_1 \\ K_2 & 0 \end{pmatrix}$ is the spatial discretization operator whose components read,

$$K_1 = -\hat{\imath}\frac{\sin\kappa\Delta x}{(2+\cos\kappa\Delta x)}, \tag{2.62}$$

$$K_2 = \frac{K_1}{\Psi}\left[\rho^2 + \alpha\,(\tilde{\kappa}\Delta x)^2\right]\left(\frac{C_0}{\Delta x}\right)^2, \tag{2.63}$$

$\mathbf{I}$ is the identity matrix and $C_0 = \sqrt{g\,h_0}$. Nontrivial solution of equation (2.61) provides the discrete dispersion relation associated to our compact finite volume method which can be written in an non-dimensional form as,

$$\begin{aligned}\frac{C_{fv}^2}{C_0^2} &= \frac{1}{C_0^2}\left(\frac{\omega_r}{\kappa}\right)^2 = -\left(\frac{3}{\kappa\Delta x}\right)^2 K_1^2\frac{\left[\rho^2+\alpha\,(\tilde{\kappa}\Delta x)^2\right]}{\rho^2\,\Psi} \\ &= \left(\frac{3\,\sin\kappa\Delta x}{\kappa\Delta x\,(2+\cos\kappa\Delta x)}\right)^2 \frac{(11+\cos\kappa\Delta x)[\rho^2+\alpha(\tilde{\kappa}\Delta x)^2]}{[\rho^2(11+\cos\kappa\Delta x)+(1/3+\alpha)(27+\cos 2\kappa\Delta x-28\cos\kappa\Delta x)]},\end{aligned} \tag{2.64}$$

with C_{fv} being the numerical phase speed associated to the finite volume scheme. Therefore, the non-dimensional discrete dispersion relation depends on the wave number, $\kappa\Delta x$, and on the parameter $\rho = \Delta x/h_0$. Although this general expression cannot be reduced to a simple form, some relevant information may be obtained by exploring its aymptotic behaviour as $\rho \to 0$ (which can be viewed as the deep water limit) and as $\rho \to \infty$ (which corresponds to the shallow water limit).

In order to do some comparisons between the discretized system of equations and the original set of PDE we recall that the non-dimensional *physical* dispersion relation that belongs to the linearized Boussinesq model can be written as [9],

$$\frac{C_{th}}{C_0} = \left[\frac{1+\alpha\,(\kappa h_0)^2}{1+(1/3+\alpha)\,(\kappa h_0)^2}\right]^{1/2} = \left[\frac{1+\alpha\left(\frac{\kappa\Delta x}{\rho}\right)^2}{1+(1/3+\alpha)\left(\frac{\kappa\Delta x}{\rho}\right)^2}\right]^{1/2}, \tag{2.65}$$

where C_{th} stands for the phase speed associated to the theoretical dispersion relation produced by the extended system of Serre equations.

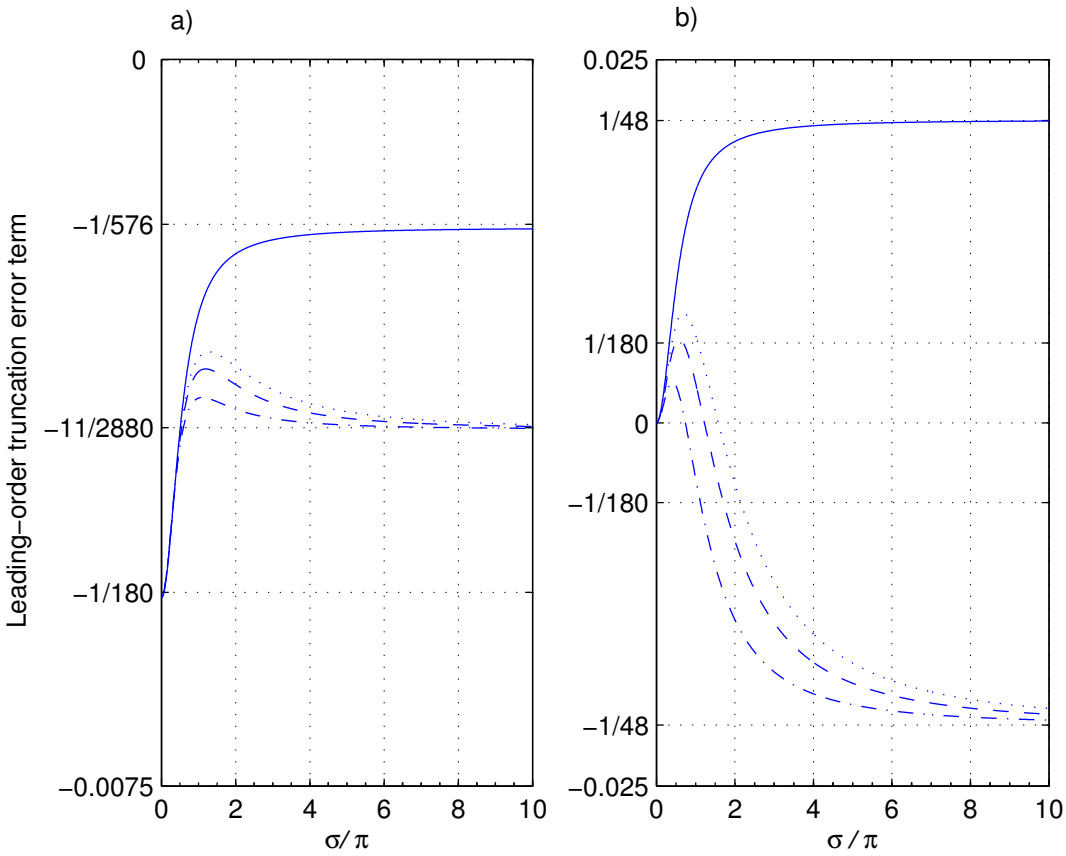

Figure 2.3: Leading-order truncation error term v/s $\sigma = \kappa h_0$ for, (—) $\alpha = 0$, $(\cdots)$ $\alpha = 1/30$, (- -) $\alpha = 1/20$ and (- · -) $\alpha = 1/10$. a) Full 4th order compact finite volume scheme. b) Mixed 4th and 2nd order discretization strategy.

In the shallow water limit it can be shown that the ratio between the *physical* and the discrete dispersion relation is,

$$\lim_{\rho\to\infty}\frac{C_{fv}}{C_{th}} = \frac{3\,\sin\kappa\Delta x}{\kappa\Delta x\,(2+\cos\kappa\Delta x)} = 1 - \frac{1}{180}(\kappa\Delta x)^4 + O[(\kappa\Delta x)^6], \tag{2.66}$$

proving that the numerical scheme mimics the exact relation with 4th order accuracy in $\kappa\Delta x$. Similarly, in the deep water limit we have,

$$\begin{aligned}\lim_{\rho\to 0}\frac{C_{fv}}{C_{th}} = \frac{3\,\sin\kappa\Delta x}{\kappa\Delta x\,(2+\cos\kappa\Delta x)}\left[\frac{6\,(11+\cos\kappa\Delta x)}{(13-\cos\kappa\Delta x)(5+\cos\kappa\Delta x)}\right]^{1/2} \\ = 1 - \frac{11}{2880}(\kappa\Delta x)^4 + O[(\kappa\Delta x)^6],\end{aligned} \tag{2.67}$$

which shows that the phase-speed error is also of 4th order in $\kappa\Delta x$. In the general case the leading-order truncation error term of $O\left[(\kappa\Delta x)^4\right]$ will be a function of the dispersive

characteristics of propagating waves, $\sigma = \kappa h_0$. In fact, it can be demonstrated that the maximum value for the leading-order coefficient will always occur at the shallow water limit, where $\sigma \to 0$, independently of the chosen α value as shown in Figure 2.3-a). It is also interesting to note that the asymptotic behaviour in deep water (i.e., $\sigma \to \infty$) changes when $\alpha = 0$ converging then to $-1/576$.

Even though it is generally acknowledged that numerical dispersion constitutes an important property of any scheme, dispersion relations associated to previously published finite difference or finite element high order Boussinesq-type models have rarely been reported. Moreover, it is commonly argued that numerical dispersion can be avoided if $O(\sigma^2)$ dispersive terms are discretized with 2nd order truncation error approximations, while convective or first order terms are approximated through 4th order centered finite difference formulae (e.g., [1, 177]). Even if from a practical point of view the latter could be sufficient for well-resolved waves, the numerical scheme will only be 2nd order accurate in $\kappa\Delta x$ and in the general case more nodal points per wave length will be needed to reproduce the associated phase speed correctly. In order to illustrate this we will discretize high order dispersive terms appearing in the flux function G_j^n of equation (2.55) and in the linearized version of the auxiliary equation (2.36) by using explicit 2nd order finite difference approximations. It is worth emphasizing that no direct comparison can be made with the finite difference technique used in [177, 178] or with finite element models based on similar *mixed* order approaches [175, 181] since our numerical resolution is based on a compact finite volume integration on a staggered grid. In spite of that, the following analysis can be useful to see what consequences this kind of strategy may have in our particular numerical method. Thus, 2nd order derivatives are approximated now using the following explicit 2nd order formula,

$$(\Phi_{xx})_j = \frac{1}{\Delta x^2}\left(\Phi_{j+1} - 2\Phi_j + \Phi_{j-1}\right), \tag{2.68}$$

and the corresponding spectral relation is found to be (after substitution of a Fourier component),

$$\left(\tilde{\kappa}'\Delta x\right)^2 = 2\left(1 - \cos\kappa\Delta x\right). \tag{2.69}$$

Similarly, using 2nd order approximations for high order derivatives in the linearized version of auxiliary equation (2.36) it can be shown that,

$$\Psi' = 1 + \frac{(1/3 + \alpha)}{\rho^2}\frac{24\left(1 - \cos\kappa\Delta x\right)}{\left(11 + \cos\kappa\Delta x\right)}. \tag{2.70}$$

Substituting relations (2.69) and (2.70) in (2.64) provides the following form for the discrete dispersion relation associated to the *mixed* approach,

$$\frac{C'_{fv}}{C_{th}} = 1 - \frac{\sigma^2}{48}\frac{[(\alpha - 1/3) + \alpha\,(\alpha + 1/3)\sigma^2]}{[1 + \alpha\,\sigma^2]\,[1 + (\alpha + 1/3)\,\sigma^2]}(\kappa\Delta x)^2 + O[(\kappa\Delta x)^4]. \tag{2.71}$$

Therefore, using second order finite difference folmulae to evaluate dispersive terms results in an overall reduction in the spectral resolution of the method. However, the coefficient that multiplies the $O\,[(\kappa\Delta x)^2]$ term will be relatively small (but positive!) near the shallow water limit (see Figure 2.3-b)) in such a way that the accuracy of the scheme would not be dramatically affected. The latter constitutes the main argument behind the *mixed* approach used in several finite difference and finite element Boussinesq-type models. Nevertheless, we will show in the rest of the section that the full 4th order scheme has better numerical properties and is more robust than its *mixed* counterpart.

Another important and challenging property to test is the ability of a particular numerical scheme to correctly reproduce group velocities. This property is related to wave energy propagation and usually imposes more severe restrictions on the application of numerical methods than the dispersion relation preservation condition. The wave group velocity associated to the numerical scheme and the linearized set of PDE can be estimated from the non-dimensional dispersion relation as,

$$\frac{1}{C_0}\frac{\partial\omega}{\partial\kappa} = \frac{C_g}{C_0} = \frac{\partial}{\partial(\kappa\Delta x)}\left[(\kappa\Delta x)\frac{C}{C_0}\right]. \tag{2.72}$$

Again, the general discrete relation will depend on $\kappa\Delta x$ and ρ but asymptotic expressions can be found as before. In the shallow water limit the ratio between the numerical and the *physical* group velocity reads,

$$\lim_{\rho\to\infty}\frac{C_{gfv}}{C_{gth}} = 1 - \frac{1}{36}(\kappa\Delta x)^4 + O[(\kappa\Delta x)^6], \tag{2.73}$$

while in the deep water case we have,

$$\lim_{\rho\to 0}\frac{C_{gfv}}{C_{gth}} = 1 - \frac{11}{576}(\kappa\Delta x)^4 + O[(\kappa\Delta x)^6], \tag{2.74}$$

showing that the truncation error is still 4th order in $\kappa\Delta x$ but with a leading-order term an order of magnitude larger than in the phase speed case. Similarly, it is possible to demonstrate that when the *mixed* order strategy is used the overall truncation error for the group velocity estimate is 2nd order in $\kappa\Delta x$, except in the shallow water limit ($\rho \to \infty$) where it has the same form as (2.73).

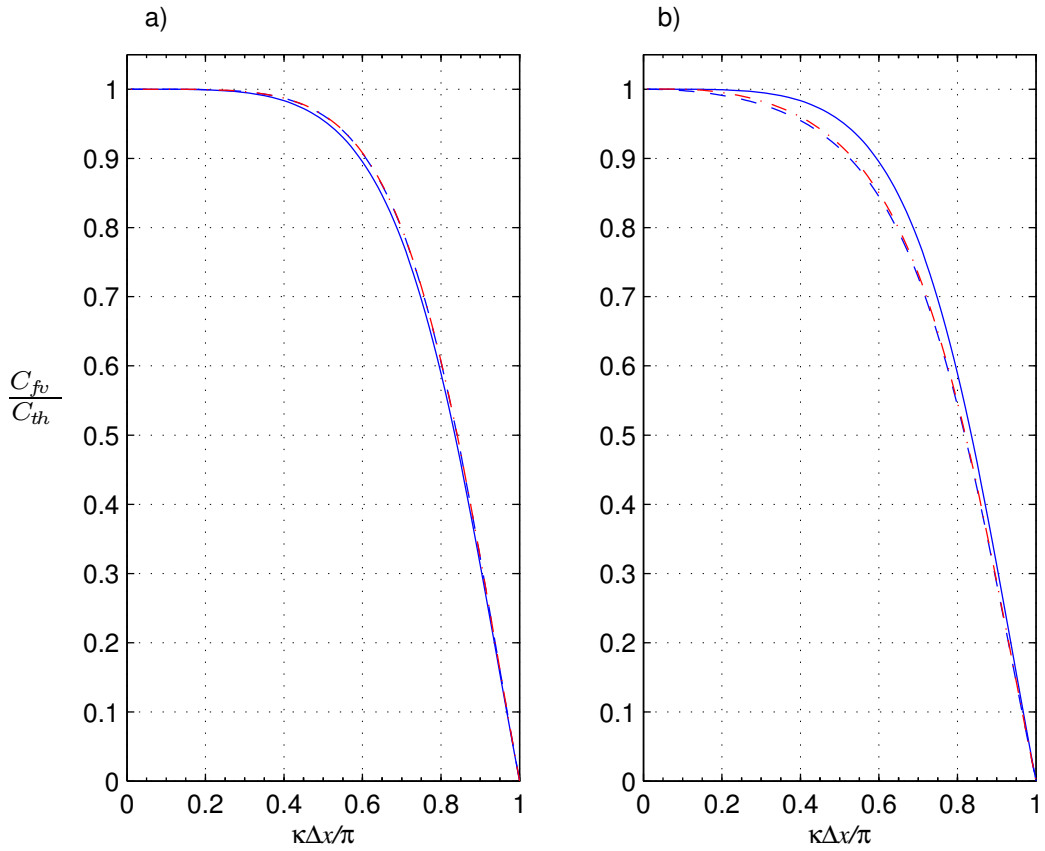

Figure 2.4: Ratio between computed and *physical* phase speed v/s $\kappa\Delta x$ for $\alpha = 1/15$, when (—) $\rho \to \infty$, (- -) $\rho \to 0$ and (-··-) $\rho = 0.1$. a) Full 4th order compact finite volume scheme. b) Mixed 4th and 2nd order discretization strategy.

Phase speed estimates using both approaches, the full 4th order and the *mixed* one, are plotted using $\alpha = 1/15$ in Figure 2.4. It can be seen that when $\rho \to \infty$, both strategies provide the same results. This means that for a given water depth, h_0, phase speed estimates get better in the *mixed* model if $\Delta x \to \infty$ which is of course rather problematic. Conversely, for a fixed spatial grid resolution, the modified finite volume method tends to give better phase speed estimates as the depth becomes shallower. However, larger errors could arise in deepest regions of the computational domain exactly where dispersive effects become predominant and the model is intended to perform better. On the contrary, the parameter ρ has only a marginal influence on phase speed errors when the full 4th order model is used. Thus the full 4th order compact finite volume method is more robust, in the sense that phase speed estimates are less sensitive to changes in the ρ parameter, than the *mixed* order version. For comparison, numerical results obtained with $\rho = 0.1$, which is a reasonable value for

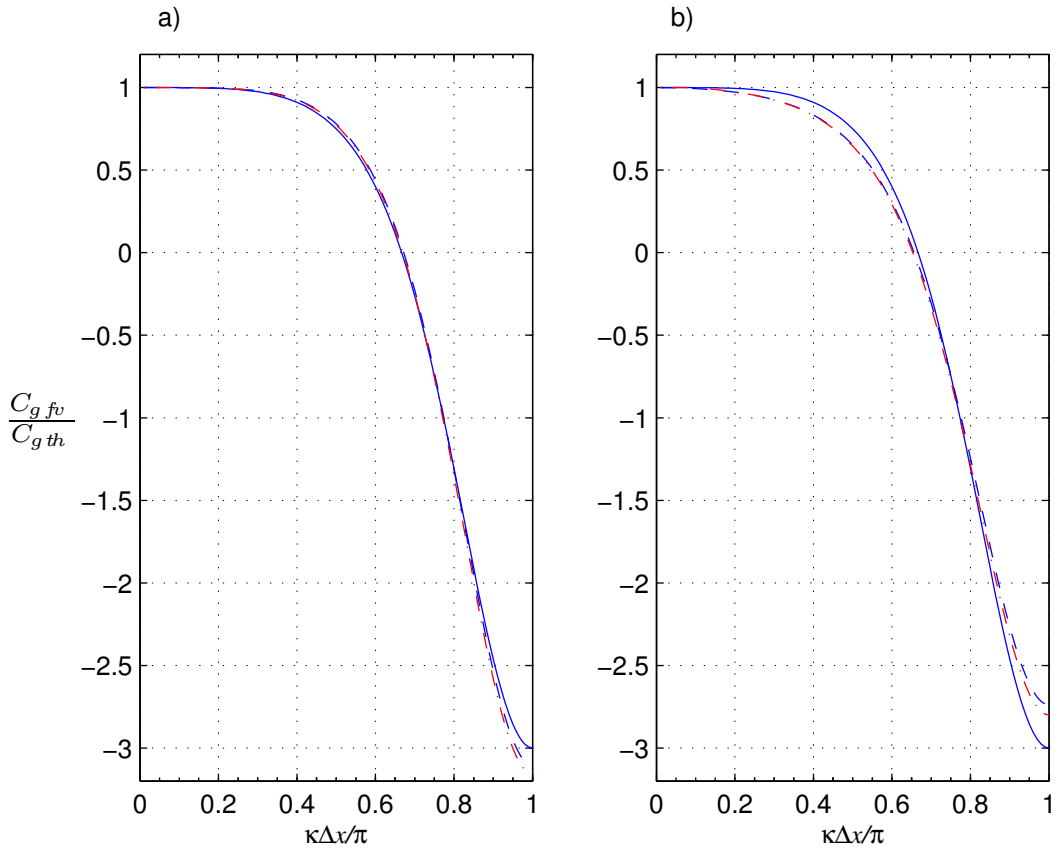

Figure 2.5: Ratio between computed and *physical* group velocity v/s $\kappa\Delta x$ for $\alpha = 1/15$, when (—) $\rho \to \infty$, (- -) $\rho \to 0$ and $(- \cdot -)$ $\rho = 0.1$. a) Full 4th order compact finite volume scheme. b) Mixed 4th and 2nd order discretization strategy.

that parameter, are also plotted in Figure 2.4. It is seen that the numerical estimate converges to the *physical* solution (within a 0.5 % error) when $\kappa\Delta x \simeq 0.325\,\pi$ ($L/\Delta x \simeq 6.1$) in the full 4th order case, and when $\kappa\Delta x \simeq 0.202\,\pi$ ($L/\Delta x \simeq 9.9$) in the *mixed* one. Hence, for a reasonable value of ρ, the *mixed* version requires nearly 62 % more nodal points per wavelength than the original one in order to properly describe linear phase speed. As explained before, the phase speed error in the *mixed* order model can be reduced if the parameter value $\rho = \Delta x/h_0$ is increased, however, the worst error occurs when $\Delta x/h_0 \to 0$. In that limit the 0.5 % error level is reached for $\kappa\Delta x \simeq 0.152\,\pi$ ($L/\Delta x \simeq 13.2$). Compared to the full 4th order scheme and for a given water depth more than twice nodal points per wavelength will be needed to achieve the same phase speed accuracy in the limit of very good grid resolution. Finally and in accordance with the leading-order truncation error analysis made before, close examination of Figure 2.4 shows that when $\rho = 0.1$ phase speed of well resolved waves (i.e. $\kappa\Delta x \ll \pi$) are

sligthly overestimated by the *mixed* order scheme.

Similar qualitative conclusions can be drawn when comparing numerical results for group velocities presented in Figure 2.5. The main difference here is that one obtains negative values for group velocities in the case of poorly resolved waves ($\kappa\Delta x > 0.67\pi$). On the other hand in order to describe group velocities within a 0.5 % error when $\rho = 0.1$, the full 4th order finite volume method requires $\kappa\Delta x \simeq 0.213\,\pi$ ($L/\Delta x \simeq 9.4$) while the *mixed* scheme reaches the same accuracy when $\kappa\Delta x \simeq 0.117\,\pi$ ($L/\Delta x \simeq 17.2$). It is confirmed then that proper numerical representation of group velocities is a more challenging task because more nodal points per wavelength are needed to converge to the *physical* solution and poorly resolved waves will transmit their energy in the wrong direction. In this particular test, the full 4th order numerical scheme shows an even better performance when compared to the *mixed* version because the latter requires roughly 83 % more nodal points per wavelength in order to reach the same level of spectral resolution. In the limit of very good grid resolution for a given water depth ($\Delta x/h_0 \to 0$) the *mixed* order model reaches the 0.5 % error in group velocities when $\kappa\Delta x \simeq 0.088$, thus requiring more than 22 nodal points per wavelength.

The analysis that have been presented not only demonstrates the clear superiority of the full 4th order version, but also shows that *mixed* order approaches must be taken with care since the associated discrete dispersion relation has a misleading dependence on $\rho = \Delta x/h_0$. On the other hand, *mixed* order strategies have been introduced in previous numerical models to avoid pentadiagonal or more complicated patterns in matrices that need to be inversed. We believe that compact schemes or deferred-correction strategies constitute a more satisfactory way to overcome this problem in the framework of dispersive wave propagation phenomena.

2.4.2 Analysis of the full discrete system

In order to achieve a comprehensive numerical analysis of the scheme we study in this section the full discrete system of equations which takes into account the Runge-Kutta time stepping. Individual Fourier components that one needs to substitute in linearized discrete equations (2.54), (2.55) and (2.56) have now the following form,

$$\begin{bmatrix} h_j^n \\ q_j^n \\ u_j^n \end{bmatrix} = \begin{bmatrix} h_\kappa \\ q_\kappa \\ u_\kappa \end{bmatrix} e^{\hat{\imath}\,(\kappa j\Delta x - (\omega_r + \hat{\imath}\omega_i)\,n\Delta t)} = \begin{bmatrix} h_\kappa \\ q_\kappa \\ u_\kappa \end{bmatrix} |\lambda|^n\, e^{\hat{\imath}\,(\kappa j\Delta x - \omega_r\, n\Delta t)}, \tag{2.75}$$

where ω_r and ω_i correspond to real and imaginary parts of the frequency and $|\lambda| = e^{\omega_i \Delta t}$ is the amplification factor of the numerical scheme. It can be seen that the analysis

expounded in the previous subsection on the semi-discrete system of equations will be equivalent to the one we are going to present now in the limit of good numerical temporal resolution as $\omega_i \Delta t \to 0$. Indeed, the real part of the frequency will give information about phase speed errors (numerical dispersion), and the associated imaginary part contains information about the stability of the scheme (numerical amplification/dissipation). Numerical properties of the discrete scheme are now driven by three free parameters, $\kappa\Delta x$, $\rho = \Delta x/h_0$ and the Courant number, $C_r = C_0\,\Delta t/\Delta x$.

It is worth to point out that analogous linear stability analysis have been performed recently on a finite element resolution of an equivalent Boussinesq set of equations by Woo and Liu [181], and on several finite volume resolutions of a KdV-like system of equations by Bradford and Sanders [24]. In what follows we will compare the numerical performance of our scheme with those previously published. Similarly, some comparisons between the full 4th order method and the *mixed* order version will be given for completion.

As before, we substitute Fourier components in the discrete system of equations (2.75). After using relation (2.59) in order to eliminate the auxiliary variable q in the 4th order Runge-Kutta time stepping process (2.53), it can be shown that the full discrete scheme takes the following form in the Fourier space,

$$\left(\mathcal{G}(\mathcal{K}) - \mathbf{I}\,|\lambda| e^{-\hat{\imath}\omega_r\,\Delta t}\right) \cdot \begin{bmatrix} h_\kappa \\ u_\kappa \end{bmatrix} = 0, \tag{2.76}$$

where $\mathcal{G}(s) = \sum_{p=0}^{4} \frac{1}{p!}\,(\Delta t \cdot s)^p$ is the Runge-Kutta time stepping operator and $\mathcal{K}$ is the spatial discretization operator introduced in the previous subsection. Nontrivial solution of equation (2.76) yields,

$$\begin{aligned} \left[1 + \frac{9}{2}\left(\frac{\Delta t}{\rho}\right)^2 K_1 K_2 + \frac{27}{8}\left(\frac{\Delta t}{\rho}\right)^4 (K_1 K_2)^2 - |\lambda| e^{-\hat{\imath}\omega_r\,\Delta t}\right]^2 \\ = \frac{9}{4}\left(\frac{\Delta t}{\rho}\right)^2 K_1 K_2 \left[2 + 3\left(\frac{\Delta t}{\rho}\right)^2 K_1 K_2\right]^2. \end{aligned} \tag{2.77}$$

Invoking definitions (2.62) and (2.63) we write,

$$K = \left(\frac{\Delta t}{\rho}\right)^2 K_1 K_2 = -\frac{\sin^2 \kappa\Delta x}{(2 + \cos \kappa\Delta x)^2} \frac{[\rho^2 + \alpha(\tilde{\kappa}\Delta x)^2]}{\rho^2 \Psi}\, C_r^2. \tag{2.78}$$

Thus, equating real and imaginary parts in equation (2.77) results in the following,

$$|\lambda| \cos \omega_r \Delta t = \mathcal{R} = 1 - \frac{9}{2}|K| + \frac{27}{8}|K|^2, \tag{2.79a}$$

$$|\lambda| \sin \omega_r \Delta t = \pm\,\mathcal{I} = \pm \frac{3}{2}\,(2 - 3\,|K|)\,|K|^{1/2}. \tag{2.79b}$$

Squaring and adding previous relations gives the amplification factor, while dividing (2.79b) by (2.79a) provides the discrete dispersion relation of the numerical scheme, i.e.,

$$|\lambda| = \sqrt{\mathcal{R}^2 + \mathcal{I}^2}, \tag{2.80a}$$

$$\tan \omega_r^{\pm} \Delta t = \pm \frac{\mathcal{I}}{\mathcal{R}}. \tag{2.80b}$$

Although the dispersion relation (2.80b) has two roots, in the frequency range of resolvable waves ($\omega_r \Delta t \in [0, \pi]$) only the root with a positive imaginary part is meaningful. Because of the change in sign of the function $\mathcal{I}$ when $|K| = 2/3$, the mode associated with the first root, $\omega_r^+ \Delta t$, remains in the plane of resolvable waves as far as $|K| \leq 2/3$. On the other hand, the second mode associated with $\omega_r^- \Delta t$, will be valid when $|K| > 2/3$. It is then concluded that, even though the numerical scheme does not have any spurious computational mode in the frequency range of resolvable waves, it is preferable to remain in the region defined by the inequality $|K| \leq 2/3$.

Numerical stability is studied now by looking at the amplification factor defined in (2.80a). The scheme produces non-amplifying solutions as far as $|\lambda| \leq 1$, so it is straightforward to show that if,

$$|K| \leq \frac{8}{9}, \tag{2.81}$$

the RK4 compact finite volume scheme is stable. In the general case, the stability condition on the Courant number will be a function of α, ρ and $\kappa \Delta x$, but it can be shown that the most stringent situation occurs when $\rho \to \infty$. Replacing relations (2.58) and (2.60) in (2.78) provides the following stability condition in that limit,

$$C_r \leq \frac{2\sqrt{2}}{3} \frac{(2 + \cos \kappa \Delta x)}{\sin \kappa \Delta x} \leq 2\sqrt{\frac{2}{3}}. \tag{2.82}$$

The numerical scheme is thus unconditionally stable if the Courant number is chosen to be less than 1.633 no matter what values of α and ρ are used and for all resolvable wave numbers. Nevertheless, the stability limit can be moved further on by decreasing the parameter value ρ, i.e. by improving the spatial grid resolution for a fixed h_0. In the limit of very good grid resolution ($\rho \to 0$), the stability condition (2.81) takes the following form,

$$C_r \leq \frac{2\sqrt{3}}{9} \frac{(2 + \cos \kappa \Delta x)}{\sin \kappa \Delta x} \sqrt{\frac{(1/3 + \alpha)}{\alpha} \frac{(5 + \cos \kappa \Delta x)(13 - \cos \kappa \Delta x)}{(11 + \cos \kappa \Delta x)}} \leq 1.603 \sqrt{\frac{(1/3 + \alpha)}{\alpha}}. \tag{2.83}$$

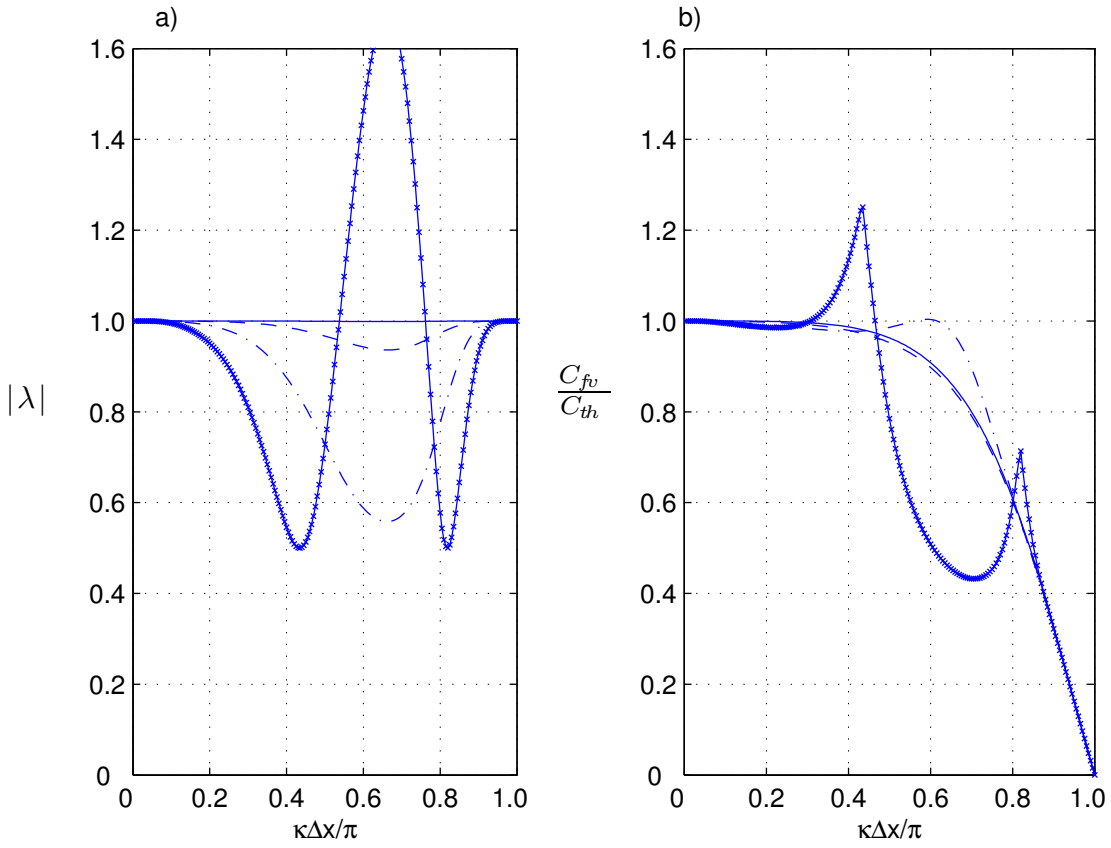

Figure 2.6: Numerical dissipation and phase speed error of the 4th order compact finite volume scheme for $\alpha = 1/15$, $\rho = 0.2$ at different Courant numbers : (—) $C_r = 1.0$, (- -) $C_r = 2.0$, (-··-) $C_r = 3.0$ and (-×-) $C_r = 4.0$. a) Amplification factor. b) Ratio between computed and *physical* phase speed.

Therefore, when taking $\alpha = 1/15$ the method remains stable for all resolvable wave numbers, $\kappa\Delta x$, if the Courant number is less than 3.926 in the limit of very good spatial resolution. It is interesting to note that the high order dispersion correction term introduces some kind of instability in the system because the stability limit is increased by reducing the weight of this term (i.e., $\alpha \to 0$). On the other hand, for finite values of ρ, it can be shown that the stability limit will be bounded by the two asymptotic values given in (2.82) and (2.83).

Even though stability is a necessary condition in order to ensure that the numerical scheme will not produce unbounded solutions in time, it doesn't say anything about the accuracy of the method in terms of dissipative and dispersive errors. For instance, Figure 2.6 shows numerical dissipation and phase speed errors for different Courant numbers and for a fixed value of $\rho = 0.2$ (keeping $\alpha = 1/15$). This particular ρ-

value has been chosen in order to perform a comparison with the numerical analysis presented in papers from Woo and Liu [181] and Bradford and Sanders [24]. It is seen in Figure 2.6-a) that when $C_r = 1.0$ the present compact finite volume scheme is stable and nearly neutral (i.e. $|\lambda| \simeq 1.0$), thus introducing a clear improvement over the Petrov-Galerkin finite element model described in reference [181] because with the same numerical parameters, amplifying modes were already present in the latter. In fact, those authors were only able to ensure stability when the Courant number was less than 0.5 which is a value more than three times smaller than the most stringent stability limit expressed in equation (2.82). Similarly, stability of several linear finite volume schemes (Lax-Wendroff, Fromm and Warming-Beam) and a centered 2nd order finite difference scheme used to solve a KdV-like system of equations was compared in reference [24]. For an almost equivalent set of numerical parameters ($C_r = 1.0$ and $\rho = \Delta x/h_0 \simeq 0.18$), Bradford and Sanders showed that only the Fromm and the Warming-Beam methods were stable but they appear to be dissipative for mid to high-range spatial frequencies. Thus, it can be concluded from this particular comparison that the present numerical scheme has a wider stability region and is less damping than those studied in references [24, 181]. Moreover, using Maclaurin series to expand (2.80a) it can be shown that for small values of $\kappa\Delta x$,

$$\lim_{\rho\to\infty}|\lambda| = 1 - \frac{C_r^6}{144}(\kappa\Delta x)^6 + O[(\kappa\Delta x)^8], \tag{2.84a}$$

$$\lim_{\rho\to 0}|\lambda| = 1 - \frac{C_r^6}{144}\left[\frac{\alpha}{(1/3+\alpha)}\right]^3 (\kappa\Delta x)^6 + O[(\kappa\Delta x)^8]. \tag{2.84b}$$

Therefore, the dissipative error for the present finite volume scheme is $O[(\kappa\Delta x)^6]$, while linear finite volume schemes studied by Bradford and Sanders [24] only showed to be $O[(\kappa\Delta x)^4]$ accurate.

Further information on the damping modes associated to our numerical model can be obtained from Figure 2.6-a) when looking at amplification factors associated to increasingly high Courant numbers. It is seen that for $C_r = 2.0$ and $C_r = 3.0$ some mid-range frequency dissipation is present with a maximum located at $\kappa\Delta x \simeq 0.662\,\pi$. Additional computations show that the numerical scheme is non-amplifying (stable) for $\rho = 0.2$ as far as $C_r < 3.71$. However, mid-range frequencies begin to be heavily damped before reaching that limit (see Figure 2.6-a)). As discussed in reference [80], this dissipative behaviour is mostly due to the Runge-Kutta time stepping.

Phase speed errors obtained for $\rho = 0.2$ and for different Courant numbers are presented in Figure 2.6-b). It is seen that phase speed estimates get worse when increasing the Courant number. Again, an unstable rapidly growing mode can be identified and

coincides with the one observed for the amplification factor. It is also evident from this figure the passage from one root to the other in the numerical dispersion relation (2.80b) that takes place between Courant numbers $Cr = 3.0$ and $C_r = 4.0$. As before and in the limit of small $\kappa\Delta x$, it can be shown that a Maclaurin expansion of the dispersion relation yields,

$$\lim_{\rho\to\infty} \frac{C_{fv}}{C_{th}} = 1 - \frac{1}{180}\left(1 + \frac{3}{2}\,C_r^4\right)(\kappa\Delta x)^4 + O[(\kappa\Delta x)^6], \tag{2.85a}$$

$$\lim_{\rho\to 0} \frac{C_{fv}}{C_{th}} = 1 - \frac{1}{2880}\left(11 + 24\left[\frac{\alpha}{(1/3+\alpha)}\right]^2 C_r^4\right)(\kappa\Delta x)^4 + O[(\kappa\Delta x)^6]. \tag{2.85b}$$

Therefore, phase errors dominate over dissipative errors in the present compact finite volume scheme. Linear finite volume schemes studied by Bradford and Sanders [24] showed similar characteristics but with larger truncation errors. Figure 2.6 also indicates that in the present example, stable neutral solutions are obtained if $C_r \leq 1.5$. It is important to note that phase speed will not be overpredicted in this range of Courant numbers.

In the general case, it is possible to construct stability and phase error contour plots in the $(C_r, \kappa\Delta x)$ plane for different values of the ρ-parameter. Before doing so we recall that, to the authors knowledge, detailed analysis of the spectral resolution of previously published numerical methods used to solve equivalent sets of Boussinesq-type equations have not been reported. However, this property is paramount when dealing with physical problems where different wavelength scales are naturally present or can emerge as a consequence of nonlinear interaction. For example, recent extended versions of Boussinesq-type equations can theoretically match the Stokes linear dispersion relation up to $\sigma \simeq 6$ when formulated in surface and horizontal velocity variables (e.g., [70, 110]), and up to even higher values ($\sigma \simeq 25$) if the vertical velocity is in addition retained as unknown (see reference [108]). Nevertheless, if numerical schemes used to solve the associated systems of PDE are not carefully concieved to correctly reproduce phase speed and group velocity for all physical wavelengths, theoretical improvements concerning the extension of the σ range may be unpractical. For instance, if the *mixed* order strategy is used to discretize convective and dispersive terms, the asympotic error analysis given in the previous section showed that the 0.5 % phase speed error limit remains between $0.15\pi < (\kappa\Delta x)_{0.5\%} < 0.3\pi$ when $\omega_i\Delta t \to 0$. Therefore, the lower limit of this inequality, which occurs asymptotically in deep waters, is an indication of the numerical resolution of the scheme when dealing with extremely dispersive waves. This means that the discretized model will correctly describe linear phase speed for wave numbers $\kappa\Delta x$ being less than 0.15π and this value fixes the ρ-parameter that will

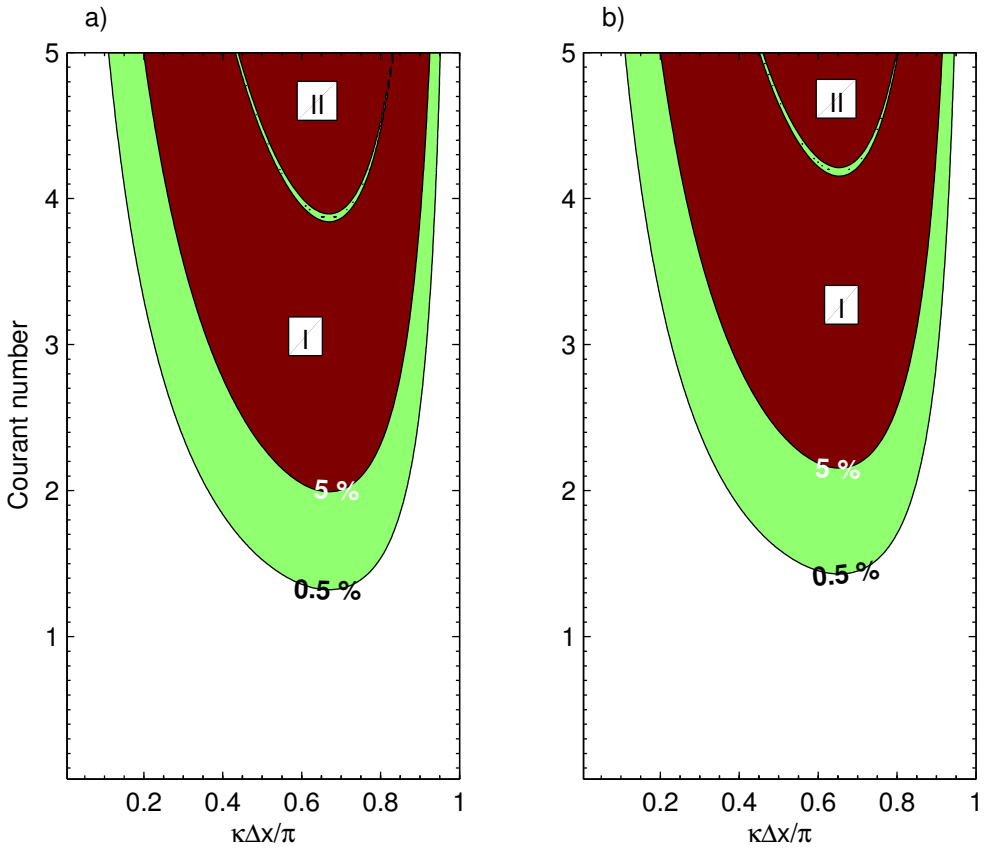

Figure 2.7: Contours of 0.5 % and 5 % dissipative errors for $\alpha = 1/15$ and $\rho = 0.1$ in the $(C_r, \kappa\Delta x)$ plane. $|\lambda| \leq 0.95$ in region I (damping), and $|\lambda| \geq 1.05$ in region II (amplifying). a) Full 4th order compact finite volume scheme. b) Mixed 4th and 2nd order discretization strategy.

ensure that all physical wavelengths will be well represented (because $\kappa\Delta x = \sigma\rho$). If the physical σ range of the discretized Boussinesq-type equations is 6, then a value of $\rho = \Delta x/h_0 \leq 0.08$ must be used in the *mixed* order finite volume scheme. Similarly, if the physical range is moved further on to reach $\sigma \sim 25$ as it is the case in reference [108], then the spectral resolution of the numerical scheme imposes the discretization parameter ρ to be less than 0.02. It is evident from results presented in the previous subsection that, for group velocities, the ratio $\Delta x/h_0$ must be further reduced to achieve an accurate representation of this property. Moreover, for finite Courant number values spectral resolution will drop even more. This simple but important discussion allows us to illustrate the relevancy of the spectral resolution in terms of phase speed and group velocity of numerical schemes. In the framework of numerical resolution of Boussinesq-type equations, this important DRP property must be studied. More specifically, if extended versions of those equations, which may allow for the

description of highly dispersive waves are to be discretized, the use of low-resolution explicit finite difference formulae can lead to overwhelming computational efforts if an accurate representation of group velocities is intended (even if high order schemes are used). Indeed, it is widely aknowledged that such approximations have significantly worse spectral properties than equivalent compact formulae [90, 93, 95].

Contour plots for the dissipative errors in the $(C_r, \kappa\Delta x)$ plane are presented in Figure 2.7 for the full 4th order scheme and the *mixed* order approach. The ρ-parameter is fixed at 0.1, a value that allows both numerical approaches to describe all physical wavelengths because the linear dispersion relation associated to the PDE system match the theoretical Stokes relation up to $\sigma \sim 3$ when $\alpha = 1/15$ [9]. This figure shows that there is a wide region where both schemes remain stable and nearly neutral (white region). In region I, the numerical scheme starts to damp mid-range frequencies but it remains stable. Amplifying unstable modes begin to disturb the numerical solution when the thin region located between zones I and II is reached. Therefore, the upper edge of region I roughly represents the stability limit of the scheme. It is seen that the full 4th order version will be stable for all frequencies if C_r is taken to be less than 3.8, and that the *mixed* order one will remain non-amplifying if C_r is less than 4.1. Hence, the use of low order explicite finite difference formulae to discretize dispersive terms results in a slight improvement in stability and similar conclusions were given in reference [63]. However, for practical computations, spectral resolution in terms of phase speed, group velocity and numerical dissipation will impose more stringent conditions than stability and the Courant number will be in general choosed to be less than 1.5 in order to ensure a proper representation of all physical wavelengths.

As discussed before, spectral resolution and DRP properties of numerical schemes used to solve wave-type equations must be studied as emphasized in reference [139]. A wide range of stability region is for sure a desired quality for any numerical solver because small unphysical perturbations will not grow unboundly. However, the use of too high Courant numbers (even if they are below the stability limit) to integrate the equations in time can produce poor results in terms of phase and group velocities and this was already illustrated in Figure 2.6. Now we generalize this result plotting countours of phase speed and group velocity errors in the $(C_r, \kappa\Delta x)$ plane in Figures 2.8 and 2.9. It is seen that numerical errors in phase speeds and group velocities are rather insensitive to changes in the Courant number as long as the latter remains below a value of 1.5. For Courant numbers laying above that limit, the extent of the DRP region in terms of wave numbers $\kappa\Delta x$ is reduced as the Courant number increased and this is more evident for the full 4th order scheme. On the other hand, the DRP region for a given Courant number is bigger when using the full 4th order approach than when

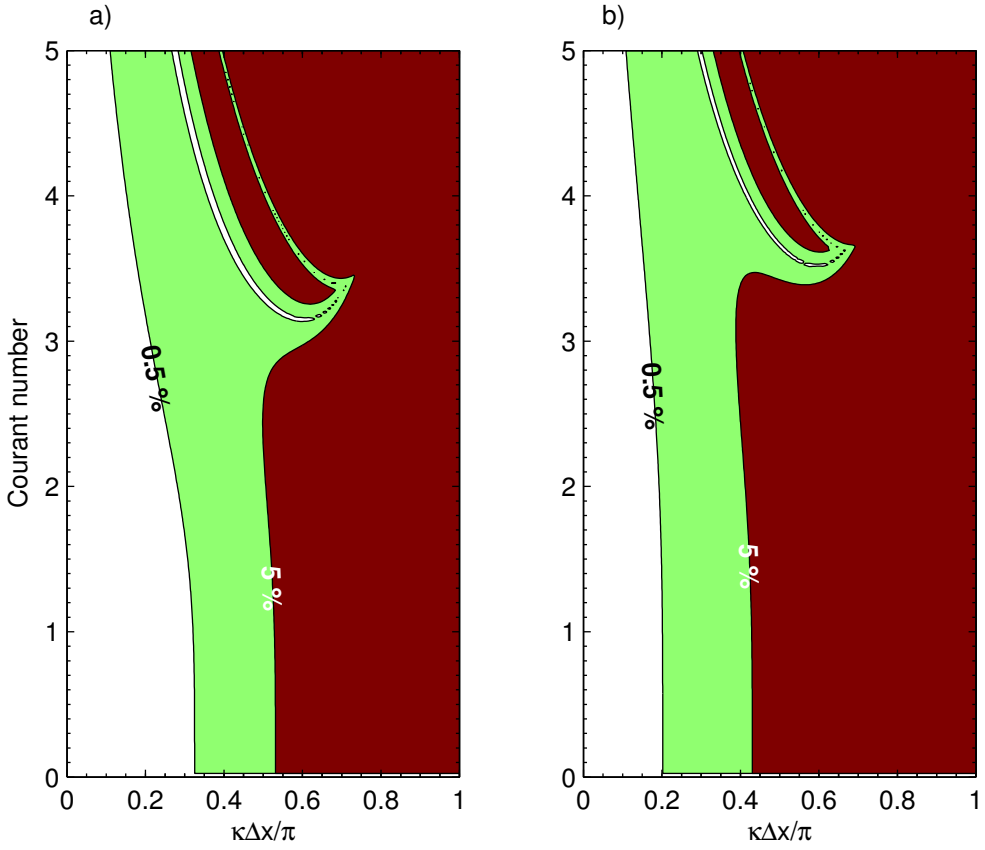

Figure 2.8: Contours of 0.5 % and 5 % phase speed errors for $\alpha = 1/15$ and $\rho = 0.1$ in the $(C_r, \kappa\Delta x)$ plane. a) Full 4th order compact finite volume scheme. b) Mixed 4th and 2nd order discretization strategy.

discretizing dispersive terms with 2nd order explicit finite difference formulae. Indeed, if the Courant number is kept below a value of 1.5, the extent of the region where numerical errors in group velocities are less than 0.5 % is almost two times bigger in the full 4th order version than in the *mixed* one. A similar trend is observed in Figure 2.8 for the comparative analysis of numerical representation of phase speeds. This clearly shows the inconvenience of using *mixed* order strategies to simplify the numerical treatment of high order terms because it results in an important overall reduction of the spectral resolution in this particular finite volume scheme. Therefore, significative more nodal points per wavelength will be needed to properly describe wave kinematics; moreover, if the numerical scheme must also be able to deal with extremely dispersive/short waves, this critical limitation may also obscure theoretical improvements in the σ-range of application of Boussinesq-type equations.

Finally, it can be concluded from the linear analysis that keeping the Courant

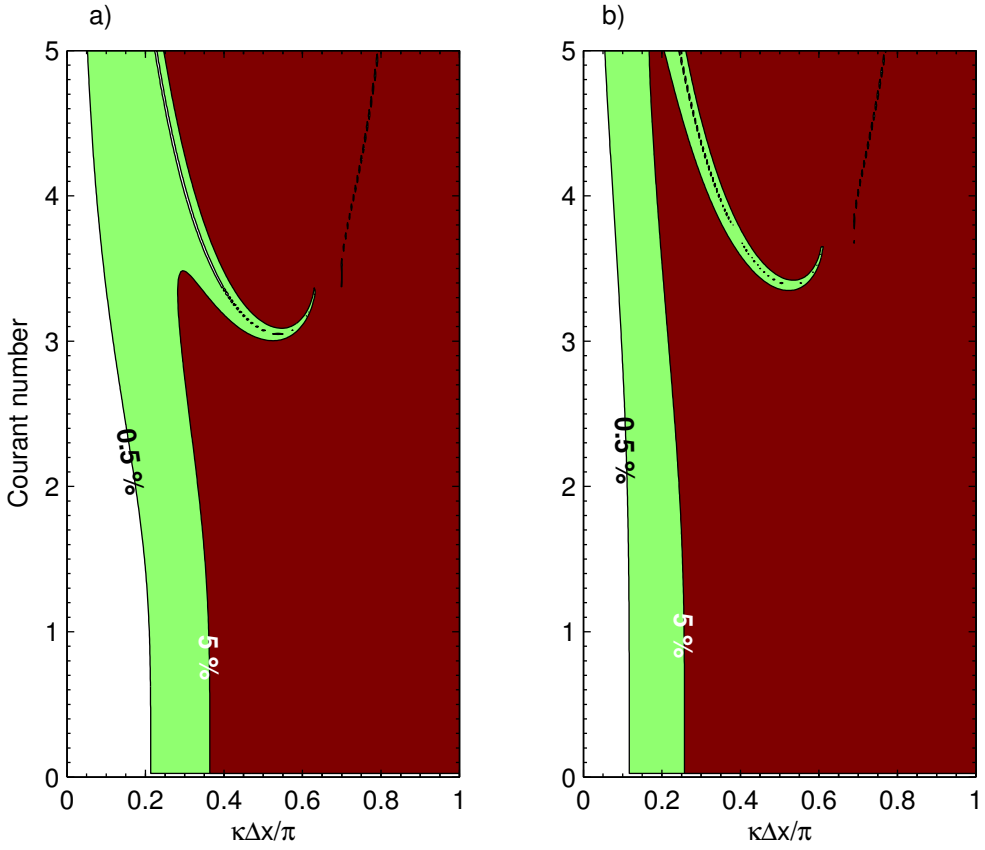

Figure 2.9: Contours of 0.5 % and 5 % group velocity errors for $\alpha = 1/15$ and $\rho = 0.1$ in the $(C_r, \kappa\Delta x)$ plane. a) Full 4th order compact finite volume scheme. b) Mixed 4th and 2nd order discretization strategy.

number below 1.5 and using $\rho = 0.1$ for numerical computations will ensure that the compact finite volume scheme used to discretize the set of PDE derived here is stable, non-damping and with a maximized DRP region.

2.5 Numerical experiments and discretization errors

In this last section we study the stability of the proposed numerical scheme using an heuristal approach that allows us to explore how this property is affected by nonlinearity. Besides, the discretization error is estimated numerically by comparing analytical and computed results using the solitary wave solution presented in Section 2. Discretization error is related to the order of approximation of the scheme and is different (although somehow related) from the spectral properties investigated in the previous section. Here, we will instead determine how truncation errors, which belong to numer-

ical approximation of partial derivatives, are reduced when the spatial and temporal grid is refined.

2.5.1 Discretization errors

Whithout dispersion correction terms (i.e. $\alpha = 0$) and for a flat bottom, equations (2.18)-(2.19) have the solitary wave solution expressed by relations (2.22)-(2.24). This interesting property is used here to estimate discretization errors by comparing the numerical and the exact solution for this particular PDE system. In order to do that, a solitary wave of relative amplitude $a/h_0 = 0.2$ is propagated during two characteristic wave periods over a still water depth of $h_0 = 1$ m. The characteristic period is estimated from the characteristic length of the solitary wave, L, following the definition used in reference [181]. Hence, L is the distance over which $\eta/h_0 \geq 0.001$, where η is the location of the free surface. The equivalent solitary wave period is then defined as $T = L/C$ and can be computed invoking the definition for the phase speed of the soliton given in equation (2.24). The average numerical error is estimated using the L_1 norm and reads,

$$L_\epsilon = \frac{\sum_{j=0}^{j=I} \|h_j^n - h_j^e\|_1}{\sum_{j=0}^{j=I} \|h_j^e\|_1}, \tag{2.86}$$

where h^e and h^n are respectively the exact and the numerically computed solution, I is the total number of finite volumes used to discretize the spatial domain, and water depth values are evaluated at cell faces of each control volume (j-nodal points). Equations are integrated using the solitary wave solution centered at $x = X_0$ as initial condition. Computations are carried out during two wave periods and results compared with the analytical soliton centered at position $x = X_0 + 2L$. All numerical tests are performed using a fixed point iteration tolerance of $\tau = 10^{-4}$ to solve (2.47). Spatial discretization error is studied using a small time step of $\Delta t = 0.002$ s in order to ensure that most of the errors belong to the spatial grid resolution used to perform computations. Estimated convergence errors obtained by increasing the number of finite volumes per wavelength (i.e. decreasing ρ) are presented in Figure 2.10-a) where it can be seen that, except for the last two computed errors using the smallest ρ, the ideal slope for a 4th order spatial discretization is fairly well recovered. It is believed that for the two last computed values, round-off errors or some influence of the time step (because it is not small enough for the prescribed ρ value) are responsible for the slight divergence from the ideal slope. Nevertheless, it is widely confirmed that the finite volume discretization of the system of PDE is $O[(\Delta x)^4]$ accurate.

An equivalent numerical test is performed on discretization errors due to time in-

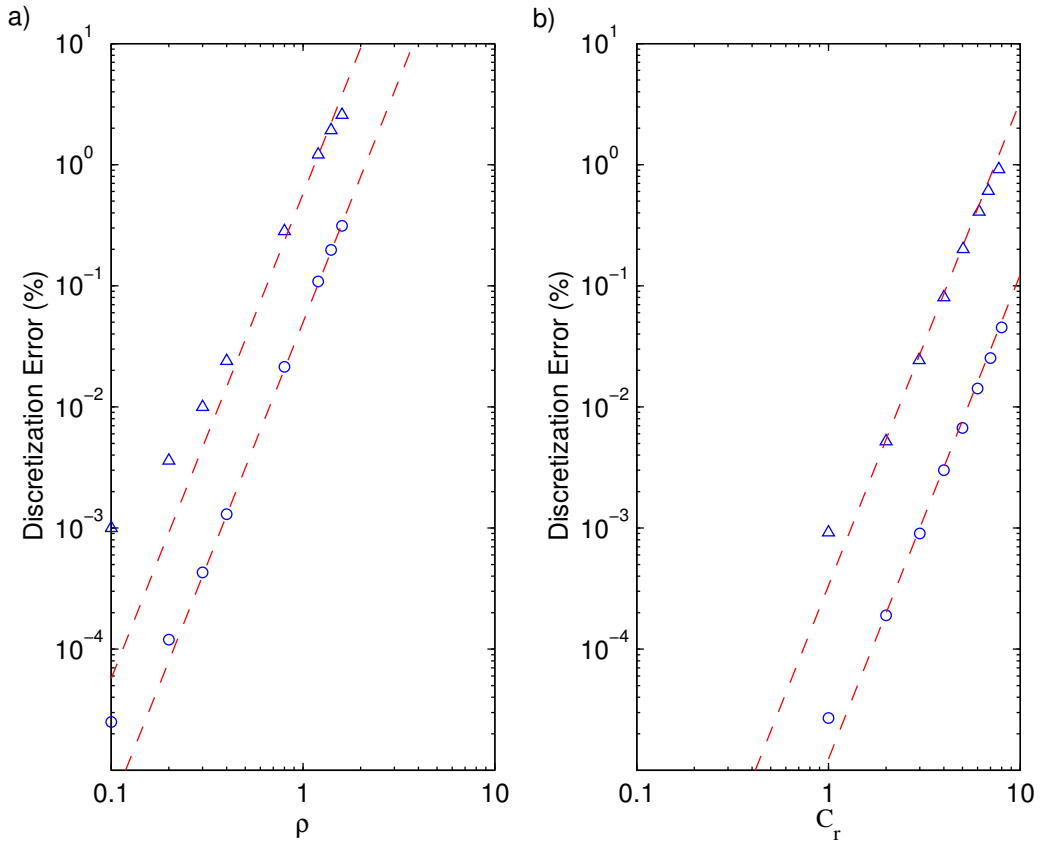

Figure 2.10: Discretization errors for a propagating solitary wave. (−−) Ideal 4th order slope; (∘) computed errors when $a/h_0 = 0.2$; (△) computed errors when $a/h_0 = 0.6$. a) Convergence error in Δx using a fixed $\Delta t = 0.002$ s. b) Convergence error in Δt using a fixed $\rho = 0.1$.

tegration for a fixed $\rho = 0.1$ and monotonically decreasing the Courant number. Associated numerical errors are presented in Figure 2.10-b) and compared against the theoretical 4th order slope. Again, it is fairly well confirmed that the convergence error is $O[(\Delta t)^4]$, except for the last point where, probably for the same reasons stated before, the computed slope slightly diverges from the theoretical one. Therefore, the proposed RK4 compact finite volume scheme is $O[(\Delta x)^4, (\Delta t)^4]$ accurate.

In addition, convergence errors obtained for a highly nonlinear propagating solitary wave ($a/h_0 = 0.6$) are also plotted in Figure 2.10. It is seen that the rate of convergence for the discretization error in Δx is slightly worse than the one observed in the moderately nonlinear case investigated before. The latter is not surprising since strong nonlinearities may affect the model performance. Nevertheless, the convergence rate is still well above $O[(\Delta x)^3]$ for this challenging test and the computed slope only starts to diverge from the theoretical one when $\Delta x/h_0 \leq 0.4$. This trend, which has

been also noticed in the previous example, is probably associated to the fixed time step value used to estimate errors since in this highly nonlinear case the equivalent wavelength (and the associated wave period) is much smaller than the previous one. On the contrary, the convergence rate for temporal discretization appears to be rather insensitive to changes in nonlinearity since the ideal slope is well recovered. Thus, the four-stage Runge-Kutta scheme used to integrate the system in time has an excellent performance even for highly nonlinear cases.

This numerical test also validates the chosen deferred-correction approach used to preserve the tridiagonal structure of the matrix that links the auxiliary variable q with the depth-averaged velocity u in matrix equation (2.47). Moreover, the convergence rate was rather insensitive to changes in the fixed point iteration tolerance as long as $\tau \leq 10^{-4}$. Indeed, $\tau = 10^{-4}$ proved to be a sufficient choice in all computations.

Another important property that any numerical scheme used to solve Boussinesq-type equations must fulfill concerns its ability to preserve wave form and phase speed in time. These qualities have been already investigated from an analytical point of view through the linear spectral analysis given in Section 4. However, it is important to test these properties in the case of highly nonlinear waves propagating over long distances. This can be achieved using again the closed form solitary wave solution of the original Serre equations. Similar tests have been reported in references [175, 177, 181] for moderately nonlinear solitary waves. For instance, Figure 2.11 shows computed results for the propagation of a solitary wave of relative amplitude $a/h_0 = 0.6$ over 50 equivalent wavelengths using $C_r = 1$ and $\rho = 0.1$. A perfect agreement between the analytical and numerical solution is noticed. It is remarkable how this result confirms the analysis given in previous section where it was shown that these set of numerical parameters may produce stable non-damping solutions for all physical wavelengths. In addition, when decreasing the number of nodal points per wavelength some phase speed and amplitude errors can be noticed. Nevertheless, even for $\rho = 0.2$ the agreement with the analytical solution is almost perfect. Although an objective comparison with previously published models used to solve equivalent set of equations cannot be performed, we recall that a similar grid resolution (~ 75 elements per wavelength but with $C_r \sim 0.5$) was used in [181] on the base of a Taylor-Galerkin finite element model and some phase speed errors were already noticed when propagating a moderately nonlinear ($a/h_0 = 0.3$) solitary wave over a shorter distance (~ 25 wavelengths). A similar trend was also reported in references [175] and [177].

Finally, when increasing the ρ-value further to reach 0.5 (~ 29 nodal points per wave lenght), bigger discrepancies show up. Nevertheless, the relative error in phase speed over this long distance appears to be less than 2 %.

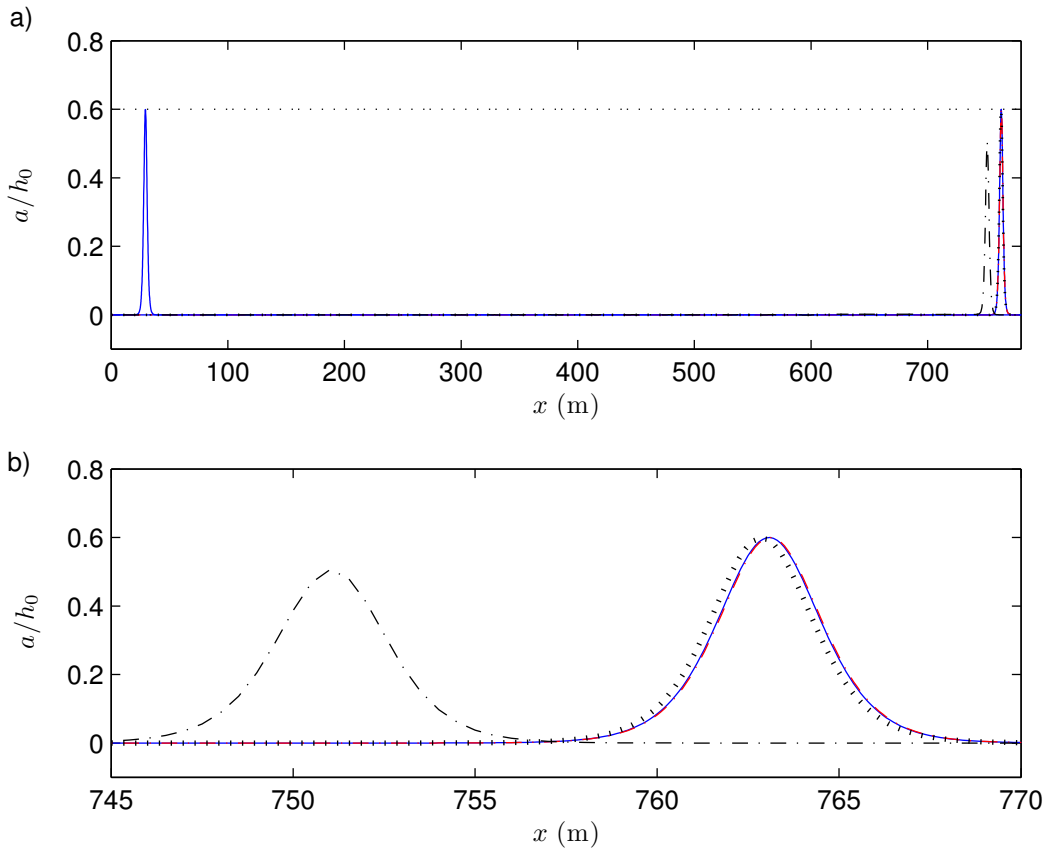

Figure 2.11: Strongly nonlinear solitary wave propagating over 50 equivalent wavelengths where $a/h_0 = 0.6$, $L = 14.7$ m, $T = 3.7$ s. Exact solution $(-)$ and numerical computations performed with $C_r = 1.0$, $\rho = 0.1$ $(--)$, $\rho = 0.2$ $(\cdot\cdot)$, and $\rho = 0.5$ $(-\cdot-)$. a) Overview of the whole domain and initial and final locations of the solitary wave. b) Close inspection of numerical results.

2.5.2 Nonlinear stability

The way nonlinearity affects the stability of the proposed scheme is investigated now performing numerical experiments where we estimate the maximum Courant number for which a propagating solitary wave remains stable. Computations are carried out over three equivalent wavelengths for different relative amplitudes a/h_0 and for monotonically increasing Courant numbers until numerical instability shows up. The influence of the correction dispersion term is also investigated because it was analytically demonstrated in Section 4 that this term may produce some destabilizing effects in the system (see inequality (2.83)). Therefore, three different α-values are investigated, namely, $\alpha = 1/15$, $\alpha = 1/30$ and $\alpha = 0$. It is important to recall that it is expected that when $\alpha = 0$ important numerical (and mathematical) properties of

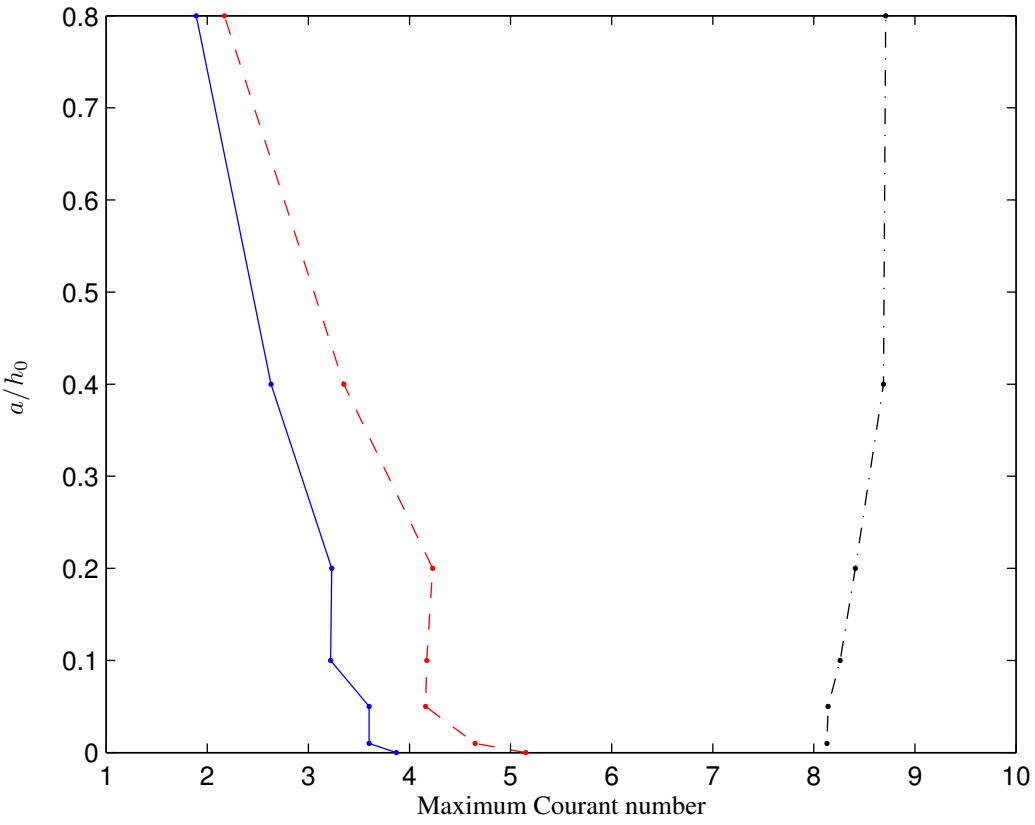

Figure 2.12: Stability limits estimated numerically using $\rho = 0.1$ for increasing nonlinear solitary waves and different values for the dispersion correction parameter : $(-)$ $\alpha = 1/15$, $(--)$ $\alpha = 1/30$, and $(- \cdot -)$ $\alpha = 0$.

the system may change as it was illustrated in Figure 2.3 where a totally different behaviour was noticed for this α-value. Numerical estimation of the stability limit in terms of the Courant number is given in Figure 2.12. Theoretical values obtained from linear analysis is also included in the figure (when $a/h_0 \to 0$) for $\alpha = 1/15$ and $\alpha = 1/30$. The limiting Courant number predicted by linear theory when $\alpha = 0$ and $\rho = 0.1$ is roughly $C_r = 16$. Such a high value was not recovered numerically probably because the stability analysis performed in Section 4 may only be valid for finite values of α as discussed before. Nonetheless, for the two finite values of α investigated here, numerical experiments confirm in a satisfactory way the linear stability analysis as depicted in Figure 2.12. Moreover, when the dispersion correction term is switched off the stability region is considerably increased as it was expected from the numerical analysis of the scheme. It is also noticed that for finite α-values, nonlinearity does affect the stability of the scheme because the maximum stable Courant number is reduced.

Nevertheless, numerical experiments show that the RK4 compact finite volume scheme remains stable, even for extremely nonlinear waves, as long as the Courant number is kept below a value of 1.9 when $\alpha \leq 1/15$. Undoubtedly, this result constitutes a major improvement in stability when compared to previously published numerical solvers for Boussinesq-type equations.

It was noticed that for the finite α-values investigated, numerical instability was mainly triggered because the resulting matrix of equation (2.47) appeared to be ill-conditioned in the presence of high nonlinearity. On the contrary, when dispersion correction terms were set to zero, numerical instability appeared to be mainly due to intrinsic properties associated to the 4th order Runge-Kutta time stepping, and this may partially explain why the region of stability was only slightly affected by changes in a/h_0 when $\alpha = 0$. We believe that this misleading dependence on the chosen α value must be further investigated on a mathematical basis because it was demonstrated that the dispersion correction strategy used here may lead to an important reduction of the stability region. Moreover, it was rather surprising to confirm numerically that the stability limit may reach such high Courant numbers when the dispersion correction term was switched off.

2.6 Conclusions

A novel approach to numerically handle a set of fully nonlinear and weakly dispersive Boussinesq-type equations was presented and deeply investigated using numerical analysis. The chosen set of extended Serre equations could be written in a weak quasi-conservative form which makes the use of finite volume methods very attractive. Indeed, recently developed compact strategies for cell-face reconstruction in the framework of finite volume methods were borrowed from CFD and adapted to this particular set of PDE. High order accuracy was achieved in spectral space and numerically estimated discretization errors confirmed that the newly developed scheme is fully 4th order in space and time while computational efforts were kept at a very reasonable level. The latter constitutes an important feature of the present scheme because extensions in two horizontal dimensions (2D-H), where relatively large scale problems ($\sim$ km) are to be discretized, may be achieved at affordable computational costs. In fact, the use of the present compact approach allowed us to reduce CPU time by more than three times when compared to our previous explicit 4th order finite volume model (see reference [39] also reprinted in Appendix C). Moreover, we believe that the particular choice of this compact finite volume method will allow us to extend the model in 2D-H

staightforwardly taking advantage of developments already available in several space dimensions and unstructured grids (e.g., [93, 142]).

On the other hand, the use of linear spectral analysis provides important information concerning the performance of the newly developed scheme. For instance, we have good reasons to believe that the widely used strategy of discretizing convective and dispersive terms using *mixed* order finite difference formulae may lead to phase and group velocity errors which are difficult to control. This drawback can be specially critical for computations dealing with extremely dispersive waves since a good description of the whole range of characteristic wavelengths will certainly impose the use of a very fine grid resolution. Therefore, some recent theoretical improvements for Boussinesq-type equations may be unpractical for real world applications. The latter has a strong analogy with some difficulties encountered in the field of CFD where, for direct numerical simulations (DNS) of Navier-Stokes equations, the range of spatial lengths that a particular numerical scheme should be able to correctly represent is broadened towards smaller scales for increasingly high Reynolds number (thus requiring further refining of the grid size). This question has not really been tackled yet in the framework of coastal engineering. However, if numerical modelling of nearshore hydrodynamics is to be handled with help of Boussinesq-type equations, efficient, accurate and stable larger scale models are to be developed.

Additionally, qualitative comparisons with previously published numerical schemes used to solve equivalent set of equations were performed in Section 4 and 5. Linear spectral analysis and some numerical experiments showed that the present RK4 compact finite volume model possesses a wide stability region, good spectral resolution and an excellent numerical behaviour even when dealing with high nonlinearities. For instance, stability is only ensured in some of the previously published numerical strategies used to solve equivalent set of equations for Courant numbers which should remain below 0.5 (e.g., [69, 141, 181]). On the contrary, the present finite volume scheme has shown to be unconditionally stable (i.e., for all wave numbers and spatial grid resolutions) if Courant number is fixed to a value below 1.6, thus introducing fundamental improvements over previous ones. Moreover, this limit could be moved further on if grid resolution was improved and it was found in Section 5 that, even in the case of the propagation of an extremely nonlinear solitary wave, solution remained stable as far as $C_r \leq 1.9$ for a grid resolution of $\rho = 0.1$. Indeed, it was found analytically in Section 4 that the dispersion correction term as given in references [109, 110] introduces some kind of numerical instability in the system. This undesirable situation was also confirmed by numerical experiments.

Ongoing developments of the present model concern its extension into the surf

zone by including extra breaking terms. In particular, the incorporation of a novel approach for wave-breaking will be investigated in Chapter 5. Similarly, the numerical treatment of appropriate boundary conditions and the validation of the model for wave propagation over uneven bathymetries will be addressed in the next chapter.

Finally, it is also worth to point out that in more complex wave propagation problems (i.e., over uneven bottoms, periodic waves and added breaking effects), high-frequency waves can arise as a consequence of nonlinear interaction. In this context, the use of high-order filters to damp out spurious wave components is of common usage. The spectral analysis performed here gives insight of how this can be achieved without affecting the range of resolved physical wavelengths.

Chapter 3

Validation of the Time Domain Wave Propagation Model

3.1 Introduction

In the previous chapter, analytical properties of the proposed compact finite volume scheme were investigated. In particular, linear stability, spectral resolution and non-linear performance of the scheme were analyzed in the framework of wave propagation over flat bottoms. In the present chapter, practical considerations intended to apply model equations to realistic problems of wave propagation over uneven bathymetries are considered. Experimental test cases will provide additional insight concerning model performance when used to describe complex wave processes.

The set of mass and momentum conservation equations has already been presented in Chapter 2. Here we only recall the weak quasi-conservative form that has been discretized with a compact finite volume method. This particular fully nonlinear and weakly dispersive set of Boussinesq-type equations reads,

$$h_t + F_x = 0, \tag{3.1}$$

$$q_t + G_x = S, \tag{3.2}$$

$$q = (1+r)u - \frac{1}{3h}(h^3 u_x)_x - \alpha\xi^2 u_{xx}, \tag{3.3}$$

where the different flux functions, source term and dependent variable are defined

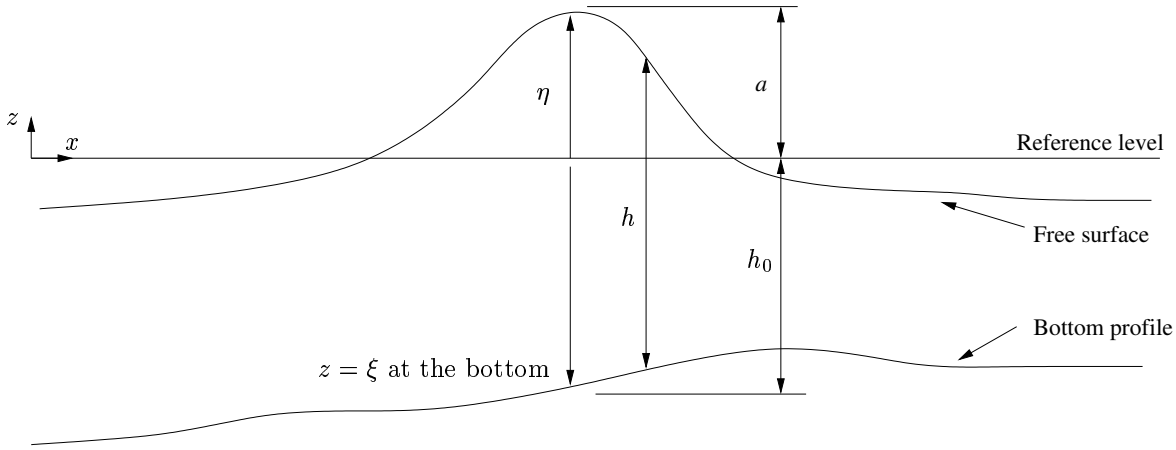

Figure 3.1: Definition sketch for wave propagation over unveven bathymetries. $z = \eta$ is the free surface elevation, $z = \xi$ is the bottom's location (here ξ has a negative value), and $h = \eta - \xi$ is the instantaneous water depth.

respectively as,

$$F = hu, \tag{3.4}$$

$$G = qu + g(h+\xi) - \frac{1}{2}u^2(1+\xi_x^2) + (\xi_x u - \frac{1}{2}hu_x)hu_x - \alpha\xi^2[u_x^2 + uu_{xx} + g(h+\xi)_{xx}], \tag{3.5}$$

$$S = -2\alpha\xi\xi_x \left[u\, u_x + g(h+\xi)_x\right]_x, \tag{3.6}$$

$$r = (h_x + \xi_x)\xi_x + \frac{1}{2}h\xi_{xx}. \tag{3.7}$$

Here h is the water depth, u is the depth-averaged horizontal velocity of the fluid, $z = \xi$ is the vertical coordinate of the bottom, g is the gravitational acceleration, and α is an adjustable parameter associated to the dispersion correction term as given for instance in references [109, 110]. The latter provides an extension of this shallow water set to deeper water wave propagation problems. The cartesian system of coordinates and a sketch of the problem is presented in Figure 3.1.

In the previous chapter, details on the application of a compact finite volume scheme to this set of equations have been given and thoroughly analyzed for wave propagation over horizontal bottoms. For readers' convenience the main features of the numerical scheme are summarized here : i) reconstruction of cell-face values from calculated cell-averaged ones is performed using a compact strategy developed in references [90, 93]; ii) high order dispersive terms are discretized using compact finite difference formulae [95]; iii) a four-stage Runge-Kutta method is used to integrate the discrete system in time; iv) 4th order accuracy in both, space and time is achieved; and v) stable non-damping solutions are obtained if the Courant number is taken to be less than 2.0

when using a grid size $\Delta x = 0.1\, h_0$ (h_0 being a representative value for the still water depth).

In the following, we will pursue the validation of the proposed model using both, numerical tests and experimental measurements for wave propagation over uneven bathymetries. The important question of conceiving and discretizing suitable boundary conditions for this system of equations will also be addressed. We are specifically interested in developing boundary conditions able to accurately describe several nonlinear wave procesess taking place in a nearshore context.

The present chapter is organized as follows : in section 3.2, dispersive properties of the model are studied, while section 3.3 deals with the numerical implementation of different types of boundary conditions. In section 3.4 a high order filtering technique is discussed and applied to damp out non-physical wavelengths not resolved by the model, and in section 3.5 a complete validation of the proposed scheme is presented using both analytical and experimental examples.

3.2 Optimal value for the dispersion correction parameter

Improvements in dispersive characteristics embedded in the Boussinesq-type model can be achieved by adjusting the α-parameter associated to the high order dispersion correction term. From an analytical point of view it was shown in reference [9] that a Padé (2,2) approximation for the exact linear Stokes dispersion relation is obtained when choosing $\alpha = \frac{1}{15}$. Therefore, this extended system of Serre equations can adequately match the Stokes relation up to $\sigma = \kappa h_0 \simeq \pi$, where κ is a characteristic wave number and h_0 is a typical water depth. Comparisons between dispersive characteristics for the partial differential equations set (PDE) and theoretical Stokes phase speed and group velocity are presented in Figure 3.2 for different values of α.

Similarly, a Stokes expansion analysis was performed by Barthélemy in the same reference [9] to investigate nonlinear properties of this particular system and the latter will not be repeated here. Nevertheless, bearing in mind that linear wave propagation properties of the set of PDE will theoretically allow for the description of wavelengths up to, say $\sigma_m = \kappa h_0 = 3.0$, one can try to find an optimum value for α by minimizing the joint root mean square error (RMS) of phase and group velocity estimates. Therefore, instead of choosing the α-value which produces the extact Padé (2,2) Stokes expansion, we will tune this parameter in order to minimize phase and group velocity errors over the dispersive range $0.0 \leq \sigma \leq 3.0$. The latter can be performed introducing the

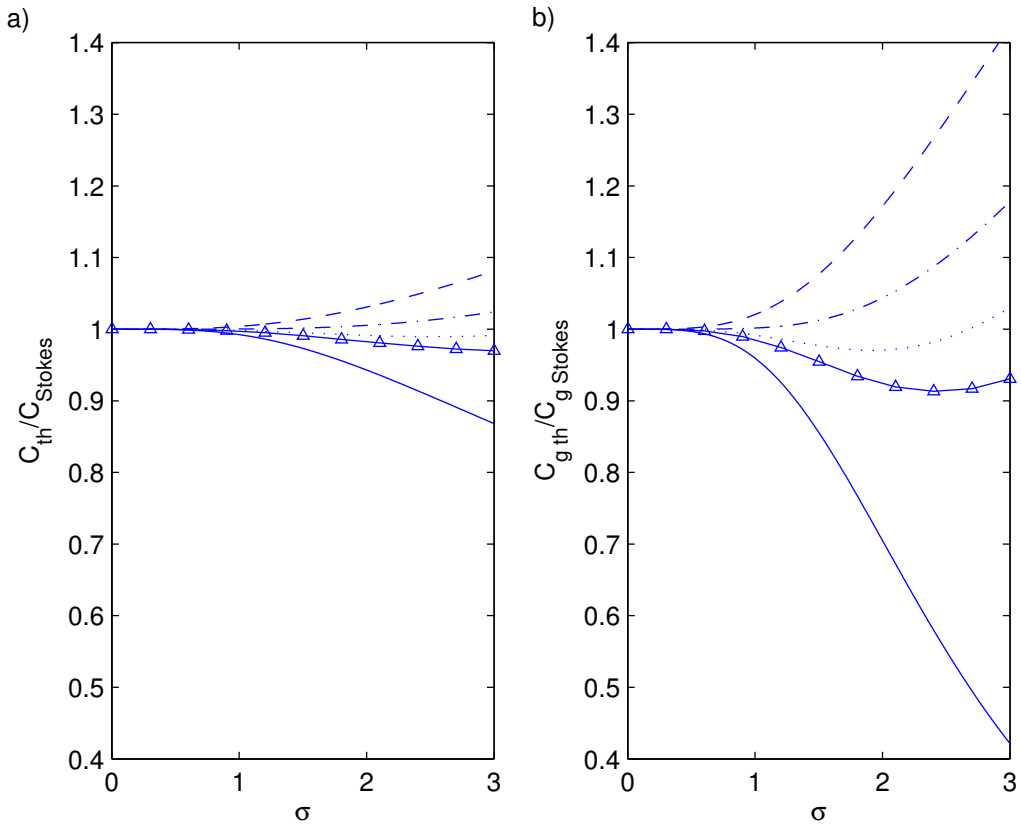

Figure 3.2: Comparisons between linear dispersion characteristics of the model and exact Stokes relations for different values of α : $(-)$ $\alpha = 0$; $(--)$ $\alpha = 1/10$; $(- \cdot -)$ $\alpha = 1/15$; $(\cdot\cdot)$ $\alpha = 1/20$; $(-\triangle-)$ $\alpha = 1/25$. a) Phase speeds. b) Group velocities.

following quadratic form for the joint error,

$$Err = \sqrt{\frac{\int_0^{\sigma_m} \left(C_{th} - C_{Stokes}\right)^2 d\sigma}{\int_0^{\sigma_m} C_{Stokes}^2 d\sigma} + \frac{\int_0^{\sigma_m} \left(C_{g\,th} - C_{g\,Stokes}\right)^2 d\sigma}{\int_0^{\sigma_m} C_{g\,Stokes}^2 d\sigma}}, \tag{3.8}$$

where C_{th} and C_{Stokes} represent respectively linear phase speeds belonging to the PDE system and to the Stokes theory, while $C_{g\,th}$ and $C_{g\,Stokes}$ are the associated group velocities. They read,

$$\frac{C_{th}}{C_0} = \sqrt{\frac{1 + \alpha\sigma^2}{1 + (1/3 + \alpha)\,\sigma^2}}, \tag{3.9}$$

$$\frac{C_{Stokes}}{C_0} = \sqrt{\frac{\tanh\sigma}{\sigma}}, \tag{3.10}$$

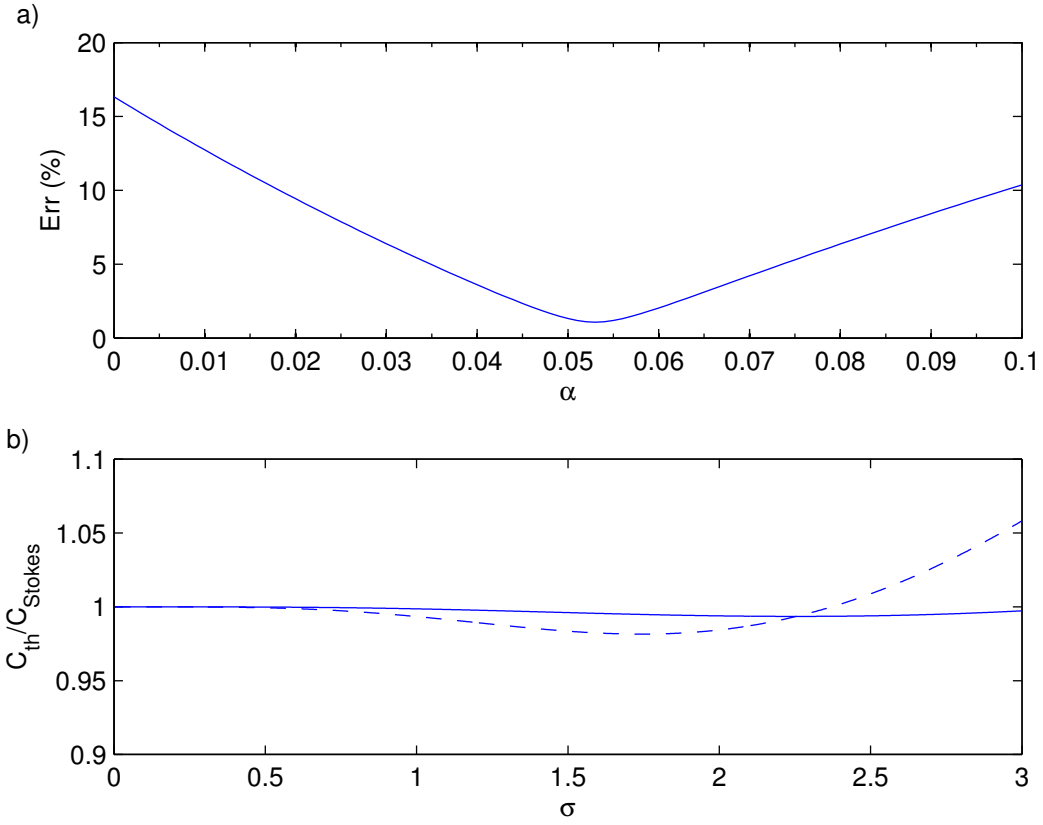

Figure 3.3: Optimal adjustement of dispersion correction parameter α over the range $0 \leq \sigma \leq 3.0$. a) Joint RMS error for phase and group velocities as a function of α. b) Comparison between model phase and group velocities and theoretical Stokes relations for the optimal value $\alpha = 0.053$: $(-)$ C_{th}/C_{Stokes}, and $(--)$ $C_{g\,th}/C_{g\,Stokes}$.

$$\frac{C_{g\,th}}{C_0} = \frac{\alpha\left(1/3+\alpha\right)\sigma^4 + 2\alpha\sigma^2 + 1}{\sqrt{\left[\left(1/3+\alpha\right)\sigma^2+1\right]^3\left(1+\alpha\sigma^2\right)}}, \tag{3.11}$$

$$\frac{C_{g\,Stokes}}{C_0} = \frac{\tanh\sigma + \sigma\left(1-\tanh^2\sigma\right)}{2\sqrt{\sigma\tanh\sigma}}, \tag{3.12}$$

with $C_0 = \sqrt{gh_0}$.

Hence, the optimization process consists in minimizing the error function (3.8) over $0 \leq \sigma \leq 3$. The associated error as a function of α is plotted in Figure 3.3-a). It is crearly seen that the joint RMSE has an absolute minimum in this dispersive range. The optimum value for α is 0.053 ($\simeq 1/19$) which is smaller than the analytical result given in reference [9]. In Figure 3.3-b) the phase and group velocities obtained with this α-value are plotted and compared against the corresponding Stokes relations. The agreement between the modelled dispersion relation and the theoretical one is

fairly good over this σ-range. Larger discrepancies exist for the group velocity but the maximum error remains below 6 % for all the physical wavelengths that the model is able to describe. Nevertheless, the error in group velocities starts to grow rapidly when $\sigma \geq 2.3$ showing that this property will be overestimated in this range of wavelengths.

Unless explicitly stated, all numerical examples that we will present in the following sections will be conducted with the dispersion correction parameter fixed to the optimal value determined here, i.e. $\alpha = 0.053$.

3.3 Boundary conditions

It is worth emphasizing that boundary conditions (BCs) affect numerical properties of the implemented scheme. Stability and accuracy of high order methods can be dramatically reduced if boundary treatment is not performed carefully [30, 139]. For hyperbolic systems it is generally acknowledged that the formal spatial accuracy of an inner Nth-order scheme is preserved if the system is closed by discretizing BCs with at least an (N-1)th-order numerical approximation (see for instance reference [76]). In the present chapter no analytical investigation of the numerical treatment of BCs is performed because of the complexity of the implemented high-order method. This important property is studied using an heuristical approach based on several benchmark tests. Our objective is to ensure that the discretized counterpart of boundary conditions does not introduce numerical instability in the system and preserves at the same time the spatial accuracy of the numerical scheme used in the inner region.

Numerical strategies intended to reproduce physical properties of the system of equations at boundaries must closely follow the intrinsic mathematical nature of it. Hence, we begin the analysis of BC's by studying the set of PDE from a mathematical standpoint. Writing Serre equations in characteristic directions provides useful information for developing suitable BC's for this set. We focus in BC's able to reproduce important physical processes in a nearshore context, namely, an open sea boundary condition, a moving shoreline strategy for the swash zone and a wall-type boundary condition.

3.3.1 Decomposition of Serre equations in characteristic directions

Serre equations, which are recovered from (3.1)-(3.3) when $\alpha = 0$ and bottom variations are neglected, can be recasted into a first order system of equations introducing

auxiliary variables following the lines given in reference [147], i.e.,

$$h_t + uh_x + u_x h = 0, \tag{3.13}$$

$$u_t + uu_x + gh_x + \frac{2}{3}h_x\Gamma + \frac{1}{3}h\Gamma_x = 0, \tag{3.14}$$

$$\Gamma = w_t + uw_x, \tag{3.15}$$

$$w = -hu_x, \tag{3.16}$$

where w is the vertical velocity evaluated at the free surface, and Γ is related to the vertical acceleration of the fluid evaluated at the same location. Thus, all dispersive terms associated to the free surface curvature are contained in Γ. This first order partial differential set writes down in the following matrix form,

$$\mathbf{A}\mathbf{\Phi}_t + \mathbf{B}\mathbf{\Phi}_x + \mathbf{C}\mathbf{\Phi} = 0 \tag{3.17}$$

with,

$$\mathbf{\Phi} = \begin{bmatrix} h \\ u \\ w \\ \Gamma \end{bmatrix} \ , \ \mathbf{A} = \begin{pmatrix} 1 & 0 & 0 & 0 \\ 0 & 1 & 0 & 0 \\ 0 & 0 & 1 & 0 \\ 0 & 0 & 0 & 0 \end{pmatrix} \ , \ \mathbf{B} = \begin{pmatrix} u & h & 0 & 0 \\ (g + \frac{2}{3}\Gamma) & u & 0 & \frac{1}{3}h \\ 0 & 0 & u & 0 \\ 0 & h & 0 & 0 \end{pmatrix} \ , \ \mathbf{C} = \begin{pmatrix} 0 & 0 & 0 & 0 \\ 0 & 0 & 0 & 0 \\ 0 & 0 & 0 & -1 \\ 0 & 0 & 1 & 0 \end{pmatrix}$$

We want to transform the preceding system into a simpler characteristic form through multiplication by a suitable bounded vector. We specifically aim at writing the system in the differential form,

$$\vec{\mu} \cdot d\mathbf{\Phi} + \vec{\lambda} \cdot \mathbf{C}\mathbf{\Phi} = 0, \tag{3.18}$$

where we have multiplied equation (3.17) by the required transformation vector $\vec{\lambda}$ and the total derivative of $\mathbf{\Phi}$ in associated charateristic coordinates reads,

$$d\mathbf{\Phi} = \left\{ dt\frac{\partial}{\partial t} + dx\frac{\partial}{\partial x} \right\} \mathbf{\Phi}.$$

Consequently, it follows that the vector $\vec{\mu}$ which allows to reduce the system of partial differential equations into an ordinary differential set must fulfill the following conditions,

$$\vec{\mu}\, dt = \vec{\lambda} \cdot \mathbf{A} \quad , \quad \vec{\mu}\, dx = \vec{\lambda} \cdot \mathbf{B}.$$

Thus, eliminating $\vec{\mu}$ from these expressions results in $\vec{\lambda} \cdot (\mathbf{A}\, dx - \mathbf{B}\, dt) = 0$, which implies for the characteristic transformation that,

$$\det\left(\mathbf{A}\, dx - \mathbf{B}\, dt\right) = \frac{1}{3}gh\, dt^2 \left(dx - u\, dt\right)^2 = 0. \tag{3.19}$$

Hence, Serre equations possess two double characteristic directions expressed by,

$$\frac{dx}{dt} = u, u \quad \text{and} \quad \frac{dx}{dt} = \infty, \infty \tag{3.20}$$

showing that the system is not of strictly hyperbolic type (see also reference [51]). From a mathematical standpoint, the latter means that it is not possible to find Riemann invariants for this PDE set. Nevertheless, in order to write BC's which would traduce this hyperbolic-parabolic mathematical nature, it is useful to recast Serre equations in the following quasi-hyperbolic form,

$$\frac{dR^+}{dt} = -\frac{1}{3h}\frac{\partial}{\partial x}\left(h^2\Gamma\right) \quad \text{along} \quad \frac{dx}{dt} = u + \sqrt{gh}, \tag{3.21}$$

$$\frac{dR^-}{dt} = -\frac{1}{3h}\frac{\partial}{\partial x}\left(h^2\Gamma\right) \quad \text{along} \quad \frac{dx}{dt} = u - \sqrt{gh}, \tag{3.22}$$

introducing positive and negative Riemann functions, $R^+ = u + 2\sqrt{gh}$ and $R^- = u - 2\sqrt{gh}$. Thus vertical accelerations, which are neglected in the nonlinear shallow water equations set (NSWE), are responsible for the loss of hyperbolicity in Boussinesq-type equations by introducing an horizontal dependence in the characteristic plane (x, t).

It is worth noting that from a physical point of view we can expect that time scales associated to dispersive effects would be larger than the ones associated to nonlinearities from intermediate to shallow waters. We may therefore assume that over short distances/times, Riemann variables might be locally conserved along characteristics. We will use this physical argument in what follows to develop suitable boundary conditions for the finite volume resolution of the extended system of Serre equations.

3.3.2 Open sea boundary condition

We seek to apply our cross-shore Boussinesq model to describe water waves propagating over a beach, thus an absorbing/generating boundary condition is required at the seaward boundary. We need to prescribe an incident wave field there allowing residual reflected waves to leave the computational domain without causing spurious oscillations. The numerical strategy consists in separating incident and outgoing waves on the base of the quasi-hyperbolic form derived in the previous subsection. This kind of approach has been applied to Boussinesq-type equations in references [119, 120] following the lines given by Van Dongeren and Svendsen [170] for fairly long waves. We will use a similar approach but without assuming that incident and outgoing waves are of small amplitude (weakly nonlinear) as it is the case in the aforementioned works. Instead, we neglect dispersive effects to estimate depth-averaged velocitiy and water

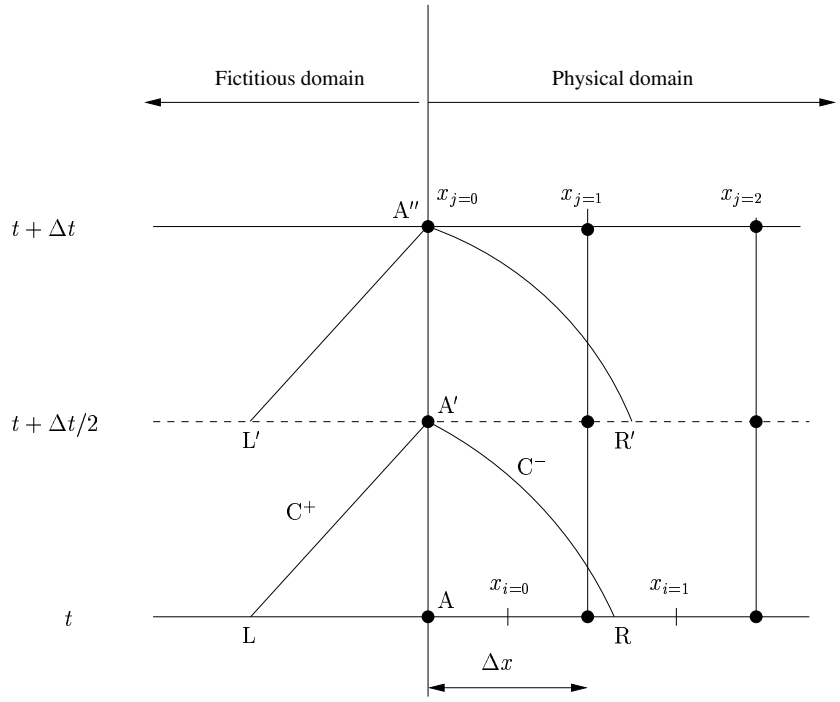

Figure 3.4: Definition sketch of characteristic decomposition of incident and outgoing waves.

depth at the seaward boundary using characteristic equations. We hypothesize that, at least locally, dispersive effects do not influence boundary values. This heuristical treatment will be validated later by numerical tests. Therefore, assuming that $\sqrt{gh} > u$, the left and right-going characteristic curves are expressed by equations (3.21)-(3.22) where vertical acceleration is neglected.

Since a four stage Runge-Kutta time stepping is applied to integrate equations at interior nodes, seaward values can be obtained taking into account that the numerical solution is evaluated twice at $t + \Delta t/2$ and twice at $t + \Delta t$. Using definitions sketched in Figure 3.4 we first integrate characteristic equations (3.21)-(3.22) from t to $t+\Delta t/2$,

$$R^+_{A'} - R^+_L = O(\sigma^2 \Delta t), \tag{3.23}$$

$$R^-_{A'} - R^-_R = O(\sigma^2 \Delta t). \tag{3.24}$$

Therefore, if left and right Riemann variables are known and time step Δt is small enough, this system can be solved for depth-averaged velocity and water depth at the boundary node A'. Thus, we need to estimate initial locations x_L and x_R from where positive and negative characteristic curves reach the point A' in a single time step of length $\Delta t/2$ (see Figure 3.4).

For incoming characteristics we assume that the incident wave field propagates from $-\infty$ (a fictitious domain) and into the seaward boundary with a constant wave form.

Hence, if the surface elevation time series of incident waves is prescribed as the function $\eta_A(t)$, the associated right-going Riemann variable should be,

$$R_L^+ = u_L + 2\sqrt{gh_L} = \sqrt{g\left[\eta_A(t+\Delta t/2) - \xi_A\right]}\left[\frac{\eta_A(t+\Delta t/2)}{\eta_A(t+\Delta t/2) - \xi_A} + 2\right], \tag{3.25}$$

where we have used a long wave approximation to relate the flow velocity to the local water depth, i.e., $h\,u = (h+\xi)\sqrt{gh}$.

The estimation of the negative Riemann variable requires more effort since the initial location, x_R, of the outgoing characteristic is not known beforehand. A first estimate for this location is obtained by integrating the left characteristic trajectory (3.22) and thus solving the following nonlinear equation for x_R,

$$x_R - x_A + \frac{\Delta t}{2}\left[u(x_R,t) - \sqrt{gh(x_R,t)}\right] = O(\Delta t). \tag{3.26}$$

Since depth-averaged velocities and water depths are known for every j-nodal point at time t, a linear interpolation is used to compute associated values at location x_R. This implicit equation is easily solved implementing for example a standard Newton-Raphson algorithm. The outgoing Riemann variable is estimated then as,

$$R_R^- = u(x_R,t) - 2\sqrt{gh(x_R,t)}, \tag{3.27}$$

once x_R has been computed. Solving the system (3.23)-(3.24) yields the first estimate for boundary values of h and u at $t + \Delta t/2$,

$$u_{A'} = \frac{1}{2}\left(R_L^+ + R_R^-\right) + O(\sigma^2\Delta t, \Delta t), \tag{3.28}$$

$$h_{A'} = \frac{1}{16g}\left(R_L^+ - R_R^-\right)^2 + O(\sigma^2\Delta t, \Delta t). \tag{3.29}$$

Cell-face values of water depth can be readily computed for interior nodal points at $t + \Delta t/2$ from the finite volume integration of continuity equation (3.1). However, numerical resolution of the PDE system requires in addition the prescription of boundary values for the dependent variable q. This variable traduces the parabolic nature of the system and its value cannot be fixed without taking into account the horizontal dependence in the (x,t) plane given by equation (3.3). Hence, numerical estimates for depth-averaged velocity and water depth at the seaward boundary are not sufficient to determine an appropriate boundary condition for the system (3.1)-(3.3). Moreover, the mathematical form of equation (3.3) imposes an implicit treatment for this boundary condition because there is a coupling between q_A and internal j-values of depth-averaged velocity as pointed out in Chapter 2. To cope with this additional

constraint it is necessary to use equation (3.3) to link the boundary value of q with information coming from the interior domain and boundary values h_A and u_A. The finite volume integration of equation (3.3) over the cell $\Omega_A = \{x \in [x_{i=-1}, x_{i=0}]\}$ using nodal definitions given in Chapter 2 yields,

$$\frac{1}{\Delta x}\int_{x_{i=-1}}^{x_{i=0}} q\,dx \simeq \frac{(1+r_A)}{\Delta x}\int_{x_{i=-1}}^{x_{i=0}} u\,dx - \frac{1}{3\Delta x h_A}\int_{x_{i=-1}}^{x_{i=0}} \left(h^3 u_x\right)_x\,dx - \frac{\alpha}{\Delta x}\xi_A^2\int_{x_{i=-1}}^{x_{i=0}} u_{xx}\,dx, \tag{3.30}$$

where $x_{i=-1} = x_A - \Delta x/2$ is a nodal point located outside the physical domain. Recall from the previous chapter that cell-averaged values of the dependent variable q are estimated at interior nodes by integrating equations (3.1)-(3.2) in time but that the reconstruction of cell-face values requires the prescription of q_A. Thus, equation (3.30) will provide an additional implicit algebraical relation that must be incorporated in the system used to compute depth-averaged velocities and q values at interior nodes.

Evaluation of variables at *ghost nodes* located outside the domain is achieved using cubic piecewise extrapolation, i.e.,

$$\Phi_{j=-1} = 4\,\Phi_A - 6\,\Phi_{j=1} + 4\,\Phi_{j=2} - \Phi_{j=3}, \tag{3.31}$$

$$\Phi_{j=-2} = 10\,\Phi_A - 20\,\Phi_{j=1} + 15\,\Phi_{j=2} - 4\,\Phi_{j=3}, \tag{3.32}$$

which provides 4th order accuracy [60]. Since velocity gradients in equation (3.30) are estimated at 4th order with help of an explicit finite difference formula (see Chapter 2), both nodal values, $u_{j=-1}$ and $u_{j=-2}$, must be extrapolated from computed data at the interior domain. On the contrary, for the dependent variable, only $q_{j=-1}$ must be extrapolated.

As outlined before, the boundary value of q cannot be prescribed directly and interior nodal values for depth-averaged velocity are estimated from q, thus an iterative procedure must be considered. The latter can be performed straigthforwardly because the deferred-correction approach implemented to estimate u_j values from the discretized counterpart of equation (3.3) is solved iteratively. Equation (3.30) is recasted as,

$$q_A = \frac{5}{26}q_{j=1} - \frac{2}{13}q_{j=2} + \frac{1}{26}q_{j=3} + \left\{\frac{1+r_A}{13} + \frac{27}{26\Delta x^2}\left(\frac{h_{i=-1}^3 + h_{i=0}^3}{3h_A} + 2\alpha\xi_A^2\right)\right\}u_A + F_{j=0}^{old}, \tag{3.33}$$

where,

$$F^{old}_{j=0} = \frac{1}{26\Delta x^2}\left(\frac{h^3_{i=-1}}{3h_A} + \alpha\xi^2_A\right) u^{old}_{j=-2} + \left\{\frac{1+r_A}{26} - \frac{1}{26\Delta x^2}\left(\frac{27h^3_{i=-1} + h^3_{i=0}}{3h_A} + 28\alpha\xi^2_A\right)\right\} u^{old}_{j=-1} + \left\{\frac{1+r_A}{26} - \frac{1}{26\Delta x^2}\left(\frac{h^3_{i=-1} + 27h^3_{i=0}}{3h_A} + 28\alpha\xi^2_A\right)\right\} u^{old}_{j=1} + \frac{1}{26\Delta x^2}\left(\frac{h^3_{i=0}}{3h_A} + \alpha\xi^2_A\right) u^{old}_{j=2}, \quad (3.34)$$

and ghost values are estimated using the cubic extrapolation expressed by relations (3.31)-(3.32).

The strategy used to advance u and q in time taking into account the boundary condition for u and h is summarized as follows :

1. Reconstruct cell-face values q_j from cell-averaged ones using the additional relation (3.33) and last computed u_j values for interior nodes.

2. Using q_j values estimated at the previous step, compute depth-averaged velocities at interior nodes solving equation (3.3).

3. If a convergence criterion for the relative error between *new* and *old* values for q_A and u_j is not satisfied, then come back to 1. Otherwise, the iterative process stops.

Errors are estimated using the same expression based on a L_1 norm given in Chaper 2. The relative tolerance is fixed at $\tau = 10^{-4}$ for all computations.

At the end of this process all cell-face values for variables h, u and q are known at $t + \Delta t/2$. Nevertheless, the Runge-Kutta scheme will produce a second estimate of variables at the same time level. In this second stage, characteristic equation (3.22) can be integrated with improved accuracy taking advantage of the previous guess. The x_R location is now computed using the following implicit equation,

$$x_R - x_A + \frac{\Delta t}{4}\left[u(x_R,t) + u_{A'} - \sqrt{gh(x_R,t)} - \sqrt{gh_{A'}}\right] = O(\Delta t^2), \quad (3.35)$$

and the second estimation for boundary values reads,

$$u_{A'} = \frac{1}{2}\left(R^+_L + R^-_R\right) + O(\sigma^2\Delta t, \Delta t^2), \quad (3.36)$$

$$h_{A'} = \frac{1}{16g}\left(R^+_L - R^-_R\right)^2 + O(\sigma^2\Delta t, \Delta t^2), \quad (3.37)$$

where Riemann variables are defined as before. Thus, at each intermediate time step of the Runge-Kutta scheme, boundary values for water depth and depth-averaged velocity are estimated with an error of $O(\sigma^2\Delta t, \Delta t^2)$. In the general case, the time step Δt will be small enough and the error associated to dispersion would be small. Similarly, the boundary value for q and velocities at interior nodes are obtained following the same iterative strategy expounded before. The solution is then advanced to the next half step $t + \Delta t$ using an analougous procedure starting from computed values at $t + \Delta t/2$.

3.3.3 Vertical wall

At a vertical and impermeable wall, horizontal velocity must vanish. Again, the characteristic decomposition of Serre equations provides a way to fix the value for the variable h. Therefore, the numerical strategy to estimate boundary values for u, h and q is equivalent to the one we used for the open sea condition. The only difference is that the fictitious right-going Riemann variable, R_L^+, must be chosen in order to ensure that the horizontal velocity is zero at the corresponding boundary.

We write this particular boundary condition for a situation where the vertical wall is located on a slopping bottom. Integration of characteristic equations provides now the following relations,

$$R_{A'}^+ - R_L^+ = -g\left(\xi_x\right)_A \frac{\Delta t}{2} + O(\sigma^2\Delta t), \tag{3.38}$$

$$R_{A'}^- - R_R^- = -g\left(\xi_x\right)_A \frac{\Delta t}{2} + O(\sigma^2\Delta t), \tag{3.39}$$

where the associated bottom slope term is included as a source in the right hand side. In order to impose a vanishing horizontal velocity at the wall we write,

$$R_L^+ = 2g\left(\xi_x\right)_A \frac{\Delta t}{2} - R_R^-, \tag{3.40}$$

$$u_{A'} = -g\left(\xi_x\right)_A \frac{\Delta t}{2} + \frac{1}{2}\left(R_L^+ + R_R^-\right) + O(\sigma^2\Delta t, \Delta t), \tag{3.41}$$

and the water depth at the boundary A' is estimated with the same expression as before (equation (3.29)). Once boundary values of u and h are computed in that way, the remaining variable q is estimated at the seaward using the same procedure outlined before. Therefore, it is possible to obtain improved accuracy in the second stage of the Runge-Kutta time stepping.

3.3.4 Moving shoreline

An adequate representation of swash motion at the shoreline is very important since infragravity waves are generated in nature by nonlinear interactions, breaking and by

partial reflection produced in particular by the runup and run-down process that takes place in the swash zone (e.g. [7, 113]). Several authors have developed numerical strategies intended to reproduce the dynamic movement of the shoreline in the framework of Boussinesq-type models. These schemes have been mainly applied using fixed grids where the moving boundary problem is only solved in an approximated way. Although it is generally acknowledged that this kind of stategy can sometimes produce loss of mass and numerical instability (see for instance reference [8]) it has been widely used in nearshore problems since the treatment of the moving shoreline is fundamentally simplified. Some recent examples of such approaches range from *ad-hoc* or essentially numerical approaches (e.g., [85, 107, 111]) to more sophisticated ones where a Riemann wet-dry problem is explicitly solved [14].

In the present work, the simple extrapolation technique given by Lynett et al. [107] has been adapted in our finite volume resolution. Lynett et al.'s [107] moving shoreline technique is based on a linear extrapolation of free surface and velocity through the wet-dry boundary. In the present finite volume scheme wet cells are included in the computation of equations (3.1)-(3.2) if,

$$\frac{1}{\Delta x}\int_{\Omega_j} h\,dx \geq h_{tol}, \tag{3.42}$$

where Ω_j denotes a finite volume, Δx is the grid size and h_{tol} is a threshold value. Cell averaged values for water depth $\frac{1}{\Delta x}\int h\,dx$ and cell averaged variable $\frac{1}{\Delta x}\int q\,dx$ are linearly extrapolated through dry cells. Following Lynett et al. [107], a four-point filter may be passed through the extrapolated region in order to avoid slope discontinuities. Equations (3.1)-(3.2) are integrated in time and the location of the wet-dry interface is determined once every half time step ($\Delta t/2$) in the Runge-Kutta time stepping. Spatial derivatives are computed in the physical and extrapolated domain where five extra dry nodal points are considered. Depth averaged velocity is finally computed from equation (3.3) in the extended domain (wet + dry).

The numerical implementation of this moving shoreline will be validated in next section where particular care must be paid to the issue of mass conservation. The linear extrapolation at the shoreline locally reduce the accuracy of the sheme to 2nd order as pointed out in reference [107].

3.3.5 Compact differencing at boundary nodes

Boundary estimates for first and second order spatial derivatives appearing in flux functions (3.4)-(3.5) are performed using compact approximations which preserve 4th order accuracy for first derivatives and third order for second derivatives. The resulting

matrix for the whole domain will be tri-diagonal even when non-periodic boundaries are considered. Matching conditions at left boundary read [95],

$$(\Phi_x)_A + 3\,(\Phi_x)_{j=1} = \frac{1}{\Delta x}\left(-\frac{17}{6}\Phi_A + \frac{3}{2}\Phi_{j=1} + \frac{3}{2}\Phi_{j=2} - \frac{1}{6}\Phi_{j=3}\right), \tag{3.43}$$

$$(\Phi_{xx})_A + 11\,(\Phi_{xx})_{j=1} = \frac{1}{\Delta x^2}\left(13\Phi_A - 27\Phi_{j=1} + 15\Phi_{j=2} - \Phi_{j=3}\right), \tag{3.44}$$

where Φ_j is a generic function evaluated at node j and A represents the left boundary (see Chapter 2 for nodal definitions). Similarly, matching conditions at right boundary can be easily derived.

3.4 Spatial filtering

For complex wave propagation problems over uneven bathymetries dispersion and nonlinearity may interact to produce higher harmonics. These shorter waves may eventually step beyond the range of physical validity of model equations and a high order filtering technique is often considered to damp them out. This is also justified since numerical schemes used to discretize PDEs are not able to properly describe all wavelengths as it was shown for our finite volume method in Chapter 2.

Regarding the latter, the spectral analysis of the numerical scheme performed in the previous chapter provides an important theoretical background to improve the performance of the method. Indeed, since the implemented Runge-Kutta finite volume scheme is based on centered in space approximations it was shown that there is almost no damping of different wave modes when appropiate discretization parameters are used. However, not all wavelengths are properly described by the numerical method and examples of dispersion relation preserving (DRP) regions were given in Chapter 2. From a practical point of view this means that high frequency waves may introduce destabilizing effects as numerical integration advances in time. These short waves can arise as a consequence of nonlinear interaction or even be introduced by approximated boundary conditions which do not match PDEs exactly. One effective way to eliminate non-physical high frequecies is to use high order filtering techniques [173]. This approach is of widespread usage in numerical resolutions of wave-type equations (e.g., [55, 65, 95]) and has also been used in the context of Boussinesq-type modelling (e.g., [69, 85, 120]).

Consequently, our main concern here is to damp out frequecies that cannot be resolved by the numerical scheme in order to eliminate non-physical wavelengths. Since spectral analysis provides reliable information on numerical properties of the finite

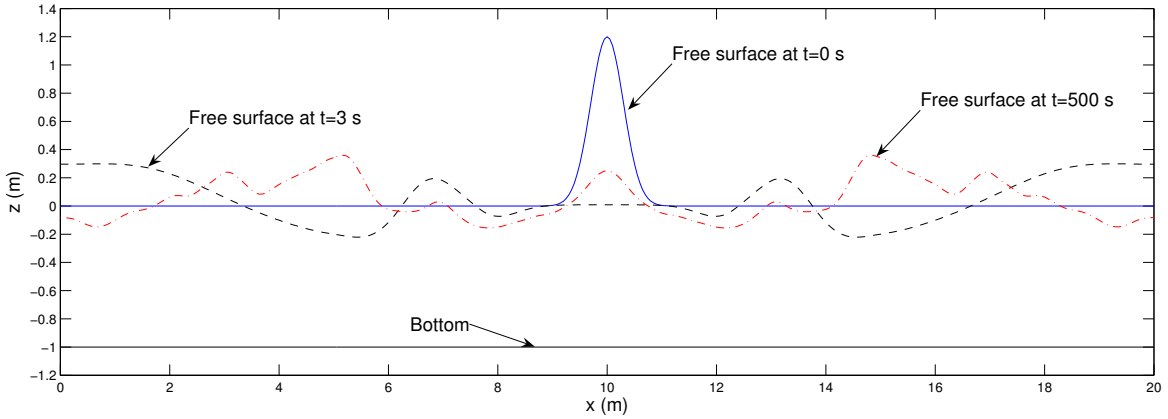

Figure 3.5: Initial free surface configuration $(-)$ for the numerical test, free surface profile after 3 seconds $(--)$ and free surface at $t = 500$ s $(- \cdot -)$.

volume scheme, an appropriate high order filter can be chosen. Hence we implement in the model the 8th-order implicit filter given in reference [65], which can be applied to cell-averaged variables,

$$\alpha_f \tilde{\widehat{\Phi}}_{i-1} + \tilde{\widehat{\Phi}}_i + \alpha_f \tilde{\widehat{\Phi}}_{i+1} = \sum_{n=0}^{4} \frac{a_n}{2} \left(\widehat{\Phi}_{i+n} + \widehat{\Phi}_{i-n} \right), \tag{3.45}$$

where $\tilde{\cdot}$ denotes filtered values, α_f is a free parameter $(-0.5 < \alpha_f < 0.5)$ and right hand side coefficients read,

$$a_0 = \frac{93 + 70\alpha_f}{128}\ ,\ a_1 = \frac{7 + 18\alpha_f}{16}\ ,\ a_2 = \frac{-7 + 14\alpha_f}{32}\ ,\ a_3 = \frac{1 - 2\alpha_f}{16}\ ,\ a_4 = \frac{-1 + 2\alpha_f}{128}.$$

When $\alpha_f = 0.5$ there are no damped frequencies and as α_f is reduced a wider range of frequencies is partially filtered as shown in reference [65]. The filter can be applied once every N_f Runge-Kutta time steps in order to eliminate high frequencies when computations are carried out for long times. When high order filtering is required, a fixed value of $\alpha_f = 0.4$ can be used thus ensuring that only unresolved frequencies are suppressed.

Even if from a theoretical point of view the chosen high order filter should not act on well resolved wavelengths, it is important to assess if the numerical representation of wave kinematics and energy are affected. Indeed, the use of a filter to damp out high frequencies is delicate since it removes energy from the system. It is paramount then to evaluate the associated energy dissipation rate. This issue will be investigated with help of the following numerical example.

Consider a periodic domain with horizontal bottom where a motionless Gaussian hump located at its center is prescribed as initial free surface condition (see Figure 3.5).

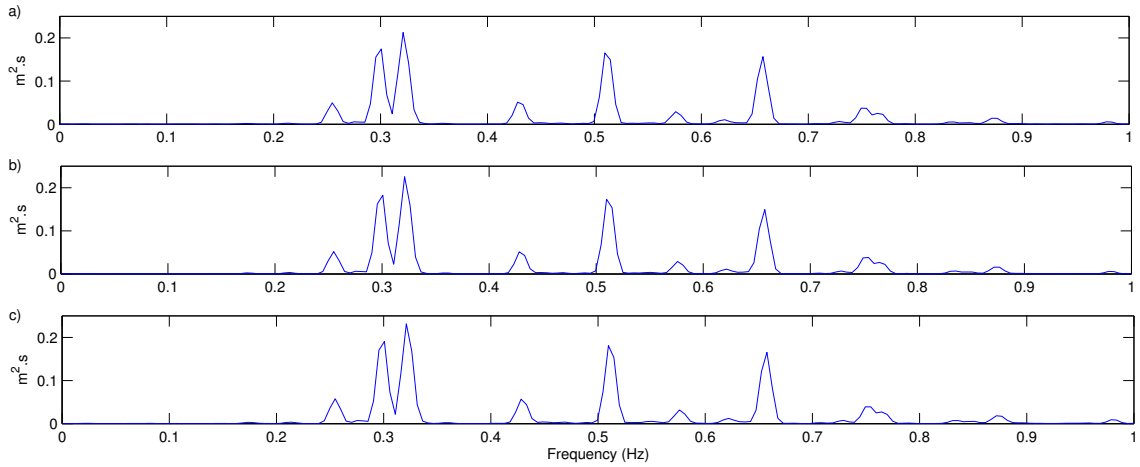

Figure 3.6: Power density spectra for the free surface time serie evaluated at $x_0 = 10$ m. a) Without using the eight order filter, b) applying the filter once every 100 time steps ($\alpha_f = 0.4$), and c) when using the filter once every time step ($\alpha_f = 0.4$).

The computational domain has a length of 20 m, and the still water depth is fixed at $h_0 = 1$ m. The initial condition reads,

$$h(x, t = 0) = H_0 \exp\left[-\frac{1}{2s^2}(x - x_0)^2\right] - \xi(x), \tag{3.46}$$

$$u(x, t = 0) = 0, \tag{3.47}$$

where H_0 is the height of the perturbated free surface, x_0 is its location and s is a shape coefficient which sets its initial spatial length. We want to run the model over a long time (say $\sim 10000 \times \Delta t$) under circumstances where nonlinear interaction may generate higher harmonics. For instance, using $H_0/h_0 = 1.2$ and $s = 0.3$ m ensures that nonlinearities are relatively important and that dispersion will also have an influence. From this initial situation we compute wave evolution in the periodic domain fixing $\Delta x = 0.05$ m and $\Delta t = 0.024$ s, which corresponds to a Courant number $C_r = 1.5$, and during 500 s ($\simeq 20.000 \times \Delta t$). A spatial snapshot of the initial perturbation, the free surface position few seconds after and at the end of the computation are presented in Figure 3.5. It is seen that at early times there are several different wavelengths interacting with each other and that wave amplitudes are not small ($a/h_0 \sim 0.3$). During the computation, nonlinearities, dispersion and wave-wave interaction should favour the redistribution of energy at different wavenumbers and at $t = 500$ s different wavelengths are visible. Thus, this numerical example may be used to illustrate how filtering may affect computations.

We perform comparisons of power density spectra estimated from free surface time

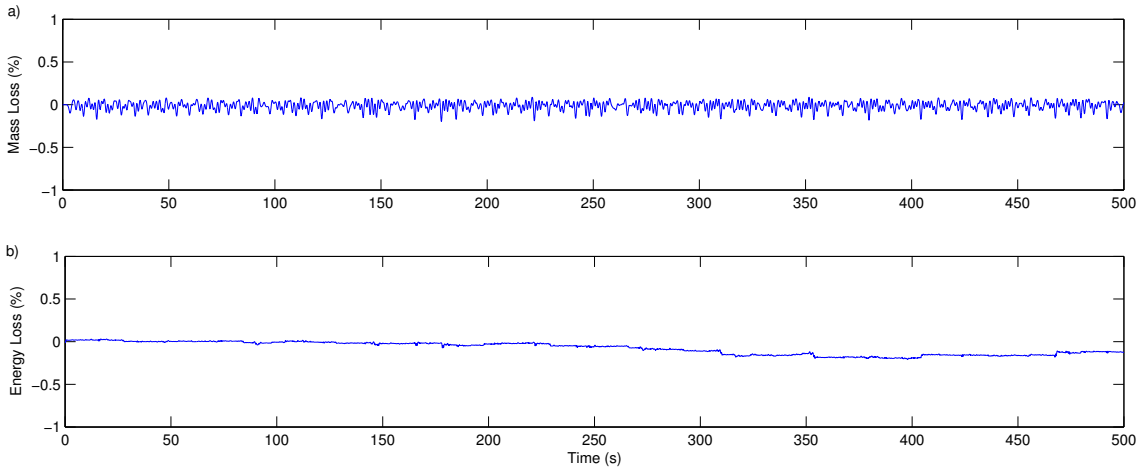

Figure 3.7: Time evolution of mass and energy in the computational domain when the high order filter is applied once per time step ($\alpha_f = 0.4$). a) Relative error on mass, and b) relative error on total energy (initial mass and energy are taken as references).

series evaluated at $x = 10$ m, i.e. at the center of the periodic domain, and results are presented in Figure 3.6. It is seen that there are no noticeable differences in the spectral distribution of energy when no filter is applied and when it is used once every 100 time steps or even once every time step. It is important to point out that for this particular example, fairly short waves have been generated since the spectral signature shows that some energy has been transferred to frequencies ranging between $0.6 - 1.0$ Hz. Using the associated linear phase speed to compute wavelengths, these frequencies roughly correspond to $h_0/L \sim 0.2 - 0.3$. Such ratios are close to the theoretical deep water limit given by $h_0/L \sim 0.5$ thus proving that the present numerical example may be useful to test the filtering technique when used in practical applications.

Another important feature that can be tested is how the total mass and energy contained in the periodic domain is affected by the application of the high order filter. In theory, those quantities must be conserved over the whole computation and differences that may arise should be attributed to the numerical method used to integrate PDEs or to the filtering technique. In order to compute the total energy evolution contained in the computational domain, we use theoretical information on horizontal and vertical velocity profiles already presented in Chapter 2. Taking now the correction dispersion parameter to be $\alpha = 0$ it is straightforward to show then that the total kinetic and potential energies can be approximated as follows,

$$E_k^T(t) = \int_{x_l}^{x_r} \frac{1}{2}\rho h \left(u^2 + h^2 u_x^2\right)\, dx + O(\sigma^4) \simeq \frac{1}{2}\rho \Delta x \sum_{j\in J} h \left(u^2 + h^2 u_x^2\right)|_j, \qquad (3.48)$$

$$E_p^T(t) = \int_{x_l}^{x_r} \frac{1}{2}\rho g \eta^2 dx \simeq \frac{1}{2}\rho g \Delta x \sum_{j \in J} \eta_j^2, \tag{3.49}$$

where x_l and x_r correspond respectively to spatial coordinates of left and right domain boundaries, and summation is carried out over the whole discrete domain where j is a nodal index and J represents the set of discrete nodes. The total mass contained in the domain can be computed in a similar way. Time evolution of mass and total energy $(E_k^T + E_p^T)$ in the case where the high order filter is applied once per time step is plotted in Figure 3.7. It is confirmed that the filter does not alter mass nor energy since the relative errors on both quantities at the end of the computation are negligible small being less than 0.2 % at $t = 500$ s.

This numerical example demonstrates that the use of the implicit 8th-order filter with $\alpha_f = 0.4$, as given in reference [65], does not significantly affect energy distribution even when it is applied once per time step. Hence the filter is only acting on unresolved wavelengths and may be useful to improve numerical stability if computations are carried out for longer times.

3.5 Model validation

In the following subsections model capabilities will be evaluated by comparing model predictions against several experimental and numerical benchmark tests. Different numerical examples have been chosen in order to test in particular the physical validity of the extended system of Serre equations and the adequacy of the numerical implementation of boundary conditions.

3.5.1 Swash motion and shoreline movement

The numerical implementation of the moving shoreline boundary condition is tested using the Carrier and Greenspan [31] analytical solution for long wave propagation over a planar beach. Dispersive terms are switched off since the analytical solution was obtained for the dispersionless set of nonlinear shallow water equations. We test the model using the same parameters as in references [85, 107, 111], i.e. an incident sinusoidal wave with height $H = 0.006$ m and period $T = 10$ s propagating over a beach of constant slope 1:25, where the depth in the horizontal part of the channel is $h_0 = 0.5$ m.

The RK4 finite volume scheme theoretically allows for larger time steps when compared to previously published numerical Boussinesq-type models, we thus perform the computation using a Courant number of 1.5 (i.e. $\Delta t/\Delta x\sqrt{gh_0} = 1.5$) and a grid size

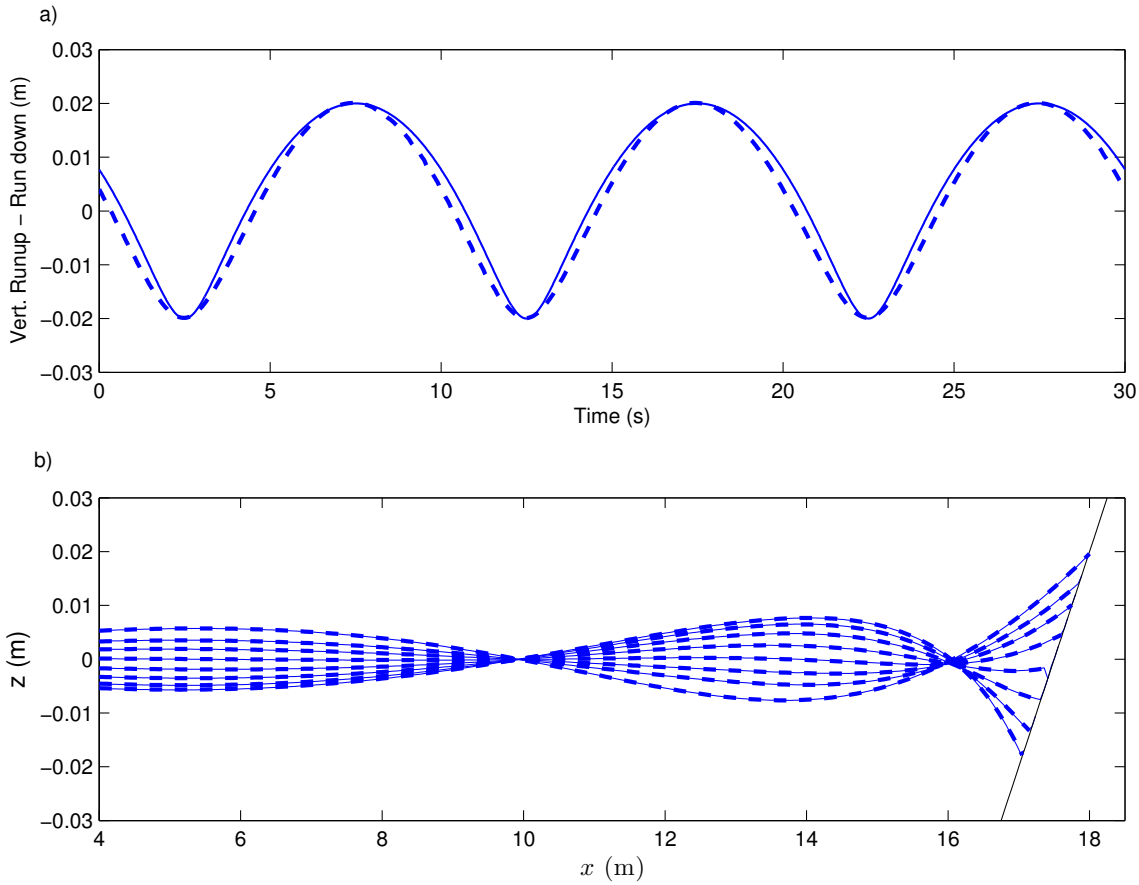

Figure 3.8: Wave runup and run-down of a periodic wave. Comparison between Carrier and Greenspan's [31] analytical solution (−) and numerical (−−) prediction using $\Delta x = 0.05$ m and $\Delta t = 0.034$ s. a) Vertical excursion at the shoreline. b) Spatial free surface profiles.

of $\Delta x = 0.05$ m. No spatial filtering is used in this particular case and comparisons between computed and analytical solutions are presented in Figure 3.8 where the threshold value for wet cells is fixed at $h_{tol} = 10^{-4}$ m. It can be seen that the agreement between numerical and theoretical solution is very good even when using a time step which is more than three times larger than the one used in results reported for the validation of the original moving shoreline approach in reference [107]. In particular, maximun and minimum wave runup and run-down are very well predicted. Additionally, mass loss was almost negligible in this numerical example being less than 0.005 % over 100 s of computation.

We conclude then that the moving shoreline boundary condition prosposed by Lynett et al. [107] can be successfully adapted to our finite volume scheme since numerical results compare favourably to the ones reported by those authors even if

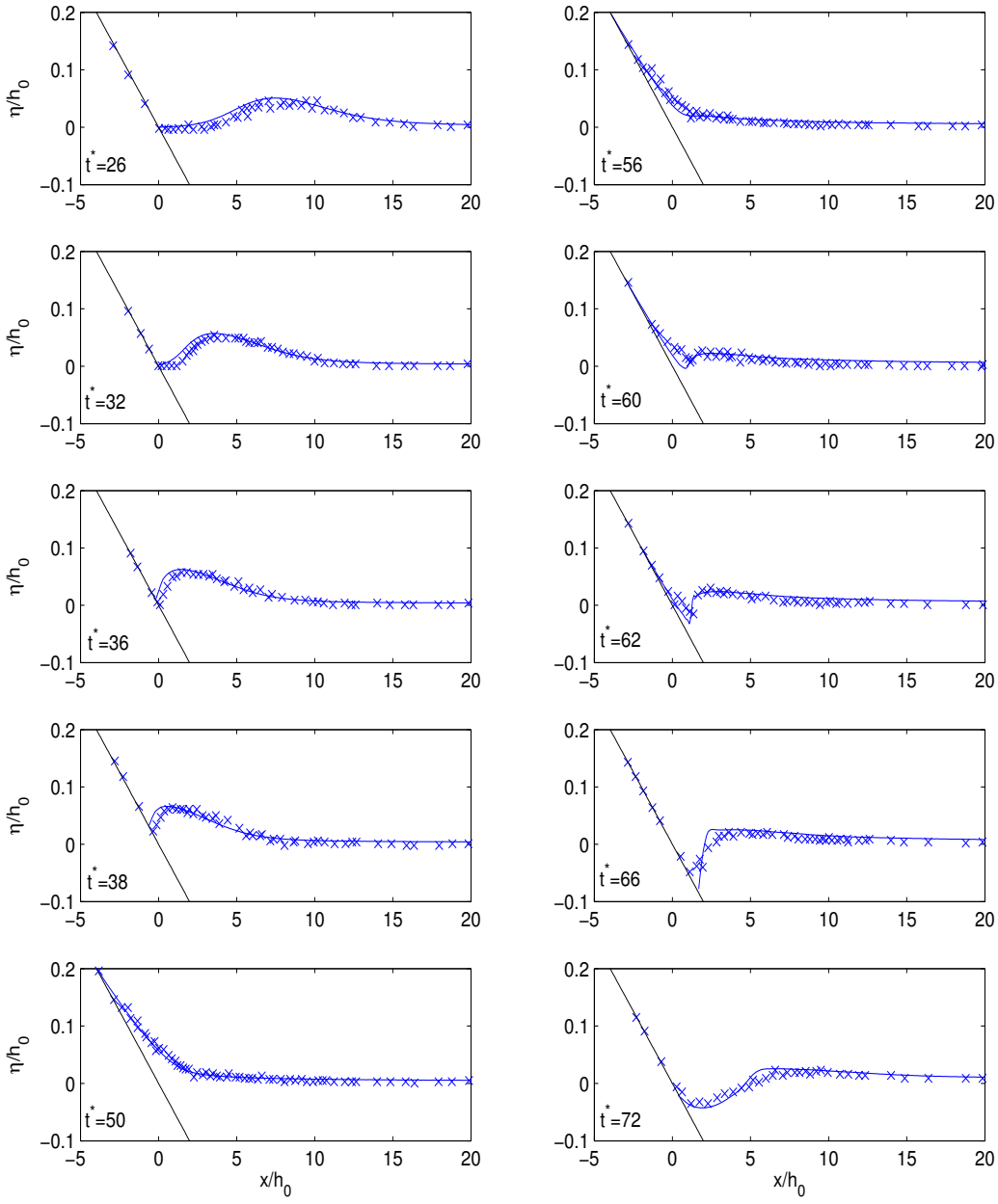

Figure 3.9: Spatial snapshots of free surface elevation for Synolakis [158] non-breaking solitary wave runup and run-down experiment. $a_0/h_0 = 0.04$, $h_0 = 0.30$ m and $t^* = t\sqrt{g/h_0}$. (x) : experimental data; $(-)$ numerical computation using $\Delta x = 0.03$ m and $\Delta t = 0.0175$ s.

larger time steps are used. However it is important to go further in the validation and test this approach in situations where dispersive terms are also included.

We consider for this purpose the runup and run-down of a non-breaking solitary wave over a planar beach of 1:19.85 slope. We compare model results to laboratory measurements made by Synolakis [158] for an incident solitary wave of relative amplitude $a_0/h_0 = 0.04$ which did not brake on runup. Numerical computation is performed using a grid size $\Delta x = 0.03$ m, $C_r = 1.0$ and $h_{tol} = 10^{-4}$ m; the still water depth at the horizontal part of the channel is fixed at $h_0 = 0.3$ m. A four point filter is passed through the extrapolated region because the solitary wave breaks on run-down thus producing some slope discontinuities in the computed free surface as shown in the last panel of results reported in Figure 3.9. The use of a local filter there allows for the computation to hold even when the free surface becomes nearly vertical at back swash. Indeed the filter is acting as a breaking model, smoothing slope discontinuities. We believe that incorporating an adequate breaking parameterization able to reproduce this phenomenon is required. However, the filtering technique constitutes a simple way to ensure stability and the associated mass loss was again negligible, being less than 0.005 % at the end of the computation.

The overall agreement between computed and measured free surface elevations is good as depicted in Figure 3.9. Even though, some slight discrepancies are noticed and this can be due to the lack of a friction term in the model. This phenomenon can be important when water depth becomes very shallow and this is in particular the case in the run-down stage.

3.5.2 Total reflection of a solitary wave at a wall

Validation of the wall boundary condition can be performed on the base of experimental measurement reported by Walkley and Berzins [175]. In this experimental set-up, two different tests where solitary waves propagate over a gentle slope of 1:50 collapsing into a vertical wall were studied. The bathymetry for this problem is presented in Figure 3.10, where following the numerical investigation performed in reference [175], at time $t = 0$ s computations are initialized with the solitary wave centered at $x = 50$ m. The vertical wall is located in our case at $x = 0.0$ m and measured time series of free surface elevation are available at $x = 2.25$ m. The still water depth in the horizontal part of the channel is $h_0 = 0.7$ m and incident solitary waves have a relative amplitude of $a_0/h_0 = 0.10$ and $a_0/h_0 = 0.174$ respectively.

Numerical integration of equations is conducted using the wall boundary condition at $x = 0.0$ m, a grid size $\Delta x = 0.07$ m and $C_r = 1.0$ in both runs and no filter is ap-

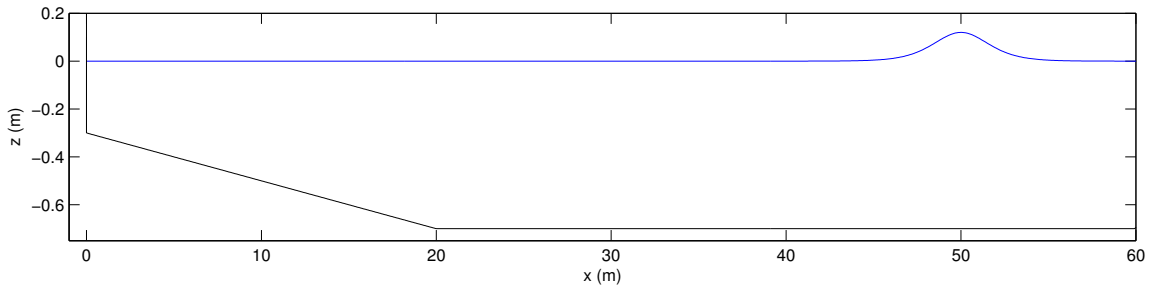

Figure 3.10: Bathymetric configuration for the solitary wave test (total reflection on a vertical wall) and initial location of the soliton.

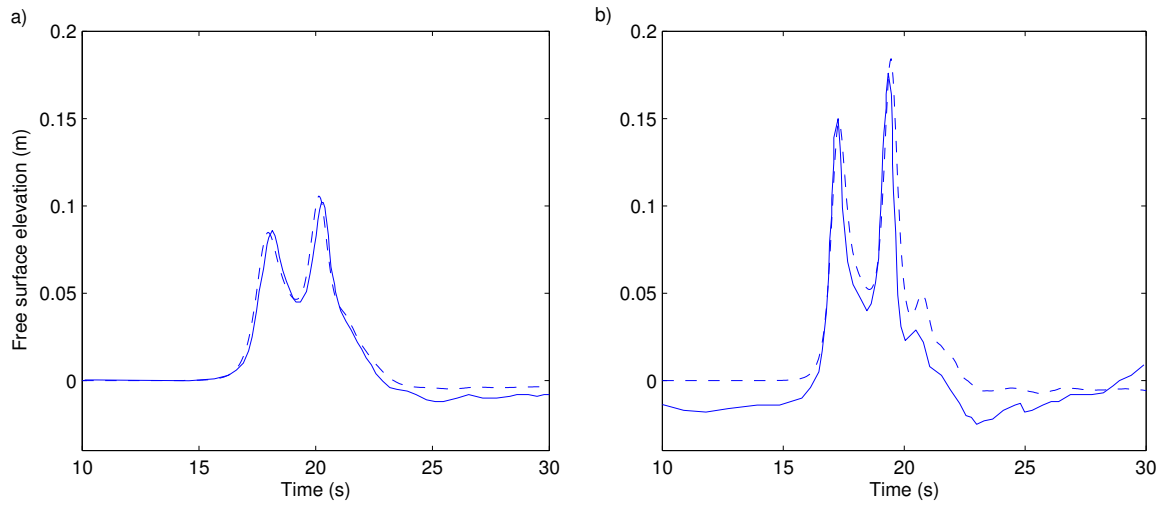

Figure 3.11: Comparison between measured (−) and computed (−−) free surface elevation time series at $x = 2.25$ m; $\Delta x = 0.07$ m and $\Delta t = 0.0267$ s. a) Incident wave amplitude : $a_0/h_0 = 0.10$. b) Incident wave amplitude : $a_0/h_0 = 0.174$.

plied. Measured and computed free surface elevation time series are compared at the section $x = 2.25$ m in Figure 3.11. Numerical results are similar than those reported in reference [175], where the first peak represents the incident wave and the second one corresponds to the reflected wave. While the first peak is very well reproduced, the second one is slightly overpredicted by the numerical model for both solitary waves. Nevertheless, this overprediction is significantly less important than results obtained with the weakly nonlinear and weakly dispersive finite element Boussinesq code developed in reference [175]. Indeed, for the incident wave of relative amplitude $a_0/h_0 = 0.10$ the maximum value of free surface elevation is roughly overpredicted by 3 % in the present computation while Walkley and Berzins [175] reported an overprediction of 8 % for this case. More importantly, for the second solitary wave of amplitude $a_0/h_0 = 0.174$, our model overpredicts the second peak by roughly 5 % while the weakly nonlinear code

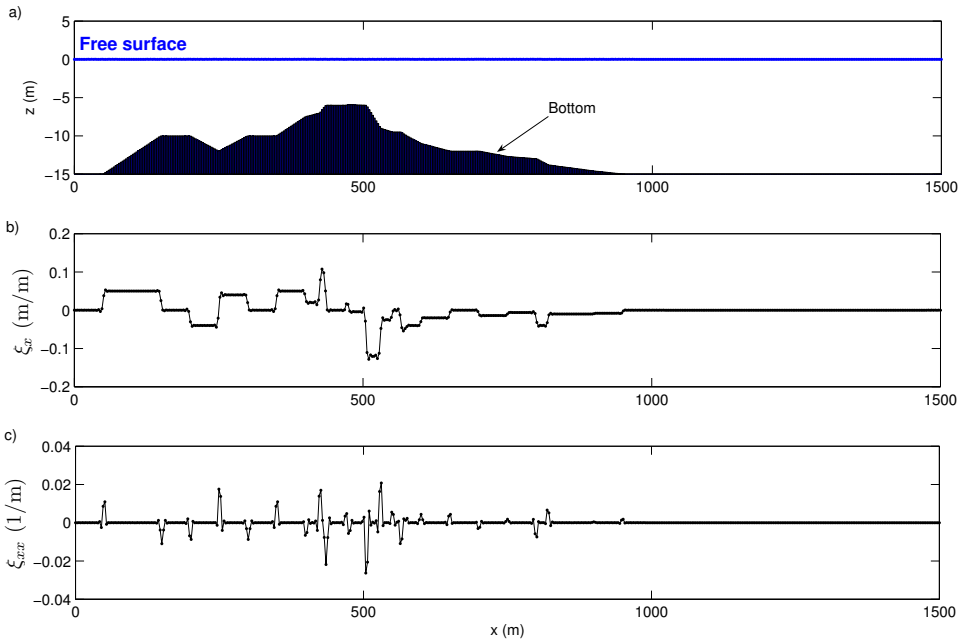

Figure 3.12: Geometrical configuration with j-nodes denoted by dots. a) Bottom bathymetry and free surface at the end of the computation, b) numerically estimated first spatial derivative of the bottom, and c) numerically estimated second spatial derivative of the bottom.

produced an error of nearly 38 %. Hence, error discrepancies must be attributed to the weakly nonlinear hypothesis embedded in Boussinesq-type equations solved with the finite element model. In our case, the slight discrepancies between measured and computed secondary peaks may be reasonably attributed to the inviscid hypothesis used to derive Boussinesq-type equations since there are no losses at the reflecting wall as pointed out by Walkley and Berzins [175].

The present numerical test validates then the wall boundary condition developed here and confirms the importance of including the so-called full nonlinearity in Boussinesq-type equations.

3.5.3 Model robustness and open sea boundary condition

In this subsection the ability of the open sea boundary condition to evacuate different wavelengths is tested. Additionally, important properties of the model are also evaluated on the base of challenging numerical tests. Our aim is to investigate the stability of the model when used to compute wave propagation phenomena over sharp bathymetries producing highly discontinous bottom gradients.

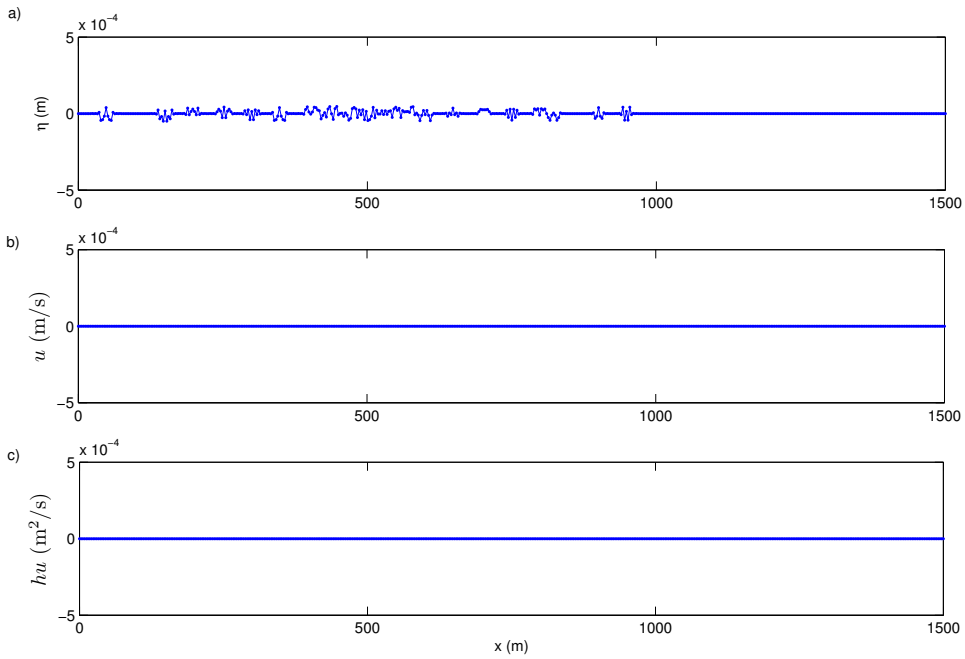

Figure 3.13: Computed results at $t = 7500$ s using $\Delta x = 0.3$ m and $\Delta t = 0.371$ s. a) Free surface, $z = \eta$, b) depth-averaged velocity, u, and c) flow rate ($=hu$).

The first example is intended to explore the influence of the source term by running the model at rest over a non-trivial bathymetry. Recall from the governing equations that the source-like term appearing in the right hand side of (3.2) contains bottom derivatives up to second order. This non-conservative term must be *well-balanced* in order to ensure the stability and accuracy of the numerical scheme (see for instance references [68, 73, 96, 171]). The chosen bathymetry for this first example was proposed in the *working group on dam break modelling* [71] to test shallow water equation solvers. The bed configuration is presented in Figure 3.12-a) and represents a very challenging geometry intended to test conservative properties of discretized source terms in numerical models. The channel length is 1500 m and the still water depth in the horizontal part is taken to be $h_0 = 15$ m. In Figure 3.12-b) and c) first and second bottom spatial derivatives are plotted as estimated from 4th order compact finite difference formulae presented in Chapter 2. It is clearly seen that this non-trivial bathymetry produces sharp gradients and consequently the numerical skillness of the discretized source term may be studied from this example.

We perform a computation using periodic boundary conditions and without applying the filter. Numerical integration is carried out with $\Delta x = 3.0$ m and $\Delta t = 0.371$ s during 7500 s running the model at rest. It is worth noting that this time step corre-

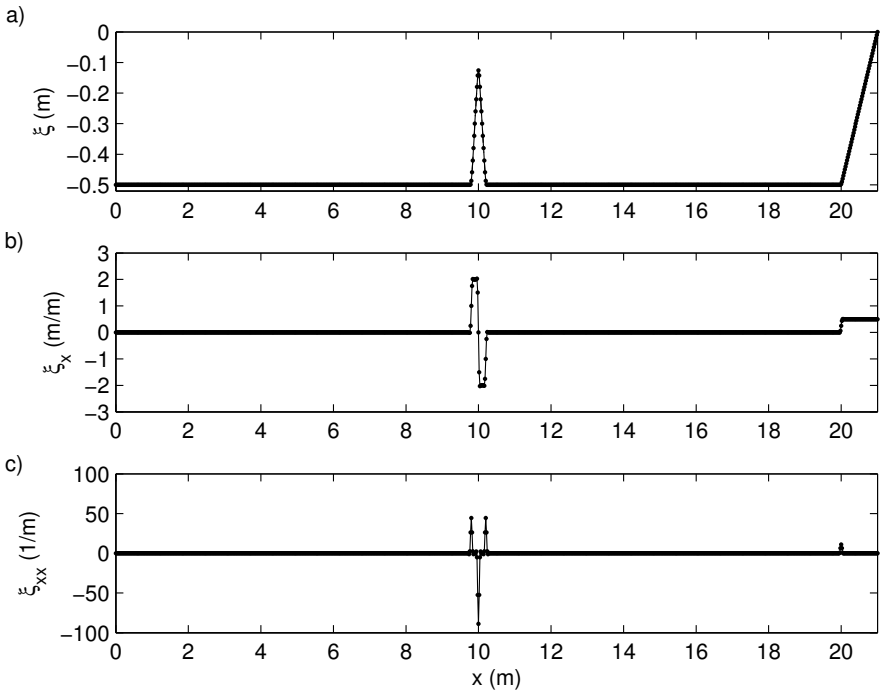

Figure 3.14: Bathymetric configuration with j-nodes denoted by dots. a) Bottom bathymetry, b) numerically estimated first derivative, and c) numerically estimated second derivative.

sponds to a Courant number $C_r = 1.5$ in the present example and that computation is thus carried out over more than 20000 time steps. These numerical values for space and time grid resolution have been chosen because the RK4 finite volume model is expected to be non-damping in this case (see Chapter 2). Free surface profile obtained at $t = 7500$ s is presented in Figure 3.13-a), while depth-averaged velocity and flow rate at the same time coordinate are depicted in Figure 3.13-b) and c). From these figures it is seen that, even if some small disturbances ($\sim 10^{-5}$ m) are visible at the free surface, the flow velocity is negligible small over the whole domain at the end of the computation. This result proves that the model is able to deal with steady state conditions and that small free surface disturbances will not be amplified when running the model at rest. Therefore, it appears that the centered in space strategy used to discretize the source term does not introduce any numerical unbalance in fluxes since no spurious behaviour has been noticed even when computations are carried out for long times over this challenging benchmark test.

A second interesting test concerns the ability of the model to reach quiescent water conditions from a perturbated initial situation. For that we use the bathymetric configuration presented in Figure 3.14-a) where a steep triangular barrier with 2:1

slope and height $\Delta h = 0.4$ m is located at the center of the domain whose still water depth is $h_0 = 0.5$ m in the horizontal part of the channel. At the left boundary, the open sea boundary condition is implemented, while at the right boundary, a moving shoreline condition is prescribed on a beach of constant 1:2 slope. A small grid size of $\Delta x = 0.02$ m is used for spatial discretization in order to ensure that each side of the barrier is covered with at least ten finite volumes. Numerical estimates for spatial derivatives of the bottom profile obtained with 4th order compact formulae can be seen in Figure 3.14-b) and c). It is worth emphasizing that this geometric configuration constitutes a very challenging test for our numerical scheme since high order derivatives need to be estimated in order to integrate the system of PDEs.

Numerical skillness of the finite volume scheme can thus be further illustrated by prescribing as initial condition a motionless Gaussian hump of water, centered at $x_0 =$ 10.0 m, the same location where the top of the triangular barrier is located. We use $H_0 = 0.05$ m and $s = 0.5$ m for the initial condition expressed by relations (3.46)-(3.47). Time stepping is performed with a Courant number $C_r = 1.5$ and no filtering is applied at the interior domain. The basic idea is to investigate whether the numerical model is able or not to reach, from this initial situation, the stable equilibrium at rest. This example may also provide some information about the efficacity of the open sea boundary condition in evacuating waves from the computational domain.

Spatial free surface evolution at different times is presented in Figure 3.15 where it is seen that the initial hump splits into two waves propagating in both directions. The left-going wave travels into the open sea boundary condition and leaves the domain without causing any spurious reflection. On the other hand, the right-going wave propagates into the beach slope, running up and down and being reflected in the opposite direction. Secondary small amplitude waves are generated by this process as can be readily seen from Figure 3.15. Because in this case the amplitude of reflected waves is small enough, the sharp barrier has only a minor influence on the shape of waves travelling back to the open sea boundary. However, the important conclusion here is that no spurious numerical noise is introduced by this sharp bottom. Furtheremore, the finite volume scheme is able to successfully recover the still water surface equilibrium as depicted in Figure 3.15.

The evolution of the total mass contained in the computational domain as a function of time is presented in Figure 3.16-a) non-dimensionalized by the total mass at rest. It is demonstrated that the initial extra mass associated to the Gaussian hump leaves the domain after 60 seconds where the still water condition is almost reached. Hence, the open boundary condition allows for reflected waves to freely travel outside the computational domain and only small residual perturbations are noticed in this

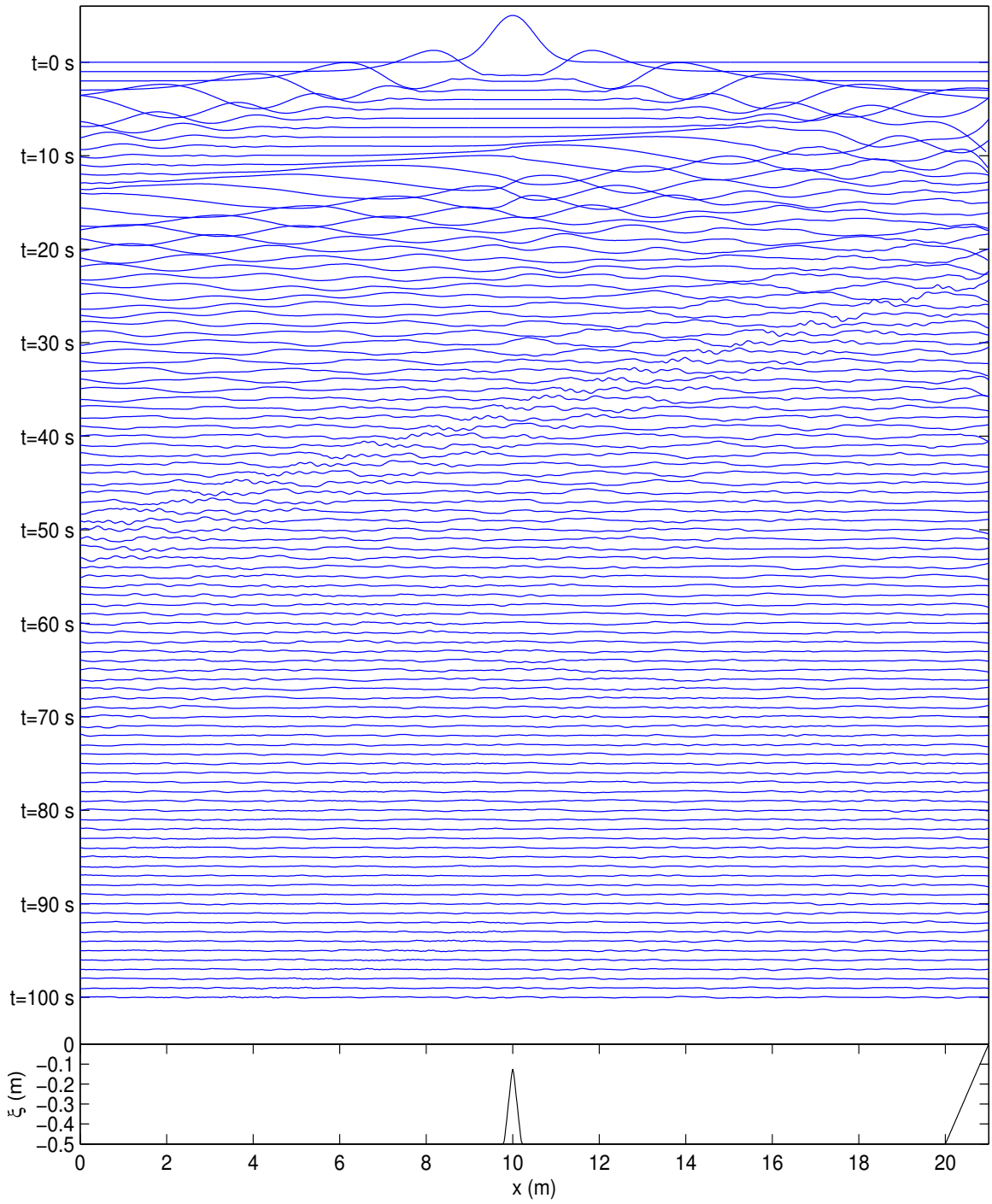

Figure 3.15: Spatial snapshots of free surface at different times using a motionless Gaussian hump of water as initial condition. $H_0 = 0.05$ m, $s = 0.5$ m, $\Delta x = 0.02$ m, $\Delta t = 0.0135$ s and no filter at interior domain.

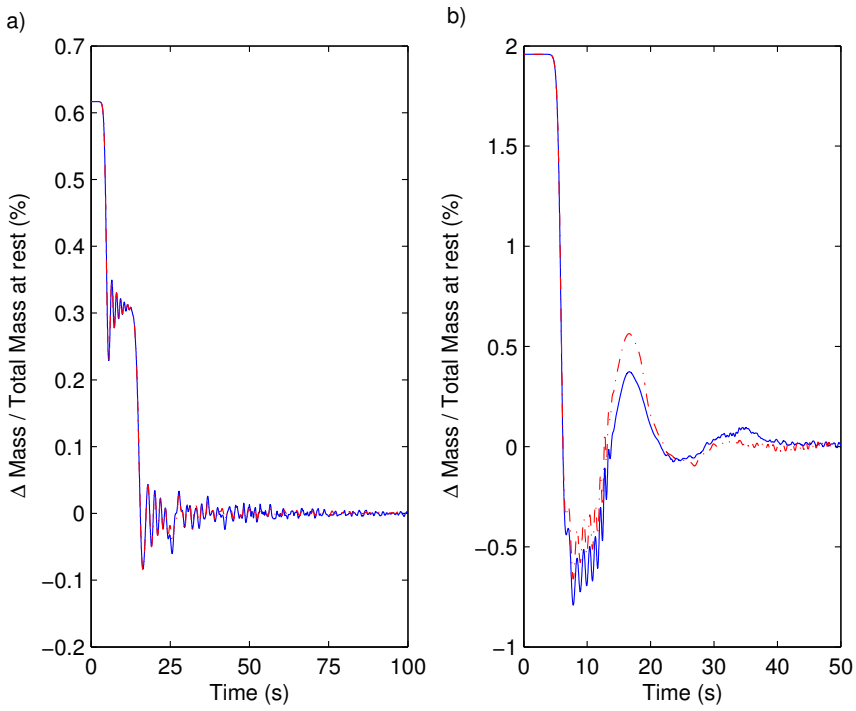

Figure 3.16: Time series of mass contained in the computational domain. Computed : (−) without filter; (−·−) with implicit 8th order filter ($\alpha_f = 0.4$). Initial motionless Gaussian hump : a) $H_0 = 0.05$ m, $s = 0.5$ m; b) $H_0 = 0.10$ m, $s = 0.5$ m.

example.

An additional computation has been conducted in this case passing the 8th-order implicit filter (eq. (3.45)) over cell-averaged variables $\widehat{h}$ and $\widehat{q}$ once per time step and with $\alpha_f = 0.4$. Results are almost identical to those presented before and are not reported here. Nevertheless, in Figure 3.16-a) we have also plotted time series of total mass contained in the domain when the filter was used. Because in this example no spurious short wave noise was generated, mass evolution is almost the same in both computations. It is clear then that the filter does not alter wave properties in this case since no spurious wavelengths were present.

In order to further investigate the adequacy of the absorbing boundary condition, an additional numerical test with a motionless Gaussian hump with $H_0 = 0.10$ m and $s = 0.5$ m as initial condition is considered. The geometrical configuration for this example is sketched in Figure 3.17 where a step with height $\Delta h = 0.4$, width $\Delta L = 5$ m and side slopes of 1:10 is centered in the computational domain whose still water depth is fixed at $h_0 = 0.5$ m in the horizontal part of the channel. At left and right boundaries the open sea condition is applied in order to evacuate the extra volume of

water associated to the Gaussian hump.

Numerical integration of equations is carried using $\Delta x = 0.025$ m and a Courant number of 1.5. The 8th-order implicit filter is passed over cell-averaged variables once per time step using $\alpha_f = 0.4$. Numerical computation is shown in Figure 3.17. In this case, shorter waves arise as the resulting perturbations travel in both directions and enter into the deep part of the channel. It is seen that different wavelengths are adequately evacuated at left and right boundaries by the open sea condition, but some small residual waves are radiated back into the computational domain as depicted in Figure 3.17. This test shows that the absorbing boundary condition works very well for long waves but that shorter ones are partially reflected. This situation is consistent with the approximation made when invoking characteristic equations and can be further improved by reducing the time step. Nevertheless, for practical purposes involving wave propagation over beaches of gentle slopes, reflected waves generated by the bottom bathymetry and the moving shoreline are expected to be of smaller amplitude and longer period than incoming waves [7, 113] because the breaking process must dissipate most of the wave energy. Hence, the present example is useful to illustrate the limitations of the open sea boundary condition but in natural nearshore environments this approach should be sufficient.

Time evolution of the total mass contained in the computational domain is shown in Figure 3.16-b) and compared against results obtained without filtering cell-averaged variables. The differences are mild and can be attributed to shorter waves that are generated by the approximated boundary condition. It is worth to point out that mass loss is negligible in both cases at the end of the computation. It can be concluded then that the implicit 8th-order filter has a beneficial impact on the numerical integration by suppressing short wave noise without changing the main feature of the propation problem. Because the initial amplitude of the Gaussian hump is large, at the early stage of the computation there is a larger volume of water leaving the domain (a negative pulse). The still water depth is reached approximately after 50 s but slightly earlier when the filter is used.

3.5.4 Regular waves propagating over a submerged bar

A very important test for wave propagation models was presented by Dingemans [50] on the framework of MAST II G8-M project. In this work the performance of several Boussinesq-type models was analyzed by comparing numerical predictions against experimental measurements of regular waves propagating over a submerged bar [13, 104]. The experimental set-up was conceived to investigate frequency dispersion character-

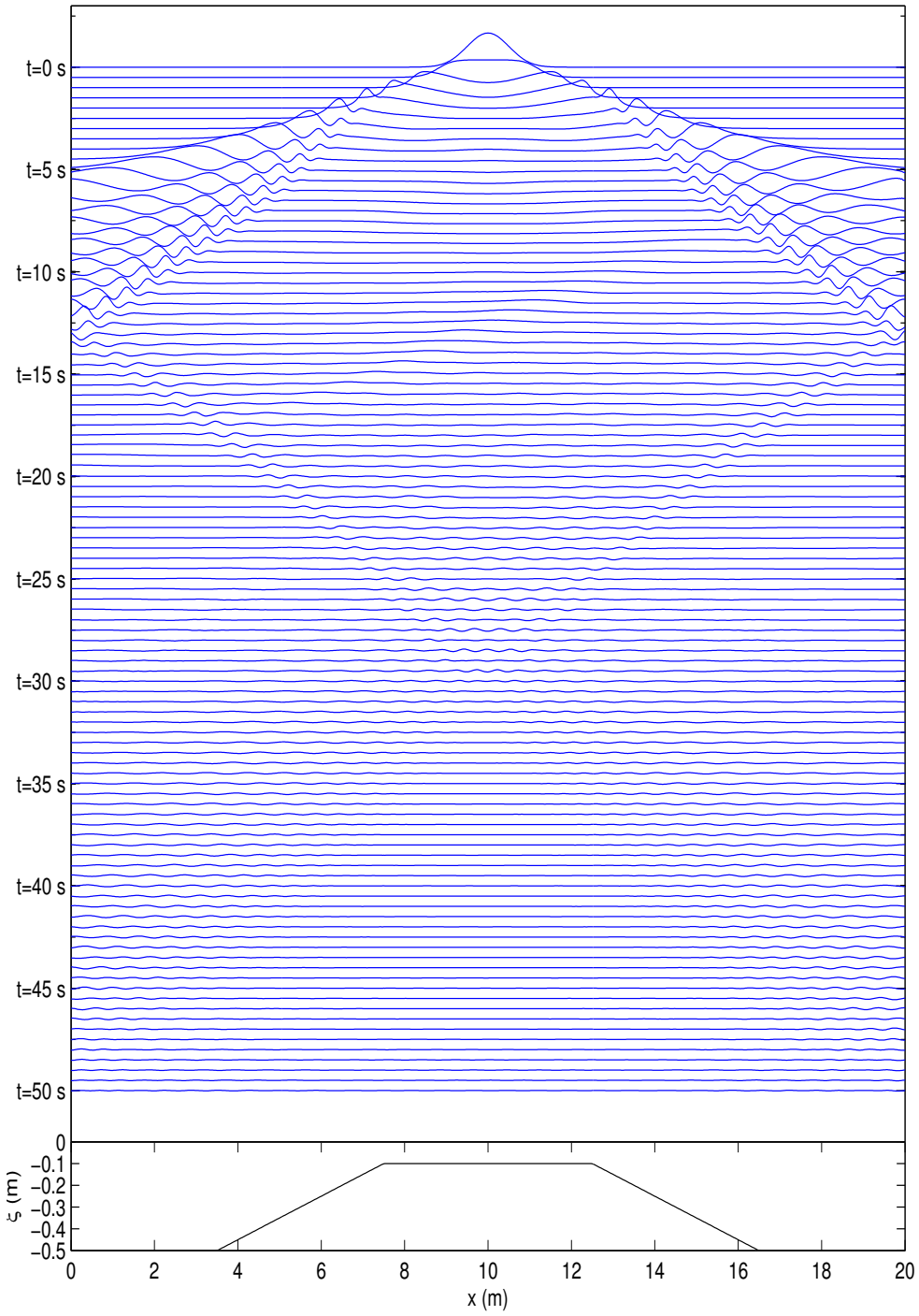

Figure 3.17: Spatial snapshots of free surface at different times using a motionless Gaussian hump of water as initial condition. $H_0 = 0.10$ m, $s = 0.5$ m, $\Delta x = 0.025$ m, $\Delta t = 0.0169$ s and passing a 8th-order implicit filter at interior domain with $\alpha_f = 0.4$.

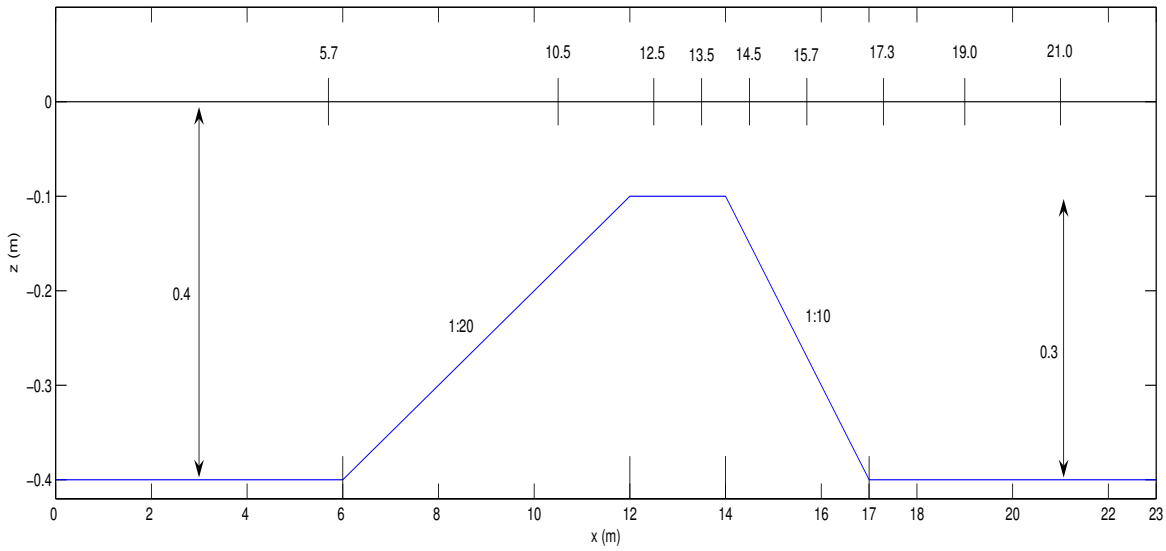

Figure 3.18: Bottom bathymetry for tests reported in reference [50] and spatial location of wave gauges (all distances in meters).

istics and nonlinear interaction of complex wave propagation phenomena and has become an unavoidable and challenging benchmark test for any phase resolving numerical model. Main difficulties arise in this experimental set-up because higher bounded harmonics, which are generated by nonlinear interaction as waves shoal in the upstream slope of the bar, are freely released as they encounter a sudden increase of water depth downslope. Thus, numerical models, usually derived using long wave approximations, are not able to correctly describe wave kinematics of shorter waves as shown in reference [50]. Both, nonlinear and dispersive properties embedded in model equations, contribute to the successful respresentation of measured time series of free surface elevation as demonstrated by Gobbi and Kirby [69], thus making this test a very demanding one.

Even though, in recent years research efforts have successfully lead to major improvements in linear dispersive characteristics and nonlinear properties of Boussinesq-type equations (see for instance reference [108] for a review), the latter has been mainly achieved by incorporating higher order terms which introduce numerical complexity. An alternative way of improving model capabilities have been recently investigated by several authors which have developed multi-layer approches for the derivation of extended Boussinesq equations allowing for a better description of short wavelengths without necessarily introducing very high order derivatives but at higher computational costs [105, 114]. Therefore, any extension of Boussinesq models to deal with

highly nonlinear and extremely dispersive waves increases the required CPU time. On the contrary, we aim at developing here an efficient numerical scheme able to describe wave propagation phenomena over natural beaches and consequently nonlinearity has been considered a more important property to enhace than dispersion. Nevertheless, wave propagation over a submerged bar constitutes a demanding test which can be used to evaluate in practice the theoretical limitations of the chosen set of Boussinesq equations.

Having the latter in mind, we compare numerical predictions against non-breaking experimental data available in references [13, 104] and summarized by Dingemans [50]. Two sets of regular waves propagating over a bar and carried out in a small wave-flume are considered (case A and C from reference [50]). Free surface elevation was measured at several wave gauges located before, above and after the bar. A sketch of the bottom configuration and the location of wave gauges is depicted in Figure 3.18. The reader is referred to Dingemans [50] and Gobbi and Kirby [69] for further information on the experimental set-up.

The first test (case A) was run for periodic waves with incident amplitude $a_0 = 0.01$ m and period $T = 2.02$ s. The absorbing-generating condition is considered at the left boundary in order to prescribe measured time series of free surface elevation at the location $x = 5.7$ m, just before the toe of the bar. The remaining wave gauges located in the shoaling region, above and behind the bar, are used to compare model predictions against laboratory measurements. Equations are integrated using a grid size $\Delta x = 0.04$ m and a Courant number $C_r = 1.5$ which corresponds to a $\Delta t = 0.303$ s. The computational domain is made long enough in order to avoid any interference with reflected waves that might be generated at the right boundary during the computation. In Figure 3.19, numerical results are compared to measured time series at same time windows taking care in synchronizing the input data because there was a mismatch error for the wave gauge located at $x = 5.7$ m as pointed out in reference [69].

The model performs very well up to the gauge located at $x = 15.7$ m downslope of the bar, while as expected from theoretical limitations of the present Boussinesq set, some discrepancies show up as higher harmonics are released behind the bar. Nevertheless, the agreement is still quite reasonable and is found to be comparable to results reported by Gobbi and Kirby [69] using the fully nonlinear and weakly dispersive model from Wei et al. [178]. However, it is worth emphasizing that in our case, time integration was performed using a Courant number of 1.5 while numerical results reported in reference [69] were conducted with a Courant number that remained below 0.3 in order to ensure stability. Therefore, the present compact finite volume scheme is more efficient than the finite difference scheme used to discretize the PDE

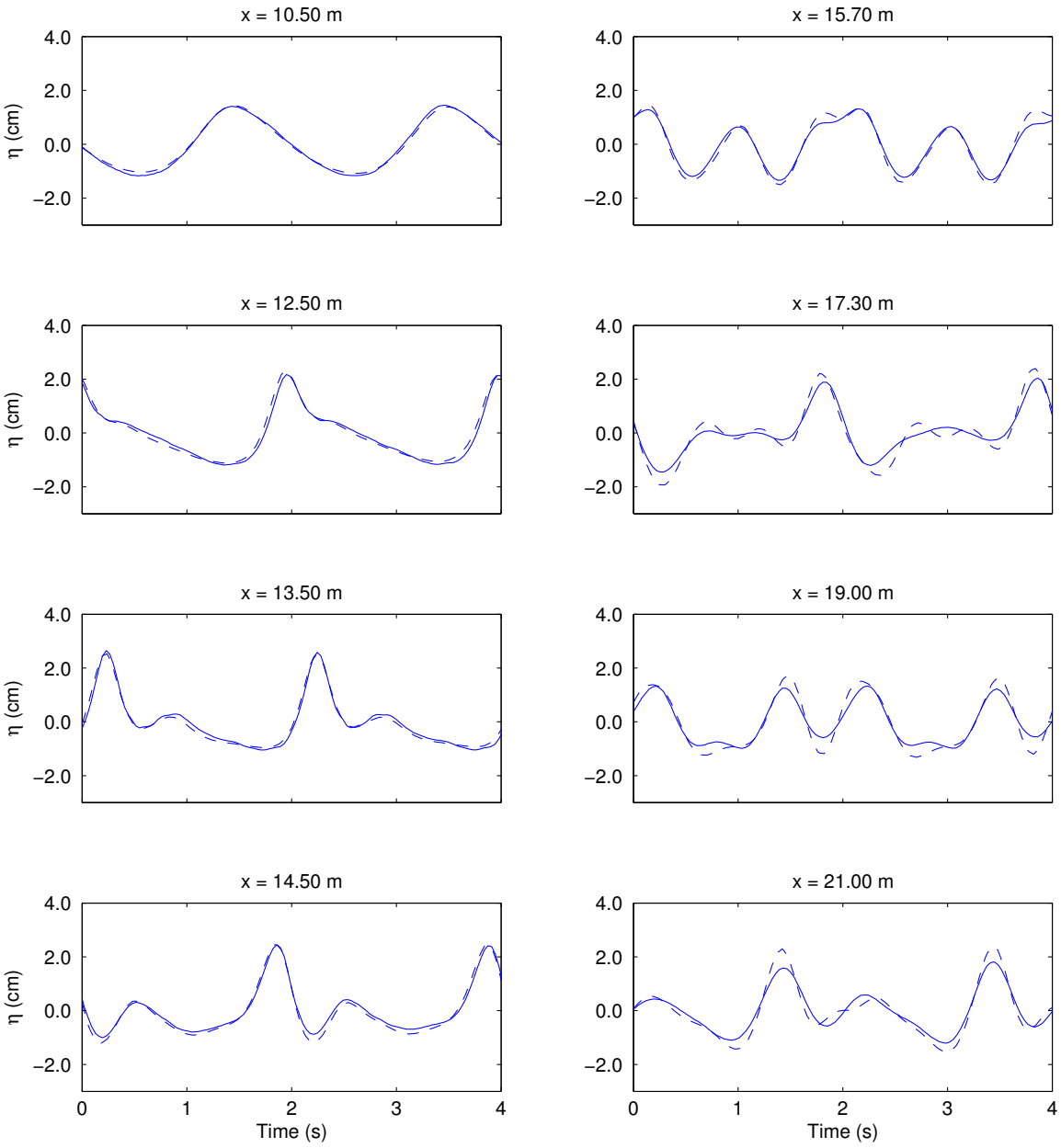

Figure 3.19: Comparison of free surface elevation time series for test case A from Dingemans [50] at several locations. $a_0 = 0.01$ m, $T = 2.02$, $\Delta x = 0.04$ m and $\Delta t = 0.303$ s. $(-)$: measured, $(--)$ computed.

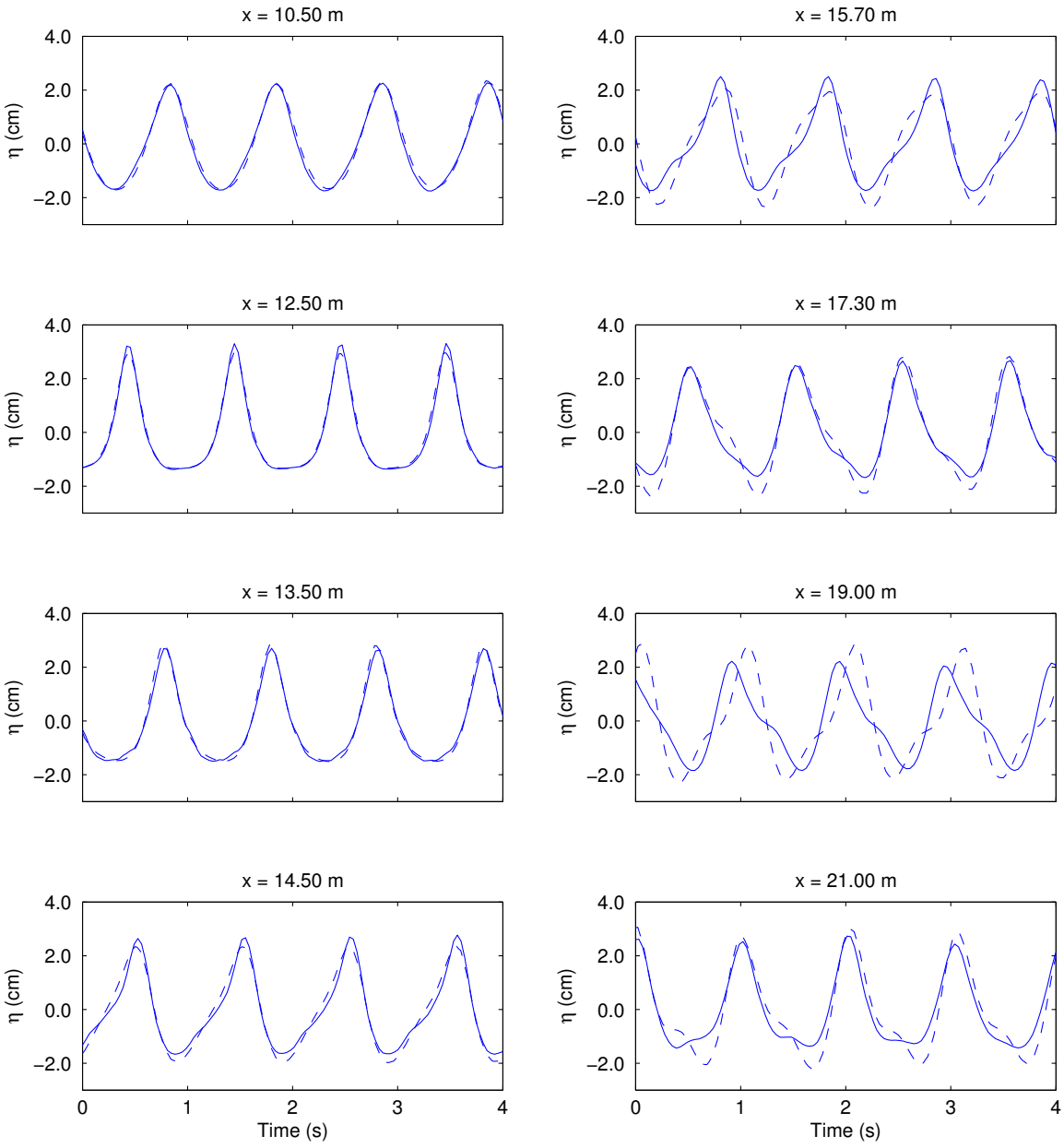

Figure 3.20: Comparison of free surface elevation time series for test case C from Dingemans [50] at several locations. $a_0 = 0.0205$ m, $T = 1.01$, $\Delta x = 0.04$ m and $\Delta t = 0.303$ s. $(-)$: measured, $(--)$ computed.

system in reference [69].

We consider next the experiment C reported by Dingemans [50], where incident waves have an amplitude $a_0 = 0.0205$ m and period $T = 1.01$. This is a far more difficult test for Boussinesq models since wave amplitude is twice the value prescribed before, and incident wavelength is nearly 2/5 times smaller. As in the previous example, the incident wave field is prescribed at left boundary using free surface time series measured by the wave gauge located at $x = 5.7$ m. The numerical model is run with $\Delta x = 0.04$ m and $\Delta t = 0.303$ s, i.e. a Courant number of 1.5 and the computational domain is again made long enough to avoid residual reflection. In this example, dispersion parameter for incident waves is $kh_0 = 1.69$, thus being more than half the theoretical dispersive limit for the present Boussinesq-type equations (see section 2). The latter means that higher harmonic decomposition that takes place after the bar will rapidly generate wavelengths that are beyond the range of validity of the model. Consequently, phase speed estimates for freely released short-length waves may not be accurately reproduced.

Numerical results are reported and compared against experimental data at several locations in Figure 3.20. On the shoal and above the bar crest up to gauge location $x = 13.5$ m, computed free surface elevations show good agreement with measurements. This result proves that the Boussinesq model is able to adequately reproduce the nonlinear energy transfer, from the leading wave component to higher harmonics, that takes place in this region. After waves pass over the bar, higher harmonics are released as free waves thus propagating at different phase speeds. Discrepancies arise then between computed and measured free surface because dispersive properties of the Boussinesq model are not accurate enough for waves which $kh_0 > \pi$. In this experiment, yet the second harmonic is well above this theoretical limit and numerical results are similar to those reported by other authors using equivalent sets of fully nonlinear and weakly dispersive Boussinesq-type equations (e.g. the one layer model in reference [105] and Wei et al.'s [178] model in reference [69]). However, temporal and spatial grid sizes used to integrate equations in the aforementioned Boussinesq models were smaller than the ones used in the present example.

3.5.5 Nonlinear shoaling of solitary waves propagating over a beach

In this subsection, nonlinear shoaling characteristics of the model are investigated by comparing numerical results against laboratory measurements of solitary waves propagating over planar beaches. This is an important check for nonlinear properties

of the chosen set of Boussinesq-type equations in the framework of nearshore wave propagation because in natural beaches, waves running up gentle slopes behave in a quasi independent manner thus showing close resemblances with solitary waves [148]. Moreover, an adequate prediction of the limiting amplitude of nearly breaking waves is paramount in the context of morphodynamics since breaking location is often related to sandbar formation.

Incident Wave Amplitude : $a_0/h_0 = 0.096$					
Probe location relative to the shoreline (m)	2.430	2.215	1.960	1.740	1.502
Measured wave amplitude ($a/\|\xi\|$)	0.368	0.415	0.495	0.582	0.725
Computed wave amplitude ($a/\|\xi\|$)	0.365	0.408	0.472	0.547	0.659
Relative error (%)	-0.7	-1.5	-4.6	-6.0	-9.2
Incident Wave Amplitude : $a_0/h_0 = 0.298$					
Probe location relative to the shoreline (m)	3.980	3.765	3.510	3.290	3.052
Measured wave amplitude ($a/\|\xi\|$)	0.631	0.699	0.766	0.843	0.940
Computed wave amplitude ($a/\|\xi\|$)	0.649	0.702	0.773	0.854	0.943
Relative error (%)	2.7	0.3	0.9	1.3	0.4
Incident Wave Amplitude : $a_0/h_0 = 0.456$					
Probe location relative to the shoreline (m)	4.910	4.695	4.440	4.220	3.982
Measured wave amplitude ($a/\|\xi\|$)	0.724	0.800	0.852	0.921	0.983
Computed wave amplitude ($a/\|\xi\|$)	0.746	0.789	0.852	0.907	0.962
Relative error (%)	3.0	-1.4	0.0	-1.5	-2.1
Incident Wave Amplitude : $a_0/h_0 = 0.534$					
Probe location relative to the shoreline (m)	5.180	4.965	4.710	4.490	4.252
Measured wave amplitude ($a/\|\xi\|$)	0.818	0.867	0.944	1.012	1.067
Computed wave amplitude ($a/\|\xi\|$)	0.807	0.861	0.920	0.986	1.063
Relative error (%)	-1.3	-0.7	-2.5	-2.6	-0.4

Table 3.1: Location of wave gauges for solitary waves shoaling on a planar beach with slope 1:30 and measured and computed wave amplitudes.

Experiments were conducted in the LEGI's wave-flume (36 m) at Grenoble with two different beach slope configurations of 1:30 and 1:60. In the first case, the still water depth was fixed at $h_0 = 0.25$ m in the horizontal part of the channel, while in the second configuration, the still water depth was $h_0 = 0.18$ m [74]. Four solitary

waves were generated for each bathymetry using a piston wavemaker and following the experimental procedure given by Guizien and Barthélemy [75]. Free surface displacements were measured at several wave gauges located just before breaking using resistive probes. Measurement locations and relative wave amplitudes for the experiments are summarized in Table 3.1 for the beach slope of 1:30 and in Table 3.2 for the planar beach with slope 1:60.

Incident Wave Amplitude : $a_0/h_0 = 0.091$					
Probe location relative to the shoreline (m)	4.500	4.285	4.030	3.810	3.572
Measured wave amplitude ($a/\|\xi\|$)	0.272	0.297	0.321	0.356	0.400
Computed wave amplitude ($a/\|\xi\|$)	0.275	0.295	0.324	0.352	0.392
Relative error (%)	0.8	-0.6	1.0	-1.0	-2.2
Incident Wave Amplitude : $a_0/h_0 = 0.286$					
Probe location relative to the shoreline (m)	5.450	5.235	4.980	4.760	4.522
Measured wave amplitude ($a/\|\xi\|$)	0.715	0.783	0.832	0.917	1.007
Computed wave amplitude ($a/\|\xi\|$)	0.724	0.773	0.847	0.909	0.993
Relative error (%)	1.3	-1.4	1.9	-0.9	-1.4
Incident Wave Amplitude : $a_0/h_0 = 0.479$					
Probe location relative to the shoreline (m)	7.950	7.735	7.480	7.260	7.022
Measured wave amplitude ($a/\|\xi\|$)	0.722	0.770	0.809	0.858	0.914
Computed wave amplitude ($a/\|\xi\|$)	0.722	0.748	0.789	0.828	0.871
Relative error (%)	0.0	-2.8	-2.5	-3.5	-4.7
Incident Wave Amplitude : $a_0/h_0 = 0.558$					
Probe location relative to the shoreline (m)	9.150	8.935	8.680	8.460	8.222
Measured wave amplitude ($a/\|\xi\|$)	0.681	0.721	0.758	0.798	0.851
Computed wave amplitude ($a/\|\xi\|$)	0.678	0.701	0.728	0.758	0.793
Relative error (%)	-0.4	-2.8	-3.9	-5.0	-6.8

Table 3.2: Location of wave gauges for solitary waves shoaling on a planar beach with slope 1:60 and measured and computed wave amplitudes.

Four solitary wave amplitudes were studied in order to investigate the performance of the Boussinesq model when used to describe the shoaling of waves with different lengths. Indeed, the smaller the solitary wave amplitude, the longer the equivalent wavelength. Since an adequate numerical representation of linear and nonlinear shoal-

ing of propagating waves would traduce good dipersive properties of the model, this is an important test which can illustrate the physical relevance of the extended system of Serre equations in real world applications.

The model is initialized using Serre's solitary wave solution [136] with the same measured incident amplitude. For both beach configurations, computations are carried out with a grid size $\Delta x/h_0 = 0.1$ and a Courant number $C_r = 1.0$. The adequacy of the numerically generated solitary wave is checked using measurements from an additional resistive probe located in the horizontal part of the flume. Similarly, this time serie is used to synchronize remaining probes located in the shoaling region.

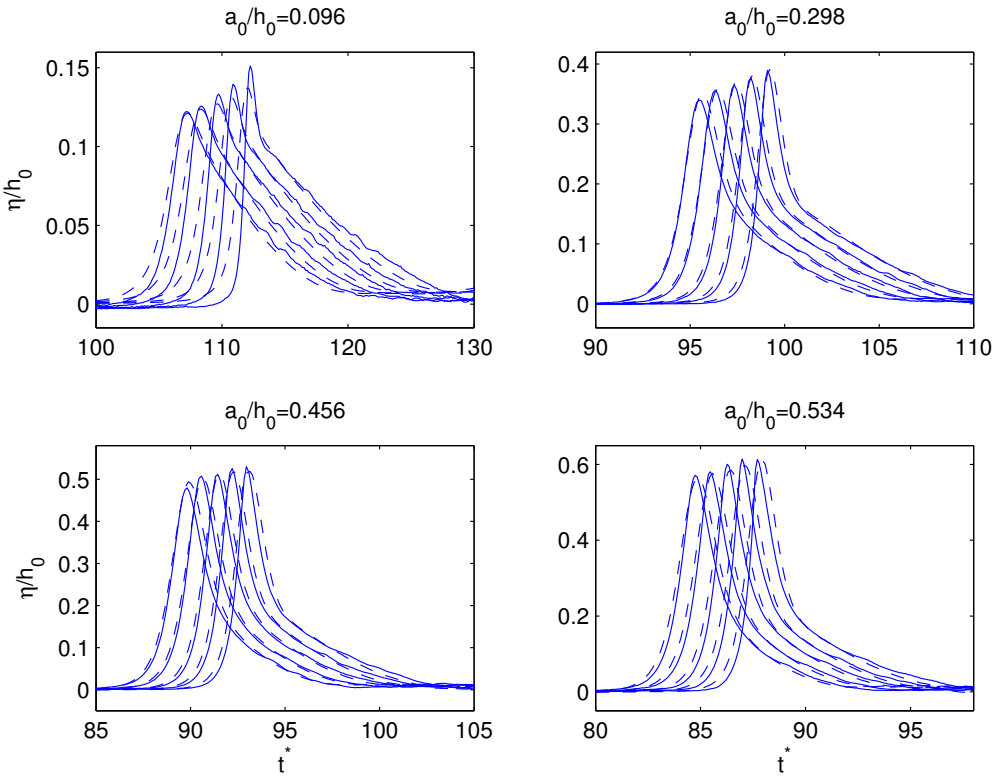

Figure 3.21: Time series of free surface elevation for solitary waves shoaling on a planar beach of slope 1:30 (where $t^* = t\sqrt{g/h_0}$). $(-)$ Measured values, and $(--)$ computed using $\Delta x = 0.025$ m and $\Delta t = 0.0160$ s.

Comparisons of free surface elevations between measured and computed waves are presented in Figure 3.21 and Figure 3.22 for the slope 1:30 and 1:60 respectively. Overall agreement between computed and measured wave amplitudes and shapes is found to be adequate for the different cases investigated. Larger amplitude errors occur for the incident solitary wave $a_0/h_0 = 0.096$ for the beach slope of 1:30, and for $a_0/h_0 = 0.558$ in the 1:60 slope thus showing the important influence of the bottom bathymetry in

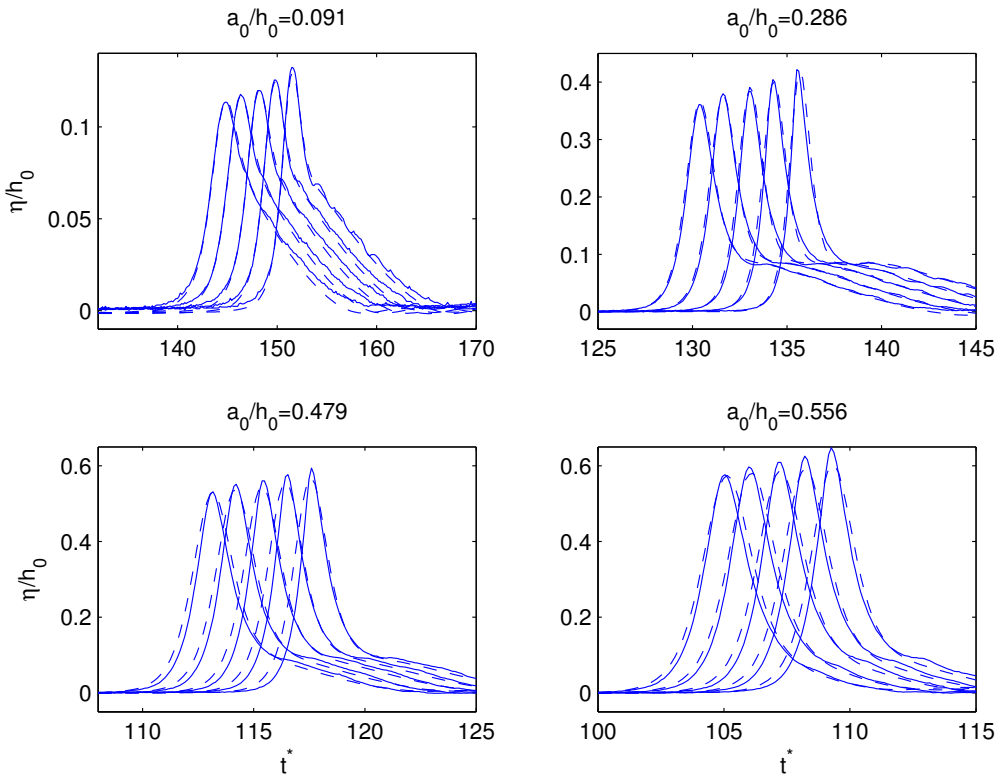

Figure 3.22: Time series of free surface elevation for solitary waves shoaling on a planar beach of slope 1:60 (where $t^* = t\sqrt{g/h_0}$). $(-)$ Measured values, and $(--)$ computed using $\Delta x = 0.018$ m and $\Delta t = 0.0135$ s.

model performance. Nevertheless, the error is never larger than 10 % as shown in Tables 3.1-3.2 and the Serre model is doing actually a pretty good job in predicting nonlinear shoaling even for relative amplitudes as high as $a/|\xi| \sim 1.0$ and for both beach slopes. This is an extremely nonlinear situation where waves are nearly breaking. We recall that the breaking criterion for horizontal bottoms based on solitary wave theory by Munk [118], predicts a limiting amplitude of $a/|\xi| \simeq 0.78$. The latter confirms then that the present experimental test is a very challenging one.

3.6 Conclusions

The numerical implementation of boundary conditions suited to describe water wave propagation problems over a beach has been studied in the present chapter. Boundary conditions intended to reproduce an absorbing/generating seaward boundary, the shoreline movement in the swash zone and an impermeable vertical wall located on a slopping bottom, were investigated with help of a quasi-hyperbolic decomposition

of Serre equations in characteristic directions. Assuming that dispersive effects act at larger time scales than nonlinear ones, but without using a weakly nonlinear hypothesis, we were able to explicitly write open sea and wall boundary conditions for the particular form of extended Serre equations that was numerically solved using a 4th order compact finite volume scheme in Chapter 2. Similarly, the numerical strategy for shoreline movement which consists in a linear extrapolation for fictitious dry nodes through the wet-dry interface proposed by Lynett et al. [107] was successfully adapted to our numerical scheme. Even though numerical approximations used to close the system of equations at boundary nodes may reduce the formal accuracy of the scheme, several benchmark tests demonstrated that accurate predictions of modelled water wave processes could be obtained without affect the stability of the high order finite volume method. Indeed, numerical examples chosen to validate the different implemented boundary conditions were conducted with large time steps using Courant numbers ranging between 1.0 and 1.5. Numerical computations performed with those high Courant numbers compare favourably with results reported in former investigations using much smaller time steps (e.g. [69, 107, 175]). In addition, mass loss in all reported numerical tests was negligible small.

On the other hand, the numerical value for the dispersion correction parameter, α, was chosen in order to minimize a joint root mean square error for phase speed and group velocity estimates over the dispersive range resolved by the extended system of Serre equations (i.e. $0 \leq \kappa h_0 \leq \pi$). Experimental tests for regular waves propagating over a bar reported by Dingemans [50] were used to check nonlinear and dispersive properties of the Boussinesq-type model. Numerical results confirmed several theoretical limitations of the chosen set of partial differential equations regarding the physical range of wavelengths that the model is able to accurately describe. Indeed, the nonlinear performance in the upstream part of the bar was very good thus showing that the extended set of Serre equations succeeds in describing the higher harmonics generation process occuring in the shoaling region. However, freely released shorter length waves propagating after the bar were not accurately captured but computed results appeared to be in agreement with those reported in references [69, 105, 175] using equivalent sets of Boussinesq-type equations. Nevertheless, it is important to emphasize that the numerical integration of equations was perfomed for Dingemans [50] benchmark tests using larger time steps (a Courant number of 1.5). It is thus confirmed that the high order finite volume scheme is far more efficient than previously published finite difference or finite elements Boussinesq-type models even for realistic applications.

Nonlinear performance of the extended system of Serre equations was further investigated with help of experimental solitary waves propagating over a slopping bottom.

Comparisons with numerical results previously reported by Walkley and Berzins [175] for total reflection and collapsing of a highly nonlinear soliton on a vertical wall clearly confirmed the importance of including the so-called full nonlinearity in Boussinesq-type equations. Moreover, sereral experimental measurements of solitary waves propagating over two different beach slopes up to nearly breaking conditions, indicated that Serre equations can accurately predict nonlinear shoaling evolution and the associated limiting wave amplitudes. The relative error between predicted and computed amplitudes was never larger than 10 % in all test cases. This important result suggests that this particular set of Boussinesq-type equations may be used to describe propagation of nearly breaking or breaking waves if an appropriate breaking model is considered.

Finally, a practical an efficient way of suppressing spurious short-wave noise that could arise as a consequence of nonlinear interaction or mismatches between discretized boundary conditions and PDEs was presented. The high order implicit filtering technique developed in reference [65] was implemented and numerical examples demonstrated that the latter may be used to improve model stability in practical applications without affecting the spectral resolution of physical wavelengths. Similarly, challenging numerical tests performed on rapidly varying bathymetries were considered in order to check the ability of the numerical model to maintain quiescent waters or even recover a still water equilibrium from a perturbated initial situation. Those applications clearly demonstrated that the finite volume scheme is conservative and that the numerical treatment of source terms is well-balanced.

Chapter 4

A Phase Averaged Breaking-Wave Model : Revisiting Svendsen's Roller Concept

4.1 Introduction

One of the key features of wave propagation in nearshore environments is related to the highly complex breaking process which is typically induced by bathymetric changes felt by waves running up natural beaches. Despite of that, no general theory has been found to explain and describe all stages of wave breaking since detailed information on vorticity and free surface generated turbulence is still sparse. This topic has been the subject of active experimental and theoretical research over many years and will certainly continue to capture researchers attention in the future. Some recent works dealing with wave breaking can be found in references [26, 28, 29, 42, 54, 72, 117, 146, 157].

As discussed in references [67, 126], natural beaches offer very often propitious conditions for breakers of spilling type to develop. In such a case, the wave crest becomes unstable and a foamy mixture of air and water starts to spill down the front part of the wave. While at early stages of this process small scale instabilities associated to capillaries seem to serve as initial source of vorticity [54, 100, 101], the topology of fully developed breakers is far more complicated. Indeed, even in a quasi-steady spilling breaker, the flow exhibits complex patterns of vortical motion where several scales may interact with each other. Experimental investigations have shown that coherent structures coexist with highly intermittent turbulent events, and that flow separation, which is triggered by sharp distorsions in the free surface near the toe of

the breaker, leads to a larger scale turbulent layer of mixing type [98, 157]. The source of vorticity for this turbulent structure is presumably associated to the sudden convective decelaration of flow velocity near the free surface which produces a flow separation. In addition, self-excited instabilities may also be observed in this region (e.g. [45, 116]). Consequently, the mathematical modelling of wave breaking must be tackled with pragmatism, combining the available empirical knowledge with simplificatory or idealized assumptions to describe the main features of flow motion.

Another type of breaking which often develops in nature is the plunging one. The wave crest curls over, collapsing into the sea surface shorewards, causing violent splash. This sudden redistribution of mass and momentum occurs over a short distance, tipically smaller than a wave length. Immediately after, waves reorganize themselves into a quasi-periodic bore-like state similar to a spilling breaker. The distance over which this rapid reorganization of the breaker takes place has been termed the *transition zone* [155]. Consequently, both types of breakers can be thought to behave as a quasi-periodic bore, except for this short transitional regime.

Even though a more detailed knowledge of the physical processes involved in wave breaking phenomenon is still required, some useful macroscopical information is available. Indeed, for practical purposes, wave-averaged models have been used to describe the main features of surf zone hydrodynamics in larger scale problems with relative success (e.g. [2, 168, 169]). In such approaches, the breaking process is parameterized by adopting the classical bore model (e.g. [94, 149, 155]) which provides an estimate of the amount of energy that need to be extracted from the mean flow. Several semi-empirical wave-averaged breaking models have been developed in this framework following in essence the classical shallow water shock theory [152, 179]. Those breaking parameterizations have been derived and calibrated both, for regular and random wave fields, and rely on strong assumptions such as the so-called *saturated spilling breaker*, and important linear simplifications to describe wave motion. The saturated surf zone hypothesis consists in assuming that the wave height is a linear function of the local water depth, while linear wave theory is invoked to get integral propeties of propagating waves. A breaking model for random wave forcing was proposed by Battjes and Janssen [11] while few years later, Thornton and Guza [161] presented a nearly equivalent approach.

Even though breaking parameterizations are generally obtained thanks to the useful physical analogy which presumably exists between surf zone waves and hydraulic jumps, Bonneton [17, 18, 21] shows, from a theoretical standpoint, that it is not necessary to introduce any simplifying assumption in the nonlinear shallow water equations (NSWE) in order to correctly predict periodic broken wave dynamics in the inner surf zone of a

gently slopping beach. The only constraint is that suitable numerical strategies must be considered to ensure that shock conditions are fulfilled.

Nevertheless, an additional practical drawback remains in both, wave-averaged and time domain approaches. This drawback is related to the important issue of mean surf zone currents organization in cross-shore and long-shore directions. The spatial distribution of wave-averaged currents is governed by complex processes associated to the breaking wave forcing and the reader is referred to references [10, 127, 156] for comprehesive reviews on nearshore hydrodynamics. The aforementioned drawback results in particular in an incorrect prediction of the spatial location of maximum intensities of cross-shore and longshore currents when classical wave theories are invoked. Furtheremore, comparisons between measured laboratory surf zone velocity profiles and predicted ones using NSWE indicate that the latter tends to underpredict the maximum depth-averaged return current just below the breaker [18]. A very similar situation occurs in phase-averaged models when no extra mass and momentum breaking roller contributions are included in hydrodynamic equations [47, 154].

Additionally, a successful prediction of mid to long term beach profile evolution requires proper estimation of mean currents in the nearshore zone. For instance, the position and motion of breaking sand bars are often related to the location of the maximum value of the return current (undertow) [66, 131]. Unfortunately, as outlined in the previous paragraph, the use of standard wave theories does not provide an adequate undertow estimate neither on its maximum intensity, nor on the location for this peak.

Based on visual observations and shallow water theory, Svendsen [154] was able to show that the breaking roller contribution in continuity and momentum conservation equations is far from being negligible in the surf zone. Using the experimental data on breaking waves behind an hydrofoil obtained by Duncan [53], he related the cross-sectional roller area to the local wave height and improved the estimation of undertow intensity in the inner surf zone. Nevertheless, his original approach cannot reproduce the transition zone that exists between the breaking point and the location where the turbulent bore is fully developed. It is evident from many laboratory or field measurements that such a transition zone is always present and is responsible for the landward shift, relative to the breaking point, of set-up and maximum cross-shore and longshore currents (e.g. [23, 35]). Nonetheless, the pioneering contribution of Svendsen provided a useful theoretical background to build more realistic roller equations. Indeed, most of the breaking roller models developed over the last 15 years rely in essence on the same conceptual approach first introduced by him.

A practical improvement for the estimation of integral wave properties was proposed

by Roelvink and Stive [131] who hypothesized that a lag between turbulence production by the breaking process and dissipation must be included in order to reproduce the observed shift in set-up and maximum mean return current. One year later, Nairn et al. [121] showed the theoretical equivalence between the k-equation model written in reference [131] and an energy balance equation for the turbulent bore embracing the simple Svendsen's roller concept. The main advantage of the energy-based roller model compared to the turbulent closure is that roller's contribution can be included in continuity and momentum equations in a straightforward way. For that reason, in recent years the energy balance equation for the roller has been included in several phase-averaged hydrodynamic models used to describe mean currents in the nearshore zone (e.g. [46, 130, 168]).

Even though it is generally acknowledged that the inclusion of a roller equation does improve the overall representation of mean cross-shore and longshore currents, the adequacy of Svendsen's roller concept and associated underlying assumptions have not been really validated by experimental data. Accurate laboratory measurements of roller properties are very difficult to obtain and calibration of model parameters must be done using indirect measurements (e.g. [47, 176]). The main drawback of this approach concerns the fact that it is rather difficult to establish whether the wave theory used to describe the *organized motion* or the roller model itself are adequate or not. Bearing the latter in mind, it is possible to understand why two different roller equations, which differ by a two factor in one of their terms, can be found in the literature : roller models proposed by Stive and De Vriend [150] (S-DV94 in the following), and by Nairn et al. [121] but verified and calibrated later by Dally and Brown [47] (D-B95 hereafter). Surprisingly, the same value for the roller parameter, which is associated to the front slope of the breaker, is commonly used to run both (e.g. [47, 130]).

The main objective of the present chapter is to investigate the physical adequacy of Svendsen's roller concept and practical simplifications that are needed to derive the governing equation for cross-sectional roller area evolution. This question is studied first by comparing model predictions against detailed experimental data on steady hydraulic jumps in Froude similarity with surf zone waves reported by Svendsen et al. [157]. A second and important question that we aim at investigating concerns existing discrepancies between S-DV94 and D-B95 models. For that, we derive a roller equation from a simple energy balance taking care in pointing out differences with previously published models. Additionally, optimal model parameters are obtained by performing inverse modelling using accurate undertow measurements conducted by Cox [41]. In order to focus on the roller concept itself, we minimize errors in the estimation of

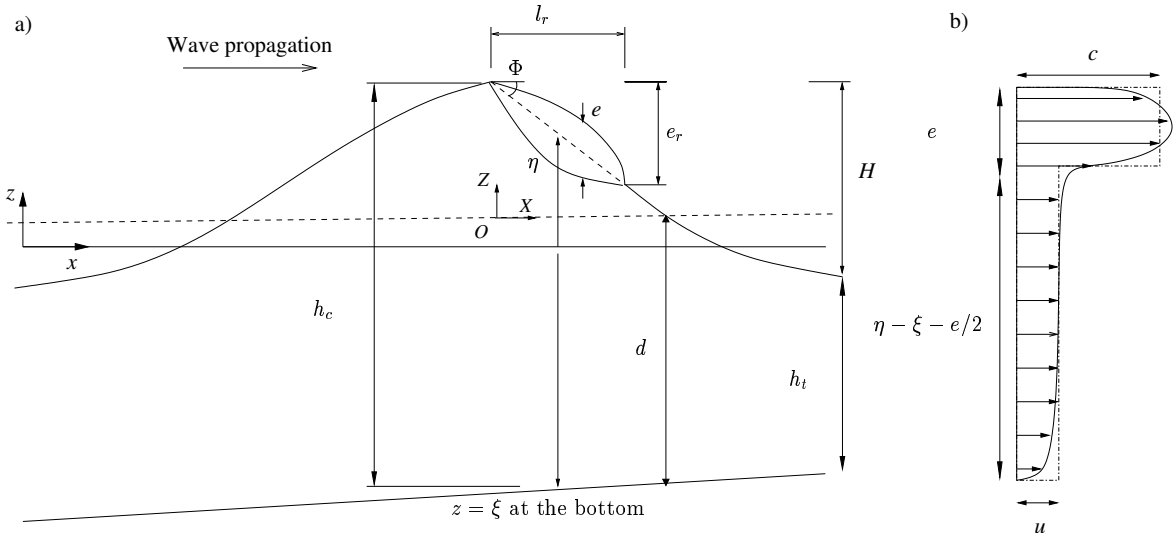

Figure 4.1: Definition sketch for the breaking roller following Svendsen [154]. a) Variables, b) Assumed velocity distribution.

integral wave properties using detailed time domain data reported by Bonneton [18] for this experimental set-up computed using the shock-capturing NSWE solver developed by Vincent et al. [174].

4.2 Conceptual model for energetic exchanges in the roller region

Following Svendsen [154] we assume a simplified velocity profile as sketched in Figure 4.1-b), where the breaking roller is simply carried by the waves at the propagating celerity c. The layer where the organized or potential wave motion takes place has a thickness $h - e/2$, while the local thickness of the roller region equals e. Here we define a characteristic water depth $h = \eta - \xi$, where $z = \eta$ is the mean location of the free surface and $z = \xi$ is the vertical coordinate of the bottom. The lower edge of the roller is assumed to be located at $z = \eta - e/2$. The x-axis coincides with the still water level (positive shorewards), and the z-coordinate is positive upwards. We also introduce local coordinates X, Z for the reference frame moving with the wave and having as origin the point of coordinates, relative to cartesian axes, $(x_O, z_O) = (x_c, d + \xi)$, where $d = \frac{1}{2}(h_c + h_t)$ is the average water depth between the crest and the trough levels, h_c and h_t. Similarly, x_c represents the x-location of the wave crest (see Figure 4.1-a). Therefore, in this moving frame of reference, the mean local position of the free surface

$Z = \eta'$ reads,

$$\eta' = h_c - d - X \tan\Phi = \left(\frac{\gamma}{2} - \frac{X}{d}\tan\Phi\right) d \ , \text{ for } 0 \leq X \leq l_r, \tag{4.1}$$

where Φ is the mean breaker angle, $\gamma = H/d$ is the breaker index with $H = h_c - h_t$ being the local wave height, and l_r is the horizontal roller length.

The roller concept is probably the simplest representation that can be imagined for the highly complex turbulent motion observed in a quasi-steady breaker. The many assumptions and simplifications that are required to write the model are undoubtedly too coarse to obtain accurate flow information from it. Nevertheless, the latter has certainly improved the state of the art of coastal engineering providing some useful scaling relations. The vertical profile depicted in Figure 4.1-b), although extremely rudimentary, has been partially supported by some recent experimental investigations (e.g. [34, 72]), being also compatible with the turbulent mixing layer analogy which has been postulated by several authors. Before going further, it is worth discussing the physical meaning of the lower edge of the roller region which, at first glance, should coincide with the location where the jump in horizontal velocity takes place.

Following Svendsen's definition, the hypothetical line which separates the turbulent region from the organized flow must belong to a dividing streamline since the roller is imagined as a recirculating eddy somehow isolated from the flow underneath. However, the assumed vertical profile implicitely introduces a physical interpretation for this curve which should rather belong to the location where maximum turbulent shear stresses develop [134]. This discrepancy is mostly academic since theoretical backgrounds supporting the roller concept itself are debatable. However, for the rest of this chapter it might be useful to keep this discussion in mind.

In order to write an energy equation for the idealized two phase flow including, on the one hand, the roller, and on the other hand, the organized or mean flow, we adopt a simplified model for energetic exchanges suggested by Duncan [53] and Nairn et al. [121]. It consists in assuming that the energy dissipated from the mean flow acts as the source of energy which enhances the development of the turbulent bore. In a second stage, turbulent shear stresses may dissipate part of this energy at the interface, which can in turn *feed* smaller scale vortical motion underneath before being totally dissipated by viscous forces. Of course, in the present context, this process must be triggered externally by some breaking criterion since the mean flow is usually described using potential theory. Anyway, this simple model for energetic exchanges is compatible with fundamental principles of fluid mechanics and in particular with the Kolmogorov energy cascade concept which serves as a basis to build more sophisticated turbulence models [160]. This idea is illustrated schematically in Figure 4.2.

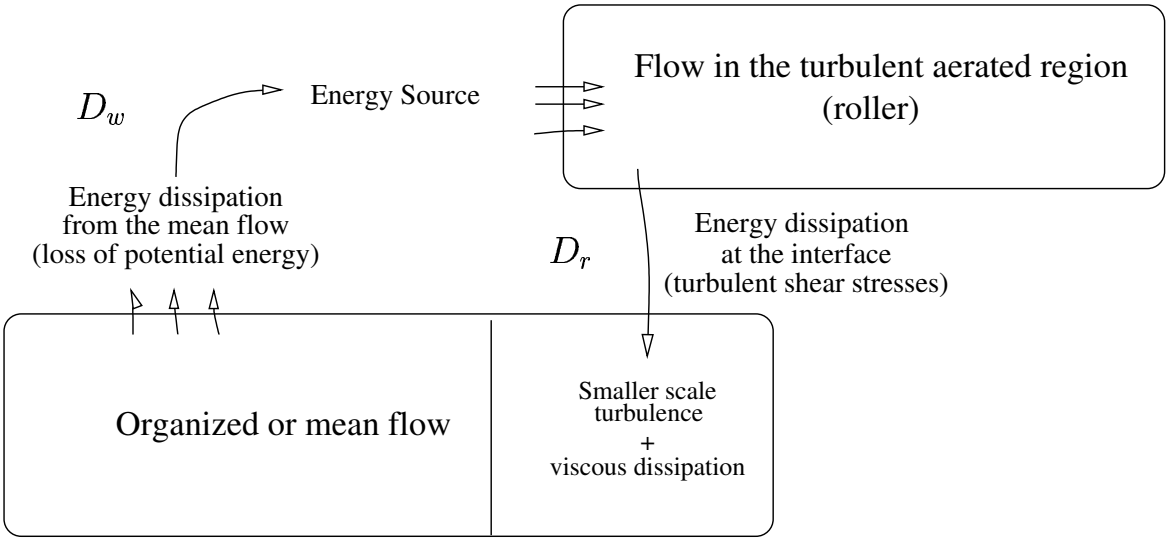

Figure 4.2: Conceptual model for energetic exchanges between organized (mean) flow and turbulent bore : energy cascade analogy.

Using now basic principles of fluid mechanics and assumptions outlined before, we can write, in the fixed frame of reference, the energy balance equation for the layer where the roller is defined as,

$$\frac{\partial}{\partial t}\int_{\eta-\frac{e}{2}}^{\eta+\frac{e}{2}} E\,dz + \frac{\partial}{\partial x}\int_{\eta-\frac{e}{2}}^{\eta+\frac{e}{2}} [(E+p)c]\,dz = D_w - D_r, \tag{4.2}$$

where $E = \frac{1}{2}\rho_r c^2 + \rho_r g z$ represents the total specific energy, p is the pressure, D_w and D_r are respectively the total energy dissipated by breaking from organized wave motion (source term) and the amount of energy dissipated from the roller by shearing stresses (sink term). Besides, ρ_r is the average mass density in the bore region, g is the downward gravitational acceleration and t is the time variable. Consistent with the simplified velocity profile and the long wave approximation, vertical accelerations are neglected and an hydrostatic pressure distribution assumed in the roller region [47, 49, 57, 150]. Nonetheless, Eq. (4.2) is not closed and other approximations must be introduced in order to solve it; we specifically need information about D_w and D_r terms. In the following subsections, we will use the shallow water approximation to relate the depth-averaged fluid velocity u to the local position of the surface elevation considering the particular case of bore propagation over a flat bottom thus assuming that the breaker is quasi-steady.

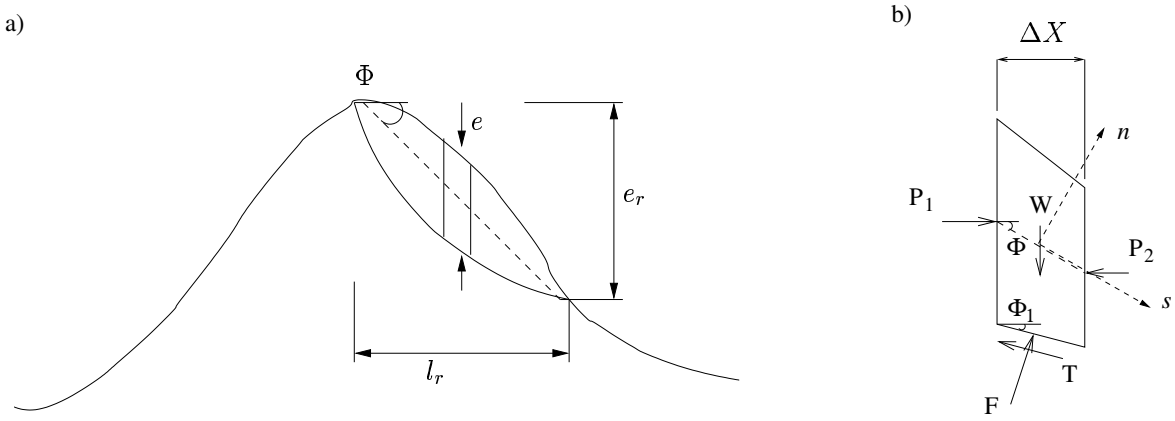

Figure 4.3: Static equilibrium of forces acting over an infinitesimal section of the roller. a) Sketch of the roller region, b) Infinitesimal cross-sectional surface.

4.2.1 Energy dissipated from the roller

An order of magnitude estimate for the amount of energy dissipated from the roller region can be obtained by looking at the work done by shear stresses on the underlying flow [53]. For the infinitesimal cross-sectional roller area depicted in Figure 4.3-b), the static equilibrium of forces acting on the control volume and projected on local orthogonal axes (o', s, n) yields,

$$s : (\mathrm{P}_1 - \mathrm{P}_2)\cos\Phi + \mathrm{W}\sin\Phi - \mathrm{T}\cos(\Phi - \Phi_1) - \mathrm{F}\sin(\Phi - \Phi_1) = 0, \tag{4.3}$$

$$n : (\mathrm{P}_1 - \mathrm{P}_2)\sin\Phi - \mathrm{W}\cos\Phi - \mathrm{T}\sin(\Phi - \Phi_1) + \mathrm{F}\cos(\Phi - \Phi_1) = 0, \tag{4.4}$$

where P_1, P_2 and F represent respectively pressure forces acting on left, right and lower faces of the control volume, W is the weight of the infinitesimal volume, and T is the total shear stress. Similarly, Φ_1 is the local slope of the curve defining the location of the lower edge of the roller.

Solving equations (4.3)-(4.4) for T and F allows us to write,

$$\mathrm{T} = (\mathrm{P}_1 - \mathrm{P}_2)\cos\Phi_1 + \mathrm{W}\sin\Phi_1,$$
$$\mathrm{F} = -(\mathrm{P}_1 - \mathrm{P}_2)\sin\Phi_1 + \mathrm{W}\cos\Phi_1,$$

while, according to definitions given before, in the moving frame of reference (O, X, Z) the following geometrical relations should hold,

$$\tan\Phi = -\frac{d\eta'}{dX} = -\frac{e_r}{l_r}, \tag{4.5}$$

$$\tan\Phi_1 \simeq -\frac{d\eta'}{dX} + \frac{1}{2}\frac{de}{dX} = \tan\Phi + \frac{1}{2}\frac{de}{dX}. \tag{4.6}$$

Where e_r is the total roller height (see Figure 4.3-a)). Invoking now the hydrostatic assumption, we are able to write the net horizontal pressure force acting on the volume and the resulting body force as,

$$(\mathrm{P}_1 - \mathrm{P}_2) = -\rho_r g e \frac{de}{dX}\Delta X + O[(\Delta X)^2],$$
$$\mathrm{W} = \rho_r g e \Delta X + O[(\Delta X)^2].$$

Therefore, an estimate for the turbulent shear stress projected on the axis (o', s) is readily obtained,

$$\begin{aligned} \tau_s &\simeq \mathrm{T}\cos(\Phi - \Phi_1)\frac{\cos\Phi}{\Delta X} \\ &= -\rho_r g e \cos\Phi \cos\Phi_1 \cos(\Phi - \Phi_1)\left[\frac{de}{dX} - \tan\Phi_1\right]. \end{aligned} \tag{4.7}$$

Now with help of definition (4.6), using trigonometric relations and a Taylor series expansion of the following function about $\frac{de}{dX}$, it is possible to show that,

$$\begin{aligned} \cos\Phi\cos\Phi_1\cos(\Phi - \Phi_1) &= \frac{2\left(2 + \sin\Phi\cos\Phi\frac{de}{dX}\right)}{4\left(1 + \tan\Phi\frac{de}{dX}\right) + \left(\frac{de}{dX}\right)^2} \\ &= \cos^2\Phi\left(1 - \frac{1}{2}\sin\Phi\cos\Phi\frac{de}{dX}\right) + O\left[\left(\frac{de}{dX}\right)^2\right]. \end{aligned}$$

Hence, the shear stress component along the straight line $Z = \eta'$, which coincides with axis (o', s), reads,

$$\tau_s = -\rho_r g e\left[\frac{1}{2}\frac{de}{dX} - \sin\Phi\cos\Phi\right] + O\left[\tan^2\Phi\frac{de}{dX}, \tan\Phi\left(\frac{de}{dX}\right)^2, \left(\frac{de}{dX}\right)^3\right]. \tag{4.8}$$

Although, it is rather difficult to say something *a priori* about the order of magnitude of $\frac{de}{dX}$, the assumed geometrical configuration for variable definitions given in Figure 4.1-a) implies relation (4.6). Similarly, $\tan\Phi_1$ should be of the order of $\tan\Phi$ except at both extremities of the breaker where the gradient of the local roller thickness, e, can be large. Nevertheless, experimental measurements for roller shape conducted by Svendsen et al. [157] for several weak hydraulic jumps, indicate that $e_{max}/l_r \sim 0.15 - 0.22$ which corresponds roughly to an angle of 10°. Duncan [53] also measured similar mean breaker angle values for quasi-steady spilling breaking produced by a towed hydrofoil. Thus, it seems reasonable to postulate that $\frac{de}{dX} \sim \tan\Phi$.

Equation (4.8) contains second order terms which are neglected in the formula proposed by Deigaard and Fredsøe [49]. For instance, assuming that $\Phi_1 \simeq \Phi \ll 1$ in

equation (4.7) produces the expression given by those authors, i.e.,

$$\tau_s = -\rho_r g e \left[\frac{de}{dX} - \tan\Phi \right]. \tag{4.9}$$

However, relation (4.8) is consistent with the one written by Duncan [53] and Dally and Brown [47]. The latter can be easily verified by integrating the shear stress over the total roller length. By doing so, the total shear required to balance the weight of the roller reads,

$$T_s^{l_r} = \int_0^{l_r} \tau_s \frac{dX}{\cos\Phi} = \rho_r g A \sin\Phi, \tag{4.10}$$

where the cross-sectional area of the roller, A, has been introduced.

In the moving frame of reference, the depth-averaged fluid velocity of the underlying organized flow reads $U = u - c$. According to Duncan [53], the amount of energy dissipated from the bore region[1] can be thought to be equal to the work done by turbulent shear stresses acting on the flow underneath. Hence, the total energy dissipated at the interface between the roller and the organized motion should be,

$$D_r = -U\tau_s \cos\Phi = -(u-c)\tau_s \cos\Phi. \tag{4.11}$$

It is important to note here that in previously published roller equations (e.g. [47, 49, 53, 150]) the flow velocity u was assumed to be negligible compared to the wave celerity c. Even though this could be a reasonable approximation for the deep water breakers studied by Duncan [53], there is some evidence indicating it is not the case in shallow waters. Indeed, using the long wave approximation it can be shown that u may reach a value of nearly 20 % of the phase speed in the inner surf zone and be even higher near the breaking point. This is also sustained by surf zone laboratory measurements (e.g. [41]).

4.2.2 Total energy dissipated from mean flow : the closure problem

Solving equation (4.2) can provide valuable information about roller geometry but it requires an estimate for the total amount of turbulent kinetic energy available to drive vortical motions. If we follow the energy cascade concept, the term D_w in that equation, which represents the total energy dissipated from the mean flow, can be viewed as the source of energy for large and small scale turbulent motion. In that sense, the right

[1] which can be viewed as residual turbulent kinetic energy still available to drive smaller scale turbulence.

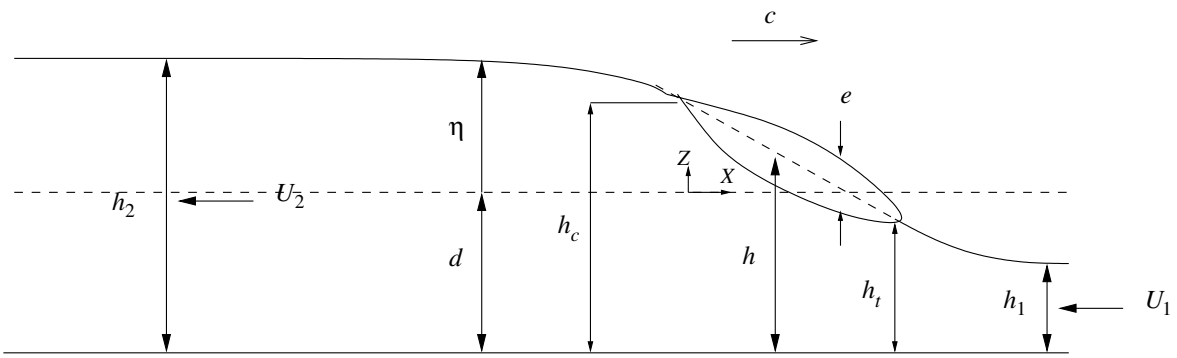

Figure 4.4: Definition sketch for a propagating bore.

hand side of equation (4.2) represents the energy available to drive the roller, which can be thought as the largest recognizable vortex in the breaking wave. Even though from a theoretical point of view a turbulent closure should be introduced at this point, the use of the shock theory in the framework of NSWE will allow us to obtain important information about the total energy dissipated in breaking waves.

Energy dissipation estimates deduced from the shallow water shock theory, or alternatively, the hydraulic jump analogy, has proven to accurately represent wave height evolution in the inner surf zone in both, wave-averaged (e.g. [11, 48, 94]) and time domain approaches (e.g. [18, 81, 91, 174]). Shock conditions thus presumably provide an adequate mathematical representation for the overall breaking process at a macroscopical scale. Using notations introduced in Figure 4.4, the energy dissipated across a shock can be written as [17, 152],

$$\mathrm{D_w} = \int_0^{l_r} D_w \, dX \equiv -\frac{\rho_w g}{4} \frac{Q_b (h_2 - h_1)^3}{h_1 h_2}, \tag{4.12}$$

where h_1 and h_2 represent respectively the water depth before and behind the shock, $Q_b = h_1 U_1 = h_2 U_2$ is the volume flux of water accross the discontinuity, while U_1 and U_2 are flow velocities before and behind the shock in the frame of reference moving with the propagating bore. Here, $\mathrm{D_w}$ denotes the total energy dissipated from the organized flow by breaking.

On the other hand, by replacing the shear stress estimate given in equation (4.8) into (4.11) and discarding terms of $O(\tan^3 \Phi)$, we are able to write,

$$\frac{D_r}{\rho_r g c} = \frac{U}{c} \left(\frac{de^2}{dX} - e \, \sin \Phi \cos \Phi \right) \cos \Phi. \tag{4.13}$$

It is worth pointing out that if we assume $u \ll c$, then $U/c \simeq -1$, and equation (4.13) is thus easily integrated over the total roller length, l_r. The total amount of energy

dissipated by shear stresses in this case reads,

$$\mathrm{D_r} = \int_0^{l_r} D_r \frac{dX}{\cos\Phi} = \rho_r g c A \sin\Phi\cos\Phi, \tag{4.14}$$

which is again consistent with analogous expressions given by Duncan [53] and by D-B95, but differs from the one obtained by S-DV94. On the other hand, if one postulates that there is an equilibrium between production and dissipation of kinetic energy inside the roller region, left hand side of the energy equation (4.2) should be zero and consequently $\mathrm{D_r} = \mathrm{D_w}$. In such a case, equating (4.12) with (4.14) produces the following expression for the cross-sectional roller area,

$$A = -\frac{\varphi}{4\sin\Phi\cos\Phi}\frac{Q_b(h_2-h_1)^3}{c\,h_1 h_2}, \tag{4.15}$$

where $\varphi = \rho_w/\rho_r$ is the density ratio between water and the air/water mixture belonging to the roller region. Using in addition a weak hydraulic jump assumption (i.e. $d = \frac{1}{2}(h_1+h_2) \sim \sqrt{h_1 h_2}$), and $Q_b = -dc$ which follows from the shallow water approximation, we obtain,

$$A \sim \frac{\varphi\gamma}{4\tan\Phi\cos^2\Phi}H^2, \tag{4.16}$$

with $\gamma = H/d$ and $H = h_2 - h_1$. This is exactly the expression first proposed by Engelund [57] except for the $\cos^2\Phi$ factor appearing at the denominator because second order terms are retained. It is important to note that when taking $\varphi = 1.0$, $\gamma = 0.6$ and $\Phi = 10°$, this expression produces $A/H^2 \sim 0.9$ which is in agreement with Duncan's [53] experimental findings.

Despite the fact that relation (4.15) seems to provide a proper estimate for the order of magnitude of the roller area, the simplifying hypothesis $u \ll c$ is neither supported by experimental findings nor by shallow water theory. As pointed out previously, in the surf zone, and specially near the breaking point, the flow velocity may not be small when compared to wave celerity. Indeed, the ratio u/c has been used as a breaking criterion to activate extra terms in Boussinesq-type equations (e.g. [25, 120]). Thus, it could be interesting to derive an expression for the energy dissipated from the roller without using this assumption. However this task requires much more effort since nonlinear terms should be wave-averaged.

In order to be able to spatially integrate equation (4.13) retaining 2nd order terms we use the shallow water approximation,

$$Q_b = -dc \simeq h\,U, \tag{4.17}$$

where the local water depth will be estimated, invoking definition (4.1), as $h = (1 + \frac{\gamma}{2} - \frac{X}{d}\tan\Phi)\, d$. We can thus simplify equation (4.13) using a Taylor series expansion about $\tan\Phi$ and then integrate the resulting expression over the roller length by parts to obtain (see Appendix B),

$$\begin{aligned} \mathrm{D_r} &= \int_0^{l_r} D_r \frac{dX}{\cos\Phi} \\ &= \frac{\rho_r g c}{\left(1+\frac{\gamma}{2}\right)} \left[A \sin\Phi\cos\Phi - \frac{\tan\Phi}{d\left(1+\frac{\gamma}{2}\right)} \int_0^{l_r} e^2\, dX \right] + O\left(\tan^3\Phi, \tan^2\Phi \frac{de}{dX}\right), \end{aligned} \tag{4.18}$$

where to be consistent, second order terms have been retained. Evaluation of the second integral in the right hand side requires the prescription of a functional form for the local roller thickness. This will be done using experimental findings in the next section.

4.3 Empirical verification of the roller concept

In the previous section we have derived, in the frame of reference moving with the breaker, the different energy dissipation terms that will allow us to write an ordinary differential equation governing cross-sectional roller area evolution in the surf zone. According to experimental measurements reported by Duncan [53], it appears that usual assumptions invoked to write roller models provide good order of magnitude estimates for wave-averaged geometrical properties of the breaking roller. In the present section we plan to go further in the verification of the roller concept and the role that second order terms may play.

Apart from scaling arguments outlined in the previous section, the basic hypothesis embedded in roller models have not been verified in detail. This partially explains the different formulations of roller equations that can be found in the literature. The evident lack of experimental information on roller dynamics has been an important obstacle to further validate this conceptual approach. For instance, Duncan's [53] experimental measurements on spilling breakers produced by a towed hydrofoil have been for long time the only available data. Nevertheless, the experimental set-up adopted in Duncan's work, produces a spilling breaker which better represents deep water breaking conditions since the depth of the water column does not play any role in results reported in reference [53]. On the contrary, surf zone waves evolve over waters of finite depth. The flow is thus confined in a shallow layer located between the free

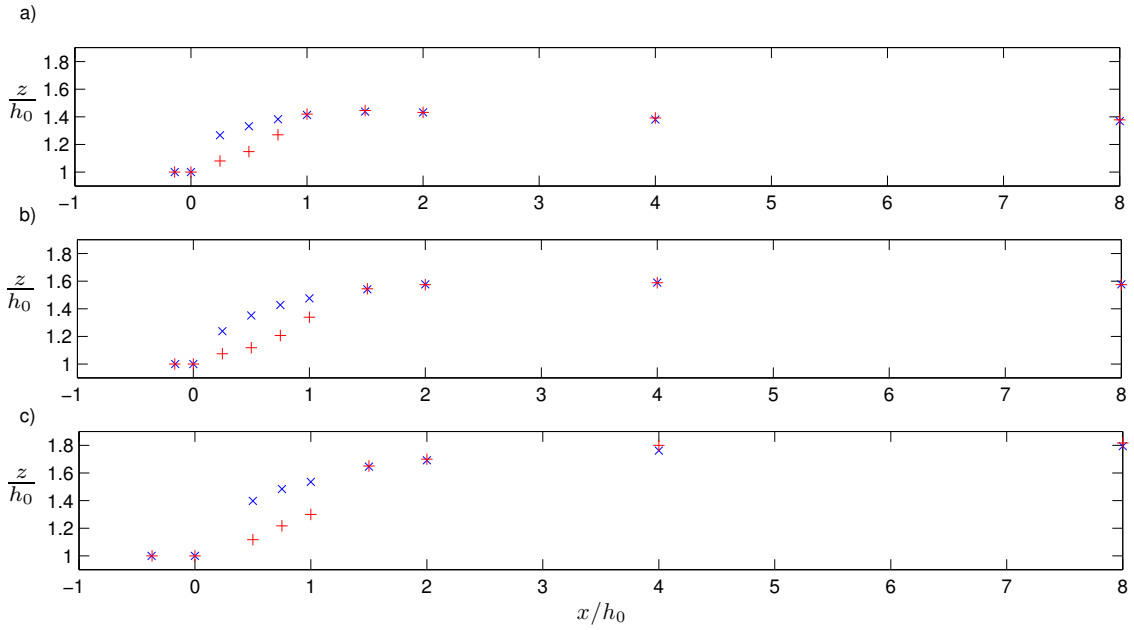

Figure 4.5: Mean free surface location (×) and estimated position of the dividing streamline (+) after Svendsen et al. [157]. a) $F_r = 1.378$, b) $F_r = 1.464$, c) $F_r = 1.562$.

surface and the bottom. Consequently, Duncan's data set may not be that suitable to test underlying roller assumptions in the framework of nearshore applications.

More recently, Svendsen et al. [157] were able to carry out several hydraulic jump experiments where flow characteristics were measured with good accuracy. The experimental set-up was conceived to produce hydraulic jumps with Froude numbers close to the ones observed in surf zone waves. The three investigated hydraulic jumps thus provide valuable experimental information which can be used to further validate roller models.

4.3.1 Empirical knowledge on quasi-steady hydraulic jumps in similarity with surf zone waves

Reliable experimental data for the flow inside hydraulic jumps is difficult to obtain owing to technical difficulties related to velocity measurements that must be conducted in the aerated turbulent front. Svendsen et al. [157] hydraulic jump experiments constitute one of the few available examples where accurate and detailed flow velocities are measured over the entire water column. Three complete data sets are available for weak hydraulic jumps in Froude similarity with surf zone waves. In addition, the authors pay particular attention in obtaining an accurate estimation of the roller

Hydraulic jump	Froude	Q_b	h_0	h_1	h_2	d	c	h_c	l_r	e_r	Φ
No.	number	m^2/s	m	m	m	m	m/s	m	m	m	deg.
1	1.378	-0.0702	0.072	0.063	0.099	0.081	0.867	0.102	0.072	0.030	22.5
2	1.464	-0.0699	0.064	0.060	0.101	0.080	0.874	0.099	0.096	0.035	19.8
3	1.562	-0.0692	0.059	0.057	0.108	0.082	0.844	0.097	0.088	0.038	23.3

Table 4.1: Characteristic flow and roller properties for the three hydraulic jumps studied by Svendsen et al. [157].

geometry and consequently, associated local roller thickness is available. Macroscopical empirical information on roller shapes is used in this section to evaluate roller cross-sectional area predictions produced by energy-based roller models. We concentrate in particular on second order effects which are usually discarded.

In order to investigate whether or not the roller equation is able to reproduce experimental data, measured locations of the mean free surface and the dividing streamline are digitized from figures published in reference [157]. Since we are not interested in detailed features of the flow in the aerated region, we only need to estimate characteristic geometrical properties of the roller, i.e., the total height, total length, mean breaker angle and associated cross-sectional area. In Figure 4.5 roller geometries for the three hydraulic jumps investigated and obtained from digitized graphs are plotted (see also [157]). In Svendsen et al.'s work, the lower edge of the roller is defined as a dividing streamline whose location is estimated using mass conservation considerations. However, it is worth pointing out that experimental results indicate that this theoretical definition coincides over a large extent of the breaker with the location where maximum turbulent shear stress occurs. It is only in the downstream end of the roller, close to the location where the dividing streamline re-attach the free surface, that both theoretical curves diverge.

In Table 4.1, relevant flow and roller properties are summarized. Even though not all the data needed to compute those values are available from Sevendsen et al.'s paper, additional information was provided by Shubhra Misra from the University of Delaware[2]. For instance, equivalent streamflow per unit width is estimated as,

$$Q_b = \frac{\overline{Q}}{(B - 2\delta)},$$

from the spatially-averaged overall streamflow reported in reference [157]. Here, δ is the wall boundary layer displacement thickness estimated by Svendsen et al. [157]

[2]personal communication.

to be respectively 4.3, 5.4 and 5.5 mm for hydraulic jumps 1,2 and 3 in Table 4.1 and $B = 30.48$ cm is the width of the flume. Similarly, e_r and l_r are obtained from raw data on mean free surface, where no interpolation has been performed between the measuring sections. This means that the toe of the roller is located at $x = 0$ in Figure 4.5, according to Svendsen et al. [157], and the position of its downstream edge is assumed to be at the first measuring section where both, the dividing streamline and the mean free surface, coincide. The error associated to this approximation should not influence very much the estimation of overall roller properties. In addition, the water depth at the top of the roller is estimated as $h_c = h_0 + e_r$ in Table 4.1. Finally, the equivalent phase speed, c, is computed using relation (4.17), which follows from shallow water theory, and using $d = \frac{1}{2}(h_1 + h_2)$.

One interesting result presented in Table 4.1 concerns the estimated values of mean breaker angle. Those values are almost two times higher than the ones measured by Duncan [53] on spilling breakers produced by a towed hydrofoil. As discussed before, Duncan's breakers are more representative of deep water breaking, and fundamental differences may exist between the latter and surf zones waves. It is then believed that the shallowness of the medium where breakers develop may produce an additional convective flow acceleration which should partially explain this important change in mean front slope. Furthermore, Yeh and Mok [183] reported even higher values for the mean breaker angle of turbulent bores propagating on an horizontal flume, roughly ranging from 25° to 30°. Similarly, Govender et al. [72] found, from video measurements, that the mean front slope of laboratory surf zone waves evolved between nearly 12° and 30° for spilling breakers, and from 16° to values as high as 40° in the plunging case. Therefore, it seems that one of the important differences between deep and shallow water breakers concerns the equilibrium value that the front slope may reach. Consequently, measured values obtained under shallow water conditions are in contradiction with the simplifying assumption of small breaker angle usually invoked to derive roller models (e.g. [49, 150]).

The knowledge of breaker angle evolution in surf zone waves is of practical importance since wave-averaged and phase-resolving breaking models usually require the prescription of a value for the latter (e.g. [47, 133, 150]). Unfortunately, no useful theory has been found yet to explain and predict the front slope variations of breaking waves.

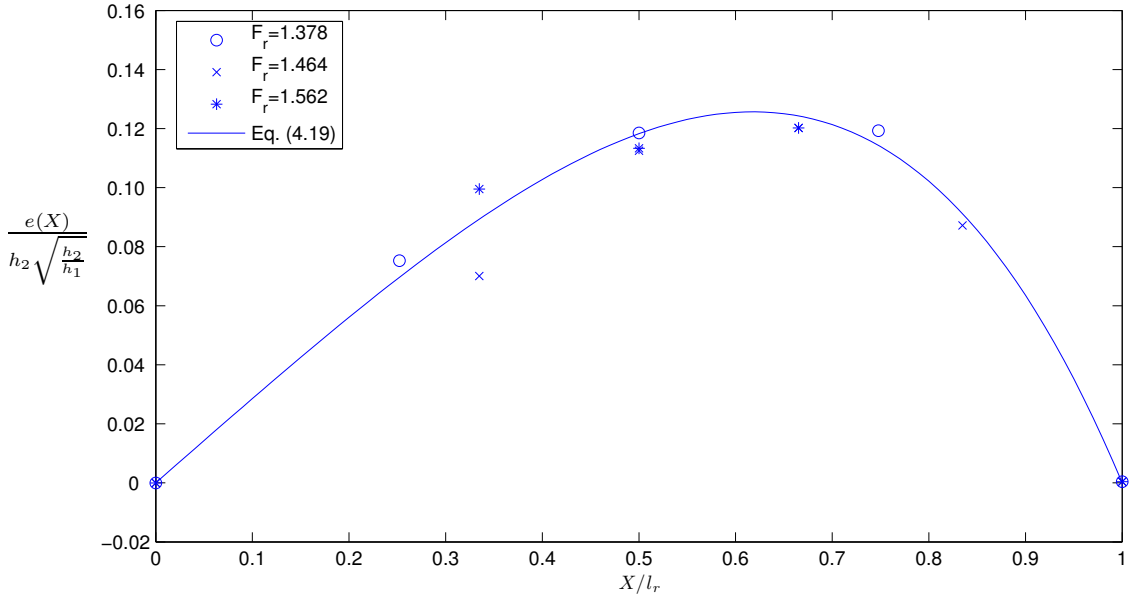

Figure 4.6: Non-dimensional roller thickness estimated from (4.19) using $p = 0.78$ for the three hydraulic jumps investigated in Svendsen et al. [157].

4.3.2 Analysis of model capabilities in a shallow water context

According to the previous discussion it seems reasonable to postulate that second order effects on mean breaker angle should be included in roller equation. However, the integral appearing in the right hand side of (4.18) cannot be reduced to a simple expression without assuming a functional form for the local roller thickness. Veeramony and Svendsen [172] proposed an empirical relation, based on Svendsen et al.'s [157] measurements on weak hydraulic jumps, able to provide an estimate for the local roller shape. Indeed, Svendsen et al.'s experimental data indicate that a reasonable similarity for the local roller thickness exists between the three quasi-steady hydraulic jumps. In the present context, and for the moving frame of reference sketched in Figure 4.4, this expression takes the following form,

$$\frac{e(X)}{h_2\sqrt{h_2/h_1}} = -p\ \exp\left(\frac{X}{l_r}-1\right)\left[\left(\frac{X}{l_r}-1\right)+\left(\frac{X}{l_r}-1\right)^2\right], \tag{4.19}$$

where p is an empirical non-dimensional parameter. A least-square error analysis using Svendsen et al.'s [157] measurements was performed in reference [172], where the optimal value $p = 0.78$ was obtained. The numerical adjustment of this empirical curve is given in Figure 4.6.

In order to evaluate the total energy dissipated from the roller given by equation

(4.18), it is convenient to re-write the previous expression for the roller thickness in a more general form,

$$e(X) = -K \exp\left(\frac{X}{l_r} - 1\right)\left[\left(\frac{X}{l_r} - 1\right) + \left(\frac{X}{l_r} - 1\right)^2\right], \tag{4.20}$$

where the new (dimensional) parameter must be $K = (3\exp(-1) - 1)^{-1} A/l_r$ in order to satisfy the additional integral condition $A = \int_0^{l_r} e\, dX$, or alternatively, $K = p\, h_2 \sqrt{h_2/h_1}$ for hydraulic jumps investigated in [157]. According to this, the integral in the right hand side of equation (4.18) can be estimated as,

$$\int_0^{l_r} e^2\, dX = \alpha_1 \frac{A^2}{l_r} \quad , \quad \text{with} \quad \alpha_1 = \frac{[1 - 7\exp(-2)]}{4\,[3\exp(-1) - 1)]^2}. \tag{4.21}$$

We are now able to integrate the left hand side of energy equation 4.2. For this we need to write this equation in the moving frame of reference (O, X, Z) for a flat bottom assuming that the spilling breaker is in quasi-steady equilibrium. Thus, the following relations must hold,

$$\begin{aligned} \frac{\partial}{\partial t} &= -c\frac{d}{dX}, \\ \frac{\partial}{\partial x} &= \frac{d}{dX}, \\ u(x,t) &= U(X,t) + c. \end{aligned}$$

Using again the hydrostatic pressure distribution assumption, $p = \rho_r g(\eta + e/2 - z)$, and vertically integrating over the roller thickness, equation (4.2) finally yields,

$$\frac{1}{2}\rho_r g c \frac{de^2}{dX} = D_w - D_r, \tag{4.22}$$

showing that locally there is no equilibrium between production and dissipation of turbulent kinetic energy. The left hand side term in this equation is associated to the work done by pressure forces. However, when energy equation (4.22) is spatially integrated over the whole roller length, this term vanishes because roller thickness is zero at outer bounds of the aerated region. Therefore, invoking definition (4.12) for the turbulent kinetic energy source, relation (4.18) for shear stress dissipation, along with the shallow water approximation given in equation (4.17) and the integral expression (4.21), the roller equation reads,

$$\cos^2\Phi \frac{A}{H^2}\left[1 - \alpha_1 \frac{\gamma}{\left(1 + \frac{\gamma}{2}\right)} \frac{H}{l_r \cos^2\Phi} \frac{A}{H^2}\right] = \frac{\varphi\left(1 + \frac{\gamma}{2}\right)}{4\tan\Phi} \frac{d\,H}{h_1 h_2}. \tag{4.23}$$

The latter contains all second order terms which are usually neglected in roller equations.

Solving equation (4.23) for the cross-sectional area of the roller requires additional knowledge on the roller length, l_r, and the prescription of model parameters, Φ and φ. However, it would be interesting at this stage to evaluate whether second order terms improve cross-sectional area computations or not. On this purpose we will compare numerical predictions for cross-sectional roller area produced by four different models against experimental data from Svendsen et al. [157]. We use a first order equation including the hypothesis $u \ll c$ (R1), a second order version with $u \ll c$ (R2), a second order version without any assumption on flow velocity but neglecting the quadratic term in (4.23) (R3), and the full second order version expressed by equation (4.23) (R4). For the reader's convience the first three models are re-written below,

$$\frac{A}{H^2} = \frac{\varphi}{4\tan\Phi}\frac{d\,H}{h_1 h_2} \qquad \text{(R1)},$$

$$\frac{A}{H^2} = \frac{\varphi}{4\tan\Phi\,\cos^2\Phi}\frac{d\,H}{h_1 h_2} \qquad \text{(R2)},$$

$$\frac{A}{H^2} = \frac{\varphi\left(1+\frac{\gamma}{2}\right)}{4\tan\Phi\,\cos^2\Phi}\frac{d\,H}{h_1 h_2} \qquad \text{(R3)}.$$

While for those three expressions model parameters can be easily isolated from measured quantities, the quadratic equation (4.23) cannot be reduced to a simple form. Moreover, the latter has two roots for A and we are not able to tell *a priori* which one should be retained. In order to evaluate the capabilities of each roller model, we will assume that $\varphi = 1.0$, without a real justification for the moment, and compute estimates for the cross-sectional roller area using measured flow and roller properties summarized in Table 4.1. On the other hand, in order to be able to compare numerical computations, an empirical estimate for the roller area is obtained by integration of expression (4.19) using $p = 0.78$. This is an useful exercise which can tell us whether second order terms, which are usually disregarded, should be considered or not and main results are summarized in Table 4.2.

Although it is rather difficult to come to a final conclusion from results reported in table 4.2, at first glance, it appears that second order terms do improve the estimation of the cross-sectional roller area when compared to empirical findings from [157]. Computed RMS error decreases firmly when models R2 and R3 are considered in comparison with R1 which retains only first order terms. Additionally, results obtained assuming that $\tan\Phi = 0.1$ in R1 are also presented. This is a widely used approximation in wave-averaged models and several authors have proposed this value for practical applications (e.g. [47, 121, 130, 132]). Nevertheless, estimates for roller area are catastrophic in this

	H	γ	Empirical	R1*	R1	R2	R3	R4[1]	R4[2]
	(m)	H/d	A/H^2	A/H^2	A/H^2	A/H^2	A/H^2	A/H^2	A/H^2
$F_r = 1.372$	0.036	0.44	0.56	1.17	0.28	0.33	0.40	3.37	0.46
$F_r = 1.464$	0.041	0.51	0.61	1.36	0.38	0.43	0.54	3.53	0.63
$F_r = 1.562$	0.051	0.62	0.41	1.71	0.40	0.47	0.62	1.44	1.08
RMSE (%)	-	-	-	175.3	39.2	32.3	29.6	452.5	73.3
RMSE* (%)	-	-	-	116.7	43.8	35.3	21.1	489.4	12.3

Table 4.2: Comparison between empirical and computed cross-sectional roller area for the three hydraulic jumps studied by Svendsen et al. [157]. R1* : model R1 using $\tan\Phi = 0.1$; R4[1] : first root for model R4; R4[2] : second root for model R4. RMSE : root mean square error considering the three jumps; RMSE* : considering only the first two jumps.

case. The latter does not mean that previously reported hydrodynamical computations are wrong, but it is a strong indication that modelling errors in both, description of integral wave properties and roller contribution, are deeply related. We believe that such a small value for the front slope of the breaker has to be chosen in order to compensate errors presumably due to the linear wave theory adopted in those models or because of an intrinsical different behaviour of surf zone breakers where much higher values for roller cross-sectional area arise. Despite of that, it is rather surprising to note that using a nonlinear wave theory and inverse modelling on measured undertows, Dally and Brown [47] concluded that $\tan\Phi \simeq 0.1$ was a reasonable value for the breaker's slope. The latter corresponds to a breaker angle of $\Phi = 5.7°$.

The analysis of results computed with help of model R4 is more subtle. From Table 4.2 it seems to be rather obvious that only the second root of equation (4.23) is physically meaningful. However, we are somehow puzzled by numerical results obtained for the third hydraulic jump with the highest Froude number, since both roots appears to be dangerously close. The latter is of course very frustating because it could indicate that underlying assumptions used to obtain roller equation are not realistic or that some kind of bifurcating mathematical behaviour could be expected in the model. However, taking into account that several uncertainities still remain, in particular on the value $\varphi = \rho_w/\rho_r$, and that additional reasonable experimental errors could exist, the overall agreement obtained with help of the different versions of the roller equation is satisfactory. Hence, there is some empirical evidence which seems to support the roller concept itself and it would not be fair stating that underlying assumptions are wrong. In addition, looking carefully at empirical results reported in Table 4.2 we notice that for the third hydraulic jump the value for A/H^2 shows an important

decrease which doesn't seem to agree with the physical intuition. Indeed, we could expect that, since this hydraulic jump is the strongest among those investigated, the aerated region should in turn be the largest. Besides, we recall that owing to a lack of experimental information, the value for h_1 was extrapolated in Svendsen et al.'s [157] work. Unfortunately, errors on the estimation for this water depth are strongly amplified in roller equations because of the nonlinear dependence on this variable.

Owing to the previous discussion, we perform an additional RMS error estimate without including the third hydraulic jump. Results are reported in the last row of Table 4.1 where it is clearly noticed that second order terms have a beneficial impact on computed cross-sectional roller areas since the RMS error is systematically reduced as additional terms are taken into account. Indeed, comparisons with the first order estimate produced by model R1, show that errors are reduced by 8.5 % when the small angle hypothesis is disregarded, by nearly 23 % when the additional assumption on flow velocities, $u \ll c$, is removed, and by 31.5 % if all second order effects are included. Even though additional experimental data are definitely required, it seems reasonable to think that model performance can be significantly improved by removing the simplifying assumptions that are usually invoked to write roller models. Nevertheless it is worth emphasizing that more empirical information would be required to further confirm that trend. We recall that there is also an uncertainity concerning the density ratio, φ, which was assumed to be equal to one. Several experimental investigations indicate that the values for this parameter can range from 1.0 to 1.4 on a spilling breaker [102], or reach slightly higher values in strong plunging events [72]. Nevertheless, Svendsen et al.'s [157] experimental set-up minimizes the entrainment of air bubbles at the turbulent front in order to be able to conduct accurate velocity measurements over the entire water column. Indeed, only for the strongest hydraulic jump, with Froude number 1.562, a significant presence of air bubbles could be noticed. Therefore, at least for the first two jumps, the assumption $\varphi \sim 1.0$ seems justified.

Whereas second order terms appears to play an important role in the present computations, we cannot tell if this would be the case in real surf zone waves owing to the intrinsic φ-parameter uncertainity and important existing topological differences. This is in particular the case for the question of including the quadratic term in equation (4.23). Furthermore, in surf zone waves, the free surface can be highly curved and the turbulence intensity more important thus leading to a violation of the hydrostatic hypothesis. Nevertheless, the present exercise has been useful to evaluate the overall validity of the roller concept.

An additional conclusion that must be highlighted concerns the total energy loss from mean flow that shallow water shock theory provides. The good agreement between

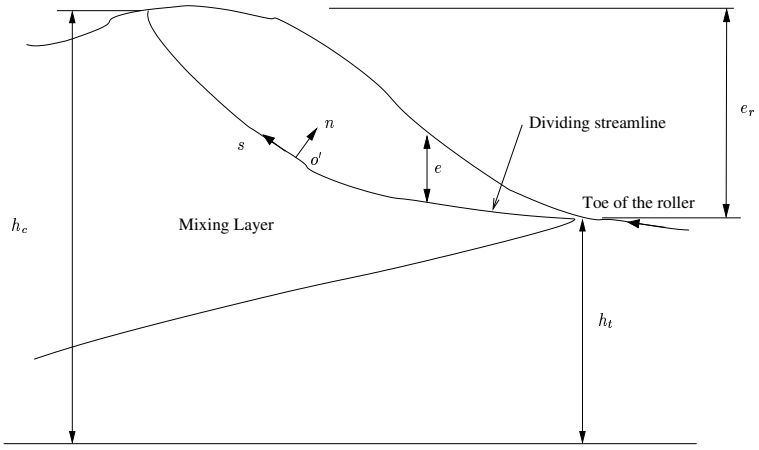

Figure 4.7: Definition sketch for flow separation at the toe of the breaker : Mixing layer model for vorticity and turbulence spreading.

empirical and computed results that was noticed gives some confidence in the energy estimation obtained from equation (4.12). Even though shallow water theory is not able to make a detailed knowledge of the complex breaking process available, it provides valuable information from a macroscopical point of view.

4.3.3 On the application of Cointe and Tulin's [40] theory of steady breakers in shallow waters

Wave-averaged roller models produce an estimate for the cross-sectional area of the aerated region. However, for practical applications it might be necessary to know in addition its relative localition over the carrying wave. This information is crucial for the determination of the total horizontal or vertical extent of the roller region. This issue will be investigated next.

Cointe and Tulin [40] introduced a theoretical approach for the description of the dynamics of quasi-steady breakers experimentally investigated by Duncan [53]. They assumed in essence that the roller region could be imagined as a stagnant eddy riding on the front face of the breaking wave. In the present subsection we focus in particular on the specific reasoning that allowed them to write a linear relationship between the wave height and the vertical distance between the toe and the top of the roller. We aim at investigating whether the proposed expression is applicable or not to shallow water breakers studied in Svendsen et al. [157].

The analytical derivation of Cointe and Tulin's relation begins by assuming that at the toe of the roller a turbulent mixing layer originates. This is a reasonable conceptual approach for the description of the flow in this region and has been supported by

several experimental investigations (e.g. [98, 116, 157]). The incoming flow is suddenly decelerated near the free surface as it approaches the toe of the breaker, where the sharp curvature of the free surface enhaces the flow separation which seems to serve as a source of vorticity according to experimental observations reported in [45, 116]. Hence, the topological behaviour of the flow has some resemblances with a plane flow in a divergent. A Tollmien mixing layer [134, 164] was thus used by Cointe and Tulin to model this situation.

We write the momentum equation on a streamline using local coordinates (o', s, n) sketched in Figure 4.7 and assuming a quasi-steady state as,

$$\frac{\partial}{\partial s}\left(\frac{v_s^2}{2} + \frac{p}{\rho} + gz - \frac{\tau_{ss}}{\rho}\right) = \frac{1}{\rho}\frac{\partial \tau_{ns}}{\partial n}, \tag{4.24}$$

where ρ is the fluid density, v_s is the flow velocity, τ_{ss} and τ_{ns} respectively represent the normal and transverse turbulent shear stresses. Now following Svendsen et al. [157] we define the streamline where the momentum equation (4.24) should be integrated, as the lower edge of the roller region. The latter is thus defined as the average location of a dividing streamline which separates this aerated region from the flow underneath. Although, it is questionable whether this curve may be rigorously thought as a streamline or not since some transverse mass transfer must presumably take place accross it [116].

Svendsen et al. [157] used accurate flow velocity measurements over the entire column of water to localize this fictitious curve. Moreover, maximum transverse turbulent shear stresses occur exactly at the same location where the dividing streamline is defined over most of the roller [157]. It is only near its downstream edge that significant spreading of vorticity can be noticed, and that maximum shear stresses do not coincide anymore with the theoretical streamline. The transverse gradient in shear stresses appearing in the right hand side of equation (4.24) can thus be reasonably assumed to be negligible over the whole extent of the dividing streamline. This allows us to integrate momentum equation between the toe and the top of the roller (see Figure 4.7),

$$\left[\frac{v_s^2}{2} + \frac{p}{\rho} + gz - \frac{\tau_{ss}}{\rho}\right]_t^c = 0, \tag{4.25}$$

where $[f]_t^c = f_c - f_t$, and indices c and t denote an evaluation of the function f at the top and the toe of the roller respectively. In addition, the pressure at both outer edges should be equal to the surrounding atmospheric pressure, and normal turbulent shear stresses τ_{ss} can also be neglected there. Hence we obtain a simple Bernoulli equation,

$$\frac{v_s^2|_c}{2} + g\,(h_c - d) = \frac{v_s^2|_t}{2} + g\,(h_t - d). \tag{4.26}$$

It is worth noting that the hydrostatic assumption has not been used so far, but only some empirical findings regarding the turbulent shear stresses distribution reported by Svendsen et al. [157]. Therefore, expression (4.26) seems to be less restrictive than the roller concept itself. Moreover, as pointed out in [40], the constancy of the total head evaluated on the dividing streamline represented by equation (4.25) has also been supported by former experimental findings on turbulent flows with similar characteristics [6].

On the other hand, invoking the Tollmien mixing layer model, the sudden deceleration in flow velocity at the toe of the roller may be represented by the following expression [40],

$$v_s|_t = \beta\, v_s|_{t^-}, \tag{4.27}$$

where β is a constant ($\beta \leq 1.0$) that is to be determined experimentally, and $v_s|_{t^-}$ is the flow velocity at the free surface just upstream of the toe that can be estimated from potential theory. Again, if viscous effects are neglected, a Bernoulli equation may be written to relate $v_s|_{t^-}$ with the (uniform) flow velocity that should occur sufficiently far upstream from this location. Whereas in the case of Duncan's [53] experiments, this velocity is the speed at which the foil is towed, for Svendsen et al.'s [157] quasi-steady hydraulic jumps it is not so clear which reference value should be considered for the estimation of $v_s|_{t^-}$. Nevertheless, for a turbulent bore propagating over a water surface initially at rest and in the associated moving frame of reference, the velocity upstream of the breaker would be exactly the speed at which the bore is running, i.e., the celerity c. Hence, since reasonable analogies exist between propagating bores and hydraulic jumps, we are able to write in the context of Svendsen et al.'s [157] experiments,

$$v_s^2|_{t^-} + 2g\,(h_t - d) = c^2, \tag{4.28}$$

where c must be estimated using relation (4.17). Replacing expression (4.28) in (4.27) provides the following relation which results from equation (4.26),

$$\frac{g\,H_c}{c^2} = 1 - \frac{2(1-\beta^2)}{\beta^2}\frac{g\,e_r}{c^2} - \frac{v_s^2|_c}{\beta^2 c^2} \tag{4.29}$$

where $H_c = 2(h_c - d)$ and $e_r = (h_c - h_t)$ is the roller height. This is exactly the expression previously published in Cointe and Tulin's [40] paper (eq. (4)), but explicitely derived here in the framework of shallow water breakers. Moreover, according to experimental findings reported in [157], at the top of the roller, velocity $v_s|_c$ appears to be negligible thus confirming that the latter should correspond to a stagnation point as suggested by Cointe and Tulin on the base of Duncan's [53] measurements.

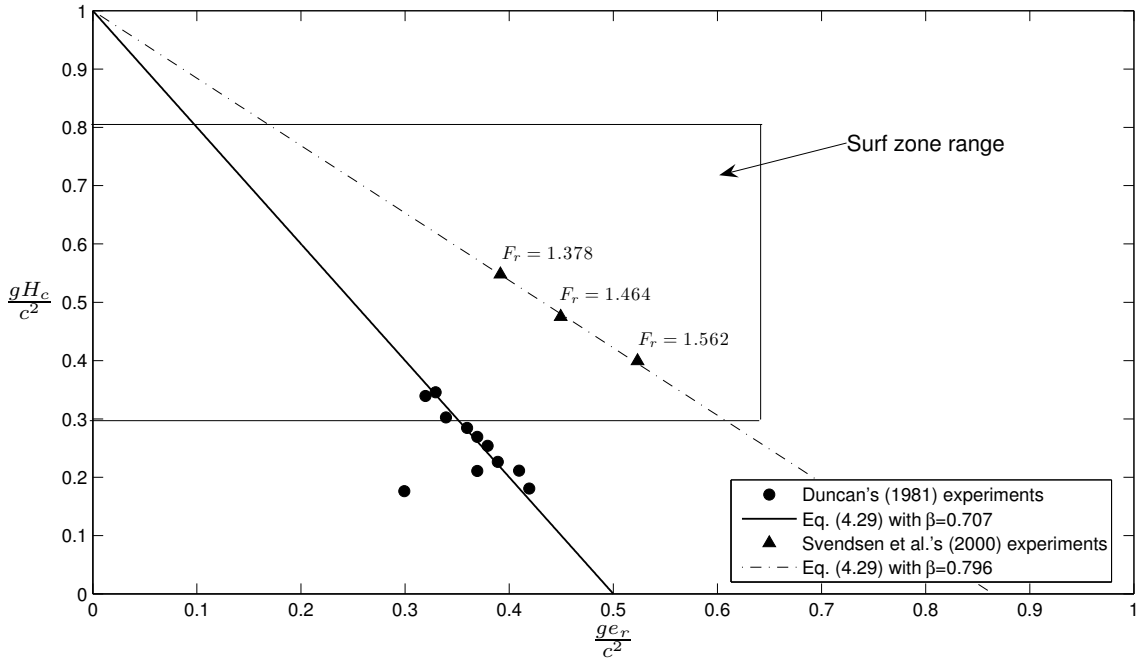

Figure 4.8: Non-dimensional breaker height v/s non-dimensional roller height using Duncan [53] and Svendsen et al. [157] experimental data.

In Figure 4.8, the non-dimensional breaker height, gH_c/c^2, is plotted versus the non-dimensional roller height, ge_r/c^2, for deep water breakers investigated by Duncan [53] and for shallow water hydraulic jumps studied in reference [157] using measured values reported in Table 4.1. It is seen that for the three hydraulic jumps the linear relationship (4.29) gives a perfect match, where the velocity at the top of the roller has been set to zero. In fact one may add an extra experimental point since the empirical linear relationship pass through coordinates $(0, 1)$. A least square error adjustment on Svendsen et al.'s [157] data provides $\beta = 0.796$ for equation (4.29). It is also evident from this figure that differences exist between breaking waves investigated in [53] and hydraulic jumps in Froude similarity with surf zone waves. Although, it is not clear if a theoretical link can be establish between both. This important result suggests that breakers generated by a towed hydrofoil are not necessarily extrapolable to surf zone waves and consequently more experimental research is definitely required for shallow water breaking.

Besides, it is worth pointing out that in relation (4.29) there is only a linear dependence on measured values for h_1 which is used to compute the mean water depth, d. Therefore, experimental errors that should presumably exist in the estimation of this variable are not dramatically amplified as it was the case in cross-sectional area com-

putations performed above. This can partially explain why the third hydraulic jump, with the highest Froude number, does not deviate from the theoretical curve. Similarly, since the hydrostatic assumption was not invoked for the derivation of relation (4.29), this expression may be thought to be more general than the roller equation.

On the other hand, if experimental results carried out in reference [157] might be reasonably extrapolated to surf zone waves as it is assumed in several wave-breaking models proposed in the framework of Boussinesq-type equations [25, 120, 172], then relation (4.29) may provide valuable additional information regarding the total vertical length of the turbulent region, where most of the energy dissipation must take place. In surf zone waves, the location of the top of the roller should coincide with the wave crest, as it is the case for Duncan's [53] breakers, and consequently the wave height, H, must be equivalent to H_c in equation (4.29). Therefore, Cointe and Tulin's [40] relation can be expressed in the following useful way (assuming $c^2 \simeq gd$),

$$\frac{e_r}{H} = \frac{\beta^2}{2\,(1-\beta^2)} \frac{(1-\gamma)}{\gamma}, \tag{4.30}$$

which allows for a direct estimation of roller's height in surf zone waves. For instance, using the adjusted β-value from Svendsen et al. [157] hydraulic jumps, and $\gamma = 0.5$, it follows that $e_r/H \sim 0.86$. Thus, according to this theoretical result, the roller region would not reach the trough of the breaking wave in the inner surf zone. Conversely, for $\gamma \sim 0.8$ which may correspond to an incipient breaking situation, this theory predicts $e_r/H \sim 0.22$, showing that the roller would be essentially localized in the upper part of the breaker. In Figure 4.8 we have delimited a typical surf zone region where $0.3 \leq \gamma \leq 0.8$. Hydraulic jump data is well inside this region, whereas most of the Duncan's [53] measurements lie outside surf zone's bounds.

Finally it is important to note that the newly adjusted β-value is higher than the one obtained using Duncan's [53] data, which means that the jump in velocity at the toe of the roller in the shallow water case is less pronounced. This seems to be reasonable since the shallowness of the water column may introduce additional convective acceleration effects on the flow underneath. The latter is unimportant in deeper waters.

4.4 Wave-averaged cross-shore model for surf zone roller evolution

In the previous section, the overall validity of the roller concept has been investigated using experimental findings on shallow water breakers reported in reference [157]. It appears that, from a macroscopic or wave-averaged point of view, model predictions

are improved if second order terms are retained. In the present section we derive a wave-averaged roller equation which can be applied in coastal engineering practice. The analytical development that we plan to present will also highlight some existing discrepancies between previously published wave-averaged roller equations, namely S-DV94 and D-B95 models. Finally, an inverse modelling approach based on Cox [41] experimental measurements on a laboratory surf zone, will provide additional insight on model performances and on the physical validity of the roller model.

4.4.1 Wave-averaging different terms

In the framework of phase-averaged models, a detailed knowledge of the local shape of the roller is not required. Instead, only the total cross-sectional area and the spatial evolution of it need to be described. Energy equation (4.2) is then averaged over a characteristic time scale, usually the wave period, and simplifying assumptions are introduced in order to integrate the equation. Modelling errors are then absorbed by the different parameters resulting from the averaging process. The most important is the mean breaker angle, Φ, which sets the intensity of the shear force required to balance roller weight. Similarly, the density ratio $\varphi = \rho_w/\rho_r$ has to be prescribed in order to obtain the spatial roller evolution from the energy equation. In practical applications it is often assumed that the latter is close to unity and consequently all uncertainities are absorbed by the remaining parameter (e.g. [47, 49, 53, 150]). In the following we integrate energy equation (4.2) vertically, over the roller thickness, and in the time domain, over a wave period for regular wave conditions. We assume that bottom variations are mild in order to be able to apply some theoretical results reported in the previous sections. The phase speed is thus assumed to be locally constant on a wave-length scale, but not when the entire surf zone is considered.

The specific energy term in equation (4.2) can be splitted into kinetic and potential contributions as follows,

$$E = E_k + E_p, \tag{4.31}$$

$$E_k = \frac{1}{2}\rho_r c^2, \tag{4.32}$$

$$E_p = \rho_r g z, \tag{4.33}$$

where variables were already defined and the fixed coordinate system is sketched in Figure 4.1-a). Since we are focussing on regular waves, the wave-averaged time derivative term in the left hand side of equation (4.2) is zero. On the contrary, the energy flux term should be integrated in space and time. Vertical integration of different terms

results in,

$$KE = \int_{\eta-\frac{e}{2}}^{\eta+\frac{e}{2}} c\, E_k\, dz = \frac{1}{2}\rho_r c^3 e, \tag{4.34}$$

$$PE = \int_{\eta-\frac{e}{2}}^{\eta+\frac{e}{2}} c\, E_p\, dz = \rho_r g\, c\, \eta\, e, \tag{4.35}$$

$$PF = \int_{\eta-\frac{e}{2}}^{\eta+\frac{e}{2}} c\, p\, dz = \frac{1}{2}\rho_r g\, c\, e^2, \tag{4.36}$$

where the hydrostatic assumption has been invoked to compute the pressure flux term, PF. Previous expressions show that wave-averaging potential and pressure flux contributions is not straightforward owing to nonlinear terms.

The wave-averaging process implies the application of the following operator,

$$\overline{f}(x) = \frac{1}{T}\int_{t}^{t+T} f(x,t')\, dt',$$

with $T = L/c$ being the wave period, and L is the associated wave-length. Since bottom variations are mild, and propagating waves are monochromatic, this time-averaged operator can be locally expressed in terms of a spatial-average over the wave length, i.e.,

$$\overline{f}(x) = \frac{1}{L}\int_{x-L/2}^{x+L/2} f(x')\, dx'. \tag{4.37}$$

The roller is only defined, in the moving frame of reference (O, X, Z), for $0 \leq X \leq l_r$, thus wave-averaging roller energy fluxes appearing in the left hand side of equation (4.2) produces,

$$\overline{KE} = \frac{\rho_r c^2 A}{2T}, \tag{4.38}$$

$$\overline{PE} = (\eta_c - \alpha_2\, l_r \tan\Phi)\, \frac{\rho_r g\, A}{T} \tag{4.39}$$

$$\overline{PF} = \alpha_1 \frac{\rho_r g A}{2T}\frac{A}{l_r}, \tag{4.40}$$

where $z = \eta_c$ is the vertical coordinate of the wave crest. In order to integrate nonlinear terms, the linear form for the mean free surface location ($\eta = \eta_c - X\tan\Phi$) and the empirical local roller thickness function (definition (4.20)), have been invoked. While the coefficient α_1 has already been introduced in expression (4.21), the second numerical coefficient, α_2, appearing in (4.39) reads,

$$\alpha_2 = \frac{[3 - 8\exp(-1)]}{[3\exp(-1) - 1]}.$$

It is worth pointing out that the factor in parenthesis in the potential energy flux (4.39) is an estimate of the vertical coordinate of the roller's centre of mass, $z = Z_r$.

Similarly, spatial integration of the energy dissipation function associated to turbulent shear stresses has been performed in the previous section. Therefore, the wave-averaged shear stress energy dissipation (4.18) can be written as,

$$\overline{D_r} = \frac{\sin\Phi\cos\Phi}{\left(1+\frac{\gamma}{2}\right)}\left[1-\alpha_1\frac{\gamma}{\left(1+\frac{\gamma}{2}\right)}\frac{H}{l_r\cos^2\Phi}\frac{A}{H^2}\right]\frac{2g}{c^2}\overline{KE}.$$

In the previous section the contribution from the second term appeared to be non-negligible for hydraulic jumps investigated in reference [157]. In surf zone applications the remaining parameter uncertainties may produce errors with a similar order. Therefore, we will not consider quadratic terms in the following numerical applications assuming that $\alpha_1 = 0$. The wave-averaged roller energy equation can then be recasted as follows,

$$\frac{d}{dx}\left[\left(1+\frac{2gZ_r}{c^2}\right)\overline{KE}\right]+\beta_\gamma\beta_\Phi\frac{2g}{c^2}\overline{KE}=\overline{D_w}, \tag{4.41}$$

where,

$$Z_r = \left[\frac{\eta_c}{H}-\alpha_2\left(\frac{e_r}{H}\right)\right]H,$$
$$\beta_\gamma = \frac{1}{\left(1+\frac{\gamma}{2}\right)} \quad , \quad \beta_\Phi = \sin\Phi\cos\Phi \quad ,$$

and e_r/H can be estimated using relation (4.30). This first order ordinary differential equation can be easily integrated over the entire surf zone using a finite difference or a finite volume scheme and taking $A = 0$ as boundary condition at the breaking point if integral wave properties are known (see for instance reference [36]).

Roller equation (4.41) has been derived using the same basic hypothesis usually embedded in previously published roller models. Main differences concern the correction for relative velocity $U = u - c$ and a reasonable estimate for the vertical location of the roller and the associated potential energy flux. The latter has been systematically discarded or approximated in former roller equations. Before going any further, it is important to point out how traditional roller models may be retrieved from this *extended* ordinary differential equation.

Careful examination of equation (4.41) shows that S-DV94 roller model is recovered when $Z_r = c^2/(2g)$, $\beta_\gamma = 1.0$ and $\beta_\Phi = \tan\Phi$. Since $c^2 \sim gd$ we notice that the average location of the roller's centre of mass is roughly estimated as $Z_r \sim d/2$ in this case. Similarly, the vertical coordinate of the crest of the wave should be $Z_c \sim H/2$, this means that the ratio $Z_r/Z_c \sim 1/\gamma$. However, since under normal conditions γ should

remain below 1.0 in the surf zone, it seems that S-DV94 model implicitly assumes an unrealistic location of the roller's centre of gravity. Rigorously speaking, the latter would imply that the roller is somehow *flying* above the crest of the wave. Nevertheless, Stive and De Vriend [150] argue that this contribution should rather belong to energetic exchanges taking place between the roller and the *organized flow* owing to the temporal evolution of the roller area (see the Appendix of the aforementioned reference).

On the other hand, D-B95 model implies $Z_r = 0.0$, $\beta_\gamma = 1.0$ and $\beta_\Phi = \sin\Phi\cos\Phi$ in equation (4.41). Therefore, besides the second order correction in the breaker slope which is included in the latter, the main difference between S-DV94 and D-B95 roller models arises in the implicit treatment of the average location of the roller's centre of mass. Indeed, while S-DV94 assumes an unrealistical high location, D-B95 considers that the roller is always centered at the still water depth. At first glance, none of the implicitly assumed average positions for the roller are reasonable, nevertheless, in the next subsection we will investigate what kind of practical consequences this may have.

It is important to recall that despite the theoretical discrepancies highlighted in the previous paragraph, several authors have recommended to use $\beta_\Phi = 0.1$ (or even lower values) for the mean breaker slope parameter in S-DV94 and D-B95 roller equations (e.g. [47, 130, 176]). The only plausible explanation for this paradox is that, since the adjustment of parameter values makes use of some kind of inverse modelling on undertow measurements, further approximations are required in order to estimate the volume flux carried by waves (i.e. the Stokes drift). Hence, the optimal breaker slope is chosen to minize modelling errors associated to the estimation of integral waves properties and to the roller model itself. In next subsection we will minimize integral wave properties estimates by coupling the roller equation (4.41) to a time-domain numerical solver for NSWE for the particular case of Cox [41] experimental measurements on regular waves propagating on a planar beach.

4.4.2 Inverse modelling of breaker angles for Cox (1995) experimental data

Detailed measurements of velocity profiles and free surface elevations were collected in the wave flume (33 m) of the Ocean Engineering Laboratory at the University of Delaware by Cox [41]. Experimental probes were located at six vertical lines in the shoaling region and in the surf zone. Incident waves, which propagated up a rough impermeable 1:35 constant slope, were generated using cnoidal theory, with height $H_0 = 11.5$ cm and period $T = 2.2$ s. The still water depth in the horizontal part of the flume was fixed at $h_0 = 40$ cm. Laser Doppler Velocimetry was deployed to measure

velocity profiles in the water column below the trough level. Further details on the experimental set-up can be found in references [41, 43, 44].

As it was briefly discussed in the previous subsection, inverse modelling of the optimal value for the mean breaker slope can be performed using the wave-averaged continuity equation. Using the definition sketch given in Figure 4.1-a) the latter reads,

$$\overline{Q} = \overline{Q_u} + \overline{Q_s} + \overline{Q_r}, \tag{4.42}$$

with definitions,

$$\overline{Q} = \overline{\int_{\xi}^{\eta+e/2} u\,dz}, \quad \overline{Q_u} = \overline{\int_{\xi}^{\eta_t} u\,dz}, \quad \overline{Q_s} = \overline{\int_{\eta_t}^{\eta-e/2} u\,dz}, \quad \overline{Q_r} = \overline{\int_{\eta-e/2}^{\eta+e/2} u\,dz}, \tag{4.43}$$

Here $\overline{Q}$ stems for the total wave-averaged volume flux over the entire water column, $\overline{Q_u}$ is the volume flux below the trough level located at $z = \eta_t$, $\overline{Q_s}$ is the Stokes drift associated to wave asymmetries and $\overline{Q_r}$ is the volume contribution from the roller region. For regular waves, and when a steady-state is reached, the total volume flux, $\overline{Q}$ must vanish. This means that, in the surf zone the volume flux below the trough level (undertow) must be compensated by the Stokes drift and the roller contribution. Velocity measurements carried out by Cox [41] provide an estimation of the mean return current or undertow. However, it was not possible to make reliable measurements in the region above the trough since at times in each wave period there is no water. Consequently, the Stokes drift shall be estimated using a wave theory and the roller's volume flux computed indirectly from equation (4.42).

Following Svendsen [154] and using a wave of constant form hypothesis in the framework of shallow water theory, it can be shown that the Stokes drift takes the form,

$$\overline{Q_s} = -c\,h_t\overline{\left(\frac{\eta-\overline{\eta}}{\eta-\xi}\right)} \tag{4.44a}$$

$$= c\,B_0\,h_t\left(\frac{H}{\overline{\eta}-\xi}\right)^2 + O\left[\left(\frac{\eta-\overline{\eta}}{\overline{\eta}-\xi}\right)^3\right], \tag{4.44b}$$

where h_t is the water depth below the trough level, $B_0 = \overline{(\eta-\overline{\eta})^2}/H^2$ is a wave-shape parameter, and $\overline{\eta}-\xi$ represents the wave-averaged water depth. The latter requires in addition an estimation for the velocity at which the fronts are propagating. Bonneton [19] has shown that a more accurate estimate of wave celerity can be obtained from a one-way shallow water shock theory. Hence, the use of his expression may contribute to reduce errors associated to the computation of this kinematic property in the present

context. Local phase speed is thus evaluated as follows [19],

$$c = -2\sqrt{g(\overline{\eta} - \xi)} + 2\sqrt{gh_t} + \sqrt{g\frac{h_c}{h_t}\frac{(h_c + h_t)}{2}}, \tag{4.45}$$

where h_c represents the water depth below the crest level.

	L1	L2	L3	L4	L5	L6
$x - x_b$ (cm)	-240	0.0	120	240	360	480
ξ (cm)	-27.97	-21.07	-17.67	-14.16	-10.76	-7.35
$\overline{\eta}$ (cm)	-0.37	-0.43	-0.11	0.22	0.75	1.15
$\overline{\eta} - \xi$ (cm)	27.60	20.64	17.56	14.38	11.51	8.50
h_t (cm)	24.02	17.48	14.79	11.86	9.15	6.55
h_c (cm)	37.24	34.58	27.50	20.10	16.23	11.60
H (cm)	13.22	17.10	12.71	8.14	7.08	5.05
γ	0.48	0.83	0.72	0.57	0.62	0.59
B_0	0.0911	0.0552	0.0703	0.0914	0.0882	0.0858
$\overline{\left(\frac{\eta-\overline{\eta}}{\eta-\xi}\right)}$	-0.0185	-0.0292	-0.0295	-0.0269	-0.0308	-0.0295
$\overline{Q_u}$ (cm^2/s)	-85.19	-96.45	-148.07	-111.82	-68.49	-44.75
c (cm/s) (eq. (4.45))	193.75	202.07	174.80	141.18	125.56	103.25
$\overline{Q_s}$ (cm^2/s) (eq. (4.44a))	86.10	103.14	76.27	45.04	35.39	19.95
$\overline{Q_s'}$ (cm^2/s) (eq. (4.44b))	97.27	133.83	95.22	49.04	38.34	20.48
$\overline{Q_r}$ (cm^2/s)	-	-	71.80	66.78	33.10	24.80
$\overline{Q_r'}$ (cm^2/s)	-	-	52.85	62.78	30.15	24.27
A/H^2	-	-	0.98	2.22	1.45	2.14
A'/H^2	-	-	0.72	2.08	1.32	2.09

Table 4.3: Measured properties for Cox [41] experiment and estimated Stokes drifts and roller contributions computed as $\overline{Q_r} = -\left(\overline{Q_u} + \overline{Q_s}\right)$ (see also reference [43] for measured quantities).

In Table 4.3 Stokes drift is computed using both, the exact expression (4.44a) where the term appearing in the right hand side is wave-averaged from measured time series available for this experiment, and the approximated expression (4.44b), which is often used in practical applications. It is worth pointing out that the exact shallow water expression (4.44a) is giving a good estimation for the Stokes drift in the shoaling region for sections L1 and L2. Indeed errors are very small, thus giving some confidence to this formula and to the analytic estimate for wave celerity proposed by Bonneton [19]. On the other hand, the approximated expression (4.44b) seems to overpredict this

contribution in the shoaling region and at the breaking point, but inner surf zone values converge to the ones predicted by expression (4.44a). Unfortunately, it is not possible to accurately determine which are the errors associated to the computation of the Stokes drift, and this will be specially critical in the transition zone between sections L2 and L4.

On the other hand, the cross-sectional roller area can be evaluated from $\overline{Q_r}$ using the expression $A = \varphi\, Q_r\, T$, which follows from the definition given in (4.43) and assuming that the horizontal velocity in this region is constant and equal to the wave celerity. The roller contribution is computed from the continuity equation (4.42) assuming $\overline{Q} = 0$, using measured undertow $\overline{Q_u}$ and invoking shallow water theory to estimate the Stokes drift $\overline{Q_s}$. It is worth emphasizing that this is an indirect estimation for roller's volume flux and that errors associated to the Stokes drift cannot be properly identified. In Table 4.3 it can be noticed that resulting estimates for A/H^2 (assuming $\varphi = 1$) in the inner surf zone are rather high compared to the ones we obtained for Svendsen et al.'s [157] hydraulic jumps but also those reported by Duncan [53]. Moreover, Govender et al. [72] were able to estimate, in the surf zone, the aerated cross-sectional area from video measurements and found that for their spilling breaking case, the ratio A/H^2 was of the order of one, thus in some agreement with Duncan's findings. Nevertheless, in their plunging case, this ratio could reach values as high as three. For Cox's experiment, Table 4.3 shows that estimated volume contributions from waves and rollers are of the same order of magnitude. It is important to mention that at the present experimental state of art, it is very difficult to conduct accurate measurements in real surf zone rollers. Since the question of mean current prediction is paramount for beach morphodynamics and it is clear that the volume flux contribution from the aerated zone is non-negligible, it is expected that novel experimental techniques could help to elucidate the puzzling problem of breaking and roller dynamics. This settled we may pursue the inverse modelling approach and compute optimum values for the remaining parameter, the mean breaker slope.

Solving roller equation (4.41) requires the knowledge of integral wave properties in the surf zone. These are given by running a NSWE shock-capturing solver developed in reference [174]. Bonneton has applied this model to Cox [41] experiment with good agreement between computed and measured kinematic quantities (see results reported in reference [18]). Therefore, this numerical tool provides accurate estimates for integral wave properties needed to drive the roller equation (4.41). This coupling strategy gives an opportunity to test the roller model itself by minimizing errors in estimated kinematic wave properties.

Comparisons between measured integral quantities and numerically computed ones

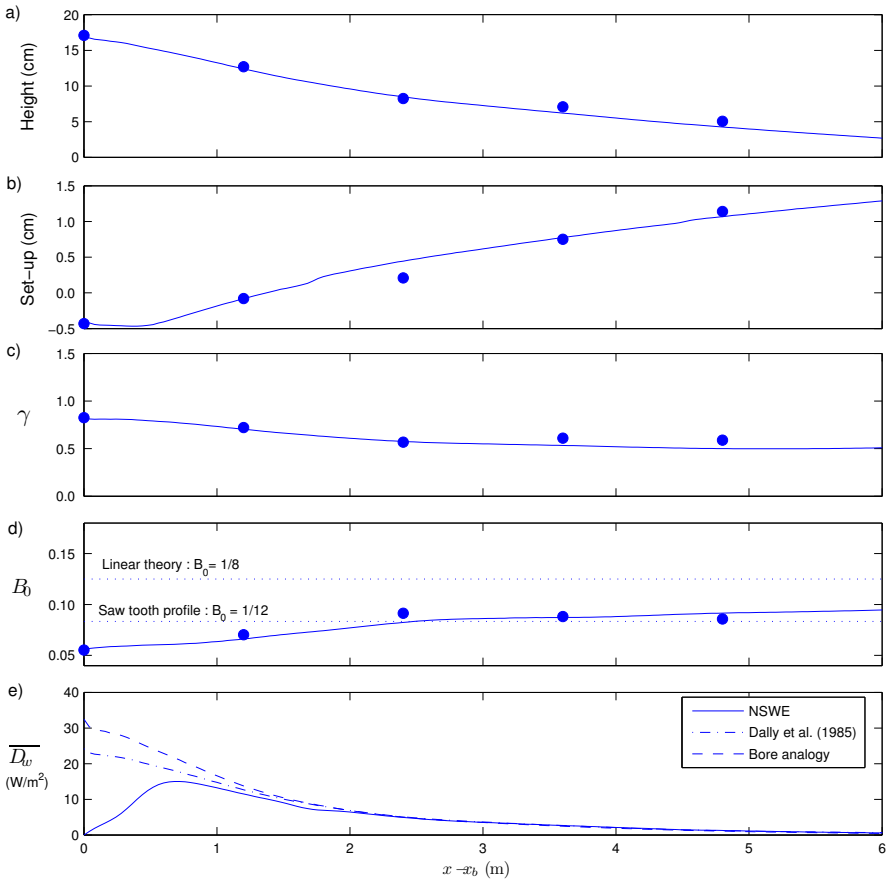

Figure 4.9: Comparison between measured and computed integral wave properties for Cox (1995) laboratory measurements where x_b is the breaking point coordinate. a) Wave height, b) wave set-up, c) breaker index, d) wave shape parameter, and e) wave-averaged energy dissipation in the surf zone. (•) : Measured quantities; (−) : estimated from the numerical model [18].

are presented in Figure 4.9. The numerical model gives good estimates for wave height, set-up, breaker index and wave shape parameter, B_0. In addition, the wave-averaged rate of energy dissipation from the mean flow, $\overline{D_w}$, has been computed from water depth and velocity time series produced by the model. Those values serve to numerically evaluate the shallow water energy equation and the associated local rate of energy dissipation. It is seen in Figure 4.9-e) that wave-averaging this local rate provides a reasonable representation which converges in the inner surf zone to the values predicted by the bore analogy and by the semi-empirical expression proposed in reference [48]. Moreover, a more plausible transition zone is predicted by the NSWE solver. Hence, since by assuming $\varphi = 1$ the mean breaker angle is the only free parameter of the roller model, we will use integral wave properties presented in Figure 4.9 to drive equation (4.41). The measured undertow given in Table 4.3 will serve as target for the

optimization procedure taking $\overline{Q} = 0$ in equation (4.42) and assuming that the Stokes drift $\overline{Q_s}$ may be computed from equation (4.44b) using results reported in Figure 4.9.

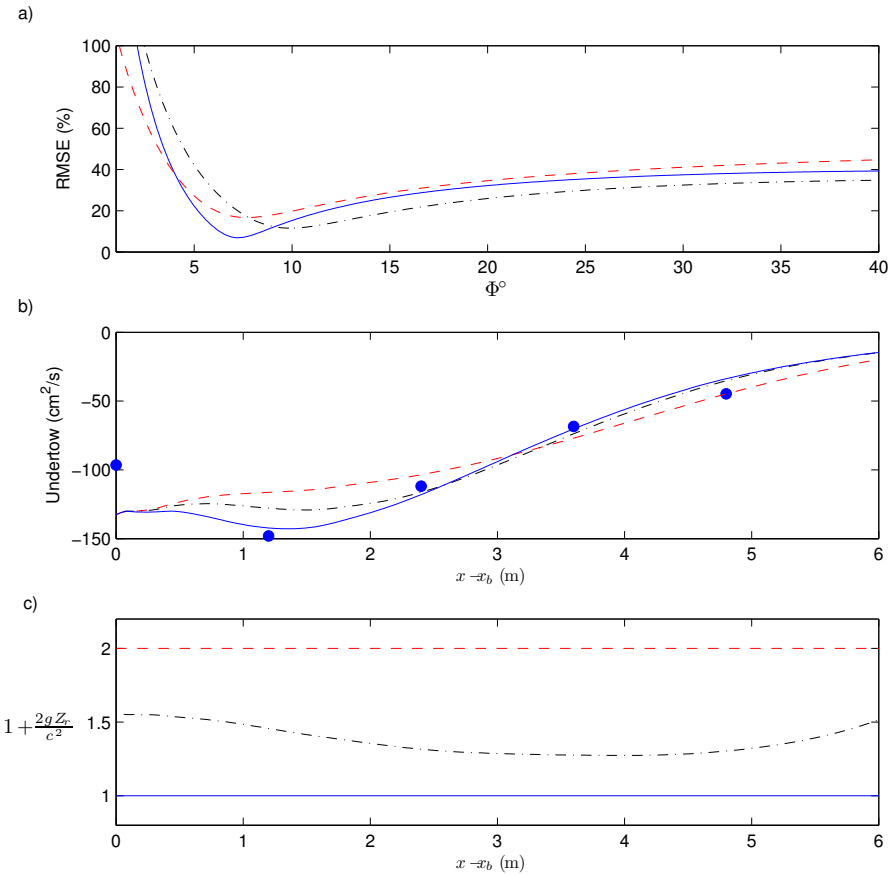

Figure 4.10: Optimal breaker slopes, Φ, from the inverse modelling approach on Cox [41] experimental measurements. ($\bullet$) : measured undertow flux; ($-$) : D-B95; ($--$) : S-DV94; ($-\cdot-$) : Equation (4.41). a) RMS error, b) undertow flux, and c) numerical factor multiplying the energy flux term.

The optimal value for breaker slope is determined by minimizing the RMSE between the measured undertow and the one determined from continuity equation (4.42) using the roller model to estimate volume flux contribution from the aerated region. The rate of energy dissipation from the mean flow, is produced by the NSWE solver. Similarly, remaining integral wave properties are computed from the time domain model while phase speed, c, is estimated using relation (4.45). On the other hand, the total roller height is evaluated from Cointe and Tulin's [40] relation (4.30) using $\beta = 0.796$. The optimization process for Φ values is carried out for $1° \leq \Phi \leq 40°$ using discrete steps of $0.1°$.

Optimal results for the inverse modelling technique applied to Cox [41] experiment

are presented in Figure 4.10. It is evident from computed undertows that at the breaking point there is an intrinsical error associated to the Stokes drift estimate given by expression (4.44b). Indeed, roller contribution at this location is by definition zero. RMS errors on the mean return current are thus estimated considering only measured values at sections L3, L4, L5 and L6. Figure 4.10-a) shows that in the present case only D-B95 formulation is able to adequately capture the maximum undertow value occuring at section L3 but the three versions of the roller equation, i.e. S-DV94, D-B95 and (4.41), give reasonable estimates in the inner surf zone. However, the important feature is that optimal mean breaker angles obtained from inverse modelling are different for each model, being $\Phi = 7.2°$ for D-B95, $\Phi = 7.7°$ for S-DV94 and $\Phi = 9.9°$ for the modified equation (4.41).

Measured undertow reported in [43] at section L3 appears to be very strong. Indeed neither Musumeci et al. [119, 120] nor Briganti et al. [25] were able to adequately predict velocity profiles under the breaker at this location using one of the most sophisticated available Boussinesq-type models. Their formulation includes roller effects by introducing vorticity at the free surface which serves as source for an additional vorticity conservation equation thus providing in theory more detailed information on the breaking process. Nevertheless, model results at this location were rather poor, and apparently those authors considered a velocity correction for longer period oscillations that could arise in the experimental wave tank. Unfortunately, it is not possible to establish whether this sloshing motion is of importance or not from the data that we dispose and we have not introduced any correction term for the undertow in our computations. Moreover, roller's volume flux is obtained assuming that it should compensate underpredicted undertow values resulting from the application of shallow water theory. It seems clear that this approach is not robust since the approximated expression (4.44b) used to compute the Stokes drift may presumably not be that suitable in the transition zone exactly where important differences arise between predictions produced by the three investigated roller equations. It is worth noting that using linear theory to compute the Stokes drift, i.e. taking $B_0 = 1/8$ in expression (4.44b), will result in an even larger overestimation of the mean return current near the breaking point.

The numerical factor in front of the energy flux term in equation (4.41) is plotted in Figure 4.10-c) for the three investigated roller models. It is seen that the modified roller equation which takes into account variations of the vertical position of the roller while propagating, produces a factor which lies between values prescribed in S-DV94 and D-B95 models. As previously discussed, from a strictly academic standpoint, neither S-DV94, nor D-B95 formulation seem to be realistic concerning the particular treatment of the potential energy contribution in equation (4.41). However, from a practical point

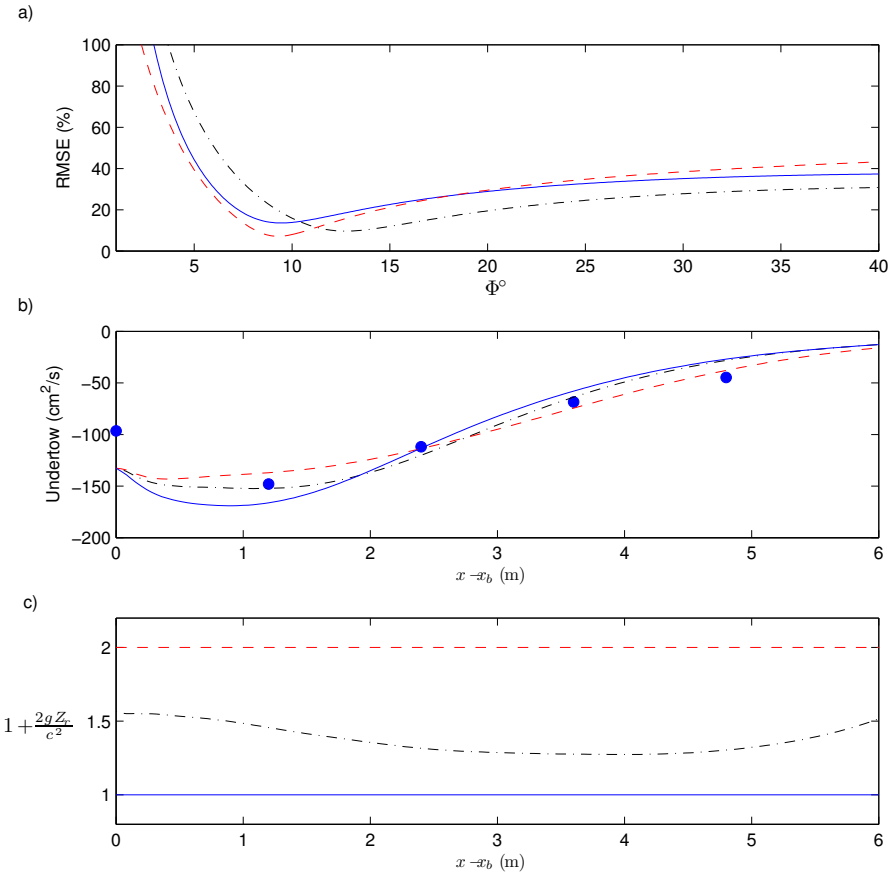

Figure 4.11: Optimal breaker slopes, Φ, from the inverse modelling approach on Cox [41] experimental measurements using Dally et al. [48] expression for the rate of energy dissipation. Same symbol definitions than Figure 4.10.

of view the latter has only a minor influence since model parameter must be chosen to minimize Stokes drift errors rather than the ones belonging to the roller concept itself. In any case, optimal breaker angles obtained with the present inverse modelling technique are higher than the ones previously reported and much higher than the ones obtained by Walstra et al. [176] using an analog inverse modelling. More importantly, the RMSE on undertow computations is minimized for the modified roller equation derived in this chapter when choosing a breaker angle which is in agreement with empirical observations made by Duncan [53].

In order to illustrate how sensitive the inverse modelling approach for the breaker front slope might be, we perform an additional optimization where only the local rate of energy dissipation in the right hand side of equation (4.41) is computed differently. We use now the semi-empirical expression proposed by Dally et al. [48] which agrees

with the estimation from NSWE in the inner surf zone as depicted in Figure 4.9. As it can be observed from results plotted in Figure 4.11, optimal breaking angle values are higher than before, being of nearly $\Phi = 9.4°$ for D-B94 and S-DV94, and $\Phi = 12.7°$ when using the roller equation (4.41). It is worth noting from Figure 4.11-a), that S-DV94 and the modified roller model give the best overall results in this case. It is also interesting to highlight that, despite the two factor difference appearing in S-DV94 and D-B95 models, the optimal breaker angle is now the same for both. This may partially explain the fact that the same numerical value for that parameter is currently recommended to run both models (e.g. [47, 130]). In addition, this example shows how incertainties in the input data may lead to very different conclusions[3]. This is particularly critical in the transition zone where the modelling of breaking process is obviously very inaccurate.

Concerning the density ratio, $\varphi = \rho_w/\rho_r$, it is important to note that since the computation of the target roller volume flux has been performed on the base of the continuity equation, the latter has no major influence in model performances. Indeed, using a different density for the roller will modify the optimal roller area but not the total amount of volume flux required to compensate the measured undertow. Similarly, including quadratic terms in equation (4.41) did not improve the overall cross-sectional area prediction but only the value for the optimal breaker angle thus being higher in this case. It is worth emphasizing then that with the present experimental knowledge on real surf zone beakers, it is not possible to clearly state whether the roller model is physically sounded or not, and specially concerning the transition zone. However, it is important to recall that the hydraulic jumps investigated in [157] showed significantly smaller values for the ratio A/H^2 than the ones reported in Table 4.3 for Cox [41] experiment. Therefore, the fact that smaller breaker front slopes must be used in this particular case to reproduce the measured undertow is not surprising. This may partially explain why such small values ($\sim 6°$) are needed in practical applications and illustrates in addition the important intrinsic differences that may exist between hydraulic jumps and breaking waves.

It is also important to recall that in the present numerical application we have not used the additional information that may be available from the momentum equation. In wave-averaged models, the roller has also a momentum flux contribution (see for instance reference [156]), which is in particular responsible for the landward shift of

[3]The reader should be aware that, even though the analytical development presented in reference [37] and reproduced in Appendix D is identical from the one followed in the present section, inaccuracies in the estimation of numerical values for the undertow used to perform the inverse modelling mistrust some of the conclusions given in this conference proceeding.

the set-up near the breaking point. Momentum equation may thus be useful to further evaluate roller models as was done for example by Walstra et al. [176].

Even though in the present section, the roller concept has been partially validated with help of detailed hydraulic jump experiments, the question of its physical validity for real surf zone waves remains unanswered.

4.5 Conclusions

In the present chapter the physical adequacy of the roller concept, first introduced by Svendsen [154], was investigated. Model performance was studied in detail by comparing its numerical predictions against one of the few available accurate experimental measurements on flow properties within this aerated region. For instance, underlying roller assumptions seem to be justified thus providing reasonable estimates for the mean volume of *dead water*, trapped between the principal flow underneath and the free surface, for quasi-steady hydraulic jumps with Froude numbers in the range of surf zone waves. The overall geometrical properties of this highly turbulent region, originating at the toe of the roller as a consequence of flow separation, is predicted in a satisfactory way when second order terms, which are usually disregarded, are included in the roller equation. On the other hand, it is demonstrated that measured front slopes for those weak hydraulic jumps are radically different from the ones reported in spilling breakers produced by a towed hydrofoil by Duncan [53]. Even though it is not clear if a reasonable link may be established between deep water breakers investigated by Duncan [53] and shallow water hydraulic jumps reported in Svendsen et al. [157], several intrinsic differences, at a macroscopic scale, have been identified.

One important result concerning the application of a Tollmien mixing layer model, as suggested by Cointe and Tulin [40] for Duncan's experiments, was presented in the framework of weak hydraulic jumps in section 4.3.3. A preliminary check of the simple linear relationship proposed in reference [40] between the vertical length of the roller region and the total wave height, was performed using experimental measurements from Svendsen et al. [157]. The agreement between theory and empirical data was found to be excellent for the three shallow water hydraulic jumps investigated. Moreover, this useful and simple relation appears to be more general than the roller model itself since neither the hydrostatic pressure assumption, nor the simplified conceptual model of an isolated recirculating vortex were invoked for its derivation. Moreover, main hypothesis embedded in Cointe and Tulin's expression were satisfactorily confirmed by empirical findings concerning the spatial turbulent shear stress distribution reported in

Svendsen et al. [157]. Nevertheless, the empirical parameter accounting for the sudden flow decelaration at the toe of the breaker had to be fixed at a different value than the one obtained for Duncan's experiments on deep water-like breakers. It is believed that the shallowness of the water column produces an additional convective acceleration on the flow underneath and consequently the jump in velocity at the toe has to be less pronounced. Certainly, more similar hydraulic jump experimental data would be required in order to properly confirm this result.

Unfortunately, our attempt to further evaluate the validity of the roller model for surf zone waves was less convincing. This is mainly due to the critical lack of accurate velocity measurements over the entire water column for breakers running up a beach. To cope with this drawback, the volume flux contribution associated to the aerated region must be estimated indirectly using measured undertow and a water wave theory invoked to compute the Stokes drift. Even though waves' volume flux contribution was estimated with help of a nonlinear shallow water theory (which should be the most suitable for surf zone waves), it was noticed that Stokes drift was overestimated near the breaking point. This was in particular the case for Cox [41] experiment on cnoidal waves breaking on a beach of constant slope. Moreover, measured undertow appears to be unusually high in this experiment, resulting in roller cross-sectional area estimates which are in more agreement with plunging events than the ones we would have expected from a spilling-like breaking. It is not clear whether these unexpected high values could be attributed to the invoked wave theory, experimental errors, a secondary longer period current or a stronger intensity of the spilling breakers investigated by Cox [41]. Consequently, it has not been possible to come to a final conclusion regarding underlying roller model assumptions in the framework of real surf zone waves. Nevertheless, a complete derivation of the roller evolution equation allowed us to highlight several theoretical discrepancies between Stive and De Vriend [150] and Dally and Brown [47] models. Indeed, radically different implicit hypothesis concerning the potential energy flux are embedded in both approaches. While Dally and Brown [47] totally neglect the latter, Stive and De Vriend [150] presumaly assume an unrealistically high value for the relative position of the roller above the carrying wave. However, for practical applications, potential energy contribution appears to be of minor importance owing to the critical uncertainties which remain. It is thus emphasized that experimental investigations where flow velocities could be accurately measured over the entire water column in surf zone waves are needed to further validate or improve roller approaches.

Finally, it is worth noting that nonlinear shallow water theory provides an accurate description for surf zone wave kinematics and the overall energy dissipated by breaking

but mean current estimates are very disappointing. The latter is certainly due to the unresolved turbulent scale which is predominant at the front face of the breaker. In this context, the inclusion of a time-domain roller model would help to improve the overall representation of mean return current without necessarily having to heavily increase the complexity of computations. In the next chapter, we will try to further develop the conceptual approach investigated here by introducing local mass transfer and convective acceleration effects in the continuity equation in the framework of surf zone modelling using Boussinesq-type equations.

Chapter 5

An Alternative Approach for Wave-Breaking in Time Domain

5.1 Introduction

In Chapter 2, we developed a novel high order finite volume scheme which provides an accurate and efficient way to integrate a particular set of fully nonlinear and weakly dispersive Boussinesq-type equations. This set is able to describe nonlinear wave processes in waters of intermediate depth, up to a value of $\kappa h_0 \simeq \pi$, where κ is a characteristic wave number and h_0 is a representative water depth. Additionally, in Chapter 3, nonlinear performances of the model were evaluated using experimental data on solitary waves shoaling over gentle slopes. It is shown that, nonlinear properties embedded in this particular Boussinesq set, allows for a very good prediction of wave height values even near the breaking point where nonlinearities may be of the order of one ($a/h_0 \simeq 1.0$ with a the wave amplitude). These results constitute an encouragement to extend the model to describe surf zone hydrodynamics. Indeed, since limiting wave amplitudes in the shoaling region could be predicted with good accuracy, it is expected that if a proper breaking criterion is adopted, not only the breaking point location but also the associated maximum wave height would be adequately captured.

Another issue that will be briefly investigated concerns the spatial distribution of mean return currents predicted by the model. In the previous chapter, important theoretical limitations related to classical approaches used to describe wave kinematics in the surf zone were clearly confirmed. Presumably, the essential assumption of irrotationality an a lack of turbulence description in nonlinear shallow water equations are responsible for an important underprediction of velocity intensities below the breaker. In theory, the latter might be only improved by fully removing these simplificatory as-

sumptions. This was partially demonstrated in a family of Boussinesq models solving in addition a vorticity conservation equation where the breaking process is enhaced by a vorticity source prescribed at the free surface using experimental findings on weak hydraulic jumps [25, 120, 172]. However, even if model performances were strongly improved and a reasonable agreement between measured and predicted velocity profiles was found for Cox [41] experiment, from a numerical and practical point of view the resulting extra CPU effort makes those approaches rather expensive, and their extension into two horizontal dimensions appears to be very challenging. On the contrary, since the use of the roller concept in wave-averaged nearshore models constitutes a simple an efficient way to overcome drawbacks of current estimations, we could expect that a time domain-like version of it would improve, at least at a wave-averaged scale, undertow predictions produced by Boussinesq-type or nonlinear shallow water equations solvers.

Over the last 15 years, much research effort carried out worldwide have produced important practical improvements for Boussinesq-type equations. The question of incorporating wave breaking effects into these kind of potential-like models was addressed very early, but it was not until the 1990s that several attempts to parameterize this phenomenon could be performed with relative success [27, 84, 133, 184]. Generally speaking, the different wave breaking approaches consider the inclusion of an extra term in the momentum equation in order to dissipate energy when wave breaking is likely to occur. Those additional *ad-hoc* terms can be thought as a force acting on the front face of the breaker. Their practical implementation requires at least : i) an explicit breaking criterion to activate extra terms, and ii) some energetic considerations in order to relate model parameters to the energy dissipated in surf zone waves. In addition, they must ensure mass and momentum conservation and preserve nonlinear wave properties such as asymmetry and skewness.

One of the earliest attempts to incorporate breaking effects was independently proposed by Zelt [184] and Karambas and Koutitas [84] using an eddy viscosity analogy to write an extra term in the momentum equation. Model performance for periodic waves was only investigated in reference [84], since Zelt [184] applied his breaking parameterization to solitary waves. However, Karambas and Koutitas [84] formulation is not momentum preserving and set-up prediction in the inner surf zone was very poor whereas wave height decay was reasonably computed. The latter illustrates the importance of ensuring that breaking terms only introduce a momentum deficit locally without affecting its overall surf zone budget. Only recently, Kennedy et al. [85] were able, embracing the eddy viscosity analogy developed in reference [184], to adequately reproduce wave height decay and set-up for regular waves breaking on planar beaches.

In parallel, a different approach was followed by Brocchini et al. [27] and Schäffer et al. [133]. Their breaking wave models were explicitly written using Svendsen's [154] roller concept where extra terms could be linked to local roller thickness and the mean front slope of the breaker. Even though, this approach stems on very different hypothesis and ideas, the overall effect in momentum equation is strictly equivalent to breaking models based on the eddy viscosity analogy, namely a local momentum deficit at the front of the breaker. The roller approach was further developed by Madsen et al. [111] and even applied to irregular wave propagation problems in references [12, 112, 124]. In addition, the roller concept also provided some theoretical background for the development of Boussinesq models with vorticity mentioned above [25, 120, 172].

Even though the current state of the art concernig breaking wave parameterizations in the framework of Boussinesq models allows for a reasonable qualitative agreement between experimental observations and numerical computations, the important lack of a comprehensive knowledge on free surface vorticity generated and turbulence dynamics has an important consequence on model capabilities. For instance each breaking model has to be built using many hypothesis and simplifications which very often cannot be properly validated on empirical basis. Consequently, extra terms are derived more from *ad-hoc* considerations than real physical arguments. Moreover, the numerous resulting parameters need to be tuned using experimental measurements and it is not possible to ensure that one particular optimal set could adequately reproduce breaking conditions different from the ones used for calibration.

On the one hand, roller-based breaking models are attractive because they have a more straightforward physical basis, but their numerical implementation is rather complicated and at least four different parameters must be tuned. On the other hand, embracing the eddy viscosity analogy results in a somehow simpler model but no direct physical meaning can be attributed to the associated scaling coefficients. In addition, results reported by Kennedy et al. [85] using an improved version of Zelt's [184] approach show a systematic overprediction of wave height in the inner surf zone. Unfortunately it has not been clearly elucidated whether modelling errors belong to the breaking parameterization or to the particular Boussinesq set of equations used to describe wave motion. Without a doubt, the lack of physical knowledge of breaking phenomena makes the task very difficult since no *universal* scaling laws have been found. In this context, none of the aforementioned breaking approaches have shown a clear superiority over the others.

In the present chapter, we develop a novel wave breaking parameterization based on theoretical and experimental findings which applies in principle only to quasi-steady spilling breakers. The new formulation stems from simple energetic principles and

can be viewed as an extension of the eddy viscosity analogy used by Zelt [184] and Kennedy et al. [85]. Local convective acceleration effects, which have been illustrated in the previous chapter, are taken into account by an extra diffusivity term in the mass conservation equation. Indeed, since the flow in the upper part of the breaker is suddenly decelarated (in the moving frame of reference), mass conservation implies a local acceleration in the flow underneath. Alternatively, this extra mass diffusivity term may be thought to enhace local mass transfer at the front face of the breaker, from the crest to the trough. This is in agreement with empirical observations and aims at traducing some potential energy loss.

In the present chapter, we investigate if Kennedy et al. [85] parameterization is able to adequately reproduce nonlinear surf zone wave properties when implemented in our particular finite volume Boussinesq model. However, it will be demonstrated that the latter is not able to properly reproduce, at the same time, wave height in the inner surf zone and the characteristic saw-tooth profile. This important practical limitation constitutes the main motivation for developing the alternative approach presented next.

5.2 Preliminary remarks

Boussinesq-type equations consitute an essentially inviscid set, hence breaking induced effects must be introduced in an external or *ad-hoc* manner. In particular, a breaking criterion must be adopted to activate extra terms, and wave crests need to be followed since a wave-by-wave approach must be considered. In addition, model parameters must be scaled to ensure that the overall externally induced energy dissipation is in agreement with the rate of energy dissipated in surf zone waves.

5.2.1 Breaking criterion

There are multiple ways of deciding whether a given wave should break or not. For instance, it is possible to use physically sound arguments, or rather adopt an empirical approach. Among the different breaking criterions that have been employed in Boussinesq-type models we should cite the critical front slope introduced by Schäffer et al. [133], a velocity gradient limit proposed by Zelt [184] and applied to solitary waves, or a similar approach used by Kennedy et al. [85] where the critical spatial velocity gradient is written instead in terms of the time derivative of the free surface with help of continuity equation. Alternatively, a threshold value for the ratio u_c/c, where u_c is the velocity at the wave crest and c is the local wave celerity, has been applied by Musumeci [119], while very recently a breaking criterion based on a relative

trough Froude number (RTFN) was proposed and verified in references [123, 166, 167]. The two last criteria, i.e., using a relative crest speed or an equivalent Froude number seem to rely on better physical backgrounds.

It has also been recognized that an additional criterion is necessary in order to decide if breaking should stop. Breaker slope, time derivative free surface and RTFN criterions do include and explicit treatment for this situation. Moreover, it can be shown that the approach proposed in reference [85] is almost equivalent to the limiting breaker angle written in [133]. Indeed, the latter reads,

$$\Phi = \Phi_t + (\Phi_i - \Phi_t) \exp\left[-\frac{(t-t_b)}{T_b}\log(2)\right] \ , \text{ for } t \geq t_b, \tag{5.1}$$

where Φ_i and Φ_t correspond respectively to breaker angles at incipient breaking and in quasi-equilibrium (bore-like) state, t_b is the time at which the wave started to break, and T_b is a characteristic transitional time scale. On the other hand, Kennedy et al. [85] criterion on free surface time derivative takes the following form,

$$\partial_t \eta^* = \begin{cases} \eta_t^{(F)}, & \text{if} \quad t - t_b \geq T_b \\ \eta_t^{(I)} + \frac{(t-t_b)}{T_b}\left(\eta_t^{(F)} - \eta_t^{(I)}\right), & \text{if} \quad 0 \leq t - t_b < T_b, \end{cases} \tag{5.2}$$

where $\eta_t^{(I)}$ and $\eta_t^{(F)}$ correspond respectively to the limiting value for time derivative breaking and a saturated value where waves stop breaking. Using a progressive wave of constant form hypothesis, we write,

$$\frac{\partial \eta}{\partial t} + c\frac{\partial \eta}{\partial x} = 0, \tag{5.3}$$

which shows that the free surface time derivative can be related, at first order, to the mean front slope of the breaker since $\frac{\partial \eta}{\partial x} \simeq -\tan\Phi$. In Kennedy et al.'s [85] work, incipient breaking occurs when $\eta_t^{(I)} = 0.65\sqrt{g|\xi|}$, where $z = \xi$ is the local vertical coordinate of the bottom (see Figure 5.1). Hence, the latter is roughly equivalent to a breaker slope $\Phi_i = 33°$. Similarly, the saturated free surface time derivative $\eta_t^{(F)} = 0.15\sqrt{g|\xi|}$ should correspond to a terminal angle $\Phi_t = 8.5°$.

The RTFN criteria is based on the following equivalent Froude number [123, 167],

$$Fr_t = \frac{c_{crest} - u_{trough}}{c_{trough}}, \tag{5.4}$$

with c_{crest} and c_{trough} being respectively the phase speed at the crest and the trough of the considered wave, and u_{trough} is the flow velocity at the trough. On the base of theoretical and experimental data, those authors have proposed the critical value for breaking initiation $Fr_t^{(I)} = 1.47$, while it should be fixed at $Fr_t^{(F)} = 1.15 - 1.2$ for

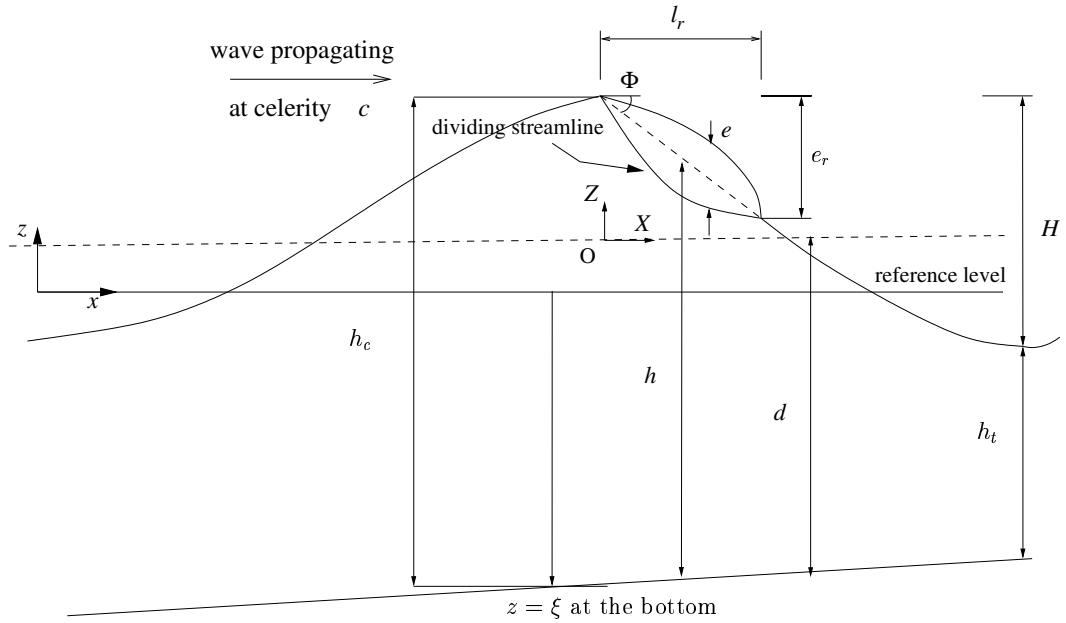

Figure 5.1: Definition sketch for a breaking wave and definition of related variables.

breaking termination. It is emphasized in reference [123] that the limiting values are not very sensitive to the type of breaking for the experimental cases investigated.

It is important to point out that no matter what breaking criterion is employed, the threshold value for breaking initiation will be strongly dependent on the particular set of Boussinesq-type equations used to describe wave motion. For instance, if a weakly nonlinear model is considered, the incipient breaker angle in Schäffer et al. [133] had to be fixed at $\Phi_i = 20°$, which is a much lower value than the one used in Kennedy et al. [85] fully nonlinear model.

5.2.2 Energetic considerations

The Boussinesq set of equations that we will use to describe wave motion is an extension of the so-called Serre equations to uneven bathymetries [136] incorporating in addition a Padé (2,2) dispersion correction [9]. This set of equations, which was introduced in Chapter 2, is actually fully nonlinear in the sense that it retains all terms up to $O(\sigma^2)$ by considering that $O(\epsilon) \sim 1$ (where $\sigma = kh_0$ and $\epsilon = a/h_0$ are respectively the dispersive and nonlinear parameters). By incorporating wave breaking terms, this particular Boussinesq set of equations can be written in the following generic form,

$$\frac{\partial h}{\partial t} + \frac{\partial}{\partial x}(hu) - D_h = 0, \tag{5.5}$$

$$\frac{\partial u}{\partial t} + \frac{1}{2}\frac{\partial u^2}{\partial x} + g\frac{\partial h}{\partial x} + \Gamma_d - \frac{1}{h}D_{hu} = 0, \tag{5.6}$$

where h is the water depth, u is the depth-averaged horizontal velocity, D_h and D_{hu} represent the extra breaking terms, Γ_d contains dispersive Boussinesq-type terms, and g is the gravitational acceleration. Here variables x and t denote space and time coordinates (see Figure 5.1). Multipying now equation (5.5) by $gh + \frac{1}{2}u^2$, equation (5.6) by hu and summing up leads to,

$$\frac{\partial}{\partial t}\left[\frac{1}{2}h\left(gh + u^2\right)\right] + \frac{\partial}{\partial x}\left[hu\left(gh + \frac{1}{2}u^2\right)\right] = -\frac{\Delta_b}{\rho} + O(\sigma^2), \tag{5.7}$$

where $-\Delta_b = \rho\left(gh + \frac{1}{2}u^2\right)D_h + \rho\, u\, D_{hu}$ is defined as the local rate of energy dissipation by breaking. In fact, the first term in the left-hand side of equation (5.7) corresponds to the time variation of local energy density per unit surface and mass, while the second term stands for the spatial gradient of energy flux in the x-direction. Thus equation (5.7) is nothing more than the energy equation associated to the generic Boussinesq set (5.5)-(5.6). It can be shown that if breaking terms are zero, energy is conserved even when dispersion is considered. A similar analysis was given in reference [88] on a linearized set of equations.

It is worth pointing out that when a Boussinesq set of equations is written in (h, u)-variables the roller-based breaking parameterization given in [133] may contain both extra terms, D_h and D_{hu} (see for instance reference [144]). On the other hand, when the eddy viscosity analogy [85, 184] is used only the breaking-induced momentum term, D_{hu} is included.

Even though the incorporation of a breaking term in the continuity equation may seem unphysical since the depth-averaging process produces (in the framework of potential theory) an exact expression, it was shown in Chapter 4 that additional convective acceleration effects should be included in wave-averaged equations in order to properly compute the undertow. It is then believed that at some stage, the irrotational assumption or the lack of a turbulence model imply a loss of information which may be responsible for the important underprediction of mean currents that was noticed in the previous chapter. Furtheremore, very recently Liu and Orfila [99] and Simarro et al. [143] have shown that, at first order, laminar bottom boundary layer effects can be represented by a convolution integral in the continuity equation of a Boussinesq model. Even though the influence of the free surface generated turbulent mixing layer on the underlying flow is far more complicated than the problem investigated in the aforementioned references, it can be reasonably expected that an additional term in the mass conservation equation may introduce first order mixing or shear layer effects.

Alternatively, incorporating a mass diffusivity term in the continuity equation may mathematically traduce the local mass transfer that takes place at the front face of the breaker. Most of the energy dissipated in breaking waves comes from potential energy loss triggered by free surface instabilities which can be easily observed in nature as the *avalanching* of a foamy mixture of air and water. Since Boussinesq-type equations are not able to represent multivariated free surfaces, this extra term is intended to mimic the physical phenomenon described above. A theoretical explanation of an analog situation which occurs in the framework of shallow water shock theory can be found in reference [21].

Finally, recall from Chapter 4 that nonlinear shallow water shock theory provides a very good estimate for wave-averaged energy dissipated from the mean flow by breaking. In the moving frame of reference (O, X, Z) of the propagating breaker (see Figure 5.1), the total dissipated energy can thus be evaluated as [17, 155],

$$\int_{shock} \frac{\Delta_b}{\rho}\, dX \simeq \frac{1}{4} g\, c\, \gamma^3\, d^2, \tag{5.8}$$

where $d = \frac{1}{2}(h_c + h_t)$ (h_c and h_t being respectively the associated trough and crest water depths), $\gamma = H/d$ (with $H = h_c - h_t$ being the wave height) and c is the local celerity of the breaking wave.

5.3 Eddy viscosity analogy for wave-breaking (Kennedy et al. [85] model)

A widely used breaking wave parameterization for Boussinesq-type equations was proposed by Kennedy et al. [85]. This model has been implemented in FUNWAVE [89], a fully nonlinear Boussinesq model developed at the University of Delaware. Breaking dissipation is introduced with help of an extra term in the momentum equation. Hence, when looking at the generic Boussinesq system expressed in equations (5.5)-(5.6), extra terms read [85],

$$D_h = 0, \tag{5.9}$$

$$D_{hu} = \frac{\partial}{\partial x}\left(\nu \frac{\partial hu}{\partial x}\right), \tag{5.10}$$

with the eddy viscosity coefficient given by,

$$\nu = B\, \delta_b^2\, h\, \partial_t \eta. \tag{5.11}$$

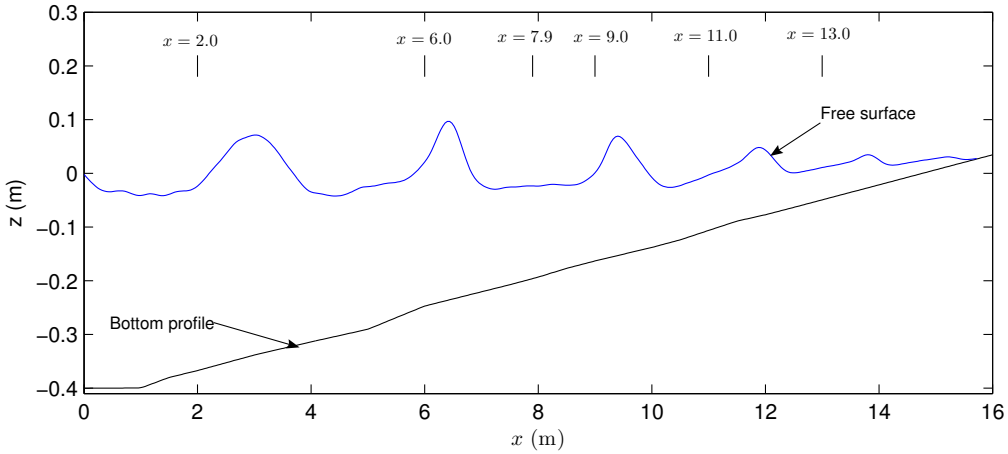

Figure 5.2: Definition sketch for Ting and Kirby's [162] spilling breaking experiment $L_0 = 3.74$ m, $\frac{a_0}{h_0} = 0.156$ and $kh_0 = 0.672$ (computed results using forced parameters in Kennedy et al. [85] breaking model). Vertical lines correspond to locations of wave gauges in meters.

Here, $\partial_t \eta$ is the time derivative of the free surface, δ_b is a mixing length coefficient, and B is a parameter conceived to activate breaking terms avoiding an impulsive behaviour. It is written as,

$$B = \begin{cases} 1, & \text{if} \quad \partial_t \eta > 2\,\partial_t \eta^* \\ \frac{\partial_t \eta}{\partial_t \eta^*} - 1, & \text{if} \quad \partial_t \eta^* < \partial_t \eta \leq 2\,\partial_t \eta^* \\ 0, & \text{if} \quad \partial_t \eta \leq \partial_t \eta^* \end{cases} \tag{5.12}$$

where the threshold value for breaking initiation, $\partial_t \eta^*$, is given by relation (5.2), and the transitional time scale was fixed at $T_b = 5\sqrt{|\xi|/g}$ in reference [85].

We have implemented this model in the finite volume scheme used to integrate the fully nonlinear and weakly dispersive Boussinesq set given in Chapter 2. The numerical implementation is straightforward since breaking terms are essentially conservative. We evaluate model performances with regular wave measurements available in references [162, 163] where two type of breaking were studied, namely a spilling and a plunging case. We will focus on reported results for spilling breakers, where cnoidal waves with incident height $H_0 = 0.127$ m and period $T = 2.0$ seconds propagate towards a planar beach of slope 1:35. The still water level was fixed at $h_0 = 0.4$ m in the horizontal part of the flume. Phase-averaged time series of free surface elevation are available at 21 locations, before and after breaking. This data set thus provides enough information to test Boussinesq wave propagation models and breaking parameterizations. A sketch of the spatial configuration of the bottom bathymetry and the location of several wave

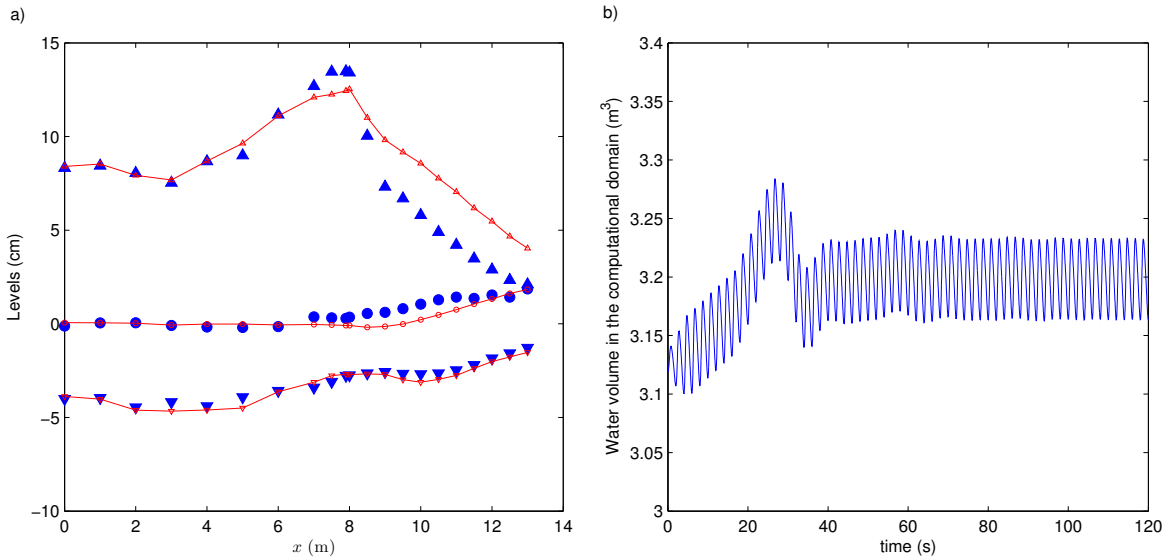

Figure 5.3: Numerical performance of Kennedy et al. [85] model implemented in the extended system of Serre equations for Ting and Kirby's [162] experiment. a) (▲) : measured crest level $\eta_c - \overline{\eta}$; (•) : measured wave-averaged free surface $\overline{\eta}$; (▼) : measured trough level $\eta_t - \overline{\eta}$. Computed properties are plotted in plain lines. b) Temporal evolution of the water volume contained in the numerical domain.

gauges is presented in Figure 5.2. Further details on the experimental set-up can be found in papers from Ting and Kirby [162, 163].

In this example, the default value for breaking initiation, $\eta_t^I = 0.65\sqrt{g|\xi|}$ had to be lowered to $\eta_t^I = 0.52\sqrt{g|\xi|}$ in order to correctly predict the breaking point. In a recent contribution, Lynett [106] was also forced to change some default values when implementing Kennedy et al. [85] parameterization in a two layer fully nonlinear Boussinesq model. Indeed he fixed the initiation threshold at $\eta_t^I = 0.5\sqrt{gh}$ where, instead of writing the model in terms of the still water depth, he used the total water depth, h. This value is in close agreement with the one we obtained with help of numerical experiments. Moreover, Lynett [106] also reported a comparative analysis for several different breaking criterions and found that a value $|\frac{\partial \eta}{\partial x}| = 0.6 \pm 0.02$ for the front slope provides good agreement for the location of the breaking point. This value corresponds to $\Phi_b = 31^\circ \pm 1.1^\circ$ and is close to the critical slope of $\Phi_b = 30^\circ$ we used in reference [38] (reprinted in Appendix E). It is then believed that Kennedy et al. [85] had to fix the breaking initiation criteria at such a high value because Wei et al.'s [178] Boussinesq set produced a systematic overshoaling due to an incorrect amplification of higher bounded harmonics. This problem is also present in a one layer Boussinesq model as discussed by Lynett [106]. Regarding nonlinear properties, the

extended system of Serre equations presented in Chapter 2 is thus presumably closer to the two layer model proposed in reference [105] than to the fully nonlinear model implemented in FUNWAVE. We will come back to this question later in this chapter.

In Figure 5.3-a) we show a comparison between computed and measured wave-averaged free surface location, crest and trough levels using default parameter values for Kennedy et al. [85] model except for the value for breaking initiation as discussed before. Additionally, in Figure 5.3-b) the temporal evolution of the water volume contained in the computational domain is depicted. Computations are performed using as left boundary condition, measured wave-averaged time series of free surface elevation at the first wave gauge located at a distance of 14.8 m from the still shoreline. At right boundary, a moving shoreline condition is applied. It can be seen that a steady state equilibrium is reached after almost 60 seconds, i.e. 30 wave periods. This also confirms that the open sea boundary condition is performing correctly by evacuating reflected waves since no longer wave oscillation or sloshing occurs in the numerical wave tank. On the other hand, it is important to point out from Figure 5.3-a) that Ting and Kirby's [162] set-up starts very early, indeed well before the location of the breaking point. Of course, this result cannot be reproduced by the model and might be due to some local disturbance influencing the transition zone in the physical wave flume or to experimental errors.

The performance of the Boussinesq model in the shoaling region is very good, and only a small amplitude underestimation is noticed near the breaking point at $x \simeq 8.0$ m. The latter is in agreement with results previously reported in Chapter 3 where nonlinear performances were tested against experimental solitary waves shoaling on a beach. Indeed, the relative error in wave height prediction at the breaking point is less than 9 % in the present computation (see also Figure 5.4). It is worth pointing out that, whereas Wei et al. [178] Boussinesq model overshoals, the extended Serre model slightly undershoals in the vicinity of the breaking point.

Computed and measured time series of free surface elevations are plotted in Figure 5.4 at two locations before breaking and four locations in the surf zone (see Figure 5.2 for gauge placements). It is important to point out that the available temporal free surface elevation corresponds to phase-averaged values over several wave periods and unfortunately those records are not synchronized. This means that in the present application we are only able to investigate model performance in terms of predicted wave profiles but not in terms of phase speed accuracy.

Figure 5.4 shows an excellent agreement between computed and measured time series in the shoaling region but important discrepancies arise inside the surf zone. Kennedy et al.'s [85] breaking wave parameterization over estimates wave height in the

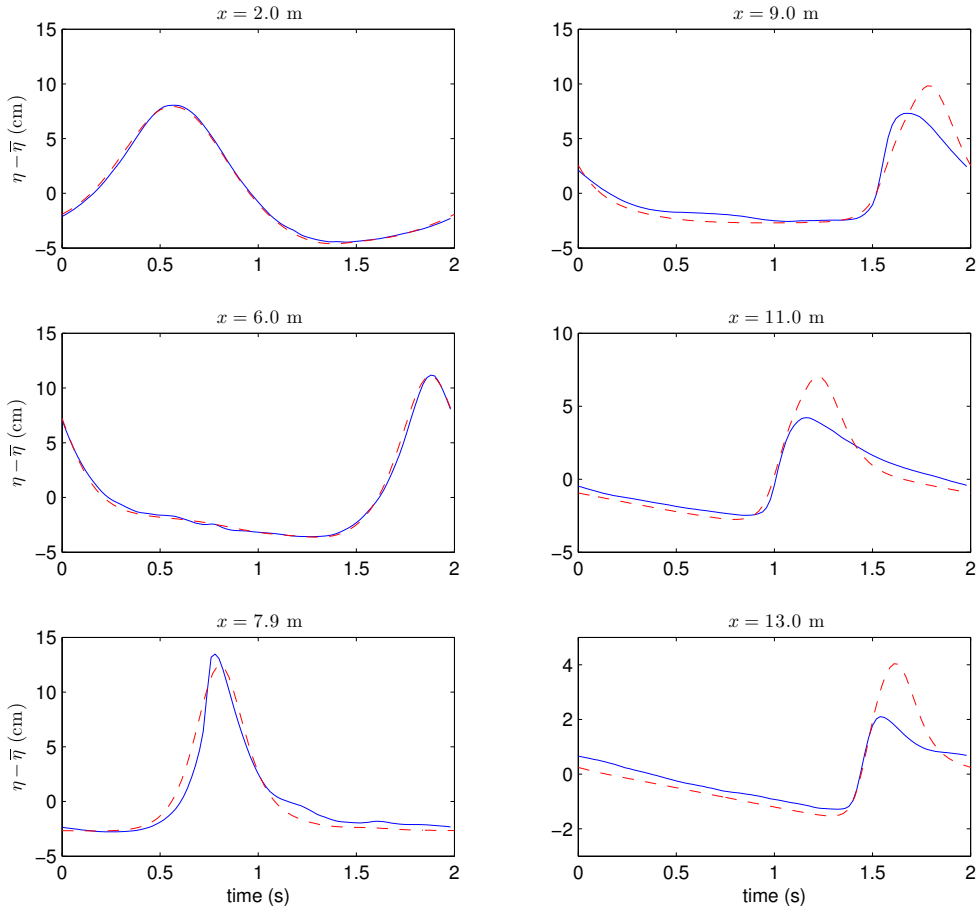

Figure 5.4: Computed and measured phase-averaged time series of free surface elevation for Ting and Kirby's [162] experiment at several wave gauges using Kennedy et al. [85] parameterization. $(-)$: measured ; $(--)$ computed.

inner surf zone as previously noted by those authors (see also Figure 5.3). Free surface elevation time series reported in Figure 5.4 show in addition that whereas wave height is heavily over predicted in the inner surf zone, left-right wave asymmetry is reasonably reproduced and wave's front slope is preserved except perhaps in the transition zone.

For this particular experiment, free surface elevation time series are available at 21 locations, it is thus possible to objectively compute an error index for predicted wave profiles over the whole domain. Following Kennedy et al. [85] we introduce left-right asymmetry as,

$$As = \frac{\langle \mathcal{H}^3(\eta - \overline{\eta}) \rangle}{\langle (\eta - \overline{\eta})^2 \rangle^{3/2}}, \tag{5.13}$$

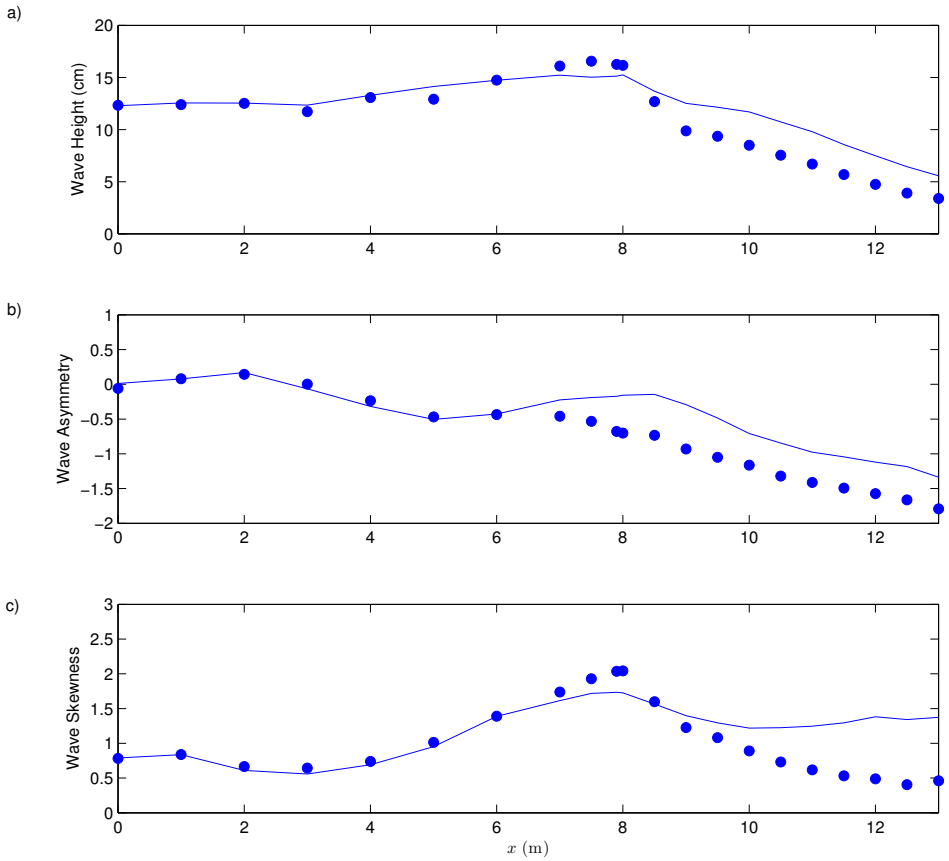

Figure 5.5: Comparison between measured (•) and computed (−) wave properties for Ting and Kirby's [162] experiment using Kennedy et al. [85] parameterization. a) Wave height, b) Wave asymmetry, and c) Wave skewness.

where $\langle\cdot\rangle$ is the mean operator and $\mathcal{H}$ is the Hilbert transform. Similarly, crest-trough asymmetry or wave skewness is defined as,

$$Sk = \frac{\langle(\eta - \overline{\eta})^3\rangle}{\langle(\eta - \overline{\eta})^2\rangle^{3/2}}. \tag{5.14}$$

Computed and measured wave properties, as estimated from free surface time series, are reported in Figure 5.5. It is noticed that asymmetry decreases steadily from the shoaling region to the surf zone where a characteristic saw-tooth wave profile is obtained. In the surf zone, the numerical model gives an adequate asymmetry gradient but absolute values appear to be vertically shifted. This difference may be mostly attributed to the overestimation of wave height since the front slope of computed waves is reasonably reproduced (see Figure 5.4).

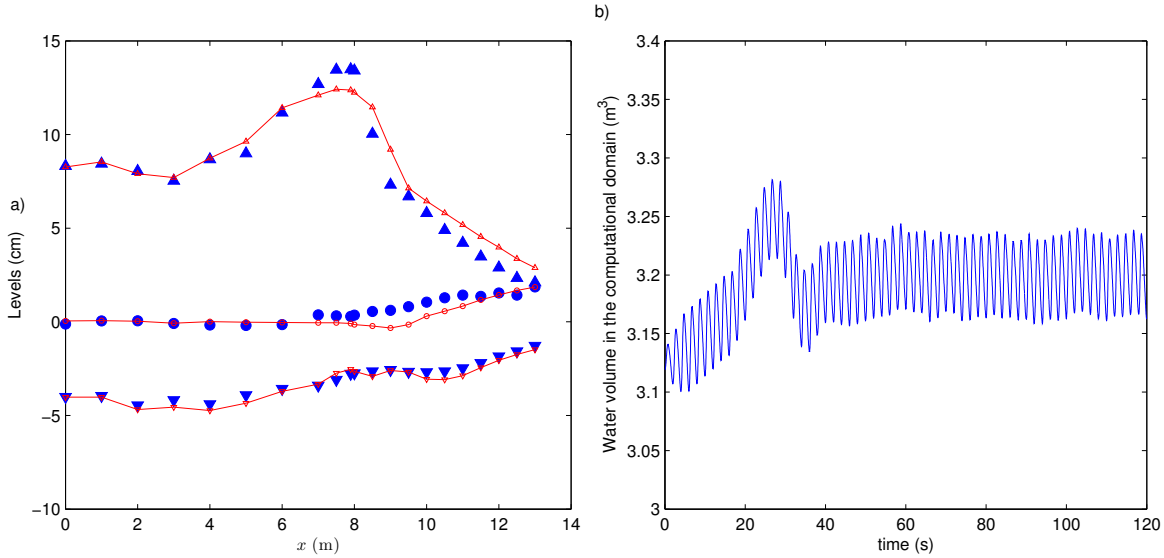

Figure 5.6: Numerical performance of Kennedy et al. [85] model with modified parameters for Ting and Kirby's [162] experiment. Same caption as Figure 5.2.

In Figure 5.5, computed skewness is also compared against the measured one. It is clear from this plot that predicted wave skewness diverges from the one estimated experimentally in the surf zone. Indeed, this property is closely related to wave height and observed errors can be explained by the important overestimation of wave height produced by the model. In this example, the RMS errors in wave height, asymmetry and skewness are respectively 17 %, 40 % and 38 %. The average numerical error can be estimated as the arithmetic mean of the these three quantities, which gives 32 % in this case.

Very recently, Lynett [106] was able to improve wave height estimations using Kennedy et al. [85] breaking model by changing the default values for some parameters. In particular, he fixed the mixing length coefficient at $\delta_b = 10$ instead of $\delta_b = 1.2$ as recommended in the original formulation. In our case, it was not possible to reach such a high value for that parameter because important spurious oscillations were triggered behind breaking waves causing numerical instability. Nevertheless, we could perform a new computation using $\delta_b = 5.5$ and results are reported in Figures 5.6, 5.7 and 5.8. In Figure 5.6 it is seen that the overall agreement between computed and measured wave height is improved, having now an RMS error of roughly 9 %. However, forcing the breaking model with this high δ_b value results in a total loss of wave left-right asymmetry as shown in wave profiles presented in Figure 5.7. This result suggests that the equivalent force that we need to apply on the front face of the breaker in order to introduce the correct energy dissipation rate might be unrealistically strong.

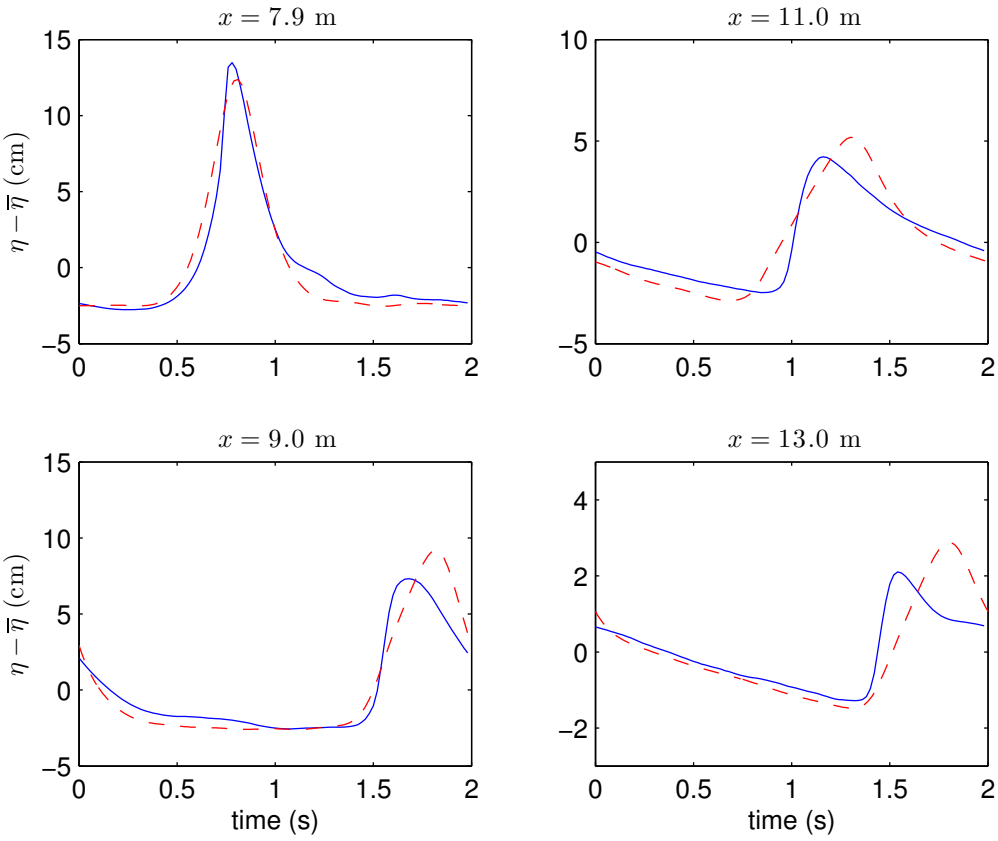

Figure 5.7: Computed and measured phase-averaged time series of free surface elevation for Ting and Kirby's [162] experiment at several wave gauges using modified Kennedy et al. [85] parameterization. $(-)$: measured ; $(--)$ computed.

Even though, Lynett [106] did not show any comparison for free surface elevation time series, there is some evidence indicating that he could not reach the typical saw-tooth wave profile in the inner surf zone and horizontal asymmetry was equally lost in his case. The spatial free surface snapshot that he did show clearly indicates that wave shape in the inner surf zone is not of asymmetric type. Indeed his plot is very similar to the one we present in Figure 5.2, which was obtained using modified model parameters. Obviously, this is an important drawback of Kennedy et al. [85] breaking parameterization since Boussinesq-type models are conceived to provide time domain information and the extra associated CPU effort will be only justified if additional information is made available when compared to wave-averaged models. Moreover, wave shape properties, and in particular horizontal asymmetry, play an important role in nearshore sediment transport processes as demonstrated by Drake and Calantoni [52] and Hsu and Hanes [79]. A comparison between numerical and experimental time

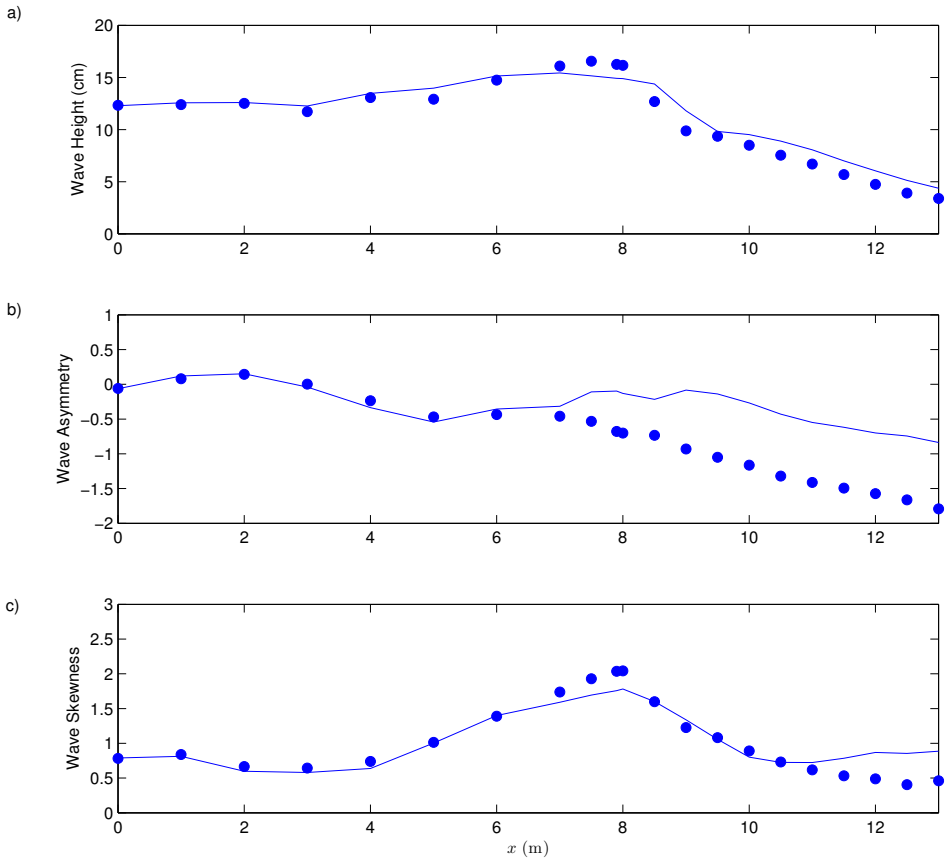

Figure 5.8: Comparison between measured (•) and computed (−) wave properties for Ting and Kirby's [162] experiment using modified Kennedy et al. [85] parameterization. a) Wave height, b) Wave asymmetry, and c) Wave skewness.

domain wave properties is presented in Figure 5.8 where it can be seen that predicted wave height and skewness could be improved by changing the value for the mixing length coefficient but that asymmetry is much worser than in the previous computation. Estimated RMS errors for wave asymmetry and skewness in this case are respectively 64 % and 17 % while the average error for H, As and Sk is found to be 30 %, hence not very different from the one obtained using default parameter values.

The implementation of Kennedy et al. [85] breaking parameterization in our finite volume Boussinesq model has confirmed that wave height is heavily overestimated in the inner surf zone when using default parameter values. However, forcing model parameters in order to fit computed wave heights with measured ones results in a total loss of left-right wave asymmetry. Unfortunately, the latter would make Boussinesq

phase-resolving approaches useless for surf zone applications. It is worth emphasizing that asymmetry is a key property for a successful sediment transport prediction, specially for breaking and nearly breaking waves. Indeed, it appears that onshore sandbar migration, which usually occurs under mild wave conditions, might be adequately predicted only if fluid acceleration effects produced by wave asymmetry are taken into account in sediment transport modules [78, 151].

From these particular numerical examples, it is then concluded that it is not possible for Kennedy et al. [85] breaking model to simultaneously provide reliable predictions on wave height and skewness, and on the other hand, horizontal asymmetry. Therefore, an alternative way to introduce breaking-induced effects is required if phase-resolving sediment transport modules are to be coupled with Boussinesq-type equations in the framework of beach morphodynamics.

5.4 A new approach for time-domain breaking

In the present section we develop a new wave-breaking model for Boussinesq-type equations using wave-averaged information previously investigated in Chapter 4. In particular, shallow water shock theory and the roller concept will provide the theoretical background for developing a novel breaking approach.

5.4.1 Functional form of breaking terms and scaling arguments

Some scaling information for wave-breaking terms can be obtained if we use the long wave approximation and the assumption of a gently slopping beach. These simplifications will allow us to use some important results presented in the previous chapter valid for quasi-steady breakers or bores.

Invoking shallow water shock theory a useful relation was found for the overall energy dissipated accross the shock in surf zone waves. This expression was written in the moving frame of reference (O, X, Z) of the propagating bore of Figure 5.1 in equation (5.8). Whereas in shock theory, the dissipation is concentrated on the discontinuity (i.e. over an infinitesimal horizontal distance), for real surf zone waves dissipation takes place over a finite distance, l_r. Hence, numerical solutions obtained using shock capturing numerical solvers have an important dependence on the spatial grid resolution, Δx, because the discrete length of the discontinuity is governed by that parameter. Consequently, in the limit $\Delta x \to 0$, l_r must tend to zero as well. Nevertheless, real breakers never show vertical fronts so Δx must be tuned in order to correctly reproduce wave asymmetry.

Even though some important and useful results concerning the application of shock capturing methods to breaking waves in the inner surf zone have been reported (e.g. [91, 174]), successful application of these methods implicitly requires some information on the finite length l_r. Owing to this unpractical dependence on the grid resolution, we prefer to follow a different approach which incorporates an explicit estimation for this horizontal distance.

Combining the energy equation (5.7) with the theoretical result given by expression (5.8) we obtain, in the moving frame of reference, the following integral scaling relation for breaking terms,

$$-\int_0^{l_r}\left[(gh+\frac{1}{2}(U+c)^2)D_h+(U+c)\,D_{hu}\right]\,dX\sim\frac{1}{4}g\,c\,\gamma^3\,d^2, \tag{5.15}$$

where l_r represents now the horizontal distance over which extra terms are applied and $U=u-c$ is the depth-averaged velocity in the moving frame of reference. In the rest of this section we will assume that breaking terms are of diffusive type following the model proposed by Zelt [184] but incorporating an extra term in the continuity equation. As discussed before, this extra contribution can be related to the underlying flow cross-sectional area reduction associated to the presence of a breaking roller, or alternatively to a local mass transfer that may take place at the front face of the breaker.

Breaking terms are thus written in the frame of reference of the propagating wave as,

$$D_h=\frac{d}{dX}\left(\nu_h\frac{dh}{dX}\right), \tag{5.16}$$

$$D_{hu}=\frac{d}{dX}\left(\nu_{hu}\frac{d}{dX}\left[h(U+c)\right]\right), \tag{5.17}$$

where ν_h and ν_{hu} are diffusivity functions that need to be defined. Therefore, in order to integrate equation (5.15) some additional information must be provided. We specifically need an estimate for l_r and the local functional forms for ν_h and ν_{hu}.

Since energy dissipation can be related to shearing stresses acting on the lower edge of the roller region as shown in Chapter 4, we take l_r to be the roller length. On the other hand, experimental results on hydraulic jumps with Froude numbers close to those encountered in inner surf zone waves reported by Svendsen et al. [157] indicate that a similar spatial distribution for the local roller thickness and shear stresses at the lower edge of the roller presumably exist. We will assume then that the spatial distribution of mass and momentum diffusivity coefficients should follow the same kind

of relation which is expressed as [172],

$$\nu_h(X) = -K_h \exp\left(\frac{X}{l_r} - 1\right)\left[\left(\frac{X}{l_r} - 1\right) + \left(\frac{X}{l_r} - 1\right)^2\right], \quad \text{for} \quad 0 \le X \le l_r, \quad (5.18)$$

$$\nu_{hu}(X) = -K_{hu} \exp\left(\frac{X}{l_r} - 1\right)\left[\left(\frac{X}{l_r} - 1\right) + \left(\frac{X}{l_r} - 1\right)^2\right], \quad \text{for} \quad 0 \le X \le l_r, \quad (5.19)$$

where K_h and K_{hu} are slowly varying functions that will be scaled using the integral form of energy equation (5.15). Previous relations provide a local spatial distribution for diffusivity coefficients and it is important to note that this functional form ensures overall mass and momentum conservation for breaking terms because $\nu_h = \nu_{hu} = 0$ at outer bounds of the region where extra terms are applied.

Similarly, roller length can be estimated from Cointe and Tulin's theory of steady breakers [40] but with the associated empirical parameter, β, adjusted using shallow water experiments in Chapter 4. It is useful to recast expression (4.30) in the following form,

$$\frac{e_r}{d} = \frac{l_r \, \tan\Phi}{d} = \frac{\beta^2}{2(1-\beta^2)}(1-\gamma) \simeq 0.865\,(1-\gamma), \quad (5.20)$$

where the new value $\beta = 0.796$ has been used. Finally, in order to be able to integrate the left hand side of equation (5.15), we use the long wave approximation which states that,

$$(U + c)\, h = c\,(h - d), \quad (5.21)$$

and assume a simple linear form for the average wave's front position where breaking terms are applied, i.e. (see Figure 5.1),

$$h = \left(1 + \gamma/2 - \frac{X}{d}\,\tan\Phi\right) d, \quad \text{for} \quad 0 \le X \le l_r. \quad (5.22)$$

Hence, the final scaling provided by energy equation (5.15) introduces two parameters which define local characteristics of surf zone waves, namely the breaker index, γ, and the mean breaker slope, Φ.

Exact integration of equation (5.15) using relations (5.16)-(5.22) is possible but it results in a very long expression. Since our goal here is to establish scaling laws for coefficients K_h and K_{hu}, numerical integration is used to find the order of magnitude of the different terms which are weakly dependent on γ. In consequence, we obtain,

$$(\alpha_h K_h + \alpha_{hu} K_{hu})\, c^2 \left(\frac{e_r}{d}\right) \tan\Phi \sim \frac{1}{4} g\, c\, \gamma^3\, d^2, \quad (5.23)$$

where α_h and α_{hu} are constants of the order $1/10$ in the inner surf zone where $\gamma \simeq 0.5$ (see Table 5.1).

γ	0.5	0.6	0.7	0.8
α_h	0.098	0.109	0.115	0.118
α_{hu}	0.111	0.089	0.074	0.062

Table 5.1: Numerical evaluation of coefficients α_h and α_{hu} for typical surf zone values of the breaker index γ.

At this stage, it is worth pointing out that if $K_h = 0$ the breaking model will be close to the one developed by Zelt [184] and Kennedy et al. [85] but with several differences concerning the magnitude and the spatial location of the so-called eddy viscosity function. In the previous section we confirmed that this breaking model overestimates wave heights in the inner surf zone (see also [85]) and demonstrated that forcing default parameter values in order to improve this behaviour was very disappointing since horizontal wave asymmetry was completely lost. Moreover, serious stability problems arose when increasing the numerical value of the mixing length coefficient. Those limitations are probably due to the location/length over which the breaking term is applied and constitute the main motivation for developing an alternative approach. Indeed, the important result concerning the application of Cointe and Tulin's [40] ideas to shallow water breakers presented in Chapter 4 introduces an additional degree of freedom in our breaking formulation since the extent and location where extra terms are applied may be explicitly controlled. Similarly, the extra contribution in continuity equation may have a positive impact in terms of numerical stability and mean return current prediction.

In order to obtain information on K_h and K_{hu} from equation (5.23), we need an additional equation/assumption to close the system. Recall from Chapter 4 that an extra roller contribution was required in the continuity equation in order to adequately predict mean return current. Therefore, it is reasonably to postulate that an analogous term would be needed in Boussinesq equations as well since nonlinear shallow water theories do not provide the correct mass flux above the trough level. Therefore, in the present context we may write the continuity equation for a quasi-steady breaker propagating over a flat bottom as,

$$\frac{d}{dX}\left[U(h-e)\right] = 0, \tag{5.24}$$

where e is the vertical distance related to the local thickness of the roller region whose lower bound corresponds to an imaginary *dividing streamline* (see Figure 5.1). By direct comparison of the latter and the continuity equation (5.5) written in the moving frame of reference as well, the mass diffusivity coefficient in breaking term D_h can be

linked to the roller thickness as follows,

$$\nu_h = -\left(\frac{dh}{dX}\right)^{-1}\left(\frac{e}{h}\right)\, c\, d \simeq \left(\frac{e}{h}\right)\frac{c\, d}{\tan\Phi}. \tag{5.25}$$

The mass diffusivity term is conceived to produce a contraction in the free stream transverse section where the underlying mean flow evolves. Consequently, a local convective flow acceleration should take place below the breaker in agreement with macroscopical effects of turbulent mixing layers discussed in Chapter 4.

The local roller thickness was estimated in the previous chapter using the same functional form than diffusivity coefficients (5.18)-(5.19). Thus, it is straightforward to show using relations (4.20) and (5.25) that,

$$K_h = \delta_h\, c\, d \quad \text{with} \quad \delta_h \sim \left(\frac{A}{d^2}\right)\left(\frac{e_r}{d}\right)^{-1}. \tag{5.26}$$

Using now the roller model as given in Chapter 4 and discarding second order terms, the scaling for the roller cross-sectional area reads,

$$\frac{A}{d^2} \sim \frac{\gamma^3}{4\tan\Phi}. \tag{5.27}$$

Therefore, invoking in addition relations (5.20) and (5.22) the order of magnitude for the mass diffusivity coefficient (5.26) appears to be,

$$\delta_h \sim \frac{\gamma^3}{(1-\gamma)}\tan^{-1}\Phi. \tag{5.28}$$

Furthermore, using the energy equation (5.23) assuming that $\alpha_h = \alpha_{hu} \sim 1/10$, as it is roughly the case in the inner surf zone (see Table 5.1), and taking $c \simeq \sqrt{gd}$, it is possible to obtain the following estimate for the order of K_{hu},

$$K_{hu} = \delta_{hu}\, c\, d, \quad \text{with} \quad \delta_{hu} \sim \frac{\gamma^3}{(1-\gamma)}\tan^{-1}\Phi, \tag{5.29}$$

showing that both breaking terms are of the same order. Numerical coefficients which follows from the integral equation (5.23) indicate that the momentum-induced contribution should be bigger than the mass-induced one. Nevertheless, since we do not have a precise knowledge of their relative weight we prefer to introduce a new parameter $\kappa = \delta_h/\delta_{hu}$. Consequently, using again the energy equation (5.23) with $\alpha_h = \alpha_{hu} \sim 1/10$ and relation (5.20) yields,

$$K_{hu} = \delta_{hu}\, c\, d \quad \text{with} \quad \delta_{hu} \sim \frac{\gamma^3}{(1-\gamma)}(1+\kappa)^{-1}\tan^{-1}\Phi. \tag{5.30}$$

The following relations will be used in numerical applications performed next to compute each diffusivity function,

$$K_{hu} = \delta_{hu}\, c\, d, \quad \text{with} \quad \delta_{hu} = \alpha_b \frac{\gamma^3}{(1-\gamma)} (1+\kappa)^{-1} \tan^{-1}\Phi, \tag{5.31}$$

$$K_h = \kappa\, \delta_{hu}\, c\, d, \tag{5.32}$$

where α_b is a parameter of order one, and $0 \leq \kappa \leq 1.0$. Recall that the local spatial distribution of diffusivity functions is computed using (5.18)-(5.19) where the horizontal distance $l_r = e_r \tan^{-1}\Phi$ will be estimated using relation (5.20).

Before going any further, it is worth noting that the scaling analysis we have performed highlights the physical meaning of the different model parameters. This is not a trivial task owing to the intrinsic difficulty of breaking phenomena and is why very often *ad-hoc* breaking formulations cannot be easily related to physical quantities. The roller analogy used by Schäffer et al. [133] is an exception to this rule since model parameters do have a straightforward interpretation. On the contrary, the mixing length model developed by Kennedy et al. [85] does not stem from clear physical backgrounds and consequently no scaling information is available for parameter values. Our breaking model lies somewhere in between the roller concept and the eddy viscosity analogy and some scaling knowledge could be obtained invoking theoretical and empirical findings on quasi-steady breakers. However, it is important to emphasize that all this information would be valid, at best, in the inner surf zone where breaking waves may be thought to be in quasi-equilibrium.

5.4.2 Parameter calibration

The new formulation for wave breaking depends on two main parameters related to macroscopic geometrical properties of surf zone waves, namely the breaker index γ and the mean breaker slope Φ. Nevertheless, we do not have a clear knowledge of how these quantities may evolve inside the surf zone. In addition neither the relative weight of continuity and momentum breaking terms, nor the numerical value for the order-one parameter α_b can be accurately determined beforehand. Indeed, all the available scaling information was derived assuming a quasi-steady equilibrium and consequently, if valid, it may be only applicable in the inner surf zone. Owing to those multiple limitations, the calibration process must be tackled with pragmatism in order to keep the model as simple as possible.

In the following subsections we introduce the heuristical procedure that will allow us to determine optimal values for model parameters. Similarly, some aspects related

to its practical implementation will be highlighted. There are two main parameters to fix, the breaker slope Φ and the breaker index γ, but two additional coefficients (α_b and κ) must be calibrated using experimental data. Our main goal is to improve the time domain representation of free surface elevations in the surf zone, in particular wave height, asymmetry and skewness estimations. Again, we will use Ting and Kirby [162] spilling breaking experiment to obtain parameter values which minimize the average error for H, As, and Sk. However, mean water level measurements in Ting and Kirby's experiment appear to be inaccurate since it was noticed in Figure 5.3 that set-up begins well before breaking. Unfortunately, numerical experiments have shown that model prediction of set-up is sensitive to $\kappa = \delta_h/\delta_{hu}$, i.e. the relative weight of both breaking terms. Hence, an additional experimental data set is considered in order to investigate the influence of this parameter. A similar spilling breaking test reported by Hansen and Svendsen [77] is chosen for this purpose.

The heuristical calibration process is carried out using a grid size $\Delta x = L_0/100$ and a Courant number $C_r = \sqrt{gh_0}\,\Delta t/\Delta x = 1.0$, where h_0 is the still water depth in the horizontal part of flumes where experiments are conducted, L_0 is the wave-length of incoming waves, Δx and Δt are respectively spatial and temporal grid resolutions. In addition, the correction dispersion parameter is fixed at $\alpha = 1/15$ thus producing a Padé (2,2) approximation for the Stokes dispersion relation.

Adopted breaking criteria

Concerning the breaking criteria, the different approaches enumerated in Section 5.2.1 were implemented in the finite volume model and their breaking point predictions analyzed. Details on this comparative study are not reported here but general conclusions were similar to those given by Lynett [106] since a criterion based on the mean wave's front slope appeared to be the least sensitive when considering spilling breaking. Hence, our numerical implementation of the breaking model utilizes this criteria to decide when extra terms should be activated. In the moving frame of reference associated to each individual wave, threshold breaking initiation and cessation reads,

$$\text{Breaking starts if} \quad \left|\frac{d\eta}{dX}\right| \geq \tan\Phi_b,$$

$$\text{Breaking stops if} \quad \left|\frac{d\eta}{dX}\right| \leq \tan\Phi_f,$$

where Φ_b is the limiting breaker angle, and Φ_f is the saturated value for this parameter. The front face slope is estimated from computed spatial derivatives of water depth and bottom bathymetry, where the maximum local value of $|\frac{d\eta}{dX}|$ over the spatial extent of

the front face is considered as reference for each breaker.

Obviously, since the breaking parameterization is applied on a wave-by-wave basis, a numerical algorithm must be developed in order to follow each wave crest. Furthermore, breaking terms are applied on the front face over an extent l_r starting at the wave crest (see Figure 5.1). Diffusivity coefficients are spatially reconstructed using local functional forms (5.18)-(5.19). Similarly, a transition zone may be included in the model and consequently the breaking inception time should be stored. Analogous approaches have been used in Schäffer et al. [133] and Kennedy et al. [85] breaking models.

Relative weight of breaking terms

Hansen and Svendsen's Test Case No. 051041 is used to investigate sensitivity of predicted set-up when changing the numerical value of κ. We are not interested yet on phase-resolved features so we focus on wave-averaged properties. Wave conditions for this test case are similar to Ting and Kirby's spilling breaking experiment. It consisted on second order Stokes waves with $H_0 \simeq 0.036$ m and $T = 2.0$ s generated off-shore by a piston wave-maker where the still water depth was fixed at $h_0 = 0.36$ m. Regular waves shoaled and breaked as they propagated up a planar beach of slope 1:34.26. We perform preliminary computations for this case focusing on the influence that numerical values of $\kappa = \delta_h/\delta_{hu}$ may have on the numerical estimation of integral wave properties. Therefore, remaining parameters are chosen in order to fit at best the breaking point location and wave height predictions in the surf zone.

Numerical computations are conducted using three different diffusivity ratios, namely $\kappa = 0.0$, $\kappa = 0.25$ and $\kappa = 1.0$, where remaining parameters are *frozen* at fixed values. Comparisons between numerical predictions of wave heights, set-up levels and wave-averaged velocities are presented in Figure 5.9. It is seen that whereas changing the value of κ has almost no influence in set-up level in the transition zone just after breaking, it is not so in the inner surf zone. Indeed, increasing the relative weight of the mass diffusivity breaking term lowers the mean water level in the inner surf zone. It is important to emphasize that wave height estimates are not significantly affected by changes in κ and that mass loss in the computational domain was negligible in all numerical tests. This means that the breaking term in the continuity equation is not introducing nor removing mass. Noticeable variations in set-up level may be thus explained by the relatively low contribution of the momentum-induced breaking term since surf zone mean water level is primarly induced by radiation stresses associated to wave-driven effects (see for instance Mei [115] pp. 453-463).

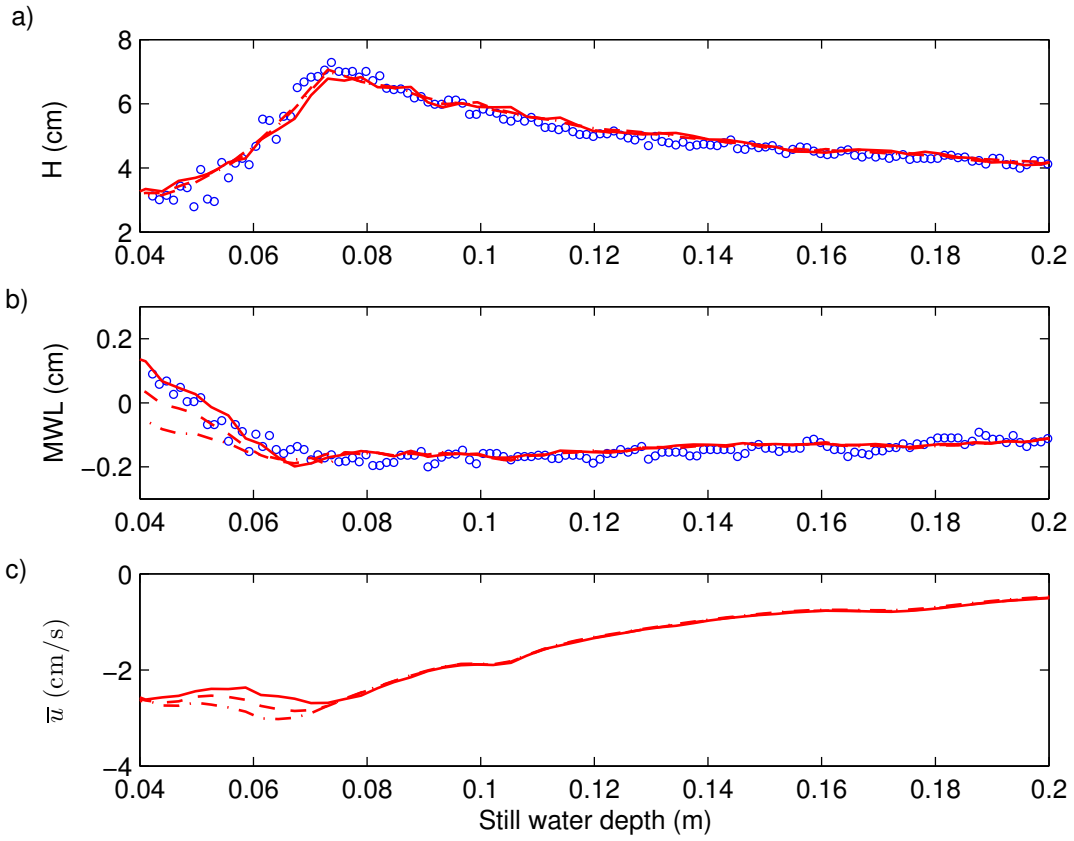

Figure 5.9: Sensibility of model results for Hansen and Svendsen [77] Test Case No. 051041 when changing the ratio $\kappa = K_h/K_{hu}$. ($\circ$) Experimental data and numerical computation using : ($-$) $\kappa = 0.0$, ($--$) $\kappa = 0.25$, and ($- \cdot -$) $\kappa = 1.0$. a) Wave height, b) Set-up level, c) Wave-average of depth averaged velocity.

In Figure 5.9-c) time averages of depth-averaged velocity u are plotted. In agreement with theoretical arguments developed before, the mass diffusivity term somehow increases the magnitude of the velocity under the breaker and shifts the location of its maximum shorewards. The effect on mean velocities is similar to the one produced by the roller in wave-averaged models studied in Chapter 4. However, in the present example computed velocities are not strictly equivalent to a mean return current since we have not performed an integration of Boussinesq velocity profiles below the trough level. Nevertheless, it is believed that some beneficial roller contributions are implicitly included in our breaking parameterization but this should be investigated in more detail in the future.

From this particular test we conclude that the additional breaking term incorporated in the continuity equation may be useful to improve undertow computations in

Boussinesq-type equations. Nevertheless, this term must be treated with caution because it has a non-negligible influence on set-up estimates in the inner surf zone. In addition it is worth pointing out that whereas increasing the ratio κ has an important effect on velocity estimates in the transition zone, it is not the case in the inner surf zone. Hence, it seems that a good compromise between computed set-up and mean currents would require the use of variable values for κ, being higher near the breaking point and tending to zero in the inner surf zone. Results reported in Figure 5.9 also indicate that the numerical value of κ should never exceed 0.25 in the inner surf zone.

Parameter calibration using Ting and Kirby's [162] laboratory surf zone

Our breaking-wave model requires the prescription of Φ, γ, κ and the order-one parameter α_b. The horizontal extent over which extra terms are applied is related to the wave's front slope and to the breaker index since $l_r/d = 0.865(1-\gamma)\tan^{-1}\Phi$. In addition, wave celerity will be computed as $c = \sqrt{gd}$ using the arithmetic mean between crest and trough local depths as a definition for the mean water depth, d (see Figure 5.1).

An important property of the new breaking formulation concerns the possibility to explicitly define the length of the segment where diffusivity terms producing a local mass transfer and a momentum deficit are applied. The latter can be achieved using physical arguments developed by Cointe and Tulin [40] in the framework of deep water breaking but verified for shallow water breakers in Chapter 4. Numerical experiments have shown that the horizontal asymmetry of predicted surf zone waves is strongly dependent on l_r. It was noticed that a combination of too large values for this distance and high magnitudes of eddy viscosity coefficients may produce important inaccuracies in left-right asymmetry estimates as it was the case for Kennedy et al. [85] breaking parameterization (see Figure 5.7). Conversely, l_r has a lower bound given by the grid size resolution Δx and the minimum possible value for this distance is taken to be $l_r = 2\,\Delta x$ in the model. Therefore, a compromise between a good representation of wave asymmetry and practical aspects of numerical computations should be determined.

On the other hand, the relative weight of mass and momentum diffusivity terms must be chosen carefully since it appears that set-up level is heavily lowered for κ-values greater than 0.25. However, the extra term added to the continuity equation does improve the numerical stability of the scheme and presumably, mean current estimates as well. Moreover, focusing all dissipation on a unique force-like term in the momentum equation does not allow for a correct simultaneous description of wave heights and horizontal wave asymmetries in surf zone waves as it was demonstrated

for the eddy viscosity model of Kennedy et al. [85]. Therefore, incorporating a mass diffusivity term intended to reproduce some mixing layer effects appears to be justified, not only on a physical basis but also from a strictly numerical point of view.

Calibration of the different model parameters is not an easy task owing to the great number of degrees of freedom and possible combinations for physical ranges of parameter values. Empirical evidence indicates that the breaker index should be bounded by $0.4 \leq \gamma \leq 0.8$ over most of the surf zone according to reference [3] but may reach higher values in the swash zone (e.g. [129, 138]). In the particular case of Ting and Kirby [162] spilling breaking experiment, $\gamma = H/d$ ranged from 0.8 near the breaking point, down to a rather constant value of 0.5 in the inner surf zone. Similarly, the mean front slope of the breaker, Φ, should evolve from a high limiting value near the breaking point to a lower one as the breaker reach a quasi-equilibrium state in the inner surf zone [72, 133]. Unfortunately, there is no clear knowledge of what kind of temporal evolution function those quantities should follow. Therefore, in order to keep the breaking model at a reasonable level of complexity we will assume constant values for coefficients δ_{hu} and parameter κ over the entire surf zone, allowing the ratio l_r/d to vary. We adopt for this purpose the same functional form proposed by Schäffer et al. [133] which reads in this particular case as (with the index notation introduced in equation (5.1)),

$$\frac{l_r}{d} = \left(\frac{l_r}{d}\right)_t + \left[\left(\frac{l_r}{d}\right)_i - \left(\frac{l_r}{d}\right)_t\right] \exp\left[-\frac{(t-t_b)}{T_b}\log(2)\right] \ , \text{ for } t \geq t_b, \tag{5.33}$$

where the transitional time scale will be estimated using the expression proposed by Kennedy et al. [85] because it allows for the application of the model in random wave propagation problems. It is written as follows,

$$T_b = k_{tb}\sqrt{\frac{d}{g}}, \tag{5.34}$$

where k_{tb} is a constant value. It is worth emphasizing that this kind of temporal evolution function is adopted in order to produce a transition zone. This choice is rather arbitrary and other possibilities can be imagined. For instance, in reference [38] we used instead a temporal variation of the breaker's front slope producing an equivalent overall effect (see Appendix E). However, since no reliable information is really available in that region, the latter is introduced more from practical considerations than physically sounded arguments. Similarly, we need to prescribe two limiting breakers angles, Φ_b and Φ_f, which respectively serve as threshold references to start and stop breaking. Remaining parameters will be calibrated in order to minimize the average error in predicted wave properties.

A large number of numerical experiments were conducted in order to determine the optimal parameter set but we only report here the main conclusions that can be drawn from this heuristical process :

1. Incorporating a breaking term in continuity equation is beneficial to avoid non-physical noise generation but using a ratio $\kappa = \delta_h/\delta_{hu}$ greater than 0.25 may significantly affect set-up estimation in the inner surf zone.

2. Two sets of optimal parameters were identified producing rather similar results in terms of wave height and skewness but showing some differences in terms of asymmetries. The first one corresponded to $l_r/d \sim 2-3$ and $\delta_{hu} \sim 4-5$, while the second one, which gave better asymmetry estimates, utilizes $l_r/d \sim 1$ and $\delta_{hu} \sim 12-20$.

3. A combination of larger l_r/d values with a strong magnitude for diffusivity coefficients produces small spurious oscillations behind breakers.

4. A transitional region must be considered from the breaking point to the location where the bore is fully developed in order to successfully capture surf zone wave height evolution.

5. The limiting front slope for breaking initiation must be fixed such that $\Phi_b \sim 30^\circ - 32^\circ$ for spilling breakers or even reach $35^\circ - 36^\circ$ for strong plunging events.

6. The threshold value for breaking termination has no influence for regular wave propagation on beaches of constant slope as long as it is fixed at a value $\Phi_f < 10^\circ$.

7. The application of the 8th order compact implicit filter given in Chapter 3 with $\alpha_f = 0.4$ improves the numerical performance of the scheme without significantly removing energy from the system (see Chapter 3). In the following applications the filter is used once per time step.

Results obtained with the first set of optimal parameters, namely $l_r/d \sim 2-3$, $\delta_{hu} \sim 4-5$ and $\kappa = 0.25$ were reported in reference [38] and can be found in Appendix E. In this work diffusivity coefficient, δ_{hu}, breaker index, γ and the ratio κ were *frozen* at fixed values, while an evolving angle Φ was assumed in order to reproduce a transitional regime. It was shown in reference [38] that optimal model parameters could be related to realistic properties of surf zone waves thus giving some confidence to the scaling analysis presented before. However, whereas wave height and skewness were correctly predicted, computed wave profiles for surf zone waves produced crests with a larger

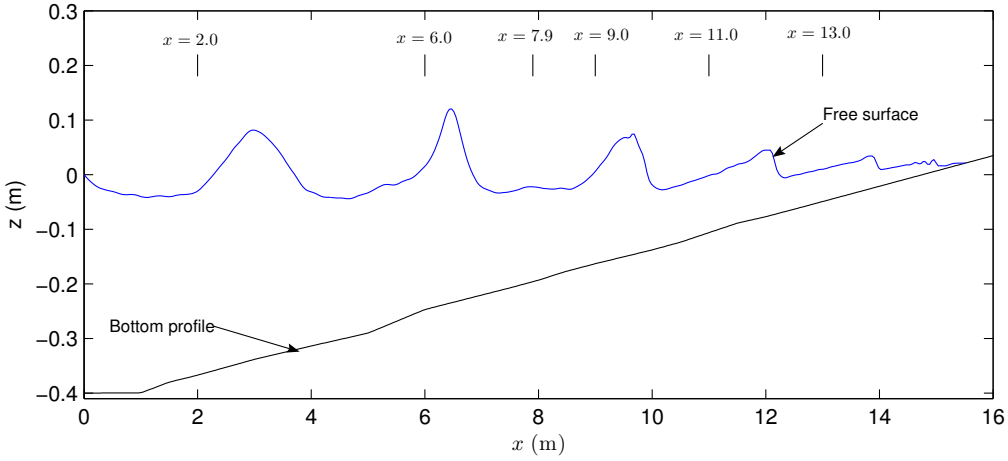

Figure 5.10: Definition sketch for Ting and Kirby's [162] spilling breaking experiment, $L_0 = 3.74$ m, $\frac{a_0}{h_0} = 0.156$ and $kh_0 = 0.672$. (computed results using the proposed breaking model). Vertical lines correspond to locations of wave gauges in meters.

width than measured ones. Hence, errors in horizontal wave asymmetry could not been properly reduced but the breaker's front slope was at least preserved.

On the other hand, concentrating breaking terms having much higher magnitudes on a smaller horizontal distance near the top of the breaker results in better agreement with measured surface elevation profiles. A good compromise between the numerical performance of the scheme and predicted properties of surf zone waves in the case of Ting and Kirby [162] spilling breaking is achieved fixing $\kappa \simeq 0.15 - 0.20$. Similarly, an adequate description of wave height, skewness and horizontal asymmetry is obtained using a constant value $\delta_{hu} \simeq 13 - 15$ for momentum diffusivity coefficient, and consequently $\delta_h \simeq 2 - 3$. The transitional time scale parameter is taken to be $k_{tb} \simeq 4 - 6$ and the horizontal length over which breaking terms are applied is computed using $\left(\frac{l_r}{d}\right)_i \simeq 0.7$ at the breaking point, and $\left(\frac{l_r}{d}\right)_t \simeq 1.2$ in the inner surf zone. Finally, threshold values for breaking inception and cessation are fixed at $\Phi_b = 31°$ and $\Phi_f = 6.5°$ respectively.

It is important to note that the energy equation (5.23) implies in the inner surf zone,

$$\delta_{hu} \simeq \alpha_b \frac{\gamma^3}{(1-\gamma)}(1+\kappa)^{-1} \tan^{-1}\Phi,$$

with $\alpha_b \simeq 3.0$, while relation (5.20) also reads,

$$\frac{l_r}{d} \simeq 0.865\,(1-\gamma)\tan^{-1}\Phi.$$

Therefore, optimal values for diffusivity coefficients and $\left(\frac{l_r}{d}\right)_t$ result from choosing a

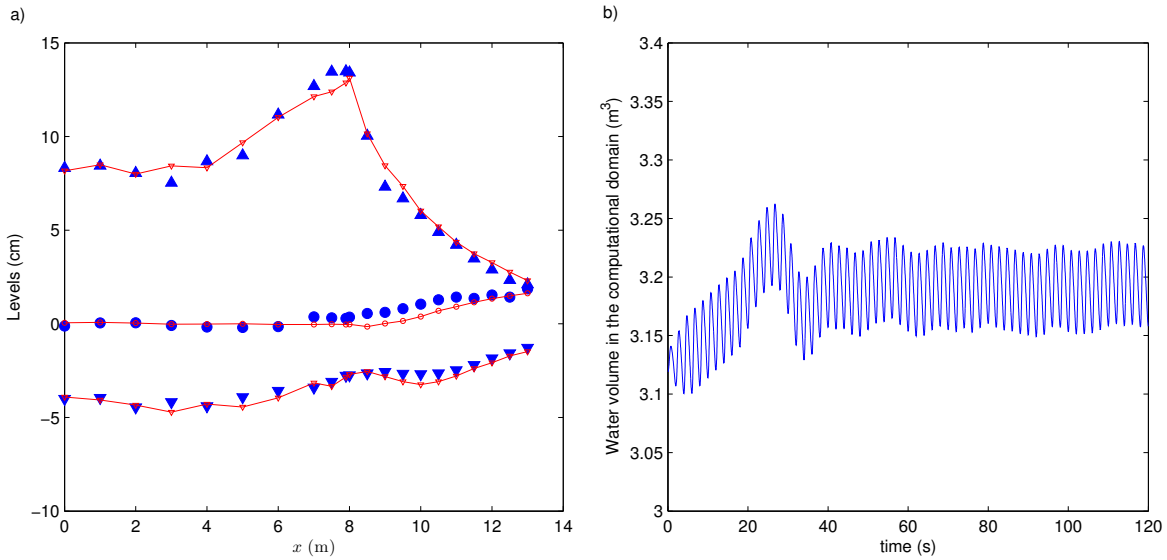

Figure 5.11: Numerical predictions for Ting and Kirby's [162] experiment using the proposed breaking model. a) (▲) : measured crest level $\eta_c - \overline{\eta}$; (•) : measured wave-averaged free surface $\overline{\eta}$; (▼) : measured trough level $\eta_t - \overline{\eta}$. Computed properties are plotted in plain lines. b) Temporal evolution of the water volume contained in the numerical domain.

front slope angle $\Phi \simeq 11°$ and a breaker index $\gamma \simeq 0.7$ thus ranging beyond observed quantities for these properties. It is also worth saying that numerical results were not very sensitive to small changes in parameter values as long as they were kept in the limits indicated above. However, in reference [38], similar predicted wave properties were obtained using in the inner surf zone a breaker slope of $\Phi_b = 6.5°$ and a breaker index $\gamma = 0.65$ which produce larger l_r/d and smaller local diffusivity intensities.

In the following, we will use $\delta_{hu} = 14.8$, $\kappa = 0.16$, $\left(\frac{l_r}{d}\right)_i = 0.7$, $\left(\frac{l_r}{d}\right)_t = 1.2$ and $k_{tb} = 5.0$. A spatial snapshot of computed free surface elevation is plotted in Figure 5.10 where it is clearly seen that the typical inner surf zone saw-tooth shape is well recovered (see also Figure 5.2 for comparison with results obtained using Kennedy et al. [85] breaking model). Wave-averaged properties produced by the model are reported in Figure 5.11 and the agreement between measured and computed crest and trough levels is almost perfect. Moreover, results concerning free surface profiles at different sections are depicted in Figure 5.12 and compared to results presented in the previous section, the achieved improvement is conclusive. Indeed, RMS error on wave height predictions over the whole domain is nearly 6 %, 26 % for horizontal asymmetries and roughly 10 % for the skewness coefficient. Hence, the average RMSE over these three important quantities appears to be of roughly 14 %. Comparisons between these measured and computed properties are reported in Figure 5.13. It is noticed that

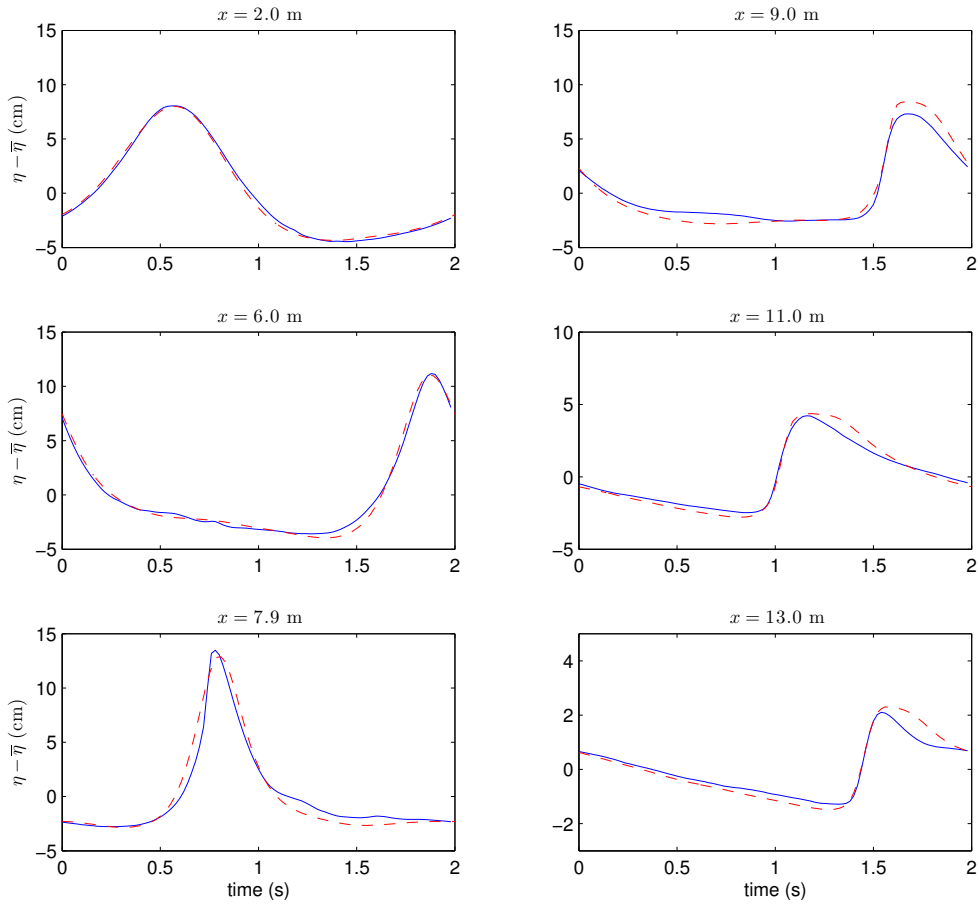

Figure 5.12: Computed and measured phase-averaged time series of free surface elevation for Ting and Kirby's [162] experiment at several wave gauges using the proposed breaking model. $(-)$: measured ; $(--)$ computed.

most of the modelling errors take place in the vicinity of the breaking point. This is more evident for the wave asymmetry coefficient since there are noticeable differences between computed and measured asymmetries in the transition zone. Nevertheless, the error is reduced in the inner surf zone thus proving that the proposed breaking model allows for a correct representation of wave height and asymmetry in this region.

In order to test model sensitivity to grid resolution, we perform an additional computation using $\Delta x = 0.05$ m which corresponds to 75 nodal points per incident wave length, i.e. a grid size 25 % coarser than the one used for calibration. Results are presented in Figure 5.14 where it is seen that predicted wave properties are almost unchaged compared to the ones estimated using a finer grid resolution. We recall that

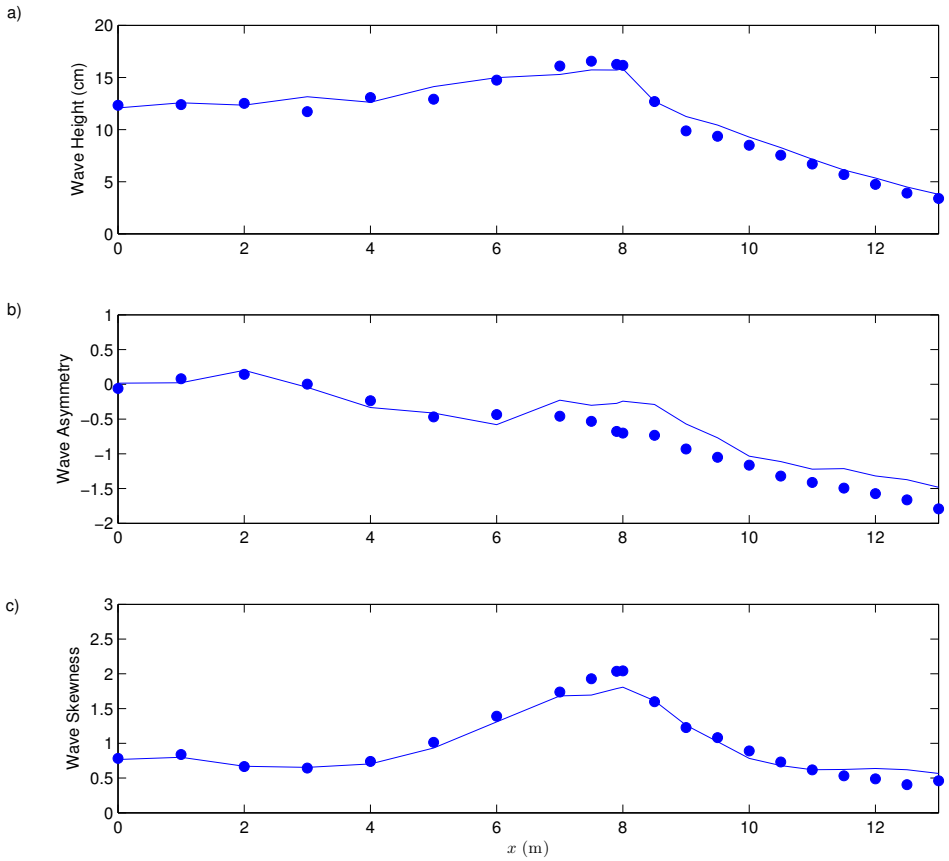

Figure 5.13: Comparison between measured (•) and computed (−) wave properties for Ting and Kirby's [162] experiment using the proposed breaking model. a) Wave height, b) Wave asymmetry, and c) Wave skewness.

using relation (5.20) to define the extent where breaking terms are applied makes the parameterization independent from the grid size. On the contrary and as previously pointed out, shock-capturing numerical strategies may have a misleading dependence on the grid resolution which can affect in particular horizontal asymmetry estimates.

Finally, it is worth noting that the chosen set of parameters is not unique in the sense that similar results may be obtained using different numerical values for them. Moreover, in the present example, no attempt have being made in order to optimize model parameters in terms of velocity predictions. The latter would presumably require the use of a variable function κ, as discussed before, and a combination of larger l_r/d and smaller diffusivity coefficients to produce the desired effect.

In the following section the proposed breaking model and the chosen set of param-

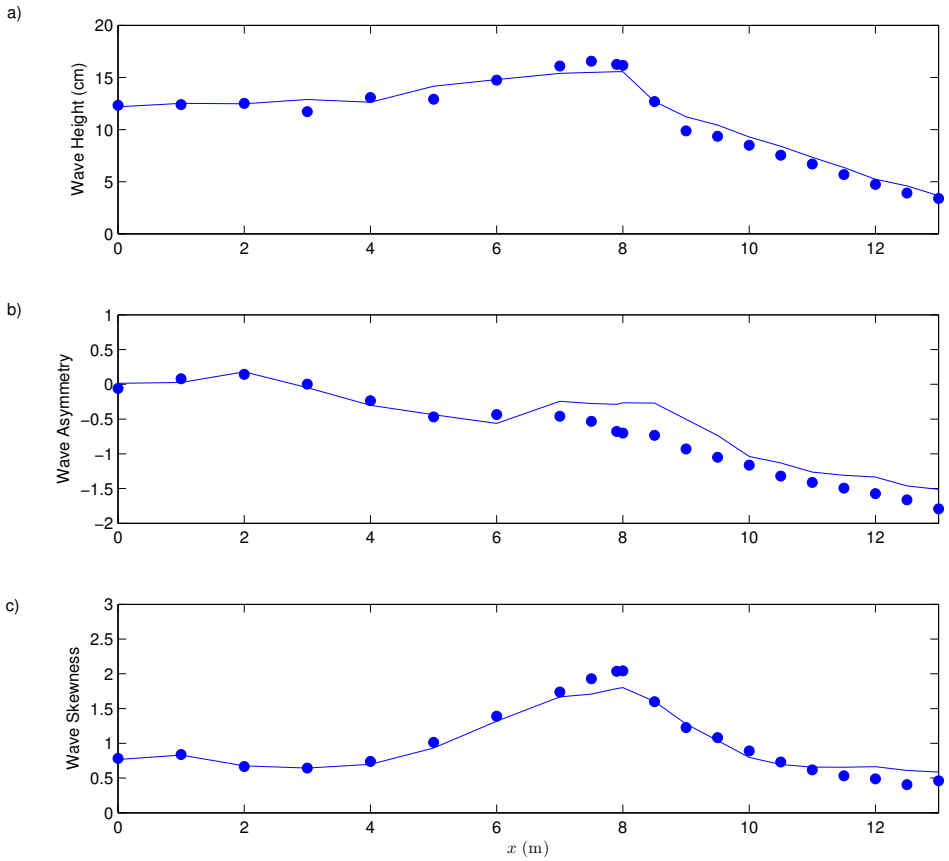

Figure 5.14: Sensitivity of results for Ting and Kirby's [162] experiment when changing the spatial grid size. Additional computation performed using a 25 % coarser grid resolution. Same captions as Figure 5.13.

eters will be validated with help of several available experimental test cases for wave propagation and breaking.

5.4.3 Model validation

In order to evaluate the ability of the new breaking model to predict surf zone wave properties we perform numerical computations for several experimental test cases keeping the same optimal set of parameter values obtained in the previous subsection. We consider Cox's regular wave experiment [41], five different tests on regular waves shoaling and breaking on a planar beach conducted by Hansen and Svendsen [77], and a solitary wave breaking on a beach investigated by Synolakis [158]. All the following computations are carried out using a grid size $\Delta x = 0.1\, h_0$ and a Courant number

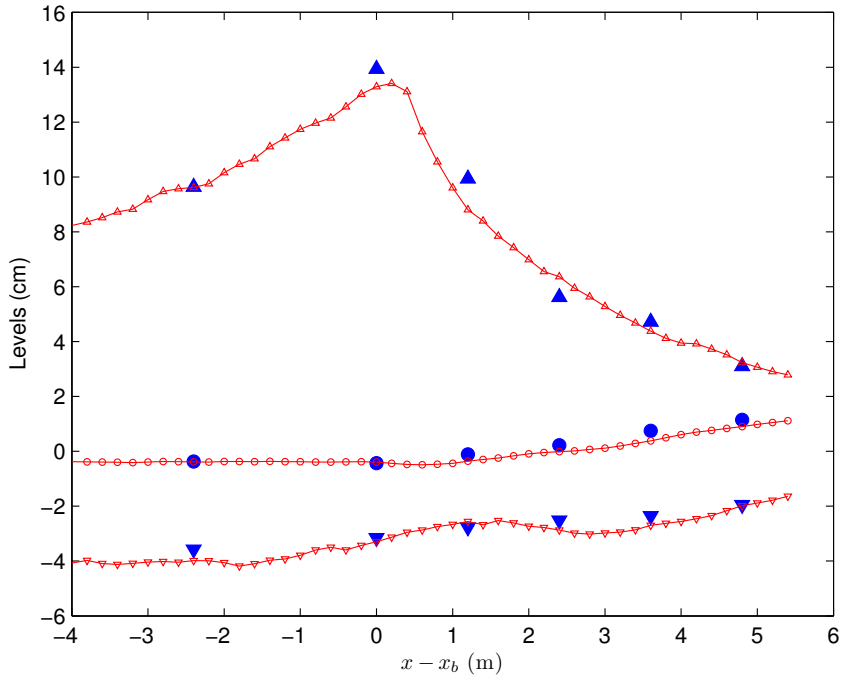

Figure 5.15: Comparisons of model predictions and experimental data for Cox's [41] spilling breaking, $L_0 = 4.19$ m, $\frac{a_0}{h_0} = 0.144$ and $kh_0 = 0.600$. (▲) : measured crest level $\eta_c - \overline{\eta}$; (•) : measured wave-averaged free surface $\overline{\eta}$; (▼) : measured trough level $\eta_t - \overline{\eta}$. Computed properties are plotted in plain lines.

$C_r = 1.0$. Recall from Chapter 2 that this temporal and spatial grid resolution ensure that the numerical method is stable, non-damping and able to describe all physical wave-lengths resolved by the extended system of Serre equations. Benchmark tests that will be investigated next correspond to a wide range of wave-lengths thus resulting in different breaker types.

Application to Cox's [41] spilling breaking experimental test

Cox [41] conducted detailed measurements for cnoidal waves shoaling and breaking on a planar beach of slope 1:35. This data set was already used in Chapter 4 and the reader is refered to the corresponding section for further information on this particular test case. Wave conditions are similar to Ting and Kirby's [163] spilling breaking case, except for a slightly longer period and a smaller incident wave amplitude. In addition, phase-averaged time series of free surface elevations at six measuring sections are available and correctly synchronized. It is then possible to use these experimental data to investigate model performance in terms of phase speed estimates.

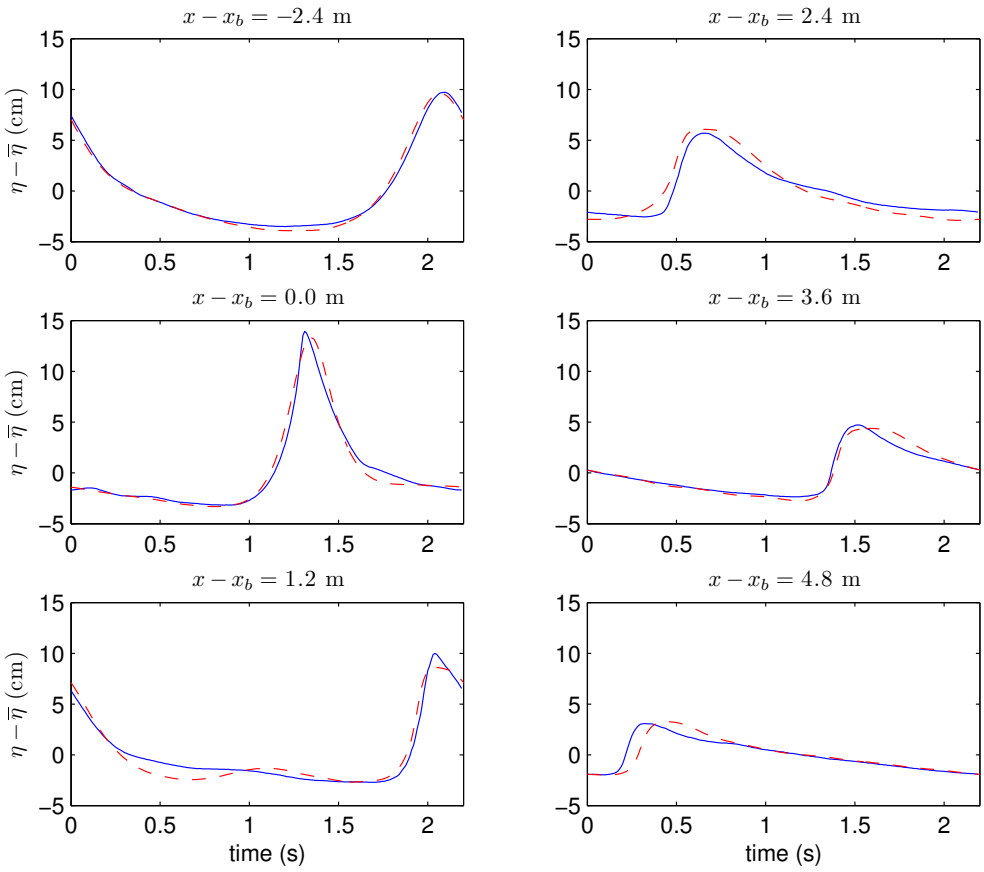

Figure 5.16: Computed and measured phase-averaged time series of free surface elevation at several wave gauges for Cox's [41] experiment. (−) : measured ; (−−) computed.

A comparison between predicted and measured set-up, crest and trough levels is presented in Figure 5.15 where the theoretical cnoidal wave solution has been used to prescribe the incident free surface time serie at the left boundary, and the moving shoreline condition is implemented at the right boundary. Numerical results compare very well with experimental data and an excellent nonlinear performance in the shoaling region is noticed. Indeed, the breaking point location and the maximum wave height are accurately predicted. Similarly, surf zone wave height evolution is fairly well reproduced by the model. Nevertheless, close inspection of numerical results indicates that set-up is slightly underestimated in the inner surf zone.

Associated phase-averaged free surface time series are reported in Figure 5.16 for the six sections where measurements were conducted. The overall agreement between measured and computed time series is good thus confirming that the breaking model allows for a proper estimation of wave asymmetries and heights in the surf zone. How-

Test Case	Wave Period (s)	Wave Height (cm)	$\epsilon = a_0/h_0$	kh_0	Breaker type
A10112	1.02	6.7	0.093	1.580	Spilling
061071	1.68	6.7	0.093	0.791	Spilling
053074	2.02	6.6	0.092	0.641	Spilling
041041	2.53	3.9	0.054	0.501	Plunging-Spilling
031041	3.37	4.3	0.060	0.369	Plunging

Table 5.2: Experimental conditions for selected series of Hansen and Svendsen's [77] regular wave test cases.

ever, there is a small phase shift in section $x = 4.8$ m which may be attributed to the slight underestimation of the mean water level noticed in Figure 5.15. Nevertheless, free surface prediction is comparable to the one reported for the same experiment by Briganti et al. [25] and Musumeci et al. [120] using a much more complex Boussinesq model where the irrotationality assumption was removed.

Model performance for Hansen and Svendsen's [77] benchmark tests on regular waves

Hansen and Svendsen's [77] experiments on regular waves shoaling and breaking on a planar beach of slope 1:34.26 have become a benchmark test for Boussinesq-type equations and associated breaking parameterizations. For instance, Kennedy et al. [85], Veeramony and Svendsen [172], Briganti et al. [25] and Musumeci et al. [120] (among others) have used these data sets to validate time domain breaking models. In addition, since a wide range of wave-lengths were investigated by Hansen and Svendsen, the available experimental information provides a good opportunity to test nonlinear shoaling characteristics of the extended system of Serre equations.

We have chosen five test cases following Kennedy et al. [85] validation procedure, for wave conditions producing breaker types ranging from gentle spilling to strong plunging events. Selected experimental series and their main characteristics are summarized in Table 5.2. Regular wave test cases range from fairly short incident waves to rather long ones. The associated dispersive coefficient for the shorter wave-length test is $kh_0 = 1.58$, thus almost one half of the theoretical limit of the extended system of Serre equations. Consequently, Hansen and Svendsen's [77] test series will provide an additional insight over nonlinear shoaling characteristics of the Boussinesq-type wave propagation model when used to describe different wave field conditions. Numerical examples reported in the following are carried out using theoretical second order Stokes

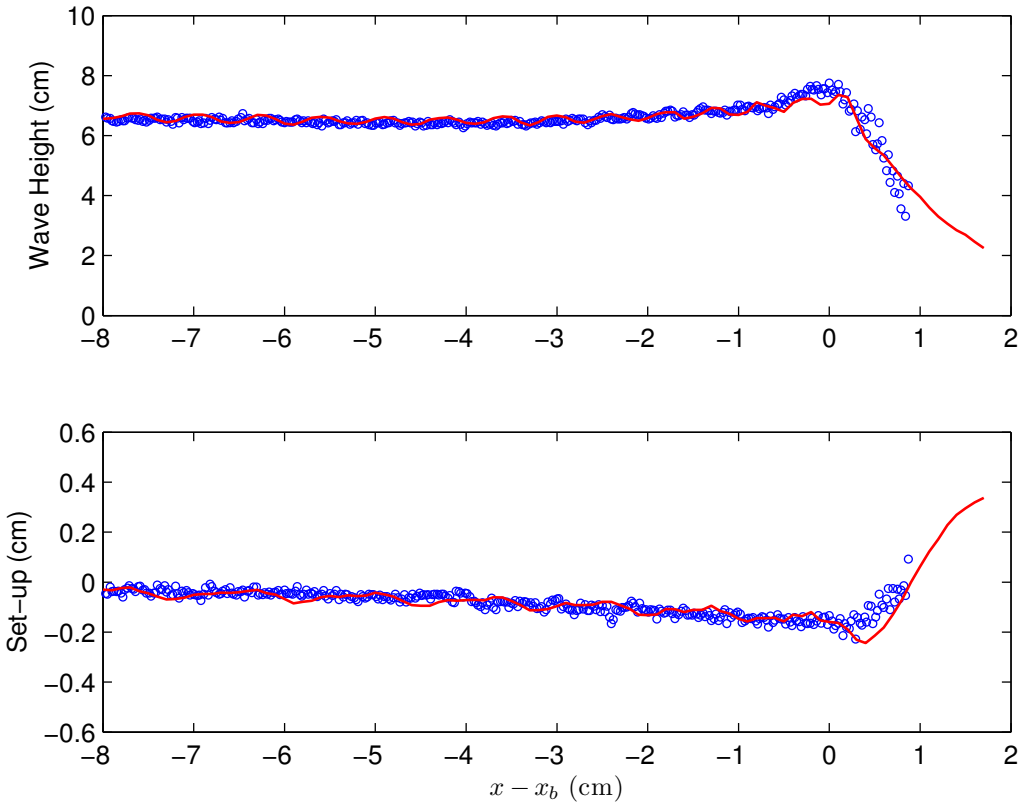

Figure 5.17: Comparisons of model predictions and experimental data for Hansen and Svendsen [77] spilling breaking test No. A10112. (∘) : measured data. Computed wave height and set-up are plotted in plain lines.

waves as free surface time domain input at left boundary, while the moving shoreline condition is prescribed at the right boundary.

Numerical results for spilling-like breakers are presented from Figure 5.17 to Figure 5.19. It is seen that the breaking point location is adequately predicted in all cases using the same numerical values for model parameters as inferred from Ting and Kirby's [162] measurements. Similarly, the shoaling region is fairly well described by the numerical model except in the vicinity of the breaking point where the limiting wave amplitude is slightly underpredicted for test cases No. 061071 and 053074. This trend was already noticed when calibrating the breaking model using Ting and Kirby's [162] experiment. Moreover, the numerical model also reproduces some nonlinear processes associated to wave reflection which is presumably generated by swash oscillations and bathymetric variations as can be readily noticed from the slight amplitude modulation appearing in wave height plots. This situation is also present in experimental

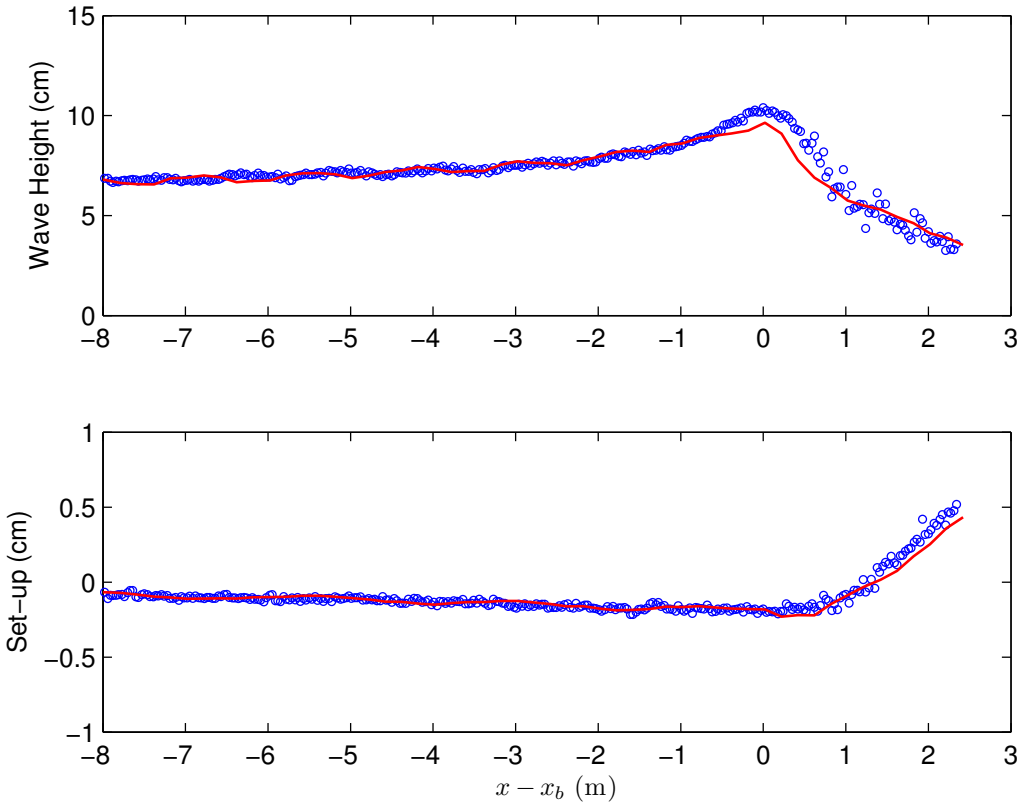

Figure 5.18: Comparisons of model predictions and experimental data for Hansen and Svendsen [77] spilling breaking test No. 061071. (∘) : measured data. Computed wave height and set-up are plotted in plain lines.

measurements so it is believed that boundary conditions are performing correctly in describing the associated complex nearshore physics.

On the other hand, surf zone wave evolution is predicted in good agreement with experimental data for all three spilling conditions. This is clearly observed in test cases No. 053074 and No. 061071 which have longer surf zone extensions. In particular, model performance in the inner surf zone is excellent since computed wave amplitudes follow the measured values with great accuracy. There are only minor differences in the transition zone which are mostly due to the initial underestimation of the maximum wave height.

Set-up levels are also satisfactorily reproduced for all three cases and the spatial lag between the breaking point location and the beginning of set-up is also recovered. However, there are minor differences in the inner surf zone where set-up level is slightly underestimated. As explained in the previous subsection, the agreement between mea-

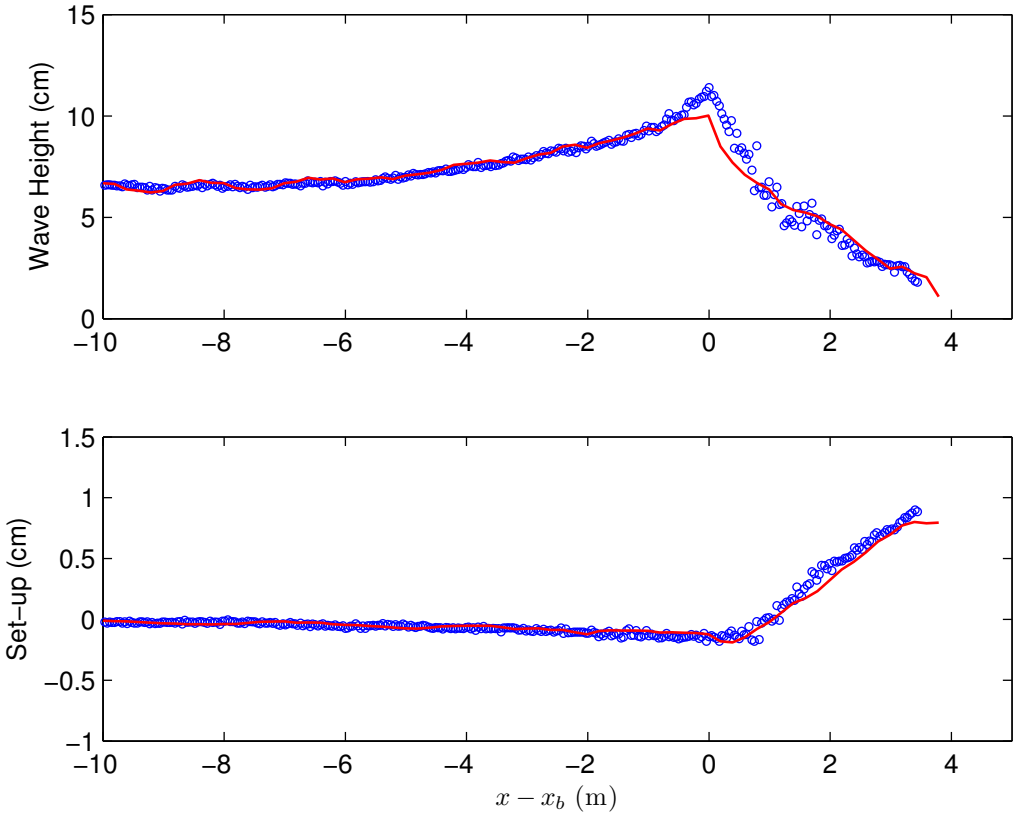

Figure 5.19: Comparisons of model predictions and experimental data for Hansen and Svendsen [77] spilling breaking test No. 053074. (∘) : measured data. Computed wave height and set-up are plotted in plain lines.

sured and computed mean water levels could be further improved by reducing the ratio $\kappa = \delta_h/\delta_{hu}$. Unfortunately, the mass diffusivity term is benificial in terms of numerical stability and a compromise between physical and practical aspects had to be determined. This limitation may be overcomed if a variable value for κ is implemented. Of course, the latter needs to be studied carefully looking in addition to the influence that this parameter may have on velocity profiles.

In summary, model performace for the spilling breaking cases investigated so far appears to be very good since wave heights, set-up levels, breaking point locations and transition zone spatial extensions are fairly well reproduced using the same parameter values. It seems then justified to infer that physical arguments developed to derive scaling relations for the new breaking parameterization are quite robust thus providing accurate information for spilling-like breaking situations.

Comparisons between numerical computations and experimental measurements for

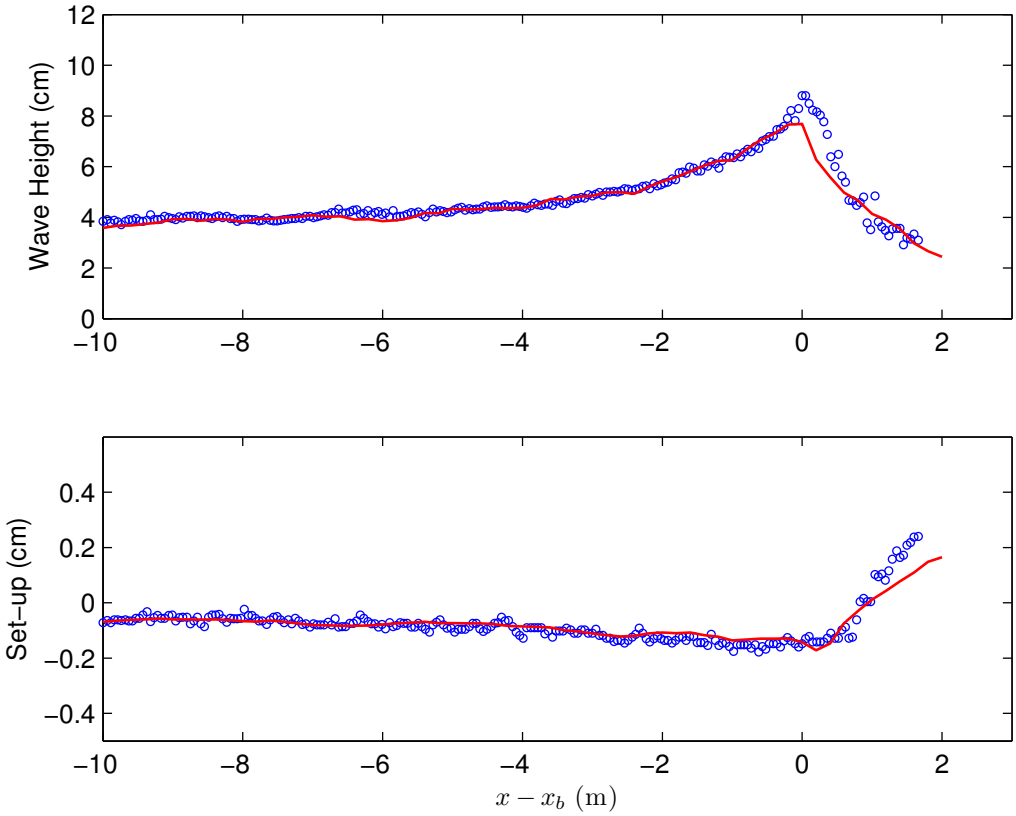

Figure 5.20: Comparisons of model predictions and experimental data for Hansen and Svendsen [77] plunging breaking test No. 041041. (∘) : measured data. Computed wave height and set-up are plotted in plain lines.

plunging breakers are reported in Figures 5.20 and 5.21. In both cases, the breaking point location is predicted offshore the physical one but wave height evolution in the inner surf zone is correctly estimated. However, computed set-up levels are badly reproduced in the inner surf zone showing a noticeable underestimation. In these particular experiments, reducing the relative weight of mass and momentum diffusivity coefficients, κ, did not improve set-up predictions. One plausible explanation for that is related to secondary waves that are generated by nonlinear interaction in the shoaling region. Indeed, prior to breaking there is a decomposition of the initial longer regular Stokes wave in a two peaked-like wave as noticed in the spatial snapshot depicted in Figure 5.22. This decomposition is triggered by the high steepening of the incident wave and the associated intense nonlinear energy transfer into higher bounded harmonics that takes place near breaking. Unfortunately, at the present stage of development, the model is not able to introduce breaking effects in these secondary waves which

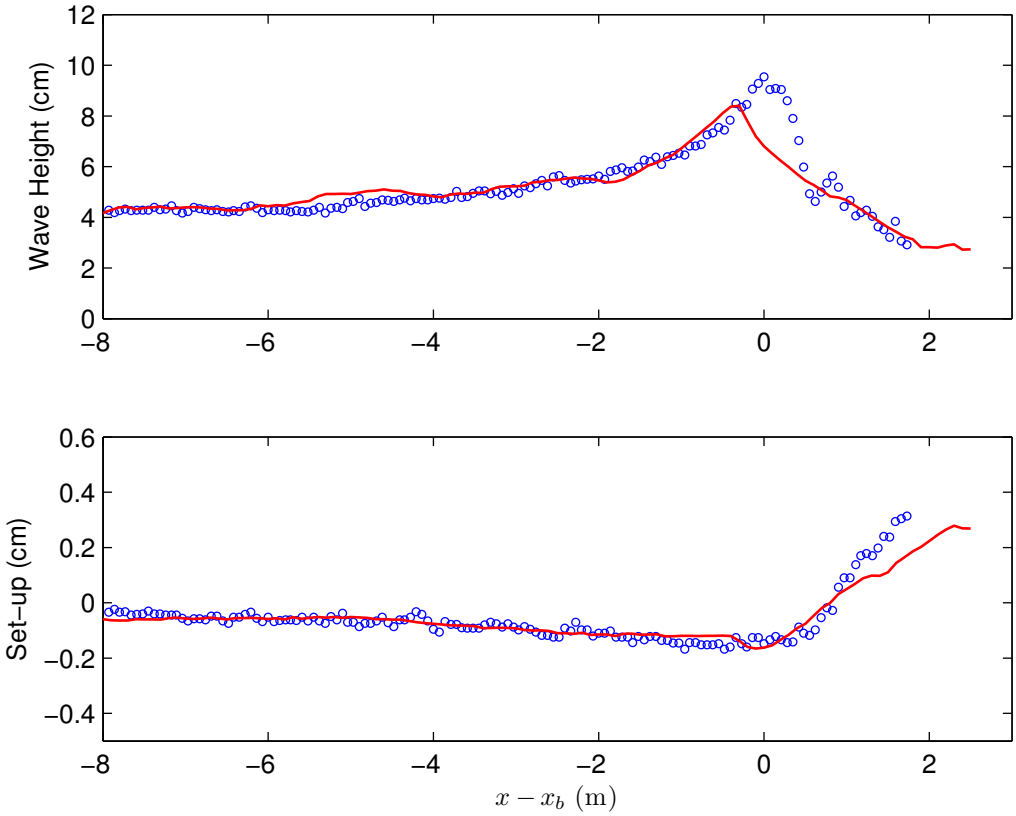

Figure 5.21: Comparisons of model predictions and experimental data for Hansen and Svendsen [77] plunging breaking test No. 031041. (∘) : measured data. Computed wave height and set-up are plotted in plain lines.

break further onshore as they propagate into the shoreline. It is evident that secondary breaking waves are responsible for an additional radiation stresses contribution and the associated increase in set-up level. Set-up underestimation may be partially due to this particular situation and not to the presence of the additional mass diffusivity term in the continuity equation.

Alternatively, measured and computed set-up discrepancies may be attributed to an inaccurate estimation of wave height gradients in the transition zone as observed in Figures 5.20 and 5.21. Indeed, in wave-averaged hydrodynamic equations, setup evolution is governed by the spatial gradient of surf zone wave amplitudes (see for instance reference [115]).

On the other hand, the noticeable offshore prediction of the breaking point location may also be explained by the high nonlinear steepening of incident waves in the shoaling region. Indeed, the front slope threshold value, $\Phi_b = 31°$, was obtained for spilling-like

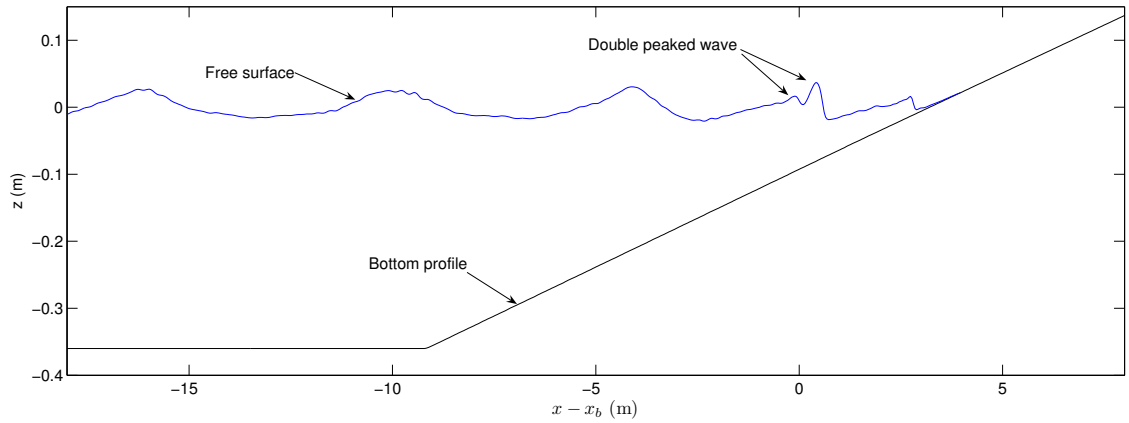

Figure 5.22: Spatial snapshot showing a secondary peak generation before breaking for Hansen and Svendsen's [77] experimental plunging test case No. 031041.

breakers and it follows from the previous discussion that for plunging events not only a higher limiting value for this property should be prescribed but also a shorter time scale for the transitional regime. In order to confirm this hypothesis we conduct an additional computation for test case No. 031041 using a threshold value of $\Phi_b = 36°$ for breaking initiation and $k_{tb} = 1.0$ in relation (5.34). Results are reported in Figure 5.23 where it is seen that the breaking point location and wave height evolution in the transition zone are better predicted. Nevertheless, set-up level is almost insensitive to this change in model parameters presumably because of the presence of unbroken secondary waves. This numerical example also demonstrates that the chosen set of Boussinesq-type equations possesses excellent nonlinear characteristics since the limiting wave height and the corresponding shoaling behaviour are accurately reproduced.

Two final conclusions should be drawn from numerical computations presented in the present section. The first one concerns the ability of the breaking model to reproduce inner surf zone wave gradients even for plunging breakers and the fact that model behaviour is rather insensitive to the chosen spatial grid resolution. The latter is further sustained by results reported for Hansen and Svendsen's [77] test cases since a constant $\Delta x = 0.1\, h_0$ was used in all computations and different wave lengths were investigated. This means that the breaking parameterization succeeds in predicting an accurate energy dissipation despite the fact that the number of nodal points per wave lengths was not constant in the different computations. This important property follows directly from Cointe and Tulin's [40] relation verified in Chapter 4 and should make the breaking model applicable in random wave propagation problems.

A second crucial feature is related to the particular extended set of Serre equations

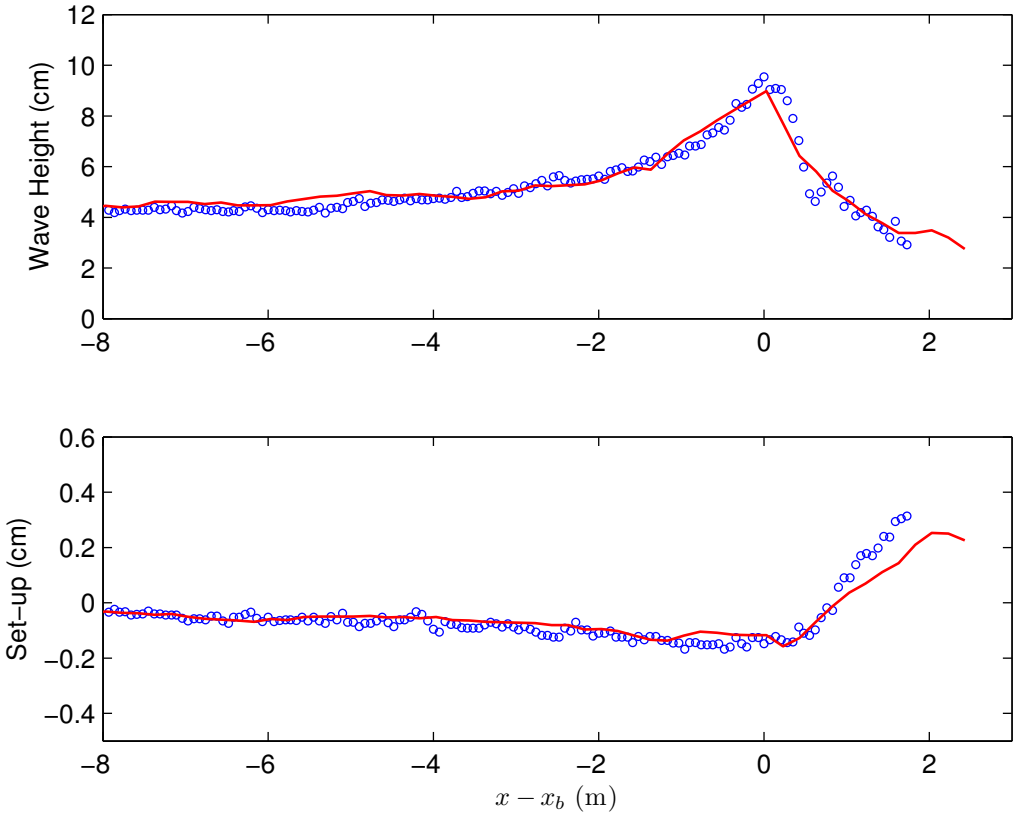

Figure 5.23: Comparisons of model predictions and experimental data for Hansen and Svendsen [77] plunging breaking test No. 031041, using $\Phi_b = 36°$ and $k_{tb} = 1.0$. ($\circ$) : measured data. Computed wave height and set-up are plotted in plain lines.

used to describe nearshore hydrodynamics. It is interesting to compare present numerical results with those reported by Kennedy et al. [85] using the fully nonlinear Boussinesq wave propagation model FUNWAVE [89, 178]. In reference [85], model performances were also tested against Hansen and Svendsen's [77] cases where Wei et al.'s [178] equations produced an unphysical amplification of bounded higher harmonics. Results reported by those authors showed a systematic overprediction of wave heights in the shoaling region thus indicating that nonlinear properties of the chosen Boussinesq-like set of equations are not accurate enough. This problem was more evident as wave lengths were decreased and a theoretical explanation for this unphysical behaviour can be found in reference [106]. On the contrary, the Boussinesq-like set derived in Chapter 2 and numerically handled using a finite volume scheme exhibits an excellent nonlinear behaviour for all test cases, and only a small underprediction of the maxium wave height (< 10 %) could be noticed in some cases. Similar conclusions

were given in Chapter 3. Hence, nonlinear characteristics of the extended system of Serre equations may be close to those achieved by Lynett and Liu [105] using a far more complex two layer Boussinesq model since present results compare favourably to those reported in reference [106].

Application to Synolakis' [158] solitary wave breaking on a beach

The last experimental test case that we consider in order to validate the numerical model corresponds to a solitary wave propagating and breaking on a 1:20 constant slope beach as studied by Synolakis [158]. This author reported time series of inicident and reflected solitary waves with a wave gauge located near the toe of the slope. This data was used to provide a common time origin for additional video measurements conducted for runup and run down stages of non-breaking and breaking solitary waves. Comparisons between predicted and measured spatial snapshots of propagating solitary waves were already reported for a non-breaking case in Chapter 3. Here we focus on a higher relative amplitude case which broke strongly on runup. This particular experiment was also used by Zelt [184] to test his breaking parameterization and the implemented Lagragian moving shoreline boundary condition.

The experimental case consists in a solitary wave with non-dimensional incident amplitude $a_0/h_0 = 0.28$ propagating over a beach of 1:20 slope. The still water depth is fixed in the horizonal part of the wave flume at $h_0 = 0.25$ m for numerical computations reported in the following. Similarly, a grid size of $\Delta x = 0.025$ m and a Courant number $C_r = 1.0$ is considered. The wave gauge located 4.775 m ($= 19.1\, h_0$) from the still shoreline is used to synchronize video measurements and numerical predictions. A comparison between available data at this location and computed results is presented in Figure 5.24.

The breaking model is driven with the same parameter values determined using Ting and Kirby's [162] experiment. It is worth noting that video measurements produced by Synolakis [158] allow for a detailed spatial comparison between experimental data and computed results. On the contrary, previous test cases studied in this section mostly concerned time-domain or wave-averaged properties so we have here an opportunity to test additional properties of the model. In particular, the ability of the implemented moving shoreline boundary condition to deal with strong breaking events will be investigated.

A free surface time series comparison for numerical and experimental data are depicted in Figure 5.24. It is seen that overall incident and reflected wave features are adequately reproduced by the numerical model. Spatial snapshots of computed and

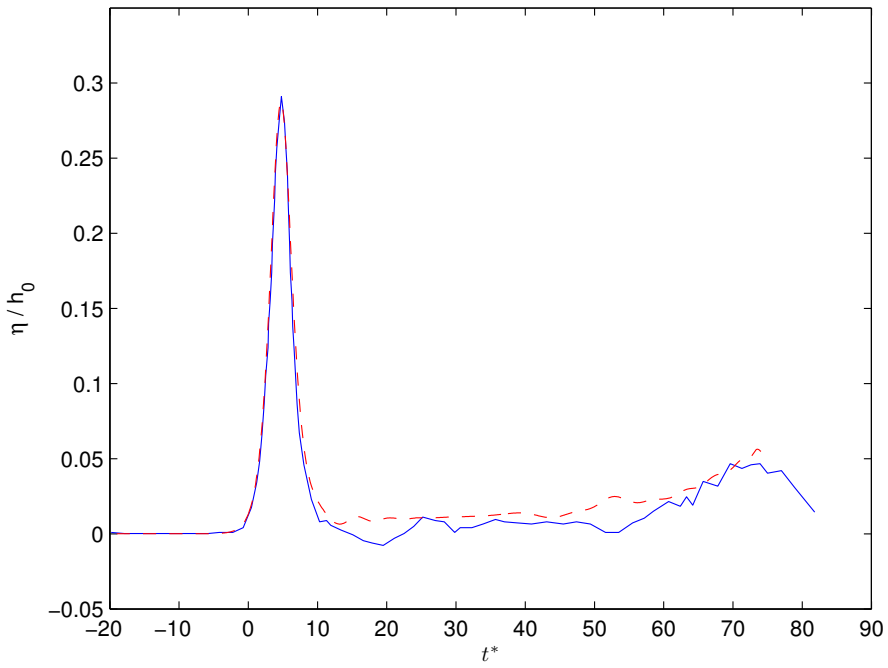

Figure 5.24: Computed and measured incident and refected solitary wave for the breaking case with $a_0/h_0 = 0.28$ investigated by Synolakis [158]. Wave gauge located 4.775 m from the still shoreline and $t^* = t\sqrt{g/h_0}$ is the non-dimensional time. $(-)$ Measured time serie, and $(--)$ predicted one using the numerical model.

measured free surface profiles in runup and run-down stages are reported in Figure 5.25. As pointed out in reference [184], incipient breaking takes place slightly before the non-dimensional time $t^* = 20$ is reached. Prior to that time, the numerical model accurately predicts the solitary wave height and the nonlinear steepening of the incident soliton. Furthermore, inception of breaking is also reasonably predicted by the model even when using parameter values obtained from a spilling breaking case. Again, embedded nonlinear characteristics of Serre equations provides very good agreement with experimental measurements near the breaking location. It is worth noting that results reported in reference [184] are slighlty less accurate in terms of spatial wave shapes in the shoaling zone. More importantly, even though it appears that breaking dissipation develops over a longer time in the numerical model since a double-peaked feature shows up between $t^* = 21$ and $t^* = 23$, the overall agreement is quite good. Soon after, the solitary wave reaches the shoreline and the moving boundary condition starts acting. The runup stage is fairly well reproduced by the numerical model despite the fact that no friction parameterization is included in the governing equations. The latter is in contradiction with some of the conclusions given by Zelt [184] who attributed some

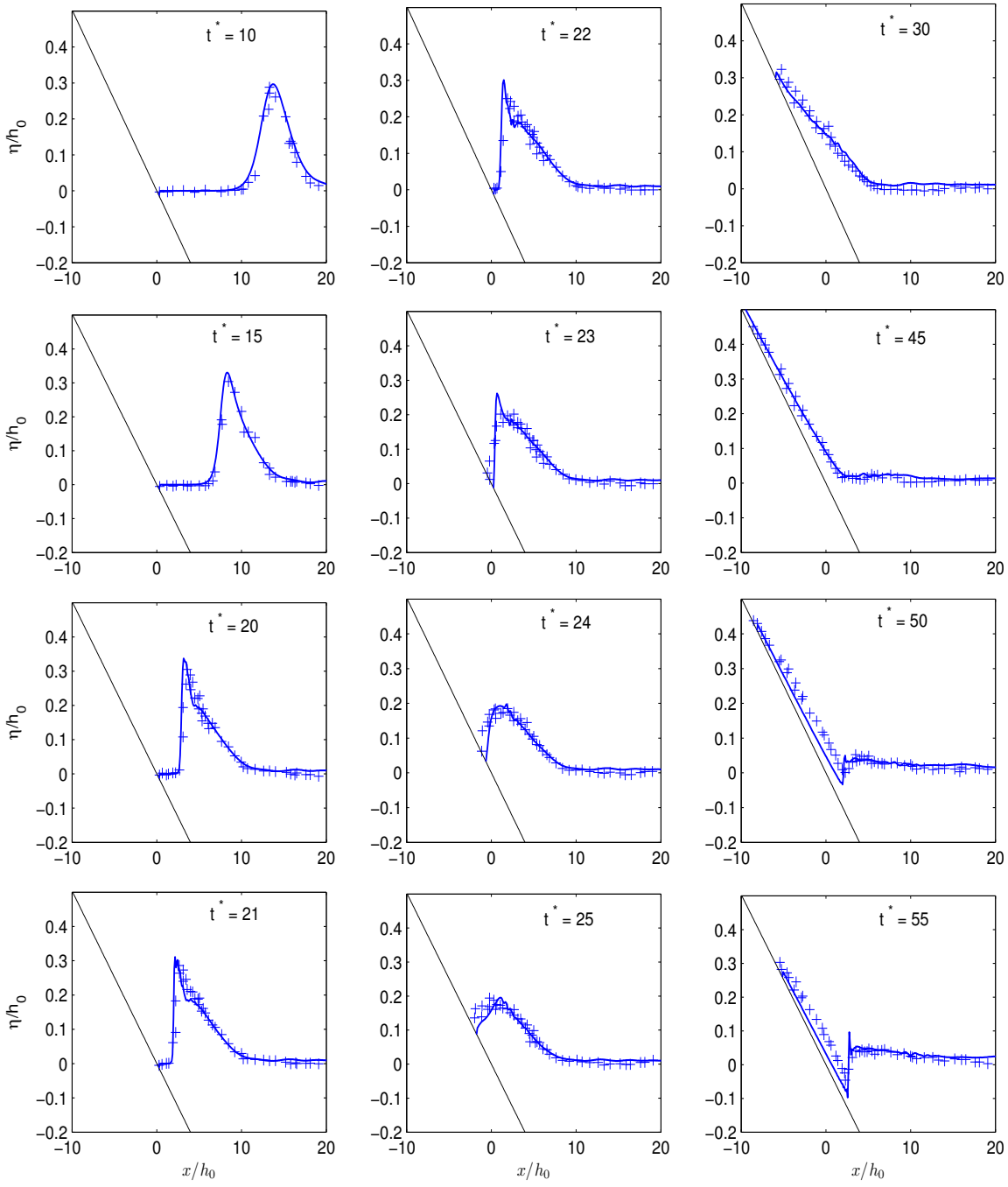

Figure 5.25: Comparisons of model predictions and experimental spatial snapshots for the breaking solitary wave with $a_0/h_0 = 0.28$ investigated by Synolakis [158]. (+) : experimental data, while numerical results are plotted in plain lines. $t\sqrt{d/h_0}$ is the non-dimensional time.

noticeable inaccuracies produced by his Lagrangian finite element model to friction effects. On the contrary, it is only in the run down phase that slight discrepancies between experimental data and computed results can be observed in our case. Close inspection of free surface evolution between panels $t^* = 45$ and $t^* = 55$ indicates that the numerical model produces a thinner water tongue than the measured one. This can be reasonably attributed to the lack of a friction term since it is well known that friction effects are inversely proportional to water depths. Finally, it is observed in the last panel of Figure 5.25 that a back swash breaking condition is reached and the numerical model is able to accurately reproduce this demanding situation where free surface slope is almost vertical. However, it is important to recall that the breaking parameterization has not been conceived to handle this kind of breaking, thus an incipient spurious numerical behaviour can be noticed in this last panel.

From this additional example, not only the ability of Serre equations to deal with strong nonlinearities is satisfactorily confirmed, but also the physical and practical adequacy of the moving shoreline boundary condition described in Chapter 3, is further validated for breaking cases.

5.5 Conclusions

The present chapter has been devoted to investigate time domain breaking parameterizations that may be used in the framework of Boussinesq-type equations. In particular, Kennedy et al. [85] breaking model was implemented in our Boussinesq-like finite volume scheme and it was clearly confirmed that the latter heavily overestimates wave heights in the inner surf zone. Hence, numerical computations producing similar results reported in reference [85] on the base of a different set of fully nonlinear Boussinesq equations show that this drawback is intrinsically due to the breaking model. Unfortunately, it was found in Section 3, that forcing Kennedy et al. [85] model with different parameter values does not allow for a proper simultaneous prediction of wave heights and the characteristic inner surf zone saw tooth profile.

Additionally, since horizontal wave asymmetry appears to be a key property for sediment transport prediction in the framework of beach morphodynamics, an alternative wave breaking parameterization was developed. Invoking nonlinear shallow water shock wave theory, energetic considerations and experimental findings on quasi-steady hydraulic jumps investigated by Svendsen et al. [157], we were able to find scaling relations for a novel breaking wave model which incorporates both, mixing layer effects in the continuity equation and associated breaking momentum deficits via the inclusion of

extra mass and momentum diffusion terms. This alternative approach, which is written as a function of the breaker index, γ, and the mean front slope, Φ, can be viewed as an extension of the eddy viscosity analogy used by Zelt [184] and Kennedy et al. [85]. In particular, the extent over which breaking terms act follows from a simple relation obtained by Cointe and Tulin [40] and calibrated under experimental conditions more representative of inner surf zone waves in Chapter 4. It is worth emphasizing that this relation introduces in the model an additional degree of freedom since the horizontal distance where diffusivity functions are applied is explicitly controlled. Indeed, numerical implementation of this breaking wave parameterization into our fully nonlinear and weakly dispersive Boussinesq-type model successfully demonstrated that wave heights and horizontal asymmetries could be better reproduced than when using Kennedy et al. [85] approach. It was also verified that the model performance is rather insensitive to the chosen grid size resolution.

From a numerical point of view, the incorporation of a mass diffusivity term in the continuity equation appears to improve local stability of the scheme near the region where breaking terms are applied. In particular, short-wave noise or spurious oscillations that could arise behind waves near the breaking point as a consequence of the impulsive application of extra terms are suppressed when the relative weight of the mass diffusion term is increased. Indeed, we were able to perform oscillation-free computations using large time steps which corresponded to a Courant number of 1.0. Moreover, diffusivity terms bear some resemblances with NSWE shock capturing solvers. Energy dissipation is accounted for in the latter by introducing viscosity-like terms acting very locally where free surface slope gradients are the highest, i.e. near the wave's crest and trough (see for instance references [97, 165]). Those strategies produce the desired energy dissipation through numerical diffusion acting on both, continuity and momentum equations.

From a physical standpoint the mass diffusivity term somehow mimics the local mass transfer that takes place by *avalanching* at the front face of the wave near the breaking point. This effect is responsible in particular for an important loss of potential energy in the transition zone.

On the other hand, it is really important to stress that the calibration process performed on Ting and Kirby's [162] spilling breaking experiment, allows us to end up with a breaking model which can successfully reproduce several different spilling breaking conditions using the same parameter values which remain in physical ranges. It is then concluded that scaling arguments developed in Section 5 provide useful relations which seem to be more general than other forms used in former breaking wave parameterizations. Nevertheless, and in accordance to underlying hypothesis, breaking

point location and the spatial length of the transition zone occuring in plunging-like breakers could not be accurately reproduced using the same parameter set. This is mostly due to the higher steepening that longer period waves can reach, thus requiring a higher threshold value for the critical front slope. Similarly, in plunging events, intense energy dissipation takes place over a shorter distance producing a more rapid transitional behaviour. In spite of that, inner surf zone wave height gradients were reasonably predicted by the model even for plunging breakers.

Additionally, we note that the proposed optimal set of model parameters is not unique in the sense that similar surf zone wave properties predictions may be obtained using different combinations for γ and Φ. It is believed that calibrating the model using an additional constraint related to flow velocity computations may help to elucidate what combination of parameter values would produce the best results. Indeed, it was also demonstrated that the additional mass diffusivity term acts as a roller since maximum mean current intensity is increased while its spatial location is shifted shorewards.

Finally, the physical adequacy of the implemented moving shoreline boundary condition was further validated using an experimental solitary wave breaking on a beach. Computed evolution for wave propagation in runup and run-down stages appeared to be in very good agreement with experimental measurements conducted by Synolakis [158]. Indeed, only slight discrepancies could be noticed in the run-down phase which may be reasonably explained by the lack of a friction term in the governing equations. Similarly, the different test cases investigated clearly confirmed that the extended system of Serre equations possesses excellent nonlinear characteristics since wave height evolution in the shoaling region was accurately reproduced. Only a minor underprediction, which was never larger than 10 %, could be noticed near the breaking point in some cases. The latter suggests that nonlinear shoaling properties embedded in this particular set are somehow closer to the two layer Boussinesq model developed by Lynett and Liu [105] than to the fully nonlinear wave propagation module implemented in FUNWAVE [89, 178].

Chapter 6

Conclusions et Perspectives

6.1 Principaux résultats

Le travail qui s'achève avec ce chapitre a été principalement consacré au développement d'un modèle numérique capable de décrire de manière efficace et précise la plus part des phénomènes physiques en rapport avec la propagation de la houle dans un environnement côtier. L'effort scientifique s'est concentré sur une approche opérationnelle applicable en milieu naturel le long d'un profil de plage en incluant à la fois, la zone de levée, le déferlement et la zone de swash. En effet, la démarche adoptée a permis de valider convenablement l'application du modèle hydrodynamique proposé dans un contexte d'ingénierie côtière.

La pertinence physique du système d'équations de Serre, ainsi que l'excellente performance du nouveau schéma numérique en volumes finis basé sur les stratégies les plus récentes de reconstruction d'interface et spécialement conçu pour sa résolution, ont été parfaitement demontrés. Il est important d'insister sur le fait que d'un point de vue strictement numérique, la nouvelle méthode est largement supérieure aux précédentes approches couramment utilisées pour intégrer des modèles de Boussinesq équivalents. Que ce soit par rapport à la résolution spectrale et la capacité à représenter efficacement la cinématique des ondes théoriquement résolvables par le modèle, ou par rapport à la limite de stabilité en terme de pas de temps, nous avons réussi a montrer que le nouveau schéma permet d'obtenir des gains en temps de calcul assez importants. En effet, tous les exemples d'application ou validation qui ont été présentés dans cette thèse ont été produits en utilisant des nombres de Courant supérieurs ou égaux à 1.0 alors que dans la plus part des cas, les méthodes aux éléments finis ou aux différences finis utilisées pour résoudre des systèmes de Boussinesq complètement non linéaires permettent l'intégration des équations avec au mieux un nombre de Courant de 0.5.

De la même manière, nous avons conçu et validé des stratégies numériques adaptées au traitement des conditions aux limites capables de reproduire la dynamique complexe des ondes de gravité se propageant sur une plage. En particulier, des techniques d'absorption et génération des vagues au large, une représentation réaliste du mouvement du trait de côte, ainsi que des conditions de réflection totale sur un mur ont été correctement validées.

D'un autre côté, la capacité à représenter des situations fortement non linéaires, théoriquement présente dans les équations de Serre, a été confirmée à l'aide de la comparaison de résultats numériques avec des mesures expérimentales. De plus, nous avons remarqué que les équations de Serre fournissent une très bonne description de la zone de levée pour une large gamme de houles incidentes, ne produisant qu'une faible sous estimation de l'amplitude maximale près du point de déferlement. Ce résultat constitue une amélioration pratique par rapport au modèle de Boussinesq complètement non linéaire inclus dans le code FUNWAVE [89] de l'Université de Delaware basé sur les équations présentées dans la référence [178]. En effet, la performance numérique dans la zone de levée de ce système d'équations semble être très sensible aux conditions des houles incidentes, en sur estimant de manière flagrante les amplitudes associées lorsque les longueurs d'onde sont de plus en plus faibles (d'après les résultats publiés dans la référence [85]). Cette situation suggère alors que le modèle de Boussinesq fondamentalement basé dans les travaux de Serre [140] possède des propriétés non linéaires plus proches du modèle bi-couche de Boussinesq récemment développé par Lynett et Liu [105] qu'aux équations présentes dans le code FUNWAVE. Tout comme les équations de Serre, les prédictions numériques obtenues avec le modèle bi-couche et présentées dans la référence [106] montrent que celui-ci fourni une excellente description des amplitudes dans la zone de levée

Les propriétés dispersives du système d'équations de Serre sur fond variable originellement obtenu par Seabra-Santos et al. [136] ont été améliorées à l'aide des techniques étudiées par Madsen et al. [109] et Madsen et Schäffer [110]. De cette manière, une extension du modèle vers des profondeurs plus importantes, ou alternativement, vers la description d'ondes de longueur plus faible, a été accomplie. La comparaison des prédictions numériques fournies par le modèle et les mesures expérimentales rassemblées par Dingemans [50] concernant la propagation de houles régulières sur une barre, ont confirmé la limite théorique d'application des équations allant jusqu'à $\kappa h_0 \simeq \pi$, avec κ le nombre d'onde et h_0 une mesure caractéristique de la profondeur d'eau. Il est important de noter que cette valeur est normalement considérée comme étant le commencement du domaine de l'eau profonde (e.g. [110]).

Une fois que le modèle numérique ait été validé, nous avons avancé dans le Chapitre

4 vers des aspects théoriques et expérimentaux concernant le déferlement bathymétrique. En particulier nous avons étudié la pertinance physiques des différentes hypothèses ayant permis à Svendsen [154] de proposer un modèle conceptuel pour le rouleau de déferlement. À l'aide des rares expériences en laboratoire disponibles sur l'organisation spatiale détaillée des vitesses sous des ondes déferlantes [157], nous avons pu vérifier la validité de cette approche. Néanmoins, il s'est avéré que les grandeurs géométriques intégrales de la zone de récirculation existante dans le cas de trois ressauts quasi-stationnaires en similitude de Froude avec des vagues en zone de surf, ne pouvaient être correctement décrites par cette théorie qu'à condition d'inclure des effets de deuxième ordre négligés par Dally et Brown [47] et Stive et De Vriend [150]. C'est ainsi que l'estimation de l'aire du rouleau de déferlement a été sensiblement améliorée dans les cas étudiés lorsque l'hypothèse de faible angle d'inclinaison moyen de celui-ci a été levée. De la même manière, le fait de rajouter une correction dans l'estimation de l'énergie dissipée par les contraintes turbulentes à l'interface entre la zone de récirculation et l'écoulement sous-jacent a permis de diminuer davantage les erreurs associées à cette modélisation.

Par ailleurs, la démarche entamée afin de réécrire le modèle de rouleau nous a permis d'approfondir l'interprétation physique des différents termes présents dans les équations différentielles couramment utilisées pour améliorer les estimations des courants moyens fournies par les modèles méso-échelles à phase moyennée. Les différences théoriques existantes entre les équations proposées par Stive et De Vriend [150], d'une part, et Dally et Brown [47], d'autre part, ont été élucidées. En effet, il est apparu que le coefficient numérique dans le terme de flux d'énergie, qui diffère d'un facteur de deux entre ces modèles, est la conséquence de différentes hypothèses implicitement introduites en ce qui concerne la contribution de l'énergie potentielle du rouleau passivement porté par la vague déferlante. Cependant, cette indétermination théorique n'a pu être surmontée qu'à condition de fournir une information supplémentaire sur la localisation relative de la zone de récirculation sur la vague. C'est à partir d'un résultat semi-empirique, précédemment développé dans les travaux de Cointe et Tulin [40], que nous avons été en mesure de préscrire une valeur numérique pour la distance verticale totale du rouleau de déferlement. Nous avons ainsi pu placer celui-ci sur les vagues concernées. Il est important d'insister sur le fait que la relation théorique obtenu par Cointe et Tulin [40] permettant de relier cette distance avec la hauteur locale des ondes, n'avait encore jamais été vérifiée dans un contexte d'eau peu profonde comme nous l'avons effectuée ici. En outre, cette relation a vérifiée de manière très satisfaisante les mesures expérimentales sur ressaut quasi-stationnaires fournies par Svendsen et al. [157] à condition de modifier la valeur numérique de l'unique paramètre empirique associé. La nouvelle

valeur qui a due être affectée a pu être expliquée en utilisant des arguments physiques en rapport avec les différences topologiques existantes entre un déferlement en eau profonde et en eau peu profonde. De plus, ce résultat semblerait être plus général que le concept de rouleau de déferlement en soi puisque l'hypothèse de distribution hydrostatique des pressions n'a pas été utilisée.

Les connaissances théoriques et expérimentales développées dans le Chapitre 4, et en particulier le résultat concernant la localisation relative du rouleau de déferlement dans une vague, ont été utilisées ensuite pour aborder la problèmatique du déferlement dans les équations de Boussinesq. Dans le cadre de la théorie des chocs en eau peu profonde nous avons entamé l'étude d'une nouvelle paramétrisation pour ce phénomène, cette fois-ci dans le domaine temporel. Pour commencer, une analyse critique, en particulier du modèle type couche de mélange proposé dans les travaux de Kennedy et al. [85], a été effectuée. Il a été clairement établi que celui-ci ne pouvait pas permettre une représentation correcte et simultanée de la décroissance en amplitude et des asymétries horizontales de vagues en zone de surf. Cette constatation nous a poussé alors à développer une approche alternative qui pourrait corriger cette importante limitation.

Le nouveau modèle de déferlement considère, en plus du terme de déficit de quantité de mouvement déjà utilisé dans les approches précédentes, l'incorportation des effets type couche de mélange turbulente qui favorisent une redistribution locale de la masse et de l'énergie potentielle, à l'aide d'un terme de diffusion supplémentaire dans l'équation de continuité. Même si à première vue, le fait de modifier l'équation de conservation de la masse qui dans le cadre de la théorie potentielle est exacte semble discutable, nous avons montré que ce nouveau terme pouvait reproduire de manière efficace certains phénomènes physiques effacés par les hypothèses de fluide parfait. Par ailleurs, nous remarquerons que d'autres équipes de recherche ont déjà avancé quelques arguments théoriques qui vont dans le même sens. En particulier, Liu et Orfila [99] et Simarro et al. [143] ont été amenés à modifier l'équation de conservation de la masse dans un système d'équations de Boussinesq de façon à introduire des effets de couche limite laminaire au fond pour des problèmes de propagation d'ondes solitaires.

Des considérations énergétiques issues de la théorie des chocs en eau peu profonde, ainsi que certains résultats en rapport avec le rouleau de déferlement présentés dans le Chapitre 4, nous ont permis de fournir des expressions mathématiques et l'interprétation physique correspondante pour les coefficients de diffusivité agissant sur la quantité de mouvement et la masse. Le modèle de déferlement a été entièrement défini par les deux paramètres physiques controllant la forme géométrique locale des vagues en zone de surf, à savoir l'index $\gamma = H/d$ et l'angle d'inclinaison moyen, Φ, du front d'onde. En outre, les expériences sur déferlement déversant de Ting et

Kirby [162], qui fournissent une information détaillée de l'évolution spatio-temporelle des vagues se propageant sur une plage à pente constante, nous ont servi à calibrer les valeurs numériques des coefficients d'échelle associés à la paramétrisation. Les valeurs optimales ainsi déterminées, ont fourni un représentation numérique très satisfaisante non seulement de la décroissance en amplitude, mais aussi des asymétries horizontales et verticales des vagues déferlantes. De plus, ce jeu de paramètres optimal a pu être convenablement justifié d'un point de vue physique.

Nous avons ensuite évalué la performance du modèle de déferlement en comparant ces prédictions avec d'autres mesures expérimentales, en gardant les mêmes valeurs numériques pour les paramètres obtenues dans le cas de l'expérience de Ting et Kirby [162]. Les résultats présentés en particulier sur les cas tests produits par Hansen et Svendsen [77] pour différentes conditions de houle régulière, ont montré que la nouvelle paramétrisation était en mesure de bien représenter les évolutions des ondes en zone de surf pour des déferlements de type glissant. Même si le point de déferlement n'a pas pu être correctement prédit dans le cas d'un déferlement plongeant, la décroissance globale en amplitude de la houle a été elle aussi, dans ce cas, convenablement reproduite dans la zone de surf interne. Ces résultats confèrent donc à l'argumentation qui nous a permis d'écrire le modèle une certaine solidité physique puisque elle est basée fondamentalement sur des informations valables pour des vagues déferlantes en quasi-équilibre. Par ailleurs, il a été démontré que les predictions numériques dans le cas des déferlements plongeants pouvaient être améliorées en augmentant la valeur critique pour la pente avale de l'onde utilisée comme déclencheur du déferlement.

Enfin, une expérience de laboratoire concernant la propagation et la déferlement d'une onde solitaire sur une plage uniforme conduite par Synolakis [158], nous a permis non seulement de confirmer les capacités du modèle hydrodynamique complet, mais aussi la performance de la condition de trait de côte variable en présence du déferlement.

6.2 Perspectives futures

Le travail accompli dans cette thèse a permis l'élaboration d'un outil de prédiction de la houle le long d'un profil perpendiculaire à la plage en incorporant la plus part des phénomènes physiques qui peuvent influencer les évolutions spatio-temporelles des ondes depuis des profondeurs intermédiaires, et jusqu'au trait de côte. L'excellente perfomance du schéma compact aux volumes finis qui a été développé encourage fortement une extension du modèle en deux dimensions horizontales (2DH). En effet, cela est techniquement faisable en raison des récents développements théoriques qui se poursuivent

de manière très active sur ce type de schémas numériques et qui ont déjà donné lieu à des modèles 3D appliqués sur des géométries complexes (e.g. [93, 142]). Néanmoins, un certain nombre d'améliorations pratiques sont requises de façon a pouvoir concevoir un modèle équivalent applicable dans un environnement côtier. En particulier, les aspects présentés ci-dessous devront être abordés de manière spécifique :

1. Développement de conditions aux limites 2DH d'absorption/génération des ondes au large.

2. Amélioration du traitement de la condition aux limites de trait de côte variable.

3. Algorithmique de suivie des crêtes des vagues efficace adaptée à la propagation 2DH et aux houles irrégulières.

4. Extension du modèle de déferlement pour des applications 2DH.

5. Amélioration des critères de déferlement utiliśees dans la pratique de manière à reproduire les différents types de déferlement qui peuvent exister en nature.

6. Incorporation éventuelle de termes supplémentaires de façon à reproduire les interactions 2DH entre structures tourbillonnaires et mélange turbulent dans la direction long-shore.

Parallèlement, dans sa forme présente le modèle hydrodynamique de Boussinesq que nous avons développé pourrait parfaitement servir à fournir des informations indispensables à une prédiction court/moyen terme des évolutions morphodynamiques d'un profil de plage sableuse. Pour cela il faudra coupler le code hydrodynamique à des formules de transport sédimentaire intra-phase qui puissent tenir compte des phénomènes d'accélération dissymétrique reponsables en particulier du remblayement des plages en périodes d'accalmie. Alternativement, des efforts de recherche pourraient encore se poursuivre de manière à mieux representer les profils de vitesses dans la verticale en incorporant à ce moment là une phénoménologie plus détaillée des processus concernées (i.e. modèle de couche limite turbulente, remise en suspension des sédiments, transport par charriage au fond et par suspension dans la colonne d'eau, intéractions entre phase solides et fluides, etc.). Cependant, cette approche mécaniciste ne pourra être convenablement abordée qu'à condition d'approfondir les connaissances fondamentales actuelles en rapport avec les différents processus complexes qui ont lieu en particulier dans la zone de surf. Dans ce sens, les mesures expérimentales de plus en plus fines qui pourront être mises à disposition dans les années à venir constribueront sans aucun doute à l'amélioration de la compréhension physique des intérations complexes

entre le fluide et les sédiments, en fournissant au même temps des meilleurs moyens de représenter mathématiquement les phénomènes concernés.

Finalement, il est parfaitement légitime de se demander dans quelle mesure les efforts de recherche concernant le développement de modèles hydrodynamiques moyennées dans la profondeur, tel que Boussinesq ou Saint-Venant, doivent se poursuivre. Et cela en raison des importantes et rapides évolutions du matériel informatique ainsi que des approches théoriques de modélisation 3D de la turbulence qui s'avèrent être de plus en plus performantes (e.g. DNS, LES, DES, etc.). Néanmoins, nous pensons fermement que plus que mettre en concurrence ces différentes approches, il est nécessaire de les faire interagir puisqu'on voit mal comment on pourrait être capable de prédire par exemple, des évolutions morphologiques dans le moyen ou le long terme à l'aide des modélisation 3D complètes, et cela au moins dans les dix années à venir. Au contraire, une approche multi-échelles, accompagnée d'efforts expérimentaux à la hauteur des besoins, à la fois en laboratoire et in-situ, devraient favoriser le développement d'outils opérationnels de modélisation hydro-sédimentaire en mesure de fournir des réponses objectives et fiables aux différentes questions qui se posent actuellement concernant la gestion durable de l'environnement littoral.

Bibliography

[1] M.B. Abbott, A.D. McCowan, and I.R. Warren. Accuracy of short-wave numerical model. *J. Hyd. Res.*, 110(10):1287–1301, 1984.

[2] J.S. Allen, P.A. Newberger, and R. Holman. Nonlinear shear instabilities of alongshore currents on plane beaches. *J. Fluid Mech.*, 310:181–213, 1996.

[3] O.H. Andersen and J. Fredsoe. *Transport of suspended sediment along the coast.* Progress Report No. 59. Institute of Hydrodynamics and Hydraulic Engineering, ISVA, Technical University of Denmark, 1983.

[4] J.S. Antunes do Carmo, F.J. Seabra-Santos, and A.B. Almeida. Numerical solution of the generalized Serre equations with the McCormack finite-difference scheme. *Int. J. Numer. Meth. in Fluids*, 16:725–738, 1993.

[5] J.S. Antunes do Carmo, F.J. Seabra-Santos, and E. Barthélemy. Surface waves propagation in shallow water: A finite element model. *Int. J. Numer. Meth. in Fluids*, 16:447–459, 1993.

[6] M. Arie and H. Rouse. Experiments on two-dimensional flow over a normal wall. *J. Fluid Mech.*, 1:129–141, 1954.

[7] T.E. Baldock, P. Holmes, and D.P. Horn. Low frequency swash motion induced by wave grouping. *Coastal Eng.*, 32:197–222, 1997.

[8] A. Balzano. Evaluation of methods for numerical simulation of wetting and drying in shallow water flow models. *Coastal Eng.*, 33:83–107, 1998.

[9] E. Barthélemy. Nonlinear shallow water theories for coastal waves. *Surveys Geophys.*, 25(3-4):315–337, 2004.

[10] J.A. Battjes. Surf zone dynamics. *Ann. Rev. Fluid Mech.*, 20:257–291, 1988.

[11] J.A. Battjes and J.P.F.M. Janssen. Energy loss and set-up due to breaking of random waves. In *16th. Int. Conf. Coastal Eng.*, pages 466–480, Hamburg, Germany, 1978.

[12] A. Bayram and M. Larson. Wave transformation in the nearshore zone : comparison between a Boussinesq model and field data. *Coastal Eng.*, 39:149–171, 2000.

[13] S. Beji and J.A. Battjes. Experimental investigation of wave propagation over a bar. *Coastal Eng.*, 19:151–162, 1993.

[14] G. Bellotti and M. Brocchini. On the shoreline boundary conditions for Boussinesq-type models. *Int. J. Numer. Meth. Fluids*, 37:479–500, 2001.

[15] R. Bernetti, E.F. Toro, and M. Brocchini. An operator-splitting method for long waves. In *Long Waves Symp.*, volume 1, pages 49–56, Tessaloniki, Greece, 2003.

[16] E.C.F. Bird. *Coastline Changes.* John Wiley & Sons, 1st edition, 1985.

[17] P. Bonneton. A note on wave propagation in the inner surf zone. *Comptes Rendues Académie des Sciences*, Série IIb:27–33, 2001.

[18] P. Bonneton. Nonlinear dynamics of surface waves in the inner surf zone. *Rév. Franç. Génie Civil*, 7(9):1061–1076, 2003.

[19] P. Bonneton. Wave celerity in the inner surf zone. In *29th. Int. Conf. Coastal Eng.*, pages 392–401, Lisbon, Portugal, 2004.

[20] P. Bonneton. Analyse physique et modélisation des processus hydrodynamiques en zone de surf. *Oceanis*, 2005. in press.

[21] P. Bonneton. A shock-wave model for periodic-wave transformation and energy dissipation in the inner surz zone. *Coastal Eng.*, 2005. submitted.

[22] J. Boussinesq. Théorie des ondes et des remous qui se propagent le long d'un canal rectangulaire horizontal, en communiquant au liquide contenu dans ce canal des vitesses sensiblement pareilles de la surface au fond. *J. Math. Pure Appl.*, 2:55–108, 1872.

[23] A.J. Bowen, D.L. Inman, and V.P. Simmons. Wave set-down and set-up. *J. Geophys. Res.*, 73(8):2569–2577, 1968.

[24] S.F. Bradford and B.F. Sanders. Finite-volume models for unidirectional, nonlinear, dispersive waves. *J. Waterw. Port Coastal Oc. Eng.*, 128(4):173–182, 2002.

[25] R. Briganti, R. E. Musumeci, G. Bellotti, M. Brocchini, and E. Foti. Boussinesq modelling of breaking waves : Description of turbulence. *J. Geophys. Res.*, 109(C07015), 2004.

[26] M. Brocchini. Free surface boundary conditions at a bubbly/weakly splashing air-water interface. *Phys. Fluids*, 14(6):1834–1840, 2002.

[27] M. Brocchini, M. Drago, and L. Iovenitti. The modelling of short waves in shallow waters. Comparisons of numerical models based on Boussinesq and Serre equations. In *23th. Int. Conf. Coastal Eng.*, pages 76–88, Venice, Italy, 1992.

[28] M. Brocchini and D.H. Peregrine. The dynamics of strong turbulence at free surfaces. Part 1 : Description. *J. Fluid Mech.*, 449:225–254, 2001.

[29] M. Brocchini and D.H. Peregrine. The dynamics of strong turbulence at free surfaces. Part 2 : Free surface boundary condition. *J. Fluid Mech.*, 449:255–290, 2001.

[30] M.H. Carpenter, D. Gottlieb, and S. Abarbanel. The stability of numerical boundary treatments for compact high-order finite difference schemes. *J. Comput. Phys.*, 108:272–295, 1993.

[31] G.F. Carrier and H.P. Greenspan. Water waves of finite amplitude on a sloping beach. *J. Fluid Mech.*, 4:97–109, 1958.

[32] B. Castelle, P. Bonneton, N. Sénéchal, H. Dupuis, R. Butel, and D. Michel. Dynamics of wave-induced currents over a multi-barred beach on the Aquitanian coast. *Continental Shelf Res.*, 2005. in press.

[33] R. Certain and J.-P. Barusseau. Sediment availability and conceptual models of sand bars morphodynamics for a microtidal beach (sète, france). In *5th. Int. Conf. Coastal Dyn.*, Barcelona, Spain, 2005. in press.

[34] K.-A. Chang and P.L.-F. Liu. Experimental investigation of turbulence generated by breaking waves in water of intermediate depth. *Phys. FLuids*, 11(11):3390–3400, 1999.

[35] J.C. Church and E.B. Thornton. Effects of breaking wave induced turbulence within a longshore current model. *Coastal Eng.*, 20:1–28, 1993.

[36] R. Cienfuegos. Rôle du rouleau de déferlement dans les courants engendrés par la houle. Master's thesis, Institut National Polytechnique de Grenoble, France, 2002.

[37] R. Cienfuegos, E. Barthélemy, and P. Bonneton. Roller modelling in the context of undertow prediction. In *29th. Int. Conf. Coastal Eng.*, pages 318–330, Lisbon, Portugal, 2004.

[38] R. Cienfuegos, E. Barthélemy, and P. Bonneton. A new wave-breaking parametrization for Boussinesq-type equations. In *5th Int. Symp. Oc. Wave Meas. Anal.*, Madrid, Spain, 2005. CD-ROM.

[39] R. Cienfuegos, E. Barthélemy, and P. Bonneton. Résolution numérique en volumes finis d'un système d'équations de Serre étendu. *Rév. Europ. Génie Civil*, 9(7-8):889–902, 2005.

[40] R. Cointe and M.P. Tulin. A theory of steady breakers. *J. Fluid Mech.*, 276:1–20, 1994.

[41] D.T. Cox. *Experimental and numerical modelling of surf zone hydrodynamics.* PhD Thesis, University of Delaware, USA, 1995.

[42] D.T. Cox and S.L. Anderson. Statistics of intermittent surf zone turbulence and observations of large eddies using PIV. *Coastal Eng.*, 43:121–131, 2001.

[43] D.T. Cox and N. Kobayashi. Kinematic undertow model with logarithmic boundary layer. *J. Waterw. Port Coastal Oc. Eng.*, 123(6):354–360, 1997.

[44] D.T. Cox, N. Kobayashi, and A. Okayasu. Bottom shear stress in the surf zone. *J. Geophys. Res.*, 101(C6):14337–14348, 1996.

[45] D. Dabiri and M. Gharib. Experimental investigation of the vorticity generation within a spilling water wave. *J. Fluid Mech.*, 330:113–139, 1997.

[46] W. Dally. Modeling nearshore currents on reef-fronted beaches. In *Coastal Dyn.'01*, pages 558–567, Lund, Sweeden, 2001.

[47] W. Dally and C.A. Brown. A modelling investigation of the breaking wave roller with application to cross-shore currents. *J. Geophys. Res.*, 100(C2):24873–24883, 1995.

[48] W. Dally, R.G. Dean, and R.A. Dalrymple. Wave height variation accross beaches of arbitrary profile. *J. Geophys. Res.*, 90(C6):11917–11927, 1985.

[49] R. Deigaard and J. Fredsøe. Shear stress distribution in dissipative water waves. *Coastal Eng.*, 13:357–378, 1989.

[50] M.W. Dingemans. Comparison of computations with Boussinesq-like models and laboratory measurements. Report H-1684.12, Delft Hydraulics, 1994. 32 pp.

[51] M.W. Dingemans. *Water Wave Propagation Over Uneven Bottoms.* World Scientific Pub., 1st edition, 1997.

[52] T. G. Drake and J. Calantoni. Discrete particle model for sheet flow sediment transport in the nearshore. *J. Geophys. Res.*, 106(15):19859–19868, 2001.

[53] J.H. Duncan. An experimental investigation of breaking waves produced by a towed hydrofoil. *Proc. R. Soc. London, A*, 377:331–348, 1981.

[54] J.H. Duncan. Spilling breakers. *Ann. Rev. Fluid Mech.*, 33:519–547, 2001.

[55] D.R. Durran. *Numerical Methods for Wave Equations in Geophysical Fluid Dynamics.* Springer, 1st edition, 1999.

[56] M. Duval, D. Astruc, and D. Legendre. Two-phase flow modelling of breaking waves without interface reconstruction. In *14th Offshore and Polar Eng. Conf. ISOPE*, Toulon, France, 2004. CD-Rom.

[57] F. Engelund. A simple theory of weak hydraulic jumps. *Inst. Hydrodyn. Hydraul. Eng. (ISVA), Tech. Univ. Denmark*, 54:29–32, 1981. Progress Rep.

[58] K.S. Erduran, S. Ilic, and V. Kutija. Hybrid finite-volume finite-difference scheme for the solution of Boussinesq equations. *Int. J. Numer. Meth. Fluids*, 2005. in press.

[59] European Union. Living with coastal erosion in Europe : Sediment and space for sustainability. Service contract B4-3301/2001/329175/MARS/B3, Directorate General Environment European Comission, 2004. http://www.eurosion.org.

[60] J.H. Ferziger and M. Perić. *Computational Methods for Fluid Dynamics.* Springer, 3rd edition, 2002.

[61] C. Fochesato, S.T. Grilli, and P. Guyenne. Note on non-orthogonality of local curvilinear co-ordinates in a three-dimensional boundary element method. *Int. J. Numer. Meth. in Fluids*, 48:305–324, 2005.

[62] D.R. Fuhram and H.B. Bingham. Numerical solution of fully non-linear and highly dispersive Boussinesq equations in two horizontal dimensions. *Int. J. Numer. Meth. Fluids*, 44:231–255, 2004.

[63] D.R. Fuhram, H.B. Bingham, P.A. Madsen, and P.G. Thomsen. Linear and non-linear stability analysis for finite difference discretizations of high-order Boussinesq equations. *Int. J. Numer. Meth. Fluids*, 45:751–773, 2004.

[64] D.R. Fuhrman, H.B. Bingham, and P.A. Madsen. Nonlinear wave-structure interaction with a high-order Boussinesq model. *Coastal Eng.*, 52:655–672, 2005.

[65] D.V. Gaitonde, J.S. Shang, and J.L. Young. Practical aspects of higher-order numerical schemes for wave propagation phenomena. *Int. J. Numer. Meth. Eng.*, 45:1849–1869, 1999.

[66] E.L. Gallagher, S. Elgar, and R.T. Guza. Observation of sand bar evolution on a natural beach. *J. Geophys. Res.*, 193(C2):3203–3215, 1998.

[67] C.J. Galvin. Breaker type classification on three laboratory beaches. *J. Geophys. Res.*, 73(8):3651–3659, 1968.

[68] P. García-Navarro and M.E. Vazquez-Cendón. On the numerical treatment of source terms in the shallow water equations. *Comput. Fluids*, 29:951–979, 2000.

[69] M.F. Gobbi and J.T. Kirby. Wave evolution over submerged sills : tests of a high-order Boussinesq model. *Coastal Eng.*, 37:57–96, 1999.

[70] M.F. Gobbi, J.T. Kirby, and G. Wei. A fully non-linear Boussinesq model for surface waves. Part 2. extension to $O(kh)^4$. *J. Fluid Mech.*, 405:181–210, 2000.

[71] N. Goutal and Maurel F. Proceedings of the 2nd Workshop on Dam-Break Wave Simulation. Technical report HE-43/97/016/a, Électricité de France, LNHE, 1997.

[72] K. Govender, G.P. Mocke, and M.J. Alport. Video-imaged surf zone wave and roller structures and flow field. *J. Geophys. Res.*, 107(C7):9.1–9.21, 2002.

[73] J.-M. Greenberg and A.-Y. Leroux. A well-balanced scheme for the numerical processing of source terms in hyperbolic equations. *SIAM J. Num. Anal.*, 33:1–16, 1996.

[74] S. Guibourg. *Modélisation numérique et expérimentale des houles bidimensionnelles en zone côtière.* PhD Thesis, Université Joseph Fourier - Grenoble I, France, 1994.

[75] K. Guizien and E. Barthélemy. Accuracy of solitary wave generation by a piston wave maker. *J. Hyd. Res.*, 40(3):321–331, 2002.

[76] B. Gustafsson. The convergence rate for difference approximations to mixed initial boundary value problems. *Math. Comput.*, 29(130):396–406, 1975.

[77] J.B. Hansen and I. Svendsen. *Regular waves in shoaling water experimental data.* Institute of Hydrodynamics and Hydraulic Engineering, Technical University of Denmark, 1979.

[78] F. Hoefel and S. Elgar. Wave-induced sediment transport and sandbar migration. *Science*, 299:1885, 2003.

[79] T.-J. Hsu and D.M. Hanes. Effects of wave shape on sheet flow sediment transport. *J. Geophys. Res.*, 109:C05025, 2004.

[80] F.Q. Hu, M.Y. Hussaini, and J.L. Manthey. Low-dissipation and low-dispersion Runge-Kutta schemes for computational acoustics. *J. Comput. Phys.*, 124:177–191, 1996.

[81] M.E. Hubbard and N. Dodd. A 2D numerical model of wave run-up and overtopping. *Coastal Eng.*, 47:1–26, 2002.

[82] D. Hurther, H. Michallet, and X. Gondran. Measurements at turbulent scales of waves, velocity and concentration in the surf zone of an irregular wave field in equilibrium with its mobile bed. In *30th. Int. Conf. Coastal Eng.*, San Diego, USA, 2006. submitted.

[83] M. Kamalinezhad. *Plages en équilibre morphologique et hydrodynamique associée.* PhD Thesis, Institut National Polytechnique de Grenoble, France, 2004.

[84] T.V. Karambas and C. Koutitas. A breaking wave propagation model based on the Boussinesq equations. *Coastal Eng.*, 18:1–19, 1992.

[85] A.B. Kennedy, Q. Chen, J.T. Kirby, and R.A. Dalrymple. Boussinesq modelling of wave transformation, breaking and runup. I : 1D. *J. Waterw. Port Coastal and Oc. Eng.*, 126(1):39–48, 2000.

[86] O. Kimmoun and H. Branger. A PIV investigation on laboratory surf-zone breaking waves over a slopping beach. *J. Fluid Mech.*, submitted, 2005.

[87] J.T. Kirby. Boussinesq models and applications to nearshore wave propagation, surfzone processes and wave-induced currents. In V.C. Lakhan, editor, *Advances in Coastal Modelling*, pages 1–41. Elsevier, 2003.

[88] J.T. Kirby and J.M. Kaihatu. Structure of frequency domain models for random wave breaking. In *25th. Int. Conf. Coastal Eng.*, pages 1114–1155, Orlando, USA, 1996.

[89] J.T. Kirby, G. Wei, Q. Chen, A.B. Kennedy, and R.A. Dalrymple. FUNWAVE 1.0. Fully nonlinear Boussinesq wave model. Documentation and user's manual. Report-CACR-98-06, Center for Applied Coastal Research, Department of Civil Engineering, Delaware University, 1998. 80 pp.

[90] M.H. Kobayashi. On a class of Padé finite volume methods. *J. Comput. Phys.*, 156:137–180, 1999.

[91] N. Kobayashi, G.S. De Silva, and K.D. Watson. Wave transformation and swash oscillation on gentle and steep slopes. *J. Geophys. Res.*, 94:951–966, 1989.

[92] D.J. Korteweg and G. de Vries. On the change of form of long waves advancing in a rectangular canal, and on a new type of long stationary waves. *Phil. Mag. J.*, 39:422–443, 1895.

[93] C. Lacor, S. Smirnov, and M. Baelmans. A finite volume formulation of compact central schemes on arbitrary structured grids. *J. Comput. Phys.*, 198:535–566, 2004.

[94] B. Le Méhauté. On non-saturated breakers and wave run-up. In *8th. Int. Conf. Coastal Eng.*, pages 77–92, Mexico City, Mexico, 1962.

[95] S.K. Lele. Compact finite difference schemes with spectral-like resolution. *J. Comput. Phys.*, 103:16–42, 1992.

[96] R.J. LeVeque. Balancing source terms and flux gradients in high-resolution Godunov methods : the quasi-steady wave-propagation algorithm. *J. Comp. Phys.*, 146(1):346–365, 1998.

[97] R.J. Leveque. *Finite Volume Methods for Hyperbolic Problems*. Cambridge Texts in Applied Mathematics. Cambridge University Press, 2002.

[98] J.C. Lin and D. Rockwell. Evolution of a quasi-steady breaking wave. *J. Fluid Mech.*, 302:29–44, 1995.

[99] P.L.-F. Liu and A. Orfila. Viscous effects on transient long wave propagation. *J. Fluid Mech.*, 520:83–92, 2004.

[100] M.S. Longuet-Higgins. Capillary rollers and bores. *J. Fluid Mech.*, 240:659–679, 1992.

[101] M.S. Longuet-Higgins. Shear instability in spilling breakers. *Proc. R. Soc. Lond. A.*, 446:399–409, 1994.

[102] M.S. Longuet-Higgins and J.S. Turner. An 'entraining plume'model of a spilling breaker. *J. Fluid Mech.*, 63:1–20, 1974.

[103] P. Lubin, S. Vincent, J.-P. Caltagirone, and S. Abadie. Three dimensional large-eddy simulation of vortices induced by plunging by plunging breaking waves. In *29th. Int. Conf. Coastal Eng.*, pages 344–356, Lisbon, Portugal, 2004.

[104] H.R. Luth, G. Klopman, and N. Kitou. Kinematics of waves breaking partially on an offshore bar; LDV measurements of waves with and without a net onshore current. Report H-1573, Delft Hydraulics, 1994. 40 pp.

[105] P. Lynett and L.-F. Liu. A two-layer approach to wave modelling. *Proc. Roy. Soc. London*, A(460):2637–2669, 2004.

[106] P.J. Lynett. Nearshore modeling using high-order Boussinesq equations. In *5th Int. Symp. Oc. Waves Meas. Anal.*, Madrid, Spain, 2005. CD-ROM.

[107] P.J. Lynett, T.R. Wu, and P.L.F. Liu. Modeling wave runup with depth-integrated equations. *Coastal Eng.*, 46:89–107, 2002.

[108] P.A. Madsen, H.B. Bingham, and H.A. Schäffer. Boussinesq formulation for fully non-linear and extremely dispersive water waves. *Proc. Roy. Soc. London*, A(459):1075–1104, 2003.

[109] P.A. Madsen, R. Murray, and O.R. Sørensen. A new form of the Boussinesq equations with improved linear dispersion characteristics. *Coastal Eng.*, 15:371–388, 1991.

[110] P.A. Madsen and H.A. Schäffer. Higher-order Boussinesq-type equations for surface gravity waves : derivation and analysis. *Phil. Trans. Roy. Soc. London*, A(356):3123–3184, 1998.

[111] P.A. Madsen, O.R. Sørensen, and H.A. Schäffer. Surf zone dynamics simulated by a Boussinesq-type model : Part I. Model description and cross-shore motion of regular waves. *Coastal Eng.*, 32:255–288, 1997.

[112] P.A. Madsen, O.R. Sørensen, and H.A. Schäffer. Surf zone dynamics simulated by a Boussinesq-type model : Part II. Surf beat and swash oscillations for wave groups and irregular waves. *Coastal Eng.*, 32:289–319, 1997.

[113] H. Mase. Frequency down-shift on swash oscillation compared to incident waves. *J. Hyd. Res.*, 33(3):397–411, 1995.

[114] K. Meftah, P. Sergent, and P. Gomi. Linear analysis of a new type of extended Boussinesq model. *Coastal Eng.*, 51(2):185–206, 2004.

[115] C.C. Mei. *The Applied Dynamics of Ocean Surface Waves.* World Scientific, 1st edition, 1989.

[116] S.K. Misra, J.T. Kirby, M. Brocchini, F. Veron, and C. Kambhamettu. Coherent turbulent structures in a quasi-steady spilling breaker. In *5th Int. Symp. Oc. Waves Meas. Anal.*, Madrid, Spain, 2005. CD-ROM.

[117] S.K. Misra, J.T. Kirby, F. Veron, and C. Kambhamettu. Extra strain rates in spilling breaking waves. In *29th. Int. Conf. Coastal Eng.*, pages 370–378, Lisbon, Portugal, 2004.

[118] W.H. Munk. The solitary wave theory and its application to surf problems. *Ann. New York Acad. Sc.*, 51:376–424, 1949.

[119] R.E. Musumeci. *The flow in the surf zone : A fully nonlinear Boussinesq model for breaking waves.* PhD Thesis, University of Catania, Italy, 2002.

[120] R.E. Musumeci, I.A. Svendsen, and J. Veeramony. The flow in the surf zone : a fully nonlinear Boussinesq-type approach. *Coastal Eng.*, 52:565–598, 2005.

[121] R.B. Nairn, J.A. Roelvink, and H.N. Southgate. Transition zone width and implications for modelling surfzone hydrodynamics. In *22th. Int. Conf. Coastal Eng.*, pages 68–81, Delft, The Netherland, 1990.

[122] 0. Nwogu. Alternative form of boussinesq equations for nearshore wave propagation. *J. Waterw. Port Coastal Oc. Eng.*, 119(6):618–638, 1993.

[123] T. Okamoto and D.R. Basco. Experimental verification of the relative trough Froude number (RTFN) method for wave breaking in Boussinesq models. In *29th. Int. Conf. Coastal Eng.*, pages 357–369, Lisbon, Portugal, 2004.

[124] F. Ozanne, A.J. Chadwick, D.A. Huntley, D.J. Simmonds, and J. Lawrence. Velocity predictions for shoaling and breaking waves with a Boussinesq-type model. *Coastal Eng.*, 44:361–397, 2000.

[125] D.H. Peregrine. Long waves on beaches. *J. Fluid Mech.*, 27(4):815–827, 1967.

[126] D.H. Peregrine. Breaking waves on beaches. *Ann. Rev. Fluid Mech.*, 15:149–178, 1983.

[127] D.H. Peregrine. Surf zone currents. *Theoretical Comp. Fluid Dyn.*, 10:295–309, 1998.

[128] W.H. Press, B.P. Flannery, S.A. Teukolsky, and W.T. Vetterling. *Numerical Recipies in Fortran.* Cambridge University Press, U.K., 2nd edition, 1992.

[129] B. Raubenheimer, R.T. Guza, and S. Elgar. Wave transformation accross the inner surf zone. *J. Geophys. Res.*, 101(C11):25589–25598, 1996.

[130] A.J.H.M. Reniers and J.A. Battjes. A laboratory study of longshore currents over barred and non-barred beaches. *Coastal Eng.*, 30:1–22, 1997.

[131] J.A. Roelvink and M.J.F. Stive. Bar-generating cross-shore flow mechanisms on a beach. *J. Geophys. Res.*, 94(C4):4785–4800, 1989.

[132] B.G. Ruessink, J.R. Miles, F. Feddersen, R.T. Guza, and S. Elgar. Modeling the alongshore current on barred beaches. *J. Geophys. Res.*, 106(C10):22451–22464, 2001.

[133] H.A. Schäffer, P.A. Madsen, and R.A. Deigaard. A Boussinesq model for waves breaking in shallow water. *Coastal Eng.*, 20:185–202, 1993.

[134] H. Schlichting and K. Gersten. *Boundary layer theory.* Springer, Berlin Heidelberg, 8th edition, 2000.

[135] F.J. Seabra-Santos. *Contribution à l'étude des ondes de gravité bidimensionnelles en eau peu profonde.* PhD Thesis, Institut National Polytechnique de Grenoble, France, 1985.

[136] F.J. Seabra-Santos, D.P. Renouard, and A.M. Temperville. Numerical and experimental study of the transformation of a solitary wave over a shelf or isolated obstacle. *J. Fluid Mech.*, 176:117–134, 1987.

[137] F.J. Seabra-Santos, D.P. Renouard, and A.M. Temperville. Etude théorique et expérimentale des domaines de validité des théories d'évolution des ondes en eau peu profonde. *Ann. Geophys.*, 6:671–680, 1988.

[138] N. Sénéchal, H. Dupuis, and P. Bonneton. Preliminary hydrodynamic results of a field experiment on a barred beach, Truc Vert beach on october 2001. *Oc. Dyn.*, 54:408–414, 2004.

[139] T.K. Sengupta. *Fundamentals of Computational Fluid Dynamics.* Universities Press (India) Private Limited, 1st edition, 2004.

[140] F. Serre. Contribution à l'étude des écoulements permanents et variables dans les canaux. *Houille Blanche*, 8:374–388, 1953.

[141] F. Shi, R.A. Dalrymple, J.T. Kirby, and A. Kennedy. A fully nonlinear Boussinesq model in generalized curvilinear coodinates. *Coastal Eng.*, 42:337–358, 2001.

[142] R.K. Shukla and X. Zhong. Derivation of high-order compact finite difference schemes for non-uniform grid using polynomial interpolation. *J. Comput. Phys.*, 204:404–429, 2005.

[143] G. Simarro, A. Orfila, and P.L.-F. Liu. Viscous effects on the propagation of solitary waves in a wave tank : a numerical model. In *5th Int. Symp. Oc. Waves Meas. Anal.*, Madrid, Spain, 2005. CD-ROM.

[144] C. Skotner and C.J. Apelt. Application of a Boussinesq model for the computation of breaking waves. *Ocean Eng.*, 26:905–925, 1999.

[145] P.K. Stansby. Solitary wave run up and overtopping by a semi-implicit finite-volume shallow-water Boussinesq model. *J. Hyd. Res.*, 41(6):639–647, 2003.

[146] P.K. Stansby and T. Feng. Kinematics and depth-integrated terms in surf zone waves from laboratory measurement. *J. Fluid Mech.*, 529:279–310, 2005.

[147] R. Staub. *Contribution à l'étude des ondes de gravité en eau peu profonde.* PhD Thesis, Université de Grenoble, France, 1972.

[148] M. Stiassnie and D.H. Peregrine. Shoaling of finite amplitude surface waves on water of slowly varying depth. *J. Fluid Mech.*, 97:783–805, 1980.

[149] M.J.F. Stive. Energy dissipation in waves breaking on gentle slopes. *Coastal Eng.*, 8:99–127, 1984.

[150] M.J.F. Stive and H.J. De Vriend. Shear stresses and mean flow in shoaling and breaking waves. In *24th. Int. Conf. Coastal Eng.*, pages 594–608, Kobe, Japan, 1994.

[151] M.J.F. Stive and A.J.H.M. Reniers. Sandbars in motion. *Science*, 299:1855, 2003.

[152] J.J. Stoker. *Water waves.* Interscience Publishers, New York, 1957.

[153] C.H. Su and R.M. Mirie. On head-on collisions between two solitary waves. *J. Fluid Mech.*, 98:509–525, 1980.

[154] I.A. Svendsen. Mass flux and undertow in a surf zone. *Coastal Eng.*, 8:347–365, 1984.

[155] I.A. Svendsen, P.A. Madsen, and J.B. Hansen. Wave characteristics in the surf zone. In *16th. Int. Conf. Coastal Eng.*, pages 520–539, Hamburg, Germany, 1978.

[156] I.A. Svendsen and U. Putrevu. Surf zone hydrodynamics. In P.L.-F. Liu, editor, *Advances in Ocean and Coastal Engineering*, volume 2. World Scientific, 1996.

[157] I.A. Svendsen, J. Veeramony, J. Bakunin, and J.T. Kirby. The flow in weak turbulent hydraulic jumps. *J. Fluid Mech.*, 418:25–57, 2000.

[158] C.E. Synolakis. The runup of solitary waves. *J. Fluid Mech.*, 185:523–545, 1987.

[159] A. Temperville. *Contribution à l'étude des ondes de gravité en eau peu profonde.* PhD Thesis, Institut National Polytechnique de Grenoble, France, 1985.

[160] H. Tennekes and J.L. Lumley. *A first course in turbulence.* MIT Press, USA, 1st edition, 1972.

[161] E.B. Thornton and R.T. Guza. Transformation of wave height distribution. *J. Geophys. Res.*, 88(C10):5925–5938, 1983.

[162] F.C.K. Ting and J.T. Kirby. Observation of undertow and turbulence in a laboratory surf zone. *Coastal Eng.*, 24:51–80, 1994.

[163] F.C.K. Ting and J.T. Kirby. Dynamics of syrf-zone turbulence in a spilling breaker. *Coastal Eng.*, 27:131–160, 1996.

[164] W. Tollmien. Berechnung turbulenter ausbeitungovargange. *Angew. Math. Mech.*, IV:468, 1924.

[165] E.F. Toro. *Shock-Capturing Methods for Free-Surface Flows.* John Wiley, New York, 1st edition, 2001.

[166] M. Utku. *The relative trough Froude number : A new criteria for wave breaking.* PhD Thesis, Old Dominion University, Norfolk, USA, 1999.

[167] M. Utku and D.R. Basco. A new criteria for wave breaking based on the relative trough Froude number. In *28th. Int. Conf. Coastal Eng.*, pages 258–268, Cardiff, Wales, 1994.

[168] A. Van Dongeren, A.J.H.M. Reniers, J.A. Battjes, and I.A. Svendsen. Numerical modeling of infragravity wave response during DELILAH. *J. Geophys. Res.*, 108(C9):3288, 2003.

[169] A.R. Van Dongeren, F.E. Sancho, I.A. Svendsen, and U. Putrevu. SHORECIRC : A quasi 3-D nearshore model. In *24th. Int. Conf. Coastal Eng.*, pages 2741–2754, Kobe, Japan, 1994.

[170] A.R. Van Dongeren and I.A. Svendsen. Absorbing-generating boundary conditions for shallow water models. *J. Waterw. Port Coastal Oc. Eng.*, 123(6):303–313, 1997.

[171] M.E. Vázquez-Cendón. Improved treatment of source terms in upwind schemes for the shallow water equations in channel with irregular geometry. *J. Comput. Phys.*, 148:497–526, 1999.

[172] J. Veeramony and I.A. Svendsen. The flow in surf-zone waves. *Coastal Eng.*, 39:93–122, 2000.

[173] R. Vichnevetsky and J.B. Bowles. *Fourier Analysis of Numerical Approximations of Hyperbolic Equations*. Soc. Ind. & App. Math. (SIAM), 2nd edition, 1982.

[174] S. Vincent, J.-P. Caltagirone, and P. Bonneton. Numerical modelling of bore propagation and run-up on sloping beaches using a MacCormack TVD scheme. *J. Hydr. Res.*, 39(1):41–49, 2001.

[175] M. Walkley and M. Berzins. A finite element method for the one-dimensional extended Boussinesq equations. *Int. J. Numer. Meth. Fluids*, 29:143–157, 1999.

[176] D.J.R. Walstra, G.P. Mocke, and F. Smit. Roller contribution as inferred from inverse modelling techniques. In *25th. Int. Conf. Coastal Eng.*, pages 1205–1218, Orlando, Florida, 1996.

[177] G. Wei and J.T. Kirby. Time-dependent numerical code for extended Boussinesq equations. *J. Waterw. Port Coastal Oc. Eng.*, 121(5):251–261, 1995.

[178] G. Wei, J.T. Kirby, S.T. Grilli, and R. Subramanya. A fully nonlinear Boussinesq model for surface waves. Part 1. Highly nonlinear unsteady waves. *J. Fluid Mech.*, 294:71–92, 1995.

[179] G.B. Whitham. *Linear and Nonlinear Waves*. Wiley Inter-Science, 1st edition, 1974.

[180] J.M. Witting. A unified model for the evolution of nonlinear water waves. *J. Comput. Phys.*, 56:203–236, 1984.

[181] S.-B. Woo and P.L.-F. Liu. A Petrov-Galerkin finite element model for one-dimensional fully non-linear and weakly dispersive wave propagation. *Int. J. Numer. Meth. Fluids*, 37:541–575, 2001.

[182] S.-B. Woo and P.L.-F. Liu. Finite-element model for modified Boussinesq equations. II : Applications to nonlinear harbor oscillations. *J. Waterw. Port Coastal Oc. Eng.*, 130(1):17–28, 2004.

[183] H.H. Yeh and K.-M. Mok. On turbulence on bores. *Phys. FLuids*, 2(5):821–828, 1990.

[184] J.A. Zelt. The run-up of nonbreaking and breaking solitary waves. *Coastal Eng.*, 15:205–246, 1991.

Appendices

Appendix A

Obtention des Équations de Serre sur Fond Variable

Le modèle de Boussinesq choisi constitue une extension des équations de Serre [140] vers des applications sur fond variable. Nous obtenons par la suite ce système à partir des équations du mouvement pour un écoulement parfait. L'adimensionnalisation des équations s'effectue en introduisant les variables et paramètres suivants,

$$\begin{array}{ccc} x = L\,x^* \;, & z = h_0\,z^* \;, & t = L\,c_0^{-1}\,t^* \;, \\ \xi = h_0\,\xi^* \;, & \eta = a\,\eta^* \;, & p = \rho\,c_0^2\,p^* \;, \\ \epsilon = \frac{a}{h_0} \;, & \sigma = \frac{h_0}{L} \;, & \lambda = \frac{\zeta_0}{L} \;, \end{array} \tag{A.1}$$

avec * l'indice désignant les variables adimensionnelles, x et z étant respectivement les coordonnées horizontale et verticale, t le temps, $\xi = -h_0 + \zeta$ la cote du fond avec $\zeta = h_0\,\lambda\,\zeta^*$ la distance algébrique verticale entre la référence $z = -h_0$ et le fond, η la cote verticale de la surface libre, p la pression, ρ la masse volumique du fluide, et g l'accélération de gravité (voir Figure A.1). Par ailleurs nous avons introduit L et a comme la longueur et l'amplitude caractéristique des ondes, $c_0 = \sqrt{g h_0}$ la vitesse de référence associée, h_0 la hauteur d'eau caractéristique dans la zone étudiée et ζ_0 l'amplitude caractéristique des variations du fond. De cette adimensionnalisation résultent trois paramètres caractéristiques, ϵ, σ et λ, qui tiennent compte respectivement de l'importance relative des non-linéarités, de la dispersion et des variations spatiales du fond. De plus nous introduissons l'opérateur de moyenne sur la profondeur totale d'eau,

$$\overline{f^*} = \frac{1}{\epsilon\eta - \xi^*} \int_{\xi^*}^{\epsilon\eta^*} f^*(x^*, z^*, t^*)\,dz^*. \tag{A.2}$$

À l'aide des définitions présentées ci-dessus, il est possible d'écrire l'équation po-

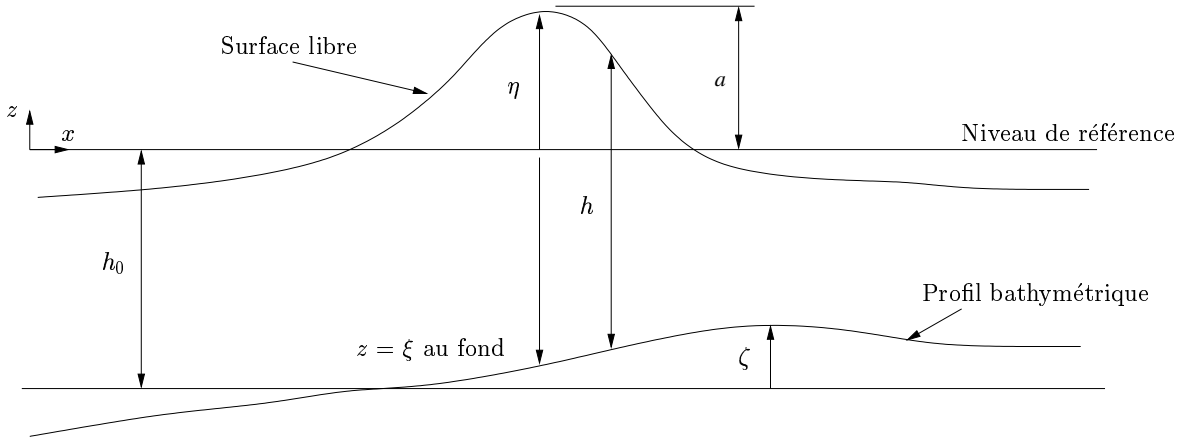

Figure A.1: Définition schématique des variables dimensionnelles pour une vague se propageant sur un fond irrégulier. $z = \eta$ correspond à la position de la surface libre, $z = \xi$ est la coordonnée vericale du fond (ξ étant ici une valeur négative), et $h = \eta - \xi$ est la hauteur d'eau instantannée.

tentielle, en variables adimensionnelles, associée aux équations de conservation de la masse et de la quantité de mouvement. Nous en déduisons le champ de vitesses compatible avec les équations qui gouvernent le mouvement des ondes de gravité dans un fluide parfait et irrotationnel en prenant soin de retenir tous les termes jusqu'à $O(\sigma^2)$. Aucune hypothèse ne sera introduite concernant la grandeur relative du paramètre ϵ car celui-ci est de $O(1)$ près du point de déferlement. En ce qui suit, nous ne tiendrons pas compte des indices * par commodité.

En variables adimensionnelles, le système d'équations en termes du potentiel de vitesses, $\phi(x, z, t)$, s'écrit de la manière suivante (voir par exemple les références [110, 115]),

$$\phi_{xx} + \frac{1}{\sigma^2}\phi_{zz} = 0 \quad \text{pour } \xi < z < \epsilon\eta, \tag{A.3}$$

$$\eta_t + \epsilon\phi_x\eta_x - \frac{1}{\sigma^2}\phi_z = 0 \quad \text{pour } z = \epsilon\eta, \tag{A.4}$$

$$\phi_t + \eta + \frac{1}{2}\epsilon\left(\phi_x^2 + \frac{1}{\sigma^2}\phi_z^2\right) = 0 \quad \text{pour } z = \epsilon\eta, \tag{A.5}$$

$$\frac{1}{\sigma^2}\phi_z - \xi_x\phi_x = 0 \quad \text{pour } z = \xi. \tag{A.6}$$

Développons maintenant la fonction potentielle $\phi(x, z, t)$ en une série de puissances de $z - \xi$ en introduisant une séparation des variables verticale et horizontale. La série de puissances s'écrit alors,

$$\phi(x, z, t) \;=\; \sum_{n=0}^{\infty} \frac{(z - \xi(x))^n}{n!}\, \Phi_n(x, t), \tag{A.7}$$

avec Φ_n les coefficients de la série.

En remplaçant la série (A.7) dans les équations (A.3) et (A.6) nous obtenons une définition récurrente des coefficients Φ_n,

$$\left\{ \begin{array}{ll} \Phi_1(x,t) & = \sigma^2[1+(\sigma\xi_x)^2]^{-1}\xi_x\frac{\partial\Phi_0}{\partial x} \\ \Phi_{(n+2)}(x,t) & = -\sigma^2[1+(\sigma\xi_x)^2]^{-1}\left[\frac{\partial^2\Phi_n}{\partial x\partial x} - \xi_x\frac{\partial\Phi_{(n+1)}}{\partial x} - \frac{\partial}{\partial x}(\xi_x\Phi_{(n+1)})\right] \end{array} \right. \tag{A.8}$$

avec $\Phi_0(x,t)$ étant le potentiel de vitesse évalué au fond ($z=\xi$). En supposant que λ est au plus de l'ordre $O(1)$ (i.e. $\xi_x \sim O(1)$), les coefficients de la série s'écrivent,

$$\left\{ \begin{array}{ll} \Phi_1(x,t) & = \sigma^2[1-(\sigma\xi_x)^2]\xi_x\frac{\Phi_0}{\partial x} + O(\sigma^4) \\ \Phi_{(n+2)}(x,t) & = -\sigma^2[1-(\sigma\xi_x)^2]\left[\frac{\partial^2\Phi_n}{\partial x\partial x} - \xi_x\frac{\partial\Phi_{(n+1)}}{\partial x} - \frac{\partial}{\partial x}(\xi_x\Phi_{(n+1)})\right] + O(\sigma^4) \end{array} \right. \tag{A.9}$$

La fonction potentielle de vitesses peut donc être estimée de la manière suivante,

$$\phi(x,z,t) \;=\; \Phi_0 - \sigma^2\frac{\partial}{\partial x}\left\{\frac{(z-\xi)^2}{2}\frac{\partial\Phi_0}{\partial x}\right\} + O(\sigma^4). \tag{A.10}$$

En définissant la vitesse horizontale évaluée au fond comme $u_0(x,t) = \frac{\partial\Phi_0}{\partial x}$, nous obtenons à partir de l'équation (A.10) les profils de vitesses horizontale et verticale,

$$u(x,z,t) \;=\; \phi_x = u_0 - \sigma^2\frac{\partial^2}{\partial x\partial x}\left\{\frac{(z-\xi)^2}{2}u_0\right\} + O(\sigma^4), \tag{A.11}$$

$$w(x,z,t) \;=\; \frac{1}{\sigma^2}\,\phi_z = -\frac{\partial}{\partial x}\left\{(z-\xi)u_0\right\} + O(\sigma^2). \tag{A.12}$$

Pour éliminer la coordonnée verticale z de l'expression (A.11), il suffit d'appliquer l'opérateur (A.2). Nous obtenons alors la vitesse horizontale moyennée sur la profondeur d'eau,

$$\begin{aligned} \bar{u}(x,t) \;=\; & [1-(\sigma\xi_x)^2]u_0 + \sigma^2\frac{(\epsilon\eta-\xi)}{2}(2\xi_x\frac{\partial u_0}{\partial x} + \xi_{xx}u_0) - \\ & -\sigma^2\frac{(\epsilon\eta-\xi)^2}{6}\frac{\partial^2 u_0}{\partial x\partial x} + O(\sigma^4). \end{aligned} \tag{A.13}$$

En inversant la relation précédente nous pouvons écrire pour la vitesse horizontale évaluée au fond,

$$u_0(x,t) = [1+(\sigma\xi_x)^2]\bar{u} - \sigma^2\frac{(\epsilon\eta-\xi)}{2}(2\xi_x\bar{u}_x + \xi_{xx}\bar{u}) + \sigma^2\frac{(\epsilon\eta-\xi)^2}{6}\bar{u}_{xx} + O(\sigma^4). \tag{A.14}$$

Ce qui nous autorise à exprimer le champ de vitesses compatible avec l'équation (A.3) et la condition aux limites (A.6) comme,

$$\begin{aligned} u(x,z,t) \;=\; & \bar{u} - \sigma^2\left[\frac{(\epsilon\eta-\xi)}{2} + (z-\xi)\right](2\xi_x\bar{u}_x + \xi_{xx}\bar{u}) + \\ & +\sigma^2\left[\frac{(\epsilon\eta-\xi)^2}{6} - \frac{(z-\xi)^2}{2}\right]\bar{u}_{xx} + O(\sigma^4) \end{aligned} \tag{A.15}$$

$$v(x,z,t) \;=\; -\frac{\partial}{\partial x}\left\{(z-\xi)\bar{u}\right\} + O(\sigma^2) \tag{A.16}$$

Le système d'équations de Serre sur fond variable s'obtient en remplaçant le champ de vitesses donné par les expressions (A.15) et (A.16) dans les équations de continuité et de conservation de la quantité de mouvement moyennées sur la profondeur totale d'eau. Ces équations sont présentées ci-dessous,

$$\frac{\partial \eta}{\partial t} + \frac{\partial}{\partial x}\left\{(\epsilon\eta - \xi)\bar{u}\right\} = 0, \tag{A.17}$$

$$\epsilon\frac{\partial}{\partial t}\left\{(\epsilon\eta - \xi)\bar{u}\right\} + \frac{\partial}{\partial x}\left\{(\epsilon\eta - \xi)(\epsilon^2\overline{u^2} + \bar{p})\right\} + \xi_x\, p|_\xi = 0, \tag{A.18}$$

$$p(x,z,t) = (\epsilon\eta - z) + \epsilon\sigma^2 \int_z^{\epsilon\eta} \Gamma(x,z,t)\, dz, \tag{A.19}$$

avec $\Gamma(x,z,t) = w_t + \epsilon(uw_x + ww_z)$ étant l'accélération verticale du fluide.

Il est important de noter que ce système constitue une forme «exacte» des équations du mouvement pour le cas d'un fluide parfait. L'utilisation du champ de vitesses exprimé par les relations (A.15) et (A.16) conduit au système de Serre qui constituera donc une approximation à l'ordre $O(\sigma^4)$. Avant d'être en mesure d'écrire ce système, il nous faut exprimer les intégrales qui apparaissent dans les équations (A.17)-(A.19). En utilisant les définitions pour les profils des vitesses on montre que,

$$\overline{u^2} = \bar{u}^2 + O(\sigma^4), \tag{A.20}$$

$$\bar{p} = \frac{1}{2}(\epsilon\eta - \xi) + \epsilon\sigma^2(\epsilon\eta - \xi)^{-1} \int_\xi^{\epsilon\eta} (z - \xi)\Gamma(x,z,t)\, dz, \tag{A.21}$$

$$p|_\xi = (\epsilon\eta - \xi) + \epsilon\sigma^2 \int_\xi^{\epsilon\eta} \Gamma(x,z,t)\, dz, \tag{A.22}$$

Similairement, l'accélération verticale peut être estimée comme,

$$\Gamma(x,z,t) = \left[\frac{(z-\xi)}{(\epsilon\eta - \xi)}\mathcal{P}(x,t) + \mathcal{Q}(x,t)\right] + O(\sigma^2) \tag{A.23}$$

où nous avons introduit deux nouvelles fonctions en rapport avec l'estimation de l'accélération verticale du fluide à la surface libre,

$$\mathcal{P}(x,t) = -(\epsilon\eta - \xi)(\bar{u}_{xt} + \epsilon\bar{u}\bar{u}_{xx} - \epsilon\bar{u}_x^2),$$

et au fond,

$$\mathcal{Q}(x,t) = \xi_x(\bar{u}_t + \epsilon\bar{u}\bar{u}_x) + \epsilon\xi_{xx}\bar{u}^2.$$

Finalement, nous pouvons écrire les intégrales associées aux termes d'accélération verticale de la manière suivante :

$$\int_{\xi}^{\epsilon\eta} \Gamma(x,z,t)\,dz = (\epsilon\eta - \xi)\left(\frac{1}{2}\mathcal{P}(x,t) + \mathcal{Q}(x,t)\right) + O(\sigma^2)$$

$$\int_{\xi}^{\epsilon\eta} (z-\xi)\Gamma(x,z,t)\,dz = (\epsilon\eta - z)^2\left(\frac{1}{3}\mathcal{P}(x,t) + \frac{1}{2}\mathcal{Q}(x,t)\right) + O(\sigma^2)$$

En remplaçant les expressions qui viennent d'être déterminées dans l'équation de quantité de mouvement horizontale (A.18), et en rappelant que $h = \epsilon\eta - z$, nous obtenons les équations du mouvement sur fond variable en retenant tous les termes jusqu'à l'ordre $O(\sigma^2)$,

$$\frac{\partial \eta}{\partial t} + \frac{\partial}{\partial x}\left\{h\,\bar{u}\right\} = 0, \tag{A.24}$$

$$\frac{\partial}{\partial t}\left\{h\bar{u}\right\} + \epsilon\frac{\partial}{\partial x}\left\{h\bar{u}^2\right\} + h\eta_x + \sigma^2\frac{\partial}{\partial x}\left[h^2\left(\frac{1}{3}\mathcal{P}(x,t) + \frac{1}{2}\mathcal{Q}(x,t)\right)\right] + \\ + \sigma^2\xi_x\,h\left(\frac{1}{2}\mathcal{P}(x,t) + \mathcal{Q}(x,t)\right) = \mathcal{O}(\sigma^4). \tag{A.25}$$

Il est facile de verifier que cette forme est équivalente au système d'équations de Serre sur fond variable écrit par Seabra-Santos et al. [136].

Appendix B

Total energy dissipated by shear stresses at the roller interface

The local rate of energy dissipation by turbulent shear stresses at the interface between the aerated region and the underlying flow reads (see Chapter 4 for variables and parameter definitions),

$$\frac{D_r}{\rho_r g c} = \frac{U}{c}\left(\frac{de^2}{dX} - e\,\sin\Phi\cos\Phi\right)\cos\Phi. \tag{B.1}$$

Using the shallow water approximation we can link the horizontal flow velocity with the water depth as $U/c = -d/h$. Using in addition the approximated expression for the mean location of the water depth, $h = (1 + \gamma/2 - X/d\,\tan\Phi)\,d$, we find,

$$\frac{U}{c} = -\frac{1}{\left(1 + \frac{\gamma}{2} - \frac{X}{d}\tan\Phi\right)}. \tag{B.2}$$

Now expanding function (B.1) in Taylor series about $\frac{X}{d}\tan\Phi$ invoking relation (B.2), we obtain,

$$\frac{D_r}{\rho_r g c} = -\frac{\cos\Phi}{\left(1+\frac{\gamma}{2}\right)}\left[1 + \frac{X\tan\Phi}{d\left(1+\frac{\gamma}{2}\right)}\right]\left(\frac{de^2}{dX} - e\,\sin\Phi\cos\Phi\right) + O(\frac{de}{dX}\tan^2\Phi, \tan^3\Phi). \tag{B.3}$$

We want to spatially integrate equation (B.3) over the roller length, l_r. Nonlinear

terms appearing above are computed using integration by parts as follows,

$$\int_0^{l_r} X\frac{de^2}{dX}\,dX = \left[X\,e^2\right]_0^{l_r} - \int_0^{l_r} e^2\,dX = -\int_0^{l_r} e^2\,dX, \tag{B.4}$$

$$-\sin\Phi\cos\Phi\int_0^{l_r} X\,e\,dX = -\frac{1}{2}\cos^2\Phi\tan\Phi\left[X^2 e\right]_0^{l_r} \tag{B.5}$$

$$+\frac{1}{2}\cos^2\Phi\tan\Phi\int_0^{l_r} X^2\frac{de}{dX}\,dX = O\left[\frac{de}{dx}\tan\Phi\right].$$

Consequently, the total energy dissipation by shear stresses at the interface is estimated as,

$$\begin{aligned}\mathrm{D_r} &= \int_0^{l_r} D_r\,\frac{dX}{\cos\Phi} \\ &= \frac{\rho_r g c}{\left(1+\frac{\gamma}{2}\right)}\left[A\sin\Phi\cos\Phi - \frac{\tan\Phi}{d\left(1+\frac{\gamma}{2}\right)}\int_0^{l_r} e^2\,dX\right] + O\left(\tan^3\Phi, \tan^2\Phi\frac{de}{dX}\right),\end{aligned} \tag{B.6}$$

where $A = \int_0^{l_r} e\,dX$.

Appendix C

Article Révue Européenne de Génie Civil

Appendix D

Conference Proceeding ICCE 2004

Appendix E

Conference Proceeding WAVES 2005